

Numerical and Experimental Studies on an Automotive Air Conditioning System

A THESIS

SUBMITTED FOR THE DEGREE OF

Doctor of Philosophy

IN THE FACULTY OF ENGINEERING

BY

Yogendra Vasantrya Kuwar



DEPARTMENT OF MECHANICAL ENGINEERING

INDIAN INSTITUTE OF SCIENCE

BANGALORE - 560 012

JULY 2019

'A student is always to be in a pursuit of knowledge'

*To my
Parents and Teachers*

Acknowledgements

I am grateful to the Indian institute of Science (IISc) for providing me an opportunity to carry out my research work here. I feel deeply indebted to several people and thank them for supporting me all through my research work at IISc, Bangalore.

This dissertation would not have been possible without the guidance of Dr. G. S. V. L. Narasimham who gave his valuable inputs in the preparation and completion of this study. His extreme cooperation and complete involvement in the research were instrumental in bringing this thesis up to its complete form. His constant support during bad times and a pat on the back for the encouragement were always timed exquisitely. I also thank Dr. G.S.V.L Narasimham's family for being friendly and cordial with me.

I express my sincere thanks to Prof. Pradip Dutta, Chairman of the Department of Mechanical Engineering, Indian Institute of Science, Bangalore, for his support.

My sincere thanks to Prof. Raghuraman N. Govardhan, for his valuable suggestions offered during my comprehensive examination in the department.

The staff of the Department of Mechanical Engineering, Indian Institute of Science, Bangalore, were very helpful for all the official works. I would like to thank my friends for all the valuable time we spent together and for making my stay at IISc a memorable one.

I am also thankful to Mr. Visheswara Rao and the employees of AVAS Pvt. Ltd., Peenya (Bangalore) for helping me in designing and fabricating the experimental test rig of the AAC system.

It was a pleasure to be a part of the Frisbee Club, Cricket club and the gym of Gymkhana and I thank all the members of the clubs for the fun and entertainment we had during various tournaments.

Last but not the least, I thank my family for their love and support in all good and bad phases of life and believing on me and my potential, and giving me the strength to plod on despite my constitution wanting to give up and throw in the towel; thank you so much.

Yogendra Vasantryao Kuwar

Abstract

The aim of the present study is to make a comparison of the performance of an Automotive Air Conditioning System with R134a and R1234yf refrigerants. To this end, a computer simulation model has been developed in the present study for a small capacity automotive air conditioning system with R134a and R1234yf refrigerants. An experimental facility has been developed for testing the automobile air conditioning system and experiments are conducted with R134a. The results of mathematical simulation and experiments are compared for R134a for various operating conditions. The performance of the system for various ambient conditions is predicted for both R134a and R1234yf. The four major components of automobile air conditioning system are a swash plate compressor, thermostatic expansion valve and compact geometry heat exchangers (evaporator and condenser). From the submodels of the components, an integrated mathematical model for the system is built up. The air conditioning system of an automobile has the main function of providing human comfort, i.e., desired temperature and humidity and air quality for cabin air. The automobile air conditioning system considered in this study pertains to a small passenger car of typical cooling capacity 3.5 kW (\approx 1 TR). The performance of system is predicted for actual conditions of operation encountered by the automobile air conditioning system. The different inputs of computer simulation are the rotational speed of compressor, and the temperature and velocity of air entering the condenser. For the various input parameters, the mathematical simulation calculates the system performance. Two simulation codes are developed one for each of the two refrigerants, namely, R134a and R1234yf. The results of the mathematical simulation model are compared and validated with the experimental results. The test rig of the system is built on a stationary metal frame with core system components fixed on the frame along with measuring instruments and air flow ducts. The compressor is run by a three-phase induction motor through a V-belt and frequency converter for achieving various rotational speeds. Plastic ducts are provided for evaporator and condenser to maintain a steady air flow with the desired quantity of air. Pressure and temperature sensors are provided at different points on the system on the air side as well as in the refrigerant circuit. A load estimation analysis is made to predict the total heat gain by the cabin for various locations and dates of the year, in particular for Bangalore for typical summer condition. Both diffuse and direct solar radiation are considered in the load es-

timation. From the load estimation it is found that for a small passenger car (5 to 6 passengers) the load value is in the range of 3 kW to 4 kW. The equations for actual volumetric and isentropic work efficiencies of the compressor are obtained from the experimental data for various compressor speeds. The power lost due to frictional effect in the compressor moving elements in the form of heat is obtained experimentally for various speeds of compressor. In the mathematical model, the thermodynamic properties and transport properties of the refrigerants are duly considered. The equations for the thermodynamic properties and transport properties of R134a and R1234yf are obtained from published literature and some of them by solving the Helmholtz free energy equation in the form of density and temperature. The properties of moist air also required for the mathematical model for which correlations are built into the codes. The numerical and experimental results of R134a show fair agreement in respect of the quantities like mass flow rate, evaporator capacity, coefficient of performance, condenser capacity and compressor work with a deviation below 20%. The numerical results obtained for both the refrigerants show that there is no wide difference in the performance of the system with the refrigerants R134a and R1234yf, although the performance with R134a is better. The differences between these refrigerants in some quantities are up to 20%, most of the differences being less than 10%. The results have shown that the performance with R1234yf is only slightly less than that with R134a. The effects of compressor speed, condenser air velocity and condenser air inlet temperature on evaporator capacity, COP, condenser capacity, evaporator air outlet temperature and humidity ratio are predicted. Higher condenser air velocity, lower condenser air inlet temperature and higher compressor speed produced better performance. In case of the evaporator, the heat transfer coefficient in the presence of wet surface is greater than that of the dry surface. Thermodynamic and transport properties of R134a and R1234yf are found to be similar and agree very well with REFPROP software values.

Nomenclature

A_{Dl}	area on which profile drag occurs	m^2
A_e	end region heat transfer area	m^2
A_l	louvered heat transfer area	m^2
A_o	outside heat transfer area	m^2
A_r	end region aspect ratio	non-dimensional
A_{s1}	plain leading and trailing heat transfer area	m^2
A_{s2}	plain turn-around heat transfer area	m^2
A_{fin}	fin surface area	m^2
$A_{u,fin}$	un-fin surface area	m^2
A_i	inner side area	m^2
A_{fr}	frontal area	m^2
A_{tm}	mean tube heat transfer area	m^2
A_{top}	top surface area of vehicle	m^2
A_{dir}	area of vehicle exposed to direct solar radiation	m^2
A_{glass}	area of glass surface of vehicle	m^2
$A_{c,p}$	cross-sectional area of the tube	m^2
$A_{evp,duct}$	cross sectional area of evaporator duct	m^2
$A_{cond,duct}$	cross sectional area of condenser duct	m^2
A_{comp}	total heat lost area of compressor	m^2
a	distance from fin base that is not louvered	m
B_η^*	reduced second viscosity virial coefficient	non-dimensional
B_o	boiling number	non-dimensional
b'_i	slop of the air sat curve at the inner tube temps	J/kg.K
b_f	slop of the air sat curve between the fin tip temp and outer tube temp	J/kg.K
C_o	convection number	non-dimensional
c_p	specific heat of liquid at constant pressure	kJ/kg.K

c_v	specific heat of liquid at constant volume	kJ/kg.K
C_p^*	ideal gas specific heat	J/mol.K
C_{Dl}	drag coefficient on the louvers	non-dimensional
C_c	contraction loss coefficient	non-dimensional
C_R	heat capacity ratio	non-dimensional
c_{pda}	specific heat of dry air	kJ/kg.K
c_{pma}	specific heat of moist air	kJ/kg.K
c_{plw}	specific heat of dry liquid water	kJ/kg.K
c_{pwv}	specific heat of water vapour	kJ/kg.K
c_{pr}	specific heat of refrigerant	kJ/kg.K
D_c	compressor cylinder diameter	m
D_{he}	hydraulic diameter of end region of fin	m
D_h	hydraulic diameter	m
D	diameter of tube	m
D_{cond}	depth of condenser	m
D_{evp}	depth of evaporator	m
E	electric power consume by compressor	kWh
F	polar light agent for R134a	non-dimensional
F_D	fin depth in the air flow direction	m
F_p	fin pitch	m
F_{th}	fin thickness	m
F_e	flow efficiency	non-dimensional
f_o	dry surface friction factor	non-dimensional
$f_{o,w}$	wet surface friction factor for louvers	non-dimensional
f_{lo}	friction factor for entire flow as liquid	non-dimensional
Fr_{le}	Froude number	non-dimensional

G	refrigerant mass velocity	kg/s.m
Ga	Galileo number	non-dimensional
g	acceleration due to earth gravity	m/s ²
h_v	refrigerant vapour enthalpy	J/kg
h_s	refrigerant superheat vapour enthalpy	J/kg
k_L	refrigerant liquid thermal conductivity	W/m.K
s	refrigerant specific entropy	J/kg.K
h_o	air-side heat transfer coefficient	W/m ² K
$h_{ma,F}$	fictitious moist air enthalpy	J/kg
h_i	air heat transfer coefficient for vehicle inside	W/m ² K
h_r	refrigerant-side heat transfer coefficient	J/kg.K
h_L	heat transfer coefficient for for all mass flow as a liquid	W/m ² K
h_l	air-side heat transfer coefficient for louvers	W/m ² K
h_{s1}	air-side heat transfer coefficient for s1 region	W/m ² K
h_e	air-side heat transfer coefficient for end region	W/m ² K
L_1	louver length	m
S_1	nonlouvered inlet and exit fin region	m
S_2	re-direction length	m
L_p	louver pitch	m
k	air thermal conductivity	W/mK
k_{fin}	fin thermal conductivity	W/mK
k_m	thermal conductivity of vehicle metal body	W/mK
k_{cov}	thermal conductivity of interior covers of vehicle	W/mK
H	fin height	m
k_v	refrigerant vapour thermal conductivity	W/mK
i_{lv}	latent heat of vaporization	J/kg
$h_{o,w}$	wet h_o corresponding to total heat transfer rate	W/m ² K

k_p	tube thermal conductivity	W/m ² K
I_{bn}	normal direct solar radiation	W/m ²
H_b	direct solar radiation	W/m ²
H_d	diffused solar radiation	W/m ²
H_g	global solar radiation	W/m ²
L_{top}	length of top roof of vehicle	m
k_{glass}	glass thermal conductivity	W/m ² K
L_{bot}	length of bottom surface exposed to road	m
h_{bot}	heat transfer coefficient between road and vehicle	W/m ² K
H_{cond}	length of condenser	m
H_{Evp}	length of evaporator	m
L_{evp}	heat load on evaporator	kW
M	molecular weight	g/mol
\dot{m}_r	refrigerant mass flow rate	kg/s
\dot{m}_a	air mass rate	kg/s
P	absolute pressure	Pa
P_{sat}	absolute saturate pressure	Pa
P_c	absolute critical pressure	Pa
P_{atm}	atmospheric pressure	Pa
R	universal gas constant	J/kmole.K
P_1	pressure at compressor inlet	Pa
P_2	pressure at compressor outlet	Pa
N_A	Avogadros constant	mol ⁻¹
n	number of cylinders in compressor	non-dimensional
N	rotational speed of compressor (rpm), day number (non-dimension)	
\dot{W}_{comp}	compressor power	kW

\dot{Q}_{cond}	heat rejection rate of condenser	kW
\dot{q}	heat flux	W/m ²
\dot{Q}_{evp}	evaporator capacity	W
N_l	number of louvers on fin	non-dimensional
P_r	Prandtl number	non-dimensional
Re	Reynolds number	non-dimensional
Nu	Nusselts number	non-dimensional
Re_{Lp}	Reynolds number for louver pitch	non-dimensional
Re_{S1}	Reynolds number for S1	non-dimensional
Re_{S2}	Reynolds number for S2	non-dimensional
Re_{Dh}	Reynolds number hydraulic diameter	non-dimensional
Re_l	Reynolds number for liquid phase flowing along	non-dimensional
Re_{lo}	Reynolds number for entire flow as liquid	non-dimensional
NTU	number of heat transfer units	non-dimensional
N_c	number of channels in tube	non-dimensional
Q_{load}	total heat gain	W
T	absolute temperature	°C
T_c	critical temperature	°C
T_R	ratio of T/T_c	non-dimentional
T_s	superheat temperature	°C
s	specific entropy	J/kg.K
S_c	compressor cylinder stroke length	m
S_p	relative piston stroke length	non-dimentional
T_p	tube pitch	m
T_w	tube width	m
u_{fr}	frontal velocity	m/s

u_1	louver velocity	m/s
u_{acc}	accelerated air flow velocity	m/s
t	tube thickness	m
w_c	tube channel width	m
w_w	tube channel height	m
$T_{w,m}$	mean water film temperature	°C
$T_{p,m}$	mean tube temperature	°C
U_o	air flow velocity flow over top of vehicle	m/s
U_i	air flow velocity flow over bottom of vehicle	m/s
$V_{evp,avg}$	average air velocity at evaporator	m/s
$T_{s,o}$	temperature of top surface of vehicle	°C
T_i	vehicle inside cabin air temperature	°C
T_{sky}	sky temperature	°C
t_m	metal body thickness of vehicle	m
t_{cov}	interior cover thickness of vehicle	m
t_{glass}	window glass thickness of vehicle	m
T_{road}	road surface temperature	°C
W_{cond}	condenser width	m
W_{evp}	evaporator width	m
t_f	fin thickness	m
t_t	tube wall thickness	m
T_a	air temperature	°C
T_r	refrigerant temperature	°C
t	time	min
V_a	air velocity	m/s
U	over all heat transfer coefficient	W/m ² .K
W	humidity ratio	kg/kg of dry air

Z	elevation from mean sea level	m
x	dryness fraction	non-dimensional
x^+	non-dimensional duct length	non-dimensional
Nu_d	Nusselt number for mix convection	non-dimensional
Nu_{dF}	Nusselt number for force convection	non-dimensional
Re_d	Reynolds number based on diameter	non-dimensional
Gr_d	Grashof number based on diameter	non-dimensional
\dot{Q}_{mix}	heat loss due to mix convection	W
\dot{Q}_{rad}	heat loss due to radiation	W

Greek Letter

ρ	density (kg/m ³) and reflectivity of metal body (non-dimensional)	
η	dynamic viscosity	Pa.s
λ'	thermal conductivity	W/m.K
v	specific volume	m ³ /kg
Ω	collision integral(non-dimensional),angle between tube axis and horizontal(degree)	
σ	collision diameter(nm),ratio of frontal velocity to minimum area velocity(non-dimensional)	
μ	dynamic viscosity	Pa.S
α	Helmholtz energy(non-dimensional),absorptivity of glass(non-dimensional)	
β_η	second viscosity viral coefficient	non-dimensional
η_v	volumetric efficiency	
η_i	isentropic efficiency	
η_f	fin efficiency	
η_m	motor efficiency	
η_t	transmission efficiency	
ϵ	pressure ratio(non-dimensional), effectiveness of fin(non-dimensional), contraction ratio(non-dimensional)	
θ	louver angle	radian
ϕ	latitude angle(degree),relative humidity of air(%)	
δ	declination angle	degree
ω	hour angle	degree
θ_z	Zenith angle	degree
ϵ_m	emissivity of metal	non-dimensional
τ	transmissivity of glass	non-dimensional

Acronyms

AACS	Automotive Air Conditioning System
CFC	Chlorofluorocarbon
COP	Coefficient of Performance
FCC	Fixed Capacity Compressor
GWP	Global Warming Potential
HFC	Hydrofluorocarbon
ODP	Ozone Deflection Potential
PSL	Piston Stroke Length
RPM	Revolution Per Minute
RH	Relative Humidity
TXV	Thermostatic Expansion Valve
VDSC	Variable Displacement Swash Plate Compressor
VCC	Variable Capacity Compressor

Subscripts

a	air
r	refrigerant
comp, cm	compressor
cond, cn	condenser
evp	evaporator
txv	thermostatic expansion valve
in	inlet
out, o	outlet
i	initial/isentropic
f	final
sat	saturation or saturated
l	liquid/louver
c	critical/cylinder
v	vapour
s	superheat/suction
maj	major
min	minimum/minor
p	piston
d	discharge
e	louver end
fin	fin
lo	liquid alone
sc	sub-cooled
TP	two phase
exp	experimental
avg	average

Contents

Acknowledgement	iii
Abstract	v
List of Tables	xxii
List of Figures	xxiv
1 Introduction	1
1.1 Need for alternative refrigerants in automotive air conditioning systems	5
1.2 Need for new simulation and experimental studies on automotive air conditioning systems	8
1.3 Automotive Air-Conditioning System (AACS)	9
1.4 Evaporators used in AACS	11
1.5 Condensers used in AACS	13
1.6 Compressors used in AACS	13
1.7 Present work	15
1.7.1 Objectives of the present work	15
1.7.2 Description of the work done	16
1.7.3 Organisation of the thesis	18
2 Literature Review	20
2.1 Automobile Air Conditioning System	20
2.1.1 Alternative refrigerants in place of R134a	21
2.1.2 Substitution of R1234yf in place of R134a in AACS	23
2.1.3 Energy and exergy analysis of AAC systems	24
2.1.4 AACS with swash plate compressor	25

2.1.5	Simulation and modelling of AACs	26
2.1.6	Performance enhancement strategies for AACs	28
2.2	Mathematical models and performance of swash plate compressor	29
2.3	Heat transfer and friction correlations for louver fin geometry	32
2.4	Heat transfer correlations for boiling in small channels	39
2.4.1	Classifications of channels	40
2.5	Heat transfer correlations for condensation in small channels	44
2.6	Pressure drop in two phase flow through small channels	56
2.7	Conclusions from the Literature review	58
3	System Analysis and Numerical Calculations	61
3.1	Correlations for the thermodynamic and transport properties of R134a	62
3.1.1	Liquid properties	63
3.1.2	Vapour properties	64
3.2	Correlations for the thermodynamic and transport properties of R1234yf	68
3.2.1	Liquid properties	68
3.2.2	Vapour properties	70
3.3	Mathematical model for the swash plate compressor	74
3.4	Correlations for flat-tube, louvered-fin condenser	80
3.4.1	Air side correlations	81
3.4.2	Refrigerant side correlations	84
3.5	Calculations for thermostatic expansion valve(TXV)	88
3.6	Correlations for flat-tube, louvered-fin evaporator	89
3.7	Moist air thermodynamic and transport property relations	97
3.7.1	Thermodynamic properties	98
3.7.2	Transport properties	100
3.8	Heat load estimation for small AAC system	101
3.9	Algorithm for computer code and geometrical data	110
3.10	Geometrical and operating data required for the computer code	114

3.10.1	Swash plate compressor.	114
3.10.2	Flat-tube louvered fin condenser.	114
3.10.3	Flat tube louvered fin evaporator.	116
4	Experimental Facility and Procedures	118
4.1	Introduction	118
4.2	Core automotive AC system	121
4.2.1	Swash plate compressor	121
4.2.2	Evaporator	122
4.2.3	Condenser	123
4.2.4	Thermostatic expansion valve (TXV)	125
4.2.5	Dryer or Receiver:	126
4.2.6	Pipes and Fittings	127
4.3	Measuring instruments and electrical equipments	128
4.3.1	Electrical equipments	128
4.3.2	Measuring instruments	132
4.4	Construction of the experimental test facility	139
4.5	Charging of the AAC System with refrigerant	140
4.6	Experimental procedure	142
5	Results and Discussion	144
5.1	Method of calculation of various quantities	144
5.1.1	Evaporator capacity (\dot{Q}_{evp})	145
5.1.2	Refrigerant mass flow rate (\dot{m}_r)	145
5.1.3	Condenser capacity (\dot{Q}_{cond})	145
5.1.4	Compressor power (\dot{W}_{comp})	146
5.1.5	Actual volumetric efficiency ($\eta_{a,v}$)	146
5.1.6	Isentropic work efficiency ($\eta_{i,w}$)	149
5.1.7	Heat loss from the compressor body due to friction (\dot{Q}_{loss})	149

5.2	Volume ratio (r_v)	152
5.3	Pressure ratio (r_p)	155
5.4	Refrigerant mass flow rate (\dot{m}_r)	158
5.5	Actual volumetric efficiency ($\eta_{a,v}$)	160
5.6	Isentropic work efficiency ($\eta_{i,w}$)	163
5.7	Compressor heat loss (\dot{Q}_{loss})	165
5.8	Compressor work (\dot{W}_{comp})	168
5.9	Condenser capacity (\dot{Q}_{cond})	171
5.10	Evaporator capacity (\dot{Q}_{evp})	174
5.11	Coefficient of performance (COP)	177
5.12	Air temperature at evaporator outlet ($T_{a,\text{evp},o}$)	180
5.13	Humidity ratio at evaporator outlet ($W_{a,\text{evp},o}$)	183
5.14	Relative humidity at evaporator outlet ($\phi_{a,\text{evp},o}$)	186
5.15	Air side dry and wet surface heat transfer coefficient (h_o) and ($h_{o,w}$)	186
5.16	Air side dry and wet surface friction factor (f_o) and ($f_{o,w}$)	187
5.17	Air side dry and wet finned-surface efficiency (η_o) and ($\eta_{o,w}$)	188
5.18	Experimental repeatability tests and error bars	189
5.19	Conclusions	190
5.20	Suggestions for further work	191

List of Tables

1.1	Comparison between R12, R134a and R1234yf.	6
3.1	Constants in Eq. 3.1.	62
3.2	Constants in Eq. 3.3.	63
3.3	Constants in Eq. 3.4.	64
3.4	Constants in Eq. 3.5.	64
3.5	Constants in Eq. 3.1.	65
3.6	Constants in Eq. 3.15.	67
3.7	Constants in Eq. 3.19.	68
3.8	Constants in Eq. 3.20.	69
3.9	Constants in Eq. 3.29.	71
3.10	Constants in Eq. 3.30.	71
3.11	Constants in Eq.(3.37), (3.38), (3.39), (3.40), (3.41) and (3.42).	74
3.12	Various areas of condenser element.	82
3.13	Constants used to calculate the Colburn j - and Fanning f -factors in Eqs. 3.55 and 3.60.	84
3.14	Various areas of evaporator element.	91
3.15	Constants to calculate the wet Colburn j - and Fanning f -factors in Eqs. 3.86 and 3.92.	93
5.1	Range of operating variable	152
A.1	Experimental data for $V_A=1.5$ m/s and $T_J=26$ °C	192
A.2	Experimental data for $V_A=1.5$ m/s and $T_J=28$ °C	193
A.3	Experimental Data for $V_A=1.5$ m/s and $T_J=30$ °C	193

A.4	Experimental Data for $V_A=1.5$ m/s and $T_J=34$ °C	194
A.5	Experimental Data for $V_A=1.0$ m/s and $T_J=26$ °C	194
A.6	Experimental Data for $V_A=1.0$ m/s and $T_J=28$ °C	195
A.7	Experimental Data for $V_A=1.0$ m/s and $T_J=30$ °C	195
A.8	Experimental Data for $V_A=1.0$ m/s and $T_J=34$ °C	196
A.9	Experimental performance variables for R134a	197
A.10	Continue experimental performance variables for R134a	198
A.11	Continue experimental performance variables for R134a	199
A.12	Numerical simulation performance variables for R134a	200
A.13	Continue numerical simulation performance variables for R134a	201
A.14	Continue numerical simulation performance Variables for R134a	202
A.15	Numerical simulation performance variables for R134a	203
A.16	continue numerical simulation performance variables for R134a	204
A.17	Numerical simulation performance variables for R1234yf	205
A.18	Continue numerical simulation performance Variables for R1234yf	206
A.19	Continue numerical simulation performance Variables for R1234yf	207
A.20	Numerical simulation performance variables for R1234yf	208
A.21	continue numerical simulation performance variables for R1234yf	209
A.22	Numerical simulation performance variables for air side	210
A.23	Comparison between experimental and numerical simulation results.	211
A.24	Comparison of formulated R134a saturation properties with REFPROP data.	212
A.25	continue...comparison of formulated R134a saturation properties with REFPROP data.	213
A.26	Comparison of formulated R1234yf saturation properties with REFPROP data.	214
A.27	continue...comparison of formulated R1234yf saturation properties with REFPROP data.	215
A.28	Comparison of formulated R134a vapour properties with REFPROP data.	216
A.29	Comparison of formulated R1234yf vapour properties with REFPROP data.	216
A.30	Uncertainty estimation for various quantities of interest	221

List of Figures

1.1	Reversed Carnot cycle for refrigeration.	1
1.2	Standred vapour compression cycle	2
1.3	Actual vapour compression cycle	3
1.4	Basic four components of AACCS	9
1.5	Schematic diagram of AACCS	11
1.6	Actual evaporator used in experimental facility	12
1.7	Actual condenser used in experimental facility.	14
1.8	Swash plate compressor used in experimental facility.	15
1.9	Schematic diagram of swash plate compressor (<i>Tian and Zhang</i> [35]).	16
2.1	COP comparison between CO ₂ and R134a air conditioning systems, <i>Domanski et al.</i> [10]	21
2.2	Experimental variation of COP with the evaporation temperature under different condensation temperatures., <i>Chen et al.</i> [13]	22
2.3	Section through louver array indicating possible flow directions. (<i>Davenport</i> [38])	33
2.4	Stanton number curves for variants demonstrating transition from duct to flat-plate flow. (<i>Achaichia and Cowell</i> [39])	34
2.5	Mean flow angle dependence in a louvered fin array (<i>Achaichia and Cowell</i> [40])	35
2.6	Visualization of flow in the louvered fin array (<i>Kajino and Hiramatsu</i> [42])	36
2.7	Streamlines in a model of the louvered fin array (<i>Kajino and Hiramatsu</i> [42])	36
2.8	Different flow regimes encountered in flow boiling in a tube (<i>Cengel and Ghajar</i> [140])	39
2.9	(a) Reynolds number factor, f (b) Suppression factor, S , <i>Chen</i> [68]	41

2.10	The chart correlations given in <i>Shah</i> [48]	42
2.11	Flow patterns in condensation in horizontal tube, <i>Soliman</i> [86]	45
2.12	Flow pattern map, <i>Mandhane et al.</i> [78]	46
2.13	Flow pattern map, <i>Taitel and Dukler</i> [79]	47
2.14	Comparison between computed and measured Nusselt numbers for stratified, transitional and annular flow, <i>Jaster and Kosky</i> [91]	52
2.15	Comparison of heat transfer coefficient(left) and pressure drop(right) between R1234yf and R134a, <i>Cavallini et al.</i> [142]	55
3.1	Variation of volume ratio with compressor speed for 72 data points.	76
3.2	Variation of efficiency ratio with volume ratio for 72 data points.	77
3.3	Variation of isentropic work efficiency with compressor speed for 72 data points.	78
3.4	Variation of friction heat loss with compressor speed for 72 data points.	79
3.5	Fin arrays of condenser.	81
3.6	Condenser element with the tube and half fin on either side.	81
3.7	Condenser fin with louvers and tube channels.	82
3.8	Evaporator element cell shows wet surface and water film formation.	90
3.9	Evaporator fin shows louvers and tube channels.	90
3.10	Different types of heat loads gained by automotive	102
3.11	Reflected solar radiation from road surface.	107
3.12	Variation of total heat gained by the vehicle at different hour angles at $\phi = 13^\circ$, on 21 April	109
3.13	Variation of total heat gained by the vehicle at different hour angles for different capitals of India on 21 April, $T_o = 45^\circ C, U_o = 15m/s$	110
3.14	Flow chart for the numerical code for AACCS	113
4.1	Schematic of the experimental setup of the automotive AC system.	120
4.2	Swash plate compressor(top view and cut view)	122
4.3	Suction and discharge valve plates of compressor	122
4.4	Evaporator front view and top view	123

4.5	Evaporator tube cross section	123
4.6	Evaporator fin structure showing louvres	124
4.7	Condenser used in experiment set-up	124
4.8	Cross section of parallel tubes showing small channels in condenser.	125
4.9	Thermostatic expansion valve used in experiment set-up	125
4.10	Receiver or Dryer	126
4.11	Aluminium pipes and fittings.	127
4.12	Three-phase AC electric motor used in the experimental setup	129
4.13	Variable frequency converter drive.	130
4.14	Electric heating load coil and bulbs.	131
4.15	Electric fans used in condenser and evaporator.	131
4.16	Variable resistant coil (Rheostat).	132
4.17	K type thermocouple and display unit.	133
4.18	Pressure gauge and its position on aluminium block.	134
4.19	Differential Pressure Sensor.	135
4.20	Digital tachometer.	136
4.21	Three phase energy meter.	137
4.22	Anemometer.	138
4.23	Air temperature and humidity sensor.	139
4.24	Evaporator and condenser ducts are mounted on frame.	140
4.25	Refrigerant bottle and weigh balance device.	141
4.26	Refrigerant charging Kit.	142
4.27	Charging of system with R134a.	142
5.1	Actual pressure-volume diagram with pressure drop at the suction and discharge valves of compressor.	147
5.2	Volume ratio verse compressor speed.	148
5.3	Efficiency ratio verses volume ratio.	149
5.4	Energy balance for compressor.	150

5.5	Variation of volume ratio with compressor speed for $T_{a,cond,in} = 26\text{ }^{\circ}\text{C}$	153
5.6	Variation of volume ratio with compressor speed for $T_{a,cond,in} = 28\text{ }^{\circ}\text{C}$	154
5.7	Variation of volume ratio with compressor speed for $T_{a,cond,in} = 30\text{ }^{\circ}\text{C}$	154
5.8	Variation of volume ratio with compressor speed for $T_{a,cond,in} = 34\text{ }^{\circ}\text{C}$	155
5.9	Variation of pressure ratio with compressor speed for $T_{a,cond,in} = 26\text{ }^{\circ}\text{C}$	156
5.10	Variation of pressure ratio with compressor speed for $T_{a,cond,in} = 28\text{ }^{\circ}\text{C}$	156
5.11	Variation of pressure ratio with compressor speed for $T_{a,cond,in} = 30\text{ }^{\circ}\text{C}$	157
5.12	Variation of pressure ratio with compressor speed for $T_{a,cond,in} = 34\text{ }^{\circ}\text{C}$	157
5.13	Variation of refrigerant mass flow rate with compressor speed for $T_{a,cond,in} = 26\text{ }^{\circ}\text{C}$	158
5.14	Variation of refrigerant mass flow rate with compressor speed for $T_{a,cond,in} = 28\text{ }^{\circ}\text{C}$	159
5.15	Variation of refrigerant mass flow rate with compressor speed for $T_{a,cond,in} = 30\text{ }^{\circ}\text{C}$	159
5.16	Variation of refrigerant mass flow rate with compressor speed for $T_{a,cond,in} = 34\text{ }^{\circ}\text{C}$	160
5.17	Variation of actual volumetric efficiency with compressor speed for $T_{a,cond,in} = 26\text{ }^{\circ}\text{C}$	161
5.18	Variation of actual volumetric efficiency with compressor speed for $T_{a,cond,in} = 28\text{ }^{\circ}\text{C}$	161
5.19	Variation of actual volumetric efficiency with compressor speed for $T_{a,cond,in} = 30\text{ }^{\circ}\text{C}$	162
5.20	Variation of actual volumetric efficiency with compressor speed for $T_{a,cond,in} = 34\text{ }^{\circ}\text{C}$	162
5.21	Variation of Isentropic work efficiency with compressor speed for $T_{a,cond,in} = 26\text{ }^{\circ}\text{C}$	163
5.22	Variation of Isentropic work efficiency with compressor speed for $T_{a,cond,in} = 28\text{ }^{\circ}\text{C}$	164
5.23	Variation of Isentropic work efficiency with compressor speed for $T_{a,cond,in} = 30\text{ }^{\circ}\text{C}$	164
5.24	Variation of Isentropic work efficiency with compressor speed for $T_{a,cond,in} = 34\text{ }^{\circ}\text{C}$	165
5.25	Variation of compressor friction loss with compressor speed for $T_{a,cond,in} = 26\text{ }^{\circ}\text{C}$	166
5.26	Variation of compressor friction loss with compressor speed for $T_{a,cond,in} = 28\text{ }^{\circ}\text{C}$	166
5.27	Variation of compressor friction loss with compressor speed for $T_{a,cond,in} = 30\text{ }^{\circ}\text{C}$	167
5.28	Variation of compressor friction loss with compressor speed for $T_{a,cond,in} = 34\text{ }^{\circ}\text{C}$	167
5.29	Variation of compressor work with air temperature condenser inlet for $N = 600\text{ rpm}$	168
5.30	Variation of compressor work with air temperature condenser inlet for $N = 800\text{ rpm}$	169
5.31	Variation of compressor work with air temperature condenser inlet for $N = 1000\text{ rpm}$	169
5.32	Variation of compressor work with air temperature condenser inlet for $N = 1200\text{ rpm}$	170

5.33	Variation of compressor work with air temperature condenser inlet for $N = 1400$ rpm	170
5.34	Variation of condenser capacity with air temperature condenser inlet for $N = 600$ rpm	171
5.35	Variation of condenser capacity with air temperature condenser inlet for $N = 800$ rpm	172
5.36	Variation of condenser capacity with air temperature condenser inlet for $N = 1000$ rpm	172
5.37	Variation of condenser capacity with air temperature condenser inlet for $N = 1200$ rpm	173
5.38	Variation of condenser capacity with air temperature condenser inlet for $N = 1400$ rpm	173
5.39	Variation of evaporator capacity with air temperature condenser inlet for $N = 600$ rpm	174
5.40	Variation of evaporator capacity with air temperature condenser inlet for $N = 800$ rpm	175
5.41	Variation of evaporator capacity with air temperature condenser inlet for $N = 1000$ rpm	175
5.42	Variation of evaporator capacity with air temperature condenser inlet for $N = 1200$ rpm	176
5.43	Variation of evaporator capacity with air temperature condenser inlet for $N = 1400$ rpm	176
5.44	Variation of coefficient of performance with air temperature condenser inlet for $N =$ 600 rpm	177
5.45	Variation of coefficient of performance with air temperature condenser inlet for $N =$ 800 rpm	178
5.46	Variation of coefficient of performance with air temperature condenser inlet for $N =$ 1000 rpm	178
5.47	Variation of coefficient of performance with air temperature condenser inlet for $N =$ 1200 rpm	179
5.48	Variation of coefficient of performance with air temperature condenser inlet for $N =$ 1400 rpm	179
5.49	Variation of air temperature evaporator outlet with air temperature condenser inlet for $N = 600$ rpm	180
5.50	Variation of air temperature evaporator outlet with air temperature condenser inlet for $N = 800$ rpm	181

5.51	Variation of air temperature evaporator outlet with air temperature condenser inlet for $N = 1000$ rpm	181
5.52	Variation of air temperature evaporator outlet with air temperature condenser inlet for $N = 1200$ rpm	182
5.53	Variation of air temperature evaporator outlet with air temperature condenser inlet for $N = 1400$ rpm	182
5.54	Variation of humidity ratio with air temperature condenser inlet for $N = 600$ rpm . .	183
5.55	Variation of humidity ratio with air temperature condenser inlet for $N = 800$ rpm . .	184
5.56	Variation of humidity ratio with air temperature condenser inlet for $N = 1000$ rpm .	184
5.57	Variation of humidity ratio with air temperature condenser inlet for $N = 1200$ rpm .	185
5.58	Variation of humidity ratio with air temperature condenser inlet for $N = 1400$ rpm .	185
5.59	Variation of relative humidity with air temperature condenser inlet for $N = 600$ rpm and $N = 1400$ rpm	186
5.60	Variation of air side heat transfer coefficient for dry and wet surface with air temperature condenser inlet	187
5.61	Variation of air side friction factor for dry and wet surface with air temperature condenser inlet	188
5.62	Variation of fined-surface efficiency for dry and wet surface with air temperature condenser inlet	189
5.63	Experimental average values of evaporator capacity, condenser capacity, refrigerant mass flow rate and COP for various compressor speed and condensing air conditions with error bars.	190

Chapter 1

Introduction

An automotive air conditioning system (AACS) and conventional air conditioning systems have many things in common, the working cycle for both being the Vapour Compression Refrigeration Cycle (VCRC). The ideal cycle for a refrigeration system is the reversed Carnot cycle consisting of the four reversible thermodynamic processes, namely, isentropic compression, isothermal heat rejection, isentropic expansion and isothermal heat addition, as shown in Fig. 1.1.

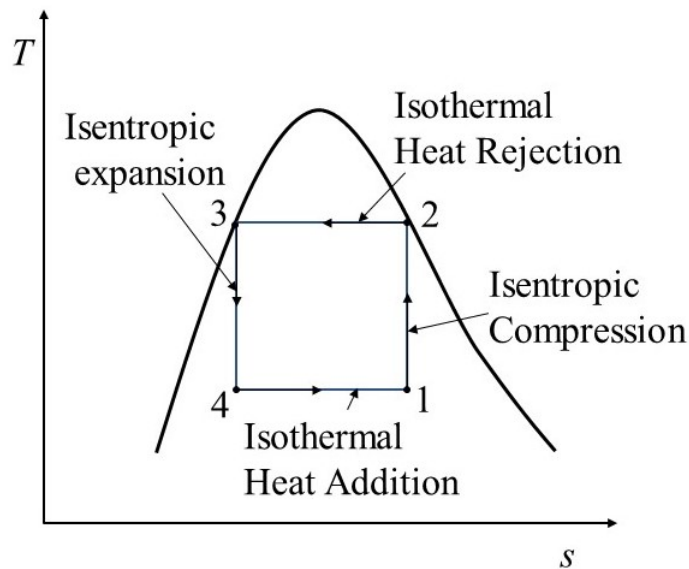


Figure 1.1: Reversed Carnot cycle for refrigeration.

It is advantageous to carry out the Carnot cycle under the saturation dome because the isothermal heat addition and heat rejection processes can be replaced by constant pressure phase change

processes, which are more appropriate from the practice point of view for execution. The working medium in the refrigeration cycle is called a refrigerant. However, there are practical difficulties with the execution of wet compression and wet expansion. Hence the wet compression is replaced by compression of dry saturated vapour and the wet expansion, by a throttling process. With these changes, the Carnot cycle will be modified to the VCRC. In the so-called standard VCRC (Fig. 1.2), all the processes except the throttling process are considered to be reversible.

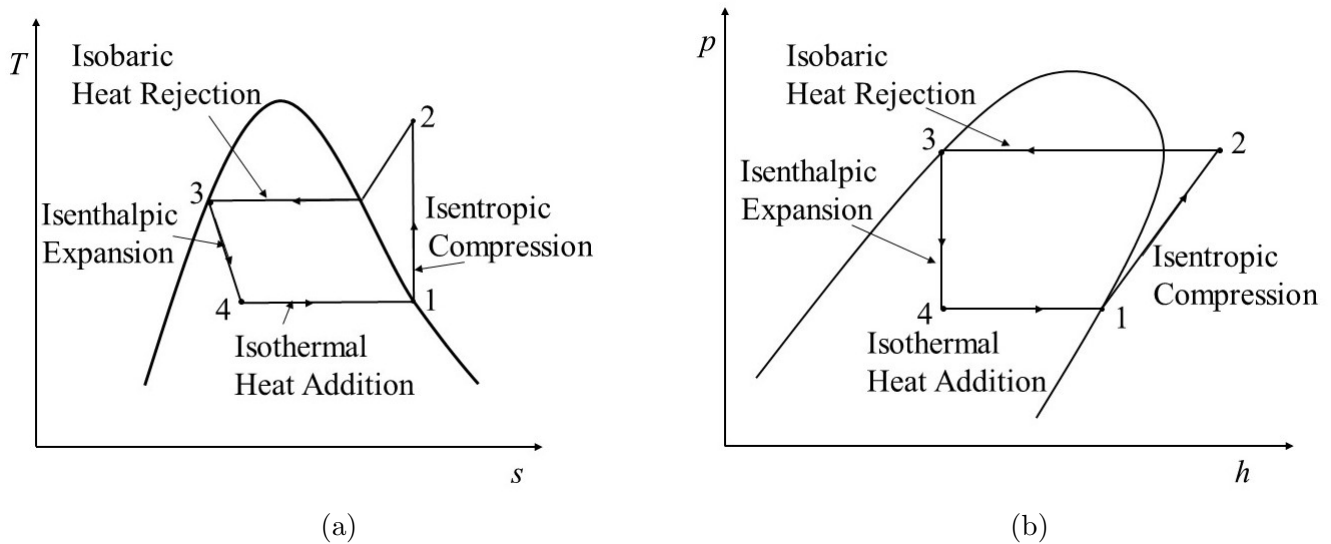


Figure 1.2: Standard vapour compression cycle

In an actual cycle there are irreversibilities such as temperature differences between the heat source and the refrigerant in the evaporator, and between the refrigerant and the cooling medium in the condenser. The vapour entering the compressor can be in a superheated state and there can be some amount subcooling in the condenser. The compression process also deviates from the isentropic process. The vapour compression cycle with superheating and subcooling is shown in Fig. 1.3. Starting from point 4 on the $T-s$ and $p-h$ diagram, process 4-e represents the heat extract from cabin air upto saturated state. In process 4-e the pressure drop occurs due to friction between refrigerant and internal wall of tubes. Process e-1 shows the heat gain and super heating of vapour in suction line. 1-a shows the pressure drop at the compressor suction valve. Process 1-b is the polytropic compression process. Process b-2 shows the pressure drop in delivery valve. Process 2-c represent the heat lost and desuperheating of the vapour in delivery line. c-d is the heat loss to

surrounding air with pressure drop in condenser. Process d-3 is subcooling of liquid from saturated state. Process 3-4 is throttling process.

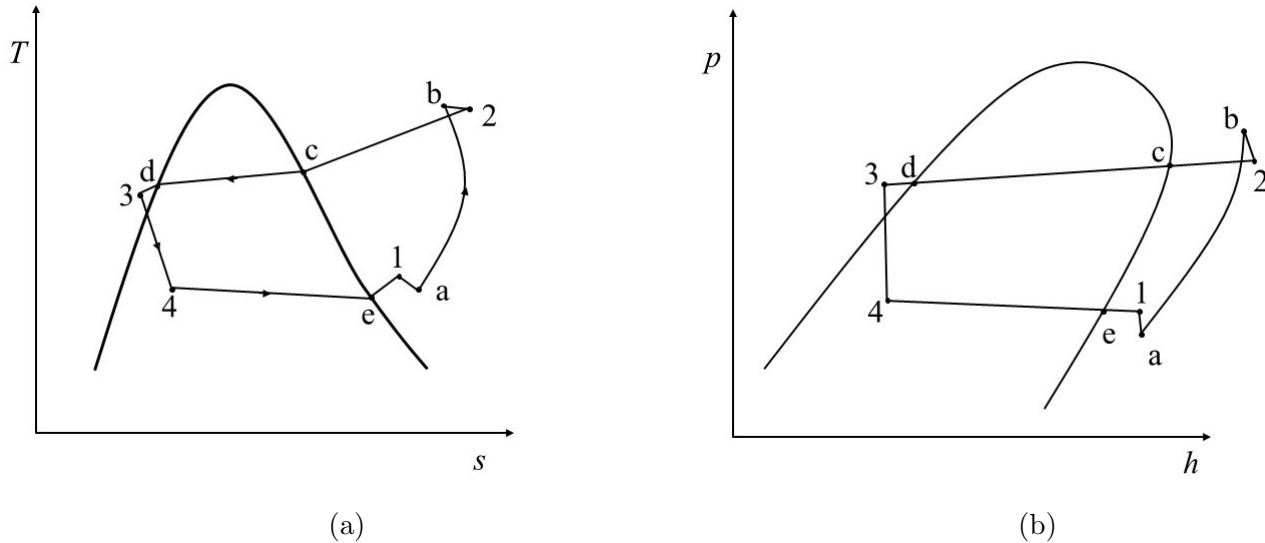


Figure 1.3: Actual vapour compression cycle

Although an AACCS and conventional refrigeration or air conditioning systems work on the same principle, the design and construction of various components depend on the application. In conventional air conditioning systems, open, semi-hermetic or hermetically-sealed reciprocating compressors with constant piston displacement or rotary compressors are used. Larger systems use mono-screw, double-screw and centrifugal compressor. The compressors are usually driven by electric power. In the case of an AACCS, fixed for variable piston displacement, multicylinder, swash plate or wobble plate compressors are used. The principle of swash plate and wobble plate compressors is similar in the sense that the rotational motion of an inclined disc or surface with respect to the axis of the driving shaft is converted into reciprocating motion with the help of ball and socket type pivoting joints. These are driven by a belt-pulley system attached to the engine shaft via clutch mechanism. The heat exchangers (condensers and evaporators) used in conventional and automotive systems differ in geometry and construction. The conventional air conditioning systems use round tubes and plate fins for condensers and evaporators while the AACCS uses the flat tube, louvered fin, aluminum brazed condenser and evaporator. The louvered fin geometry gives higher performance than plain finned geometry and are also more compact and light in weight.

In stationary air-conditioning systems the problem of refrigerant leakage is less compared to the AACCS. In an AACCS, the components and interconnecting pipe lines are subject to constant vibration leading to breakage of pipe lines and leakage of refrigerant into the atmosphere. The currently employed HydroFluoroCarbons (HFCs) have high Global Warming Potential (GWP) although they are safe to stratospheric ozone.

In the present study, attention is focused on an AACCS of small cooling capacity (≈ 1 TR). A mathematical model of an AACCS is developed by integrating the component models. The results of the mathematical model for R134a refrigerant are compared with those obtained from an experimental test rig of an AACCS. Predictions are also made of the performance of the system with the new refrigerant R1234yf. The mathematical model of an AACCS requires the thermodynamic and transport properties of the refrigerants (R134a and R1234yf). The model calculates several important quantities like the volumetric efficiency for a 5-cylinder swashplate compressor, refrigerant mass flow, air-side heat transfer coefficient for both condenser and evaporator, refrigerant-side heat transfer coefficient, pressure drops through both condenser and evaporator, overall heat transfer coefficient, heat transfer for dry as well as wetted surfaces, refrigerant mass distribution in system and the coefficient of performance. The computer code predicts the two-phase flow heat transfer coefficient and pressure drop variation along the flow direction of refrigerant in both condenser and evaporator at various speeds of compressor, at various atmospheric air temperatures and humidities and at various loads on evaporator. The code predicts the air side parameters such as the heat transfer coefficient at various frontal air velocities and air temperatures.

The experimental facility is constructed for a small passenger car air conditioning system for validation of the simulation results. The load estimation is also done in the present study to have an idea of the cooling capacity requirement. The load estimation shows that for a five passenger car, the cooling capacity is approximately 1 TR ($\cong 3.5$ kW) including solar direct and diffuse radiation load, metabolic heat load of passengers, conduction and convection of transmission load, engine heat and road reflection load. The test rig is designed and fabricated in such a way that it can predict the performance at various operating conditions. In the test rig, the swash plate compressor is driven by an electric motor via frequency converter drive arrangement which provides different rotational

speed for the compressor ranging from 500-1400 rpm. The condenser and evaporator are fitted in to the rectangular ducts along with fans and are provided with electric heaters and filament bulbs for applying heat load on the evaporator to provide various temperatures ranging from 20°C to 40°C and various frontal velocities ranging from 1 m/s to 1.5 m/s. The experimental study in the present work yields the refrigerant side pressure drops between the inlet and outlet of both the condenser and the evaporator, heat capacity of condenser, heat capacity of evaporator and the power required by compressor at various operating conditions.

1.1 Need for alternative refrigerants in automotive air conditioning systems

Refrigerants are pure substances or mixtures of pure substances used as working fluids in refrigeration and air-conditioning systems. There is a long history of refrigerants beginning from “ether” used by Perkins in a hand-operated system. In modern refrigeration and air conditioning systems organic compounds are basically used as refrigerants which contain carbon, hydrogen and halogens like chlorine, fluorine and bromine. Inorganic substance like CO₂, H₂O, NH₃ etc. are also used as refrigerants in refrigeration and air-conditioning systems. Up to 1986, the ChloroFluoroCarbons (CFCs) and HydroChloroFluoroCarbons (HCFCs) were much used as refrigerants but the problem with CFCs is the depletion of the ozone layer in the stratosphere which allows the entry of ultra-violet solar radiation in to the earth’s atmosphere. This is harmful to humans, animals and plants. The chlorine present in the CFCs is the main cause of ozone layer depletion. After the Montreal Protocol in 1987, the substances which are responsible for ozone layer depletion were phased out permanently. Hence the use of CFCs and HCFCs like R11, R22, R113, R114, etc. had to be discontinued. New refrigerants have come into use and these do not contain chlorine and hence do not deplete the ozone layer. These are mainly the HydroFluoroCarbons (HFCs) such as R32, R125, R134a, R143a, R236 and R245, etc. R134a is now a widely used refrigerant in the refrigeration and air-conditioning field and has become the replacement for the older refrigerant R12 and other refrigerants. R134a (1,1,1,2-Tetrafluoroethane) is suitable for automotive air-conditioning applications due to its favourable physical and chemical

Table 1.1: Comparison between R12, R134a and R1234yf.

	R12	R134a	R1234yf
Name	Dichlorodifluoromethane	Tetrafluoroethane	Tetrafluoropropene
Chemical formula	CCl_2F_2	CH_2FCF_3	$\text{CH}_2 = \text{CH} - \text{CF}_3$
ODP	1.0	0	0
GWP	2400	1300	4
Boiling point ($^{\circ}\text{C}$)	-29.8	-26	-29
Critical temperature ($^{\circ}\text{C}$)	111.97	100.95	95
Critical pressure (bar)	41.36	40.6	33.85
Molecular weight (kg/kmol)	121	102.03	114.042
Toxicity	toxic	non-toxic	non toxic
Flammability	non-flammable	non-flammable	mildly flammable

properties, non-toxicity and non-flammability. The main disadvantage of R134a is its higher Global Warming Potential (GWP) which is approximately 1300. This means that compared to the reference GWP of 1 for CO_2 , the GWP of R134a is 1300 times higher than that of CO_2 . In 2011 the European Union decided to phase out R134a and other substances having GWP more than 150 from automotive air-conditioning applications by 2017. Therefore there was a new research challenge to find out new refrigerants with low GWPs for the replacement of R134a. In Europe and other countries like the United States, efforts are being made to replace R134a with the new refrigerant R1234yf (2,3,3,3-Tetrafluoropropene). R1234yf is a HydroFluoroOlefin (HFO) with the chemical formula $\text{CH}_2 = \text{CFCF}_3$. It is a colourless gas having similar thermodynamic and transport properties to that of R134a, with zero ozone depletion potential and with a GWP of 4. Due to its very low GWP value it is very much suitable for Mobile Air-Conditioning field and in particular for AACs. Table 1.1 shows the comparison between R12, R134a and R1234yf. It can be seen that R1234yf is very similar to R134a and can be used in old as well as new vehicles. In the present study, computer codes are developed for finding the performance of R134a and R1234yf. Experiments are conducted to obtain the performance of R134a and the results are compared with results obtained from the numerical simulation. Also the numerical and experimental results of R134a are compared with the predicted performance of R1234yf.

It is difficult to find refrigerants that are simultaneously ozone-friendly and non-global-warming, without accepting flammable refrigerants. Even then the options available are very few and the applications covering different evaporating temperatures are many. A consensus that has emerged is

that rather than the GWP, the total equivalent warming impact (TEWI) is a more rational index to indicate global warming. TEWI is defined as the sum of the impact of the global warming due to the amount of refrigerant released through leaks plus that of carbon dioxide generated in the power plant in the process of supplying electrical energy to the equipment through its life time.

$$\text{TEWI} = \text{Direct GWP} + \text{Indirect GWP}$$

$$\text{Direct GWP} = \text{GWP} \cdot L \cdot n + \text{GWP} \cdot m \cdot (1 - \alpha)$$

$$\text{Indirect GWP} = n \cdot E \cdot \beta$$

where L is the leakage rate per year in kg, n is the mean time between failures of the AC system in years, m is the refrigerant charge in kg, α is the recycling factor, E is the energy consumption by the compressor per year in kWh and β is the carbon dioxide emission per kWh. The GWPs of R134a and R1234yf are taken as 1300 and 4 respectively.

Typical carbon dioxide emission from a small passenger car is 2.2 kg per liter of petrol. Taking density of petrol as 0.74 kg per liter, calorific value as 45800 kJ/kg and average brake thermal efficiency as 25 percentage, the brake energy produced per liter of petrol is $(25/100) \cdot (0.74) \cdot (45800) = 8473$ kJ/liter or 2.35 kWh/liter. Therefore $\beta = \text{carbon dioxide produced per kWh} = 2.2/2.35 = 0.936$ kg/kWh.

Taking the combined transmission and mechanical efficiency of the compressor as 0.7, refrigerating capacity as 3.5 kW and COP of the system as 3.0 for R134a and 2.7 for R1234yf (as from our calculations the COP of R1234y is about 10 percent less that of R134a), the power drawn by the compressor from the engine is $3.5/(3.0 \times 0.7) = 1.8$ kW for R134a and $3.5/(2.7 \times 0.7) = 1.85$ kW for R1234yf. Considering that the vehicle in question is a vehicle for hire, the number of hours of operation per day will be typically 10 h or the number of hours of operation per year = $10 \times 30 \times 12 = 3600$ h/year. Therefore $E = \text{Energy consumption by the compressor per year} = 1.8 \times 3600 = 6480$ kWh and $1.85 \times 3600 = 6660$ for R134a and R1234yf respectively.

In addition, considering a charge m of 0.2 kg, leakage rate L as 0.02 kg/year, mean time n between failures of AC system as 5 years and recycling factor α as 0.75, the TEWI values are calculated for the refrigerants R134a and R1234yf as follows:

$$\begin{aligned}
\text{TEWI} &= \text{GWP} \cdot L \cdot n + \text{GWP} \cdot m \cdot (1 - \alpha) + n \cdot E \cdot \beta \\
\text{TEWI (R134a)} &= 1300 \times 0.02 \times 5 + 1300 \times 0.2 \times (1 - 0.75) + 5 \times 6480 \times 0.936 \\
&= 130 + 65 + 30326.4 = 195 + 30326.4 = 3.052 \times 10^4 \text{ kg CO}_2 \\
\text{TEWI (R1234yf)} &= 4 \times 0.02 \times 5 + 4 \times 0.2 \times (1 - 0.75) + 5 \times 6660 \times 0.936 \\
&= 0.4 + 0.2 + 31168.8 = 0.6 + 31168.8 = 3.11 \times 10^4 \text{ kg CO}_2
\end{aligned}$$

Thus the increase in the indirect global warming impact of R1234yf due to its lower performance is compensated by the reduction in direct global warming impact due to low GWP value, and the TEWI is maintained at about the same value as that of R134a.

1.2 Need for new simulation and experimental studies on automotive air conditioning systems

Older works on automotive AC systems were concerned with experimental and simulation studies with CFC refrigerants like R12 and R22 which are now phased out due to their high stratospheric ozone depletion potentials. In their place have emerged new HFC refrigerants like R134a and R245fa, which despite having zero ozone depletion potential, have high global warming potentials. Domanski et al. [10] performed a comparative analysis between CO₂ and R134a refrigerants in a vapour compression system. Ghodbane [11] examined the use of R152a and hydrocarbon refrigerants in a mobile air conditioning and showed that alternative refrigerants with lower ODP and GWP could be used in place of R134a which has a high GWP. Performance simulations done with R152a and hydrocarbon refrigerants to see their potential as alternatives to R134a in an AACS showed that R152a had considerably low value of GWP and better transport properties than R134a. Yoo and Lee [12] performed the experimental analysis of AACS with R134a and R152a. Chen et al. [13] performed the experimental analysis for R134a and the mixture of R134a and R161 with mass fraction of 60%: 40%. However, literature reveals little or no work in respect of simulation and experimental

studies with R1234yf. As has already been mentioned, R1234yf has emerged as a very low GWP refrigerant suitable especially for automotive systems. Considering now the automotive evaporators and condensers, these were of round-tube and continuous fin type in very old systems. Due to advances in compact heat exchanger heat transfer studies and manufacturing technologies, flat-tube, louvered fin, brazed aluminium heat exchangers have emerged as the state-of-the-art heat exchangers for evaporators and condensers in modern systems. These developments have necessitated new simulation and experimental studies to be undertaken with the present-day refrigerants and heat exchanger geometries.

1.3 Automotive Air-Conditioning System (AACS)

The main function of an AACS is to provide comfort environment in the passenger cabin of a vehicle (in summer 15 °C to 26 °C air temperature with $\approx 60\%$ Relative Humidity (RH) and in winter 20 °C to 26 °C with around 30% RH). The AACS controls the cabin air temperature, humidity, circulation of fresh and recirculating air, cleanliness of air (i.e. filtering air from dust and other pollutants) and noise. An AACS consists of basic four components, the swash plate compressor, flat-tube louver-finned evaporator, thermostatic expansion valve (TXV) and flat-tube louver-finned condenser. Fig. 1.4 shows the basic four components of the system and Fig. 1.3 shows the actual thermodynamic processes on $T - s$ and $p - h$ diagram.

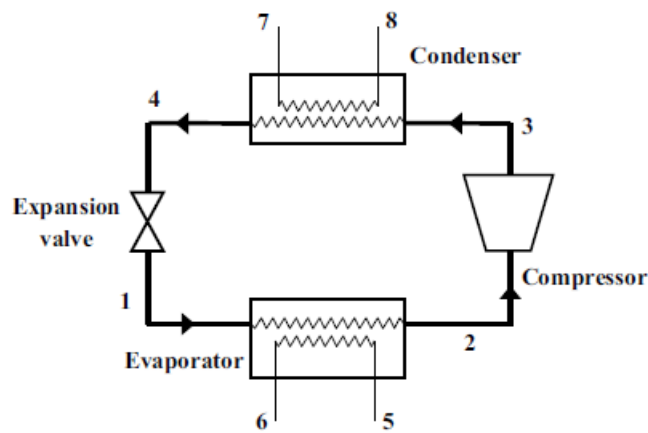


Figure 1.4: Basic four components of AACS

The working fluid, namely the refrigerant, is an important part of an AACCS and has a bearing on the design, compactness, performance and cost of the system. An AACCS is closed system and working mainly between two pressures, the high pressure side (condenser pressure) and the low pressure side (called evaporator pressure). In an AACCS the refrigerant undergoes two-phase boiling and condensation processes in the heat exchangers. R12 was widely used as refrigerant in the AACCS but due to ozone layer depletion problems it was phased out and replaced by R134a which has zero ODP and a GWP of about 1300. The new refrigerant R1234yf, having zero ODP and a GWP of only 4 has emerged as a better choice for an AACCS. Fig. 1.5 shows the schematic of AACCS in which the colours inside the tubes indicate the state of refrigerant in the high pressure and low pressure side. The evaporator and blower are placed in the cabin where cooling effect is required. The compressor and condenser are placed outside the cabin. The red colour inside the tubes indicates higher pressure and blue colour, the lower pressure. The high pressure and high temperature superheated refrigerant vapour (shown in pink colour) from compressor enters the condenser, where it is condenses and converts into high pressure, moderate temperature, subcooled liquid (shown in red). This subcooled liquid is expanded in the thermostatic expansion valve to become low-pressure, low-temperature, two-phase mixture of vapour quality typically 0.2 to 0.4. This is the isenthalpic expansion process in TXV. This two-phase refrigerant then enters the evaporator and is converted in to low-pressure superheated vapour (shown by blue colour) by taking heat load from cabin air. Air is circulated from cabin to evaporator duct with 20% to 30% fresh air from outside with an equal mass of cabin air exhausted. A blower is used to circulate the air. In advanced AAC systems, a heater is placed after the evaporator to increase the air temperature to the required value. This heater uses the warm engine coolant.

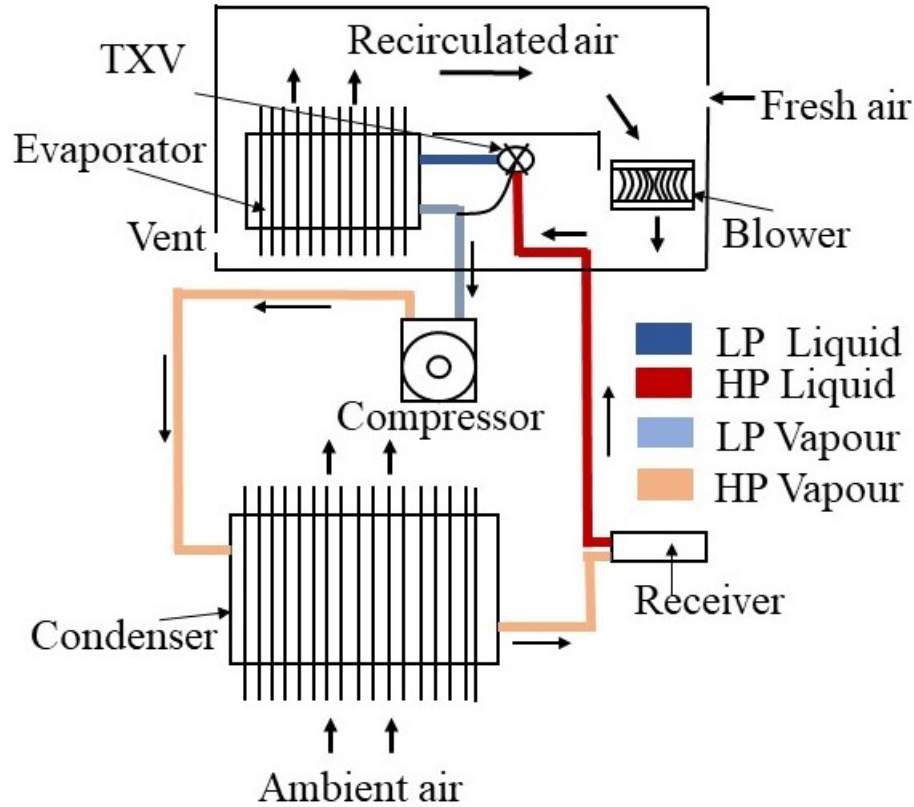


Figure 1.5: Schematic diagram of AACS

1.4 Evaporators used in AACS

In AACS, brazed aluminium light weight evaporators are used. These are heat exchangers with multichannel flat tubes and continuous louvered fins, which offer high thermal performance and lower pressure loss as compared to continuous fin, round-tube evaporators. Webb and Lee [1] describe a brazed aluminium condenser and compare its heat transfer and pressure drop performance with a finned round-tube condenser. Wu and Webb [2] performed the thermo-hydraulic numerical study of a brazed aluminium evaporator to describe the design methodology for a brazed aluminium evaporator that is intended to compete with currently used finned round-tube evaporators. Fig. 1.6 shows the actual brazed aluminium evaporator and TXV as a one unit used in experimental facility. Each flat tube of evaporator have multiple channel ports with square cross-section through which a refrigerant is flowing and air is pass through the space between the louvered fins. The inner temperature of tube

and fins is always kept below dew point of moist air and therefore the outer surface of evaporator get wetted and water film is formed on it. Chwalowski et al. [3] and Domanski [4] calculated the performance of a finned tube evaporator based on a tube-by-tube approach, evaluating the performance of one tube at a time and using outlet data as inlet data for the next tube; however, no incremental calculation was done. The actual evaporator used in the present study is such an evaporator that is employed in small cars. This kind of evaporator is simple in design, of about 1 TR capacity and is used for small vehicles like cars accommodating a maximum of five passengers. These do not have a two-pass structure. Refrigerant flow takes place in a single condenser or evaporator tube attached to louvered fins. The working of such an evaporator is similar to the one described by Wu and Webb [2]. The flow of refrigerant inside the evaporator tube is divided into three regions, the two-phase, liquid deficient and superheated regions. For each region, correlations from the published literature are employed to calculate the heat transfer and pressure drop. Pressure losses at the tube entrance and exit also accounted for [5]. The air-side finned surfaces of evaporator are assumed to operate at the fully wet condition and overall heat transfer coefficient is calculated using the enthalpy driving potential method [6]. The pressure losses at the tube entrance and exit are calculated using the Collier's correlations [7].

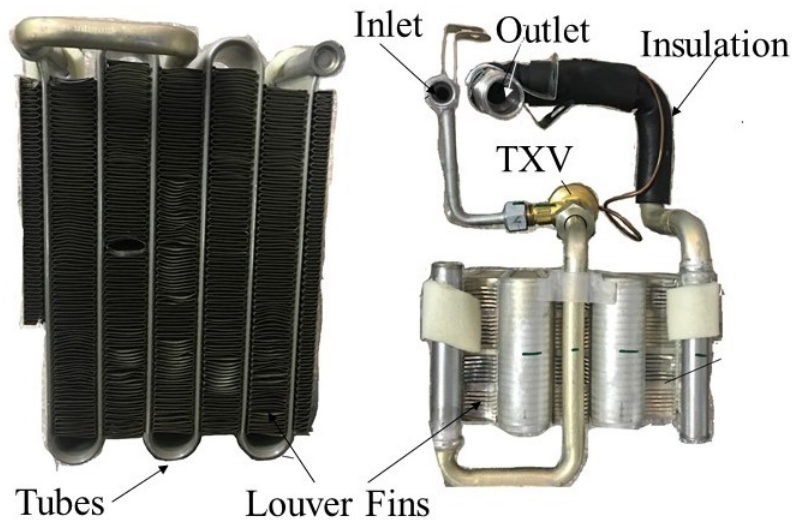


Figure 1.6: Actual evaporator used in experimental facility

1.5 Condensers used in AACS

The geometrical parameters of the condenser are very similar to evaporator. Condensers used in AACS are flat tubes with louvered fin geometry. The size of the condenser is bigger than that of the evaporator and depends on required cooling capacity of system. Condensers are single pass and simple in geometry with usually horizontal tubes. Fig. 1.7 shows the actual condenser used in the present experimental facility. The tubes and fins of the condenser are smaller in size as compared to the evaporator. The vertical parallel tubes are connected between two headers and the fins are brazed between two tubes. The main function of the condenser is to remove the sensible and latent heat from refrigerant flow inside the tubes. The refrigerant enters as a superheated vapour and leaves as a subcooled liquid. The condenser is operates at high pressure and under dry condition of the outer fins because the surface temperature is greater than the dew point temperature of moist air. On the air side of condenser forced convection is at work in removing the total heat, the air flow having been produced by the fan placed on the front side of the condenser. In the AACS of a moving vehicle, the condenser fan is at work when the speed of the vehicle is low and is switched off when the vehicle gains speed, the flow of air into the condenser being provided by the vehicle motion. The refrigerant flow inside the tubes is a two-phase condensation process. In the present study, the heat transfer coefficient correlations employed for two-phase condensation are taken from the work of Shah [8], the pressure drop correlations being the same as those employed for the evaporator.

1.6 Compressors used in AACS

The compressor is often said to be the heart of a vapour compression system. The compressors of AACS are different from those used in conventional (or stationary) systems. In stationary systems, vibrations are not a major issue and chances of leakage of refrigerant are very less. But in the automotive, the air conditioning system is subject to a large vibration due to the motion of the vehicle. Therefore leakages problems are very common with AACS. The compressors of AACS are reciprocating type with multi cylinders and double acting. Two types of compressors are used in AACS; the wobble plate compressor and the swash plate compressor with fixed or variable displace-

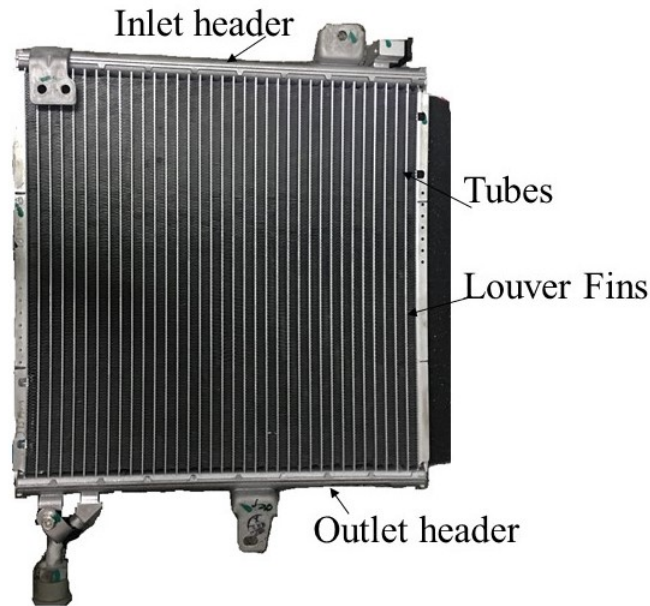


Figure 1.7: Actual condenser used in experimental facility.

ment stroke. Variable displacement stroke compressor (VDSC) are more suitable for automotive air conditioning system when continuous operation, better thermal comfort inside the car, and lower engine fuel consumption are desired. In the wobble plate compressor, the wobble plate and pistons are connected with the piston rods and in the swash plate compressor there is no piston rod but the swash plate inserts into the pistons directly. Due to this simple structure, low noise and excellent performance, it is used more widely. Fig. 1.8 shows the compressor used in experimental facility. This is a five-cylinder, double acting, swash plate compressor with fixed stroke.

The main components of variable displacement stroke compressor are: a main shaft, a drive rotor, a swash plate, and number of pistons as shown in Fig. 1.8. The swash plate is driven by rotor which is fixed on main shaft. The rotational motion of swash plate is converted in to the reciprocating motion of pistons through the sliding shoes inside the pistons. In a variable displacement stroke compressor a control mechanism changes the piston stroke length according to the heat load on the system. Throttling orifice and a mass flow compensation control valve are used for controlling the mass flow rate of refrigerant.

In the present study a constant piston stroke swash plate compressor is used in the experimentation due to the small cooling capacity of the system. In numerical code, the actual volumetric efficiency, isentropic work efficiency and the mass flow correlations are used. Darr and Crawford [9] in their work

explained the procedure for the calculation of the refrigerant mass flow rate from experiments. In the test rig, the compressor was driven by electric motor with a frequency converter drive to achieve different speeds ranging from 500-1400 rpm. More geometrical details of automotive compressor is shown in Fig. 1.9.

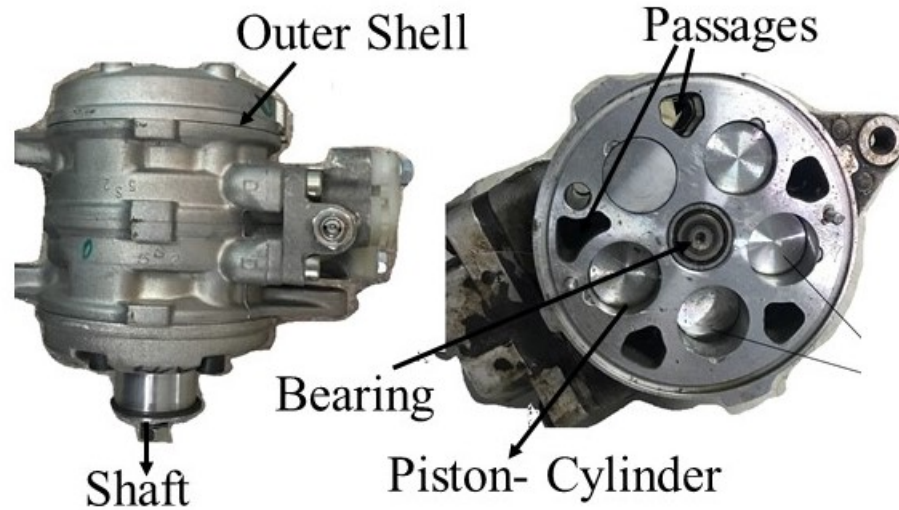


Figure 1.8: Swash plate compressor used in experimental facility.

1.7 Present work

1.7.1 Objectives of the present work

The objectives of the present work are:

- To develop numerical simulation models to predict the performance of an AACS with the refrigerants R134a and R1234yf.
- To validate the simulation results with the experimental results in case of R134a.
- To predict the performance of the AACS with the refrigerant R1234yf.
- To make a comparison of the performance of R134a (both simulated and experimental) with the simulated performance of R1234yf in respect of various quantities of interest such as evaporator capacity, COP, condenser capacity and mass flow rate of the refrigerant.

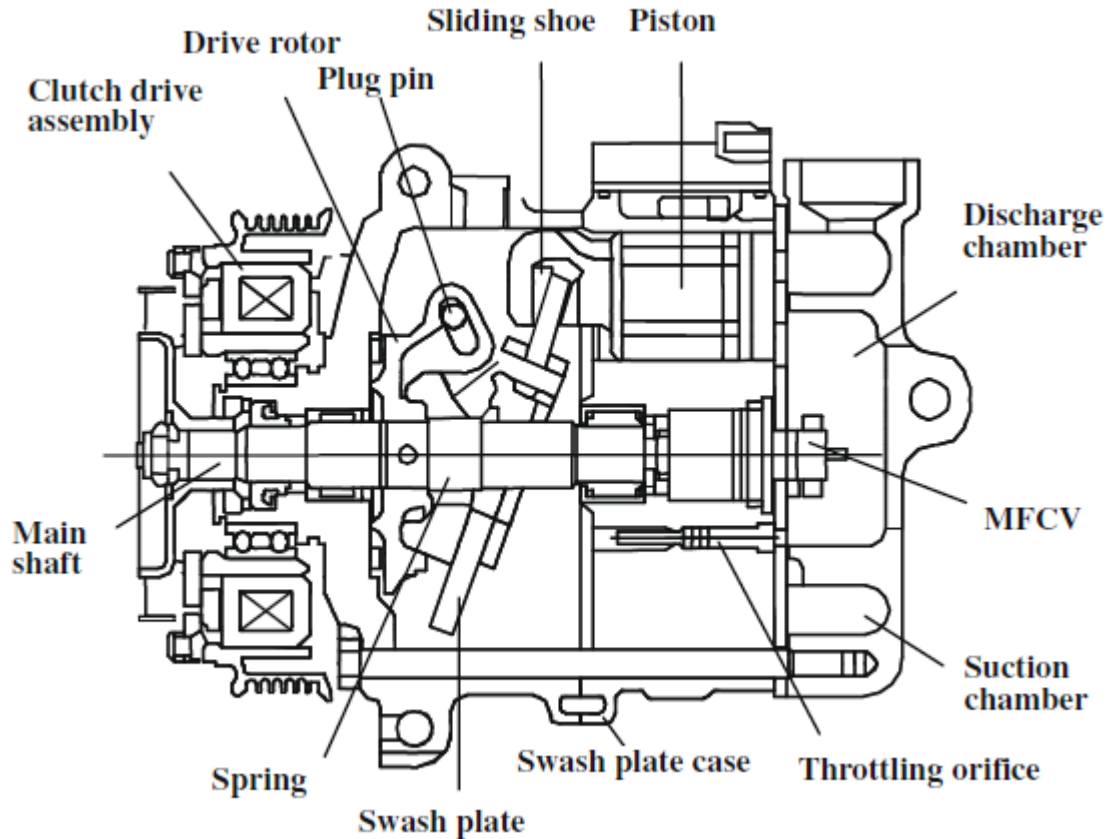


Figure 1.9: Schematic diagram of swash plate compressor (*Tian and Zhang [35]*).

1.7.2 Description of the work done

Two computer codes, one for R134a and the other for R1234yf, are prepared to solve the mathematical models of AACs. The numerical results obtained for R134a are compared against the experimental results obtained from the test rig. In the case of R1234yf, the performance is predicted from the computer code.

The experimental work consists in the development of a test rig for a small capacity, i.e., five seater passenger car, air conditioning system of about 3.5 kW capacity. The test rig is designed and fabricated in a such way that it can be operated at various speeds and states of condenser air, as encountered by the automobile. The test rig in the present study contains two parts; the air conditioning system and the instrumentation to measure the performance. The system is fixed on a frame along with air ducts and instruments. The system is driven by an electrical motor which is also placed on the main frame. The frame is made of steel channels such that it can withstand and provide

support at various running conditions. Various quantities like temperature, velocity, humidity, etc. can be measured by locating sensors and instruments at different points within the system and inside the air duct. A control panel is attached to the frame and all the parameters are controlled from that control panel. The AACCS consists of swash plate compressor, evaporator, condenser, thermostatic expansion valve, filter-dryer and aluminium circular pipes and fittings, all of which form a closed system. A three-phase induction motor is used to drive the compressor with variable frequency drive to control the speed of compressor. An energy meter is connected to the motor for measuring the energy input in kWh. The pulleys of the motor and compressor are connected by rubber V-belts. The evaporator is fixed inside the rectangular transparent plastic duct. Heat load is applied with the help of electric bulbs of wattage 400 W. Some heat load also occurs because of the heat transmission across the duct wall from the atmosphere. There are two air circulation fans and three air control valves inside the duct. The evaporator duct has two passages such that a mixture of fresh air and recirculated air can flow through the evaporator. The duct is provided with ports for placing different sensors at the inlet and outlet of the evaporator. By closing and opening of three air control valves fresh air alone or recirculated air can flow inside the duct. The condenser is fixed inside a single straight transparent plastic rectangular duct. Variable heat load (electric heaters) and variable speed air flow fan are provided in the condenser duct. A rheostat is used to control the heating of heater and an electrical controller is used to control the speed of condenser fan. Various digital and analogue measuring instruments are used in AACCS set up, of which some instruments like pressure gauges, thermocouples and differential pressure sensor etc. were directly connected to the system while the other instruments such as the digital tachometer were used as and when required.

The component mathematical models of the system are presented along with the property correlations of the refrigerants. The correlations for the thermodynamic and transport properties of the R134a and R1234yf and moist air are obtained from published literature. Properties for liquid and vapour saturation states and superheated state of both the refrigerants are required for formulating the complete mathematical model of the AACCS. The thermodynamic and transport properties for R134a can be directly obtained in equation form. However, the thermodynamic properties for R1234yf are generated from an equation of state formulation expressing the Helmholtz free energy

in terms of temperature and density. Equations are required for the double-acting, five-cylinder, swash plate compressor for the actual volumetric efficiency, isentropic work efficiency, mass flow rate of refrigerant, heat lost from compressor body due to friction of internal rotating elements and the compression power. The equations for actual volumetric, isentropic work efficiencies and heat lost from compressor are obtained from curve fits of experimental data taken from tests conducted on the experimental test rig from 72 data points corresponding to different working conditions. The compressor is a fixed stroke swash plate compressor; therefore, both the efficiencies and heat lost are functions of only the rotational speed of compressor. Mathematical models are also formulated for the condenser, evaporator and the thermostatic expansion valve. The models for the heat exchangers (condenser and evaporator) entail two-phase flow and liquid deficient/superheated regions and the calculation of heat transfer coefficient, pressure drop and heat capacities of condenser and evaporator. The required equations for the thermodynamic and transport properties of moist air also included in the formulation. The details of the mathematical model of the AACCS are presented in appropriate sections.

1.7.3 Organisation of the thesis

The thesis is organized into five chapters as follows:

Chapter 1 (Introduction) discusses the ideal and actual vapour compression cycles and refrigerants finding application in the AACCS. The special features of the AACCS and its components, namely, the compressors, evaporator and condensers, compared to stationary systems, are elaborated.

Chapter 2 (Literature overview) discusses the important previous work done. A comprehensive literature overview has been presented covering possible alternative refrigerants for R134a and in particular the suitability of low global warming potential refrigerant R1234yf for replacing R134a, mathematical modelling aspects, performance enhancement strategies and intube boiling, condensation and two-phase flow studies. The chapter concludes by mentioning important observations from the previous works and some areas needing further attention.

Chapter 3 (System Analysis and Numerical Calculations) presents the required correlations for the calculation of thermodynamic and transport properties of the refrigerants in liquid and vapour

form, correlations for the properties of moist air and heat and mass transfer correlations for air side and refrigerant side for flat tube louvered fin heat exchangers. The method of numerical calculation for the complete system is presented both in the form of equations and a flow chart. Apart from these, heat load calculations are also presented for an automobile. The heat load gives an idea of the required capacity of the air conditioning system to be employed in the automobile.

Chapter 4 (Experimental Facility and Procedures) discusses the development of the test facility. Detailed descriptions are presented of all the components of the system along with diagrams and photographs. Details are also presented of the electrical equipment and measuring instruments (like thermocouples, pressure gauges, tachometers, anemometers and other sensors). The method of charging the system with the refrigerant is presented in a detailed manner.

Chapter 5 (Results and Discussion) is devoted to the calculation methods of various quantities of interest and presentation of a large number of results for R134a and R1234yf. Results are presented for the volume and pressure ratios, refrigerant mass flow rate, volumetric efficiency, isentropic work efficiency, evaporator and condenser capacities, coefficient of performance and air side performance of the evaporator. The graphs facilitate comparison of the performance of the refrigerants in the system as well as the comparison of numerical and experimental results. It is concluded that R1234yf is a good alternative refrigerant in place of R134a for the automotive sector and that it can be directly charged into an existing R134a without major design modifications.

Appendix A includes tables of experimental observations, numerical simulation readings, comparison of the properties of the refrigerants and uncertainty analysis.

Chapter 2

Literature Review

The literature review is organized into the following sections:

- Automobile Air Conditioning system.
- Mathematical model and performance of swash plate compressor.
- Heat transfer and friction correlations for the louver fin geometry.
- Heat transfer correlations for boiling in small channels.
- Heat transfer correlations for condensation in small channels.
- Pressure drop in two-phase flow through small channels.

2.1 Automobile Air Conditioning System

Only a few studies on automotive air conditioning systems are reported in the open literature because of the competitive and technology-oriented nature of the industry. After the Montreal Protocol, new investigations were carried out to determine the performance of AACCS using alternative refrigerants (like R1234yf) as replacements to chlorinated refrigerants, which were the widely used refrigerants in AACCS until 1994.

2.1.1 Alternative refrigerants in place of R134a

Domanski et al. [10] performed the comparative analysis between CO₂ and R134a refrigerant in vapour compressor system. For R134a the vapour compressor system is run with compressor, condenser, evaporator and expansion device. For CO₂ the vapour compressor system is modified with liquid line and suction line heat exchangers. It was observed from the comparison that R134a gives better performance than CO₂, i.e. the COP of R134a is greater than CO₂. At 1000 rpm compressor speed the COP of CO₂ shown 29% less value than COP of R134a at 32 °C and 34% less CO₂ COP than R134a COP at 48.0 °C. From the entropy generation calculation it was found that the main cause of lower CO₂ performance is the large entropy generation in gas cooler in the CO₂ system. Fig. 2.1 shows the COP comparison between CO₂ and R134a.

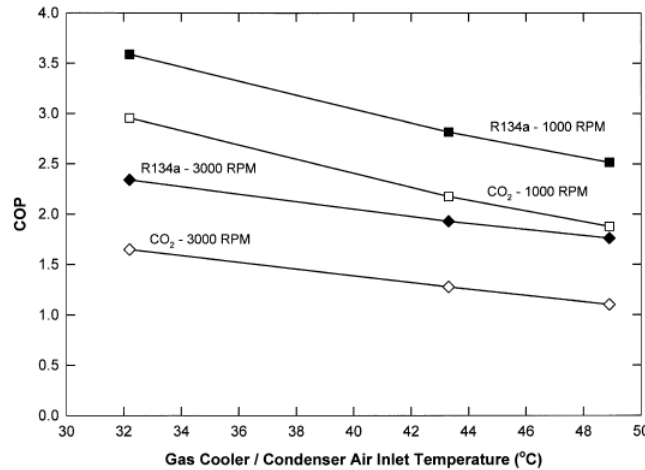


Figure 2.1: COP comparison between CO₂ and R134a air conditioning systems, *Domanski et al.* [10]

Ghodbane [11] examined the use of R152a and hydrocarbon refrigerants in mobile air conditioning and showed that alternative refrigerants with lower ODP and GWP could be used in place of R134a which has a high GWP. Performance simulations done with R152a and hydrocarbon refrigerants to see their potential as alternatives to R134a in an AACS showed that R152 had considerably low value of GWP and better transport properties than R134a. R152a and cyclopropane (RC270) exhibited superiority as refrigerants compared to R134a in an AACS. The results showed clearly that R152a could be regarded as an optimum substitute for R134a while cyclopropane was also more than adequate. It was also found that though the operating pressures of propane (R290) were higher, it

had marginal improvement over the R134a baseline case and that isobutane (R600a) was not suitable for AACCS because of its low COPs and high compressor displacement requirement.

Yoo and Lee [12] performed the experimental analysis of AACCS with R134a and R152a. Experimental facility consists of a cabin and engine room structure as placed in real automotive system. The evaporator capacity, heat rejection rate of condenser, coefficient of performance (COP) and power consumption by compressor are calculated at different compressor speeds and air velocities at condenser inlet. It was observed from the analysis that R152a showed slightly better performance than R134a at driving conditions as well as under idling condition. The conclusion of study shows that the R152a is an alternative refrigerant to for AACCS.

Chen et al. [13] performed the experimental analysis for R134a and the mixture of R134a and R161 with mass fraction of 60%: 40%. The mixture of R134a and R161 was named as M5 and whose GWP was 527. The comparison was made between M5 and R134a. It was observed from the analysis that the COP of M5 is greater than R134a and refrigeration capacity and power of compressor for M5 are 32% and 30% higher than R134a respectively. It was also found that the compressor outlet temperature and pressure ratio of compressor of M5 were about 15% higher and 10.9% lower than those of R134a respectively. Fig. 2.2 shows the COP comparison between M5 and R134a.

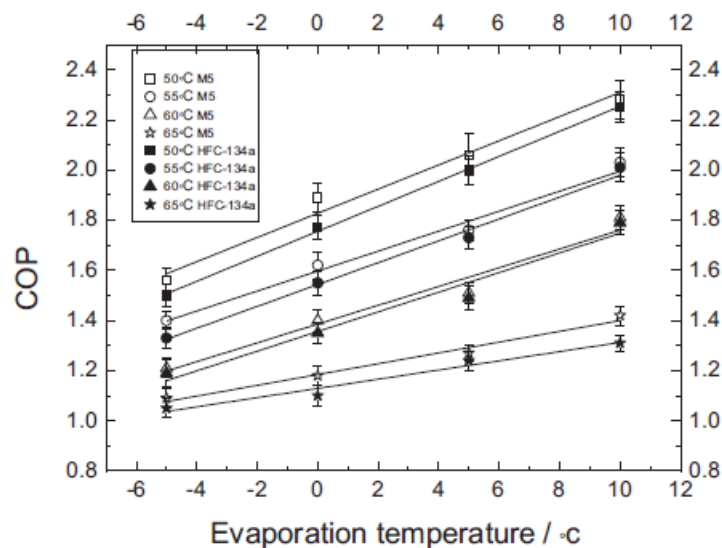


Figure 2.2: Experimental variation of COP with the evaporation temperature under different condensation temperatures., *Chen et al.* [13]

Devotta et al. [14] made a search for R22 alternatives for air conditioning systems. Selected fluids were assessed for their suitability for alternatives to R22. Only the refrigerants with zero ozone depletion potential were considered in the study. It was found that among R134a, R290, R407C, R410A and three blends of R32, R134a and R125, R134a had the highest COP, its capacity was the lowest and required much larger compressors. The characteristics of R290 were very close to those of R22 and compressors required less modification. Therefore, R290 was identified as a potential refrigerant provided that the concerns regarding risks were accomplished for refrigerators. For retrofitting applications, R407C is probably the best refrigerant.

2.1.2 Substitution of R1234yf in place of R134a in AACS

Lee and Jung [15] conducted the tests on heat pump bench tester with R1234yf and R134a for summer and winter conditions for AACS. The heat pump bench tester used the open type compressor. It was observed from the study that COP and refrigeration capacity of R1234yf are 3% and 4% lower than R134a respectively. Also compressor outlet temperature and amount of charge of R1234yf are 6.5 °C and 10% lower than that for R134a respectively. Conclusion of study state that R1234yf has no ODP and very low GWP, it can be used as alternative environment friendly refrigerant in AACS.

Pamela et al. [16] have compared the performance of three refrigerants, namely, R1234yf, R410A and R134a. R1234yf has a low GWP value only 4 compared to 1400 for R134a and has thermodynamic and transport properties similar to R134a, making it a good choice among alternatives for AACS. Therefore in future, R1234yf has a significant potential as a drop-in replacement for R134a. This study has also examined whether R1234yf shows any drop-in potential for systems designed with R410A, another commonly used refrigerant. Comparisons are made for the performance as well as the thermophysical properties of R1234yf, R134a, and R410A. Simulations work has done to determine the feasibility of using R1234yf as a replacement for R134a or R410A proved to be promising.

Navarro et al. [17] performed the comparative analysis between R134a, R1234yf and R290. The experiments were done with open type compressor for AACS used in bus application. Thermodynamic and transport properties of three refrigerant are investigated. It was observed from the study that R290 shows 30% greater volumetric efficiency and 15% greater compressor efficiency than other two

refrigerants. This improvement in volumetric efficiency reduces the size of compressor. R1234yf showed high heat losses even at low discharge temperature than R290. Conclusion of study showed that R1234yf and R290 can be good replacements for R134a in AACs.

Navarro et al. [18] performed the experimental analysis of an vapour compression system with R134a and R1234yf for wide range of working conditions. Experiments were conducted for 104 steady states for changing the condenser air inlet temperature, the evaporating temperature, the super heating degree, the rotational compressor speed, and the internal heat exchanger. Energy analysis for each component were performed on the basis of the cooling capacity, the volumetric efficiency, the compressor power consumption, and the COP. R1234yf showed 9% lower cooling capacity, 5% lower volumetric efficiency and 5%-30% lower COP as compared to R134a. Conclusion of study shows that the energy performance of R1234yf in a drop-in replacement are close to those obtained with R134a.

Cho et al. [19] performed the experimental analysis by charging the same automotive air conditioning systems with the R134a and R1234yf. Refrigeration cycle characteristics compared for both R134a and R1234yf. It was observed that power consumption and cooling capacity of R1234yf was 4% and 7% lower than that of R134a respectively. Evaporator capacity and *COP* of the R1234yf system without the internal heat exchanger decreased by up to 7% and 5%, respectively, but with the internal heat exchanger decreased by up to 2% and 3%, respectively.

Moles et al. [20] investigated the effect of an internal heat exchanger (IHx) on the performance of a vapour compression system using R1234yf and R134a. Experimental tests were carried out varying the condenser air inlet temperature, the evaporating temperature and the internal heat exchanger used in vapour compression system. It was observed that without IHx cooling capacity and COP were shown 6% and 13% lower than that of R134a and with IHx 2% and 6% lower than that R134a respectively. It was also observed that experimental results obtained agree with the theoretical evaluations neglecting the pressure drops in system.

2.1.3 Energy and exergy analysis of AAC systems

Hosoz et al. [21] performed an energy and exergy analysis with R134a for an automobile air conditioning system. At various operating conditions exergy and energy analyses were carried out for

each of the components of the AAC system. The results showed that the performance of the system degraded with increasing compressor speed. For the same cooling capacity, the coefficient of performance of the system is lower at higher condensing temperatures at different compressor speeds. Also the COP increased with increasing evaporator load and decreased with increasing compressor speed and condenser air inlet temperature. It was found that the rate of exergy destruction in each component of the AACs increased with compressor speed, with the the largest exergy destruction occurring in the compressor.

2.1.4 AACs with swash plate compressor

Alkan and Hosoz [22] investigated the performance of an AACs with fixed capacity compressors (FCC) and variable capacity compressors (VCC) with R134a. Experiments were conducted under steady state condition by varying the rotational compressor speed, temperatures of the air entering the condenser and evaporator as well as the velocities of these air streams. Energy and exergy analysis has been applied for both the compressors to evaluate their performance. From the results of the study it was proven that the COP of AACs with variable capacity compressor was greater than the COP of AACs with fixed capacity compressor. After a certain compressor speed, the evaporator capacity and the rate of total exergy destruction in the variable capacity compressor remain almost constant while they increased continually with the compressor speed in the fixed capacity compressor (FCC).

Jabardo et al. [23] performed the numerical simulation and experimental analysis of an AACs with a variable capacity compressor(VCC). Mathematical formulation was done for each component of AACs including evaporator, micro channel parallel flow condenser, thermostatic expansion valve, variable capacity compressor and integrated model was obtained for system. For simulation results validation, experiments were performed with original components from an AACs of a compact passenger vehicle. The experiments were performed by varying various operational parameters such as compressor speed, return air in the evaporator and condensing air temperatures. It was found that there was a maximum deviation of 20% between the results of the model and experiments but most of them were within a 10 % range. It was proven that there was no effect on the system performance

over a wide range of refrigerant charges (refrigerant inventory experimentally evaluated). It was concluded that for overcharged refrigerant conditions the COP was always affected negatively. Due to the action of the capacity control mechanism, the condenser air inlet temperature and compressor speed did not affect the refrigerating effect of system. Recirculating air temperature in evaporator significantly affected the refrigerating capacity. It was observed that the compressor control device can accommodate a significant range of heat loads even those associated to return temperatures higher than the ones in the typical range (from 20 °C to 30 °C). The evaporator capacity, mass flow rate and COP were found to vary more or less linearly with the condensing and return air temperatures and rotational compressor speed.

Tian [24] developed a mathematical model of the control mechanism for a variable displacement swash plate compressor (VDSC) based on the force balance, mass and energy conservation equations for an AACCS. Then a model of the moving components dynamics was developed by analysing the forces and moments of forces acting on the pistons and the swash plate of the variable displacement swash plate compressor (VDSC). The compression model was developed by curve fitting of the experimental results. By combining the above three sub-models, a steady-state mathematical model of VDSC was developed. A test bench for control mechanism and the test system for VDSC were established and experimental results were obtained for verification of the mathematical model. It was observed that the simulated results agreed well with the experimental data. Employing constant and variable, rotational speed and piston stroke, found operational modes were identified for the VDSC. It was found that a hysteresis zone and multiple-valued relationship existed between the compressor parameters when piston stroke was changed.

2.1.5 Simulation and modelling of AACCS

Lee and Yoo [25] performed the simulation analysis of an AACCS under various working conditions. The AACCS consisted of a swash plate compressor, evaporator (laminated type), parallel flow condenser, receiver and an externally equalized TXV. On the basis of overall heat transfer coefficient and pressure drop, a computer program of laminated evaporator was developed. An equation for the heat transfer coefficient was developed which predicted the condensing capacity for the parallel flow type condenser

which was shown to be in very close agreement with the experimental data. The integrated model of AACCS was developed by combining the sub models of the system components. It was concluded that system performance was affected by the condenser size and refrigerant charge. It was concluded that an overcharge of 10% proved to be most effective for various operating conditions. With an overcharge above this level, the COP of system tended to drop. For various operating conditions of the system, it was easy to select the appropriate size of condenser by executing the system performance simulation program. The simulation and experimental results agree to within 7%.

Hendricks [26] performed the transient air conditioning analysis for the optimization of an AACCS. By utilizing the SINDA/FLUINT analysis software, a transient air conditioning system model was developed by National Renewable Energy Laboratory (NREL) which took into account all the relevant physics including refrigerant two-phase flow in the evaporator and condenser channels, system mass effects, air side heat transfer rate in both heat exchangers (condenser and evaporator), vehicle speed effects, temperature sensible properties and integration with a simplified cabin thermal model. This demonstrated that robust and powerful system design optimization capabilities and also presented single and multiple variable design optimizations. System *COP*, cool down time of cabin, and system heat load capacity were optimized. Attention was focused on the R134a AC system and an effort was also made to modify the model for the transient performance with CO₂. For optimisation of AC system designs within the overall vehicle design optimization, the National Renewable Energy Laboratory (NREL) integrated its transient air conditioning model into NREL's ADVISOR vehicle system analysis software.

Kamar et al. [27] predicted the performance of an AACCS by an Artificial Neural Networks (ANN) model. Cooling capacity of evaporator, compressor work input and the *COP* of the AACCS were predicted by developing the ANN model for a standard air conditioning system of a passenger car. Various compressor speeds and air temperatures and velocities at evaporator and condenser inlets were considered. The network using Levenberg-Marquardt (LM) variant was optimized for 4 – 3 – 3 (neurons in input, hidden and output layers) configuration. The analysis showed good performance with an error index in the range of 0.65 to 1.65%, mean square error (MSE) between 1.09×10^{-5} and 9.05×10^{-5} and root mean square error (RMSE) in the range of 0.33 to 0.95%. The correlation which

relates the predicted outputs of the ANN model to the experimental results had a high coefficient in predicting the AACS performance.

Hosoc et al. [28] adopted the Adaptive Neuro-Fuzzy Inference System (ANFIS) approach to develop the modelling of an R134a AACS. The experimental setup was developed with variable capacity swash plate compressor and a thermostatic expansion valve along with various instruments for mechanical measurements. The experimental system of AACS was operated at steady state conditions by changing the compressor speed, dry bulb temperatures and relative humidity of the air streams entering the evaporator and condenser as well as the mean velocities of these air streams. The data obtained from experiments was used to develop the ANFIS model which predicted the various performance parameters of the system including the air dry bulb temperature at the evaporator outlet, cooling capacity, coefficient of performance and the rate of total exergy destruction in the refrigeration circuit of the system. In the study it was determined that the predictions usually agreed well with the experimental results with correlation coefficients in the range of 0.966-0.988 and mean relative errors in the range of 0.23-5.28%. Finally it was proven that ANFIS approach can be used successfully for predicting the performance of AACS.

2.1.6 Performance enhancement strategies for AACS

Bhatti [29] deals with the potential augmentation of the AACS with R134a to lower its global warming impact and Total Equivalent Warming Impact (TEWI), which are very important parameters for environment friendly systems. It was observed that the most effective augmentation strategy includes increase in isentropic efficiency of compressor, increase in effectiveness of condenser, decrease in lubricant circulation through the system, decrease in air side pressure drop in evaporator through improved condensate management, increase in air flow through the condenser, decrease in air conditioning load via permissible increase in the amount of recirculated air through the passenger compartment and reduction in direct emission of R134a from the system through conservation and containment measures. It is observed that COP of the system is affected by each of these augmentations in a rigorous fashion. This study also provided extensive comparisons of the TEWI of the R134a system with the flammable subcritical systems (R152a, R290 and R717), supercritical carbon

dioxide (R744) system and conventional open air (R729) cycle system. Finally from the study it has been proven that R134a was most pragmatic solution to deal with the issue of the automotive air conditioning system TEWI.

Chen et al. [30] proposed two retrofitted compact and high efficient microchannel heat exchangers for the performance enhancement of an AACS. It was observed that new microchannel heat exchangers had advantages in compactness (17.2% and 15.1% volume reduction for evaporator and condenser, respectively), weight (2.8% and 14.9% lighter for evaporator and condenser, respectively) and heat transfer characteristics compared with the currently used heat exchangers in mobile air conditioning (MAC) industry. The experimental setup consisted of psychrometric calorimeter test bench for both the new microchannel heat exchangers as well as the traditional MAC heat exchangers. System performances were experimentally obtained under variable ambient conditions. It was shown that more compact heat exchangers required less refrigerant charge than baseline system. It was also proven that due to high performance of compact heat exchangers in the system, the cooling capacity was more and the COP of enhanced system was higher under all test conditions except at idle conditions during which they were lower. Finally it was observed that cooling capacity and COP of the enhanced system was increased by about 5% and 8% under high vehicle speeds.

2.2 Mathematical models and performance of swash plate compressor

In the field of mobile air conditioning, there are two types of reciprocating compressors, namely, wobble plate and swash plate, each with variable or fixed displacement. Due to the need of continuous operation, better thermal comfort inside vehicle, and lower fuel consumption, both types of compressors are very popularly in the automotive air conditioning system. In wobble plate type, the wobble plate and pistons are connected with the piston rods. In the swash plate type there are no piston rods and the swash plate inserts into the pistons directly. Therefore the swash plate type is used more widely due to its simple structure, low noise and excellent performance. Very few studies

were reported in the open literature on variable displacement swash plate compressor (VDSC) due to the proprietary nature and competition between the various companies.

Tian and Zhang [35] developed a test bench with a new device to measure the piston stroke length (PSL) of the variable displacement swash plate compressor in AACs. In this experimental study, volumetric efficiency, piston stroke length and displacement control and transient behaviour along with air conditioning load and compressor rotary speed were investigated. The results show that volumetric efficiency of the VDSC is directly proportional to the PSL due to the constant absolute clearance at different piston stroke lengths. At different compressor rotary speeds or vehicle speeds, the PSL and displacement of the VDSC were regulated to meet the air conditioning load. It was also observed that when the air conditioning load changed gradually the PSL underwent a number of small step changes so that the refrigerating capacity of the VDSC could well fit the air conditioning load. The piston stroke length, refrigerant mass flow rate, and other parameters change with a very short time delay to ensure a nearly constant refrigerating capacity of compressor for abruptly changed compressor speeds.

Darr and Crawford [9] developed a steady state model for determining the performance of an automotive air conditioning reciprocating compressor working with R134a. The model equations were developed by energy and mass balances of system components using experimental data. The equations developed are of simple form and can be solved easily in less time without very complicated equation solving methods and the constants in equations were obtained by least square analysis of experimental data. The algorithm could easily be extended to other reciprocating compressors with a minimal amount of experimental data. The developed model was verified by a comparison of simulation results with experimental data. It was claimed that the analytical equations contained physical parameters which can be varied to provide simulations of various compressor geometries with sufficient accuracy.

Miyagawa and Kayukawa [31] developed the one sided swash plate compressor, having a continuously variable displacement mechanism. It was claimed that compressor is simple in structure and having attractive features like excellent noise and vibration characteristics, displacement controllability and reliability up to a maximum compressor speed of 9200 rpm. The authors described the

structure and working principle of the VDSC, however, no details were provided on the steady-state performance or transient behavior.

Yuan [32] introduced the wobble plate type swash plate compressor in AACCS with electronic control device. The displacement was controlled by electronic control (which is replacement of pneumatic valve) valve thus less noise. From geometrical and kinematic information of compressor, the mathematical model was developed to estimate the effect of relevant parameters on variable displacement control. It was claimed that the new electronic control valve can get provide effect than the conventional pneumatic valves.

Tian et al. [33] performed the mathematical formulation and experimental analysis of VDC. A mathematical model of control valve was based on mass and energy conservation, and force and momentum balance equations acting on the piston, piston rod, wobble plate, rotating journal and shaft sleeve. Experimental data fitted for the model for compression process. A steady state mathematical model was developed by combining above three models. Simulation results of combined model was validated with experimental results conducted on a test bench for the control valve and the test system for the VDC. It was claimed that the simulation results show that there are four operation modes for the VDC, i.e. constant rotary speed and constant piston stroke length (PSL), variable rotary speed and constant PSL, constant rotary speed and variable PSL, variable rotary speed and variable PSL, which have included almost all operation modes of the refrigeration compressor.

Delvaux et al. designed an apparatus to measure the Piston Stroke Length (PSL) for a variable displacement wobble plate compressor and observed how PSL changes the system operation. For the measurement of PSL, a position sensor was set in the center of the wobble plate at the end near the discharge cavity and its displacement signal was obtained outside the compressor. However there was the risk of refrigerant leakage because of the installation of the position sensor at a location with a complicated structure.

Tian et al. [34] developed the dynamic mathematical model of VDC in AACCS. Transient response of piston stroke length (PSL), refrigerating capacity, compressor power consumption were investigated by dynamic model. In order to verify the simulation results the experimental facility was developed for same AACCS used in model. The dynamic model simulated the transient behavior of AAC system

when the compressor rotary speed or evaporator fan speed changes suddenly. Conclusion of study shows that whether the piston stroke length changes or not was determined by not only the changing values but also the changing direction of external parameters in the AAC system, the variation of piston stroke length which usually has a time lag when the external parameter varies and a greater counterregulation for the refrigerating capacity and compressor power consumption when the compressor rotary speed changes suddenly due to the adjustment of piston stroke length.

2.3 Heat transfer and friction correlations for louver fin geometry

Beauvais [36] performed the experimental analysis on radiator fin model(10 times size) tested in low turbulence wind tunnel. For the measurement of air velocity profiles, boundary layer thickness, and turbulence within the fin passages hot-wire anemometer method was implemented in analysis. Flow inside the fins was investigated by smoke and china clay. It was noted that the louver angle θ was approximately 30° and the louver to fin pitch ratio (L_p/F_p) was approximately 0.8. It was observed that the main flow was nearly parallel to the louvers for the velocities tested. Before the start of the study it was speculated that louvers might act as surface roughness to enhance turbulence and thereby the performance of the fin arrays. It was claimed that the approach used in study gave the understanding of how a compact fin surface performs and gives a basis for systematic design of heat exchangers. Final conclusion stated that the application of the technique has led to significant improvements in radiator fin performance.

Wong and Smith [37] performed the experimental analysis for a 5:1 scale model of a portion of a typical louvered-fin heat-exchanger core in a controlled turbulence wind tunnel. The comparison was made between scaled model and full model of louvered-fins to investigate the performance characteristics of both models. The air-pressure drop and heat-transfer rate were measured in terms of drag coefficient and Nusselt number as a function of Reynolds number based on the face velocity. It was observed that the scale model and full model show close correlation and air flow phenomena

was similar for both the models. Hot wire and thermocouple probes were used to measured the distributions of airspeed and air temperature at selected locations in the wake.

Davenport [38] investigated that the flow structure within louvered arrays was a function of the Reynolds number (Re_{LP}) by flow visualization experiments similar to the one used by Beauvais [36]. The louvers has only a slight influence on the flow structure and at high values of Re_{LP} the flow became nearly parallel to the louvers. Thus the main flow stream did not pass through the louvers in case of lower Re_{LP} . Finally it was speculated that the boundary layers were developed on adjacent louvers and becomes thick enough to effectively block the passage at a low air velocities which gave nearly axial flow through the arrays. Fig. 2.3 shows the flow direction in louver section at high and low Reynolds number.

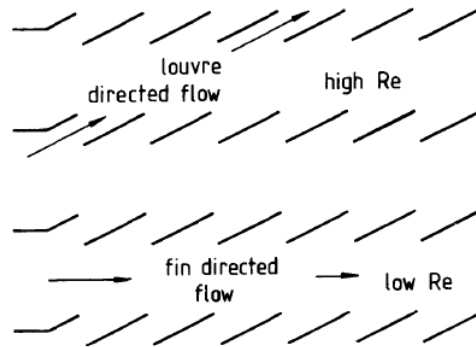


Figure 2.3: Section through louver array indicating possible flow directions. (Davenport [38])

Achaichia and Cowell [39] performed the comprehensive studies for investigating the performance data for flat tube and louvered plate fin surfaces which covered the Reynolds number range from 120 to 8000 for the heating of air at ambient temperatures. The complex flow behavior was obtained by the Stanton number curves which explained that the transition from a ‘flat plate’ to a ‘duct flow’ characteristic as Reynolds number is reduced (Fig. 2.4). This transition occurs when the boundary layers building up on the louver leading edges become thick enough to effectively block off the gap between adjacent louvers in a fin. The simple and accurate correlating equations were developed to describe the flow patters through louver arrays which can be used for fin design.

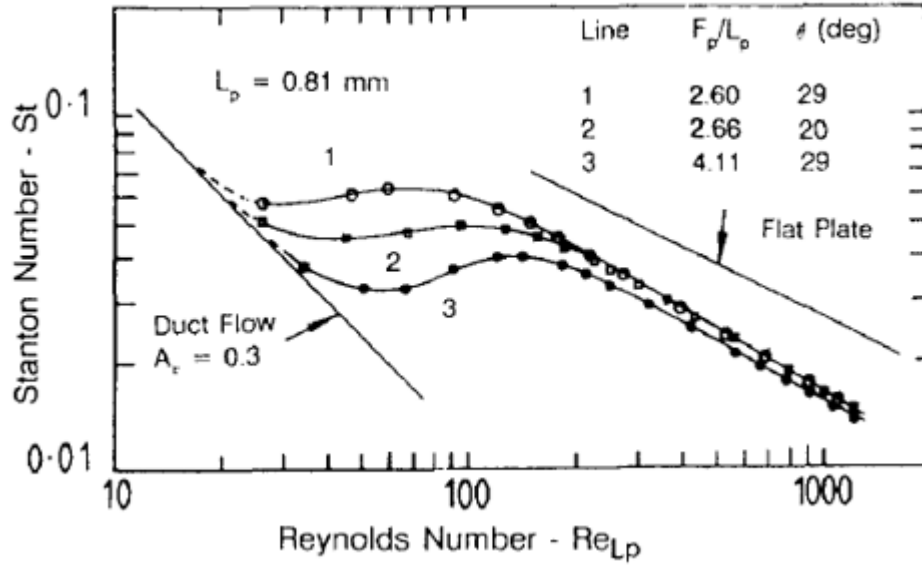


Figure 2.4: Stanton number curves for variants demonstrating transition from duct to flat-plate flow. (Achaichia and Cowell [39])

Achaichia and Cowell [40] investigated the flow through the louvered fin array. The results of numerical modelling is shown in Fig. 2.5. It was observed that the mean flow angle α approached the louver angle θ to within a few degrees as the Reynolds number approaches large values. The mean flow angle α was the integrated average value over the lengthwise directional flow path. At low values of Re_{LP} , fully developed, periodic laminar flow, supports the Davenport's hypothesis concerning the boundary layer development on the louver. It was proven that the Reynolds number Re_{LP} , the louver-to-fin pitch ratio L_p/Fp and the louver angle θ controlled the flow structure. It was also observed that mean flow angle was a strong function of Re_{LP} at low Re_{LP} and was independent of Re_{LP} at high Re_{LP} as shown in Fig. 2.5. The effects of eddy formation in flow on the heat transfer coefficient and friction factor were not predicted because the flow was not parallel to the louvers in cases where eddies were shed from the louvers.

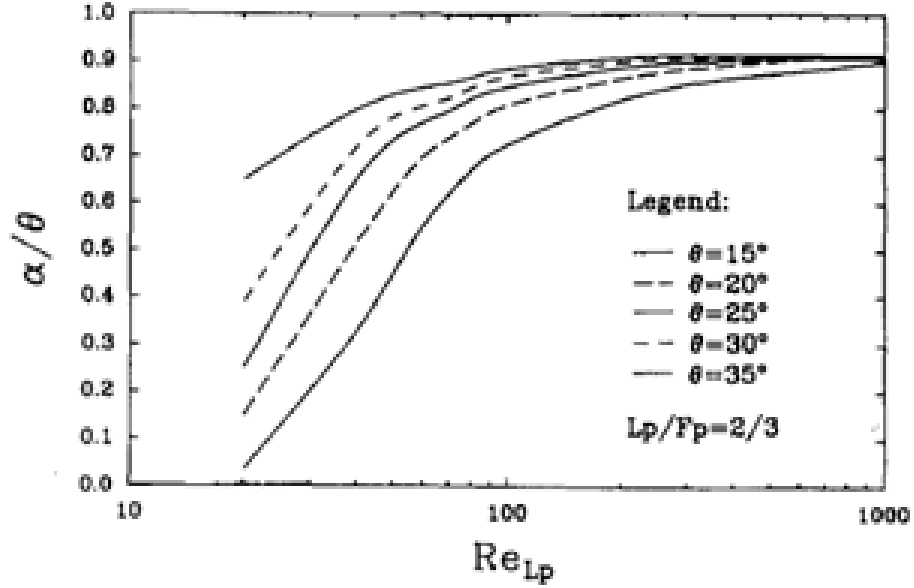


Figure 2.5: Mean flow angle dependence in a louvered fin array (*Achaichia and Cowell* [40])

Howard [41] performed the experimental analysis on two-dimensional louvered fin array (10:1 scale model) by flow visualization using dye injection method. The effect of velocity and Reynolds number on the flow pattern was observed. The vortex shedding commenced at a Reynolds number 30 based on fin thickness and it progressed upstream (from the exit end of the array) as further velocity was incremented. The flow was characterized as ‘efficient’ or ‘inefficient’ flow. If the flow is parallel to the louvers then it is considered as efficient and if predominantly axial (not through the louvers) then considered as inefficient. This classification of flow was based on assumption that the high heat transfer coefficient yielded at efficient flow and consistent with the duct flow and flow over the flat plate. It was observed that at 20° louver angle transition from inefficient flow to efficient flow occurred at $L_p/F_p = 0.7 - 0.8$. The flow structure was considered to be efficient if L_p/F_p greater than 0.8 and inefficient if L_p/F_p is less than 0.7.

Kajino and Hiramatsu [42] used dye injection and hydrogen bubbles method for flow investigation in louvered fin array. The flow pattern over the louvered fin array at louver angle of 26°, $L_p/F_p = 0.67$ and low Reynolds number ($Re_{Lp} = 500$) was captured in photographic form as shown in Fig. 2.6. It was observed that boundary layers appeared on the upper and lower surfaces of the louver and a laminar wake presented itself on the downstream of each louver. It was also shown that on the

back side of inlet louvers the flow got separated. It was concluded that the heat transfer enhancement was due to the thin boundary layers that form at the leading edge of each louver if the flow passed through the louvers. Two louver arrays that have the same louver pitch but different fin pitches were used in the study. From Fig. 2.7 it is clear that on the left hand side portion a significant fraction of flow bypasses the louvers due to the fact that the hydraulic resistance of the duct flow region was substantially smaller than for boundary layer flow across the louvers. When the fin pitch was reduced as in the right hand side part of Fig. 2.7, the hydraulic resistance of duct is increased so that most of the flow passes through the louvers.

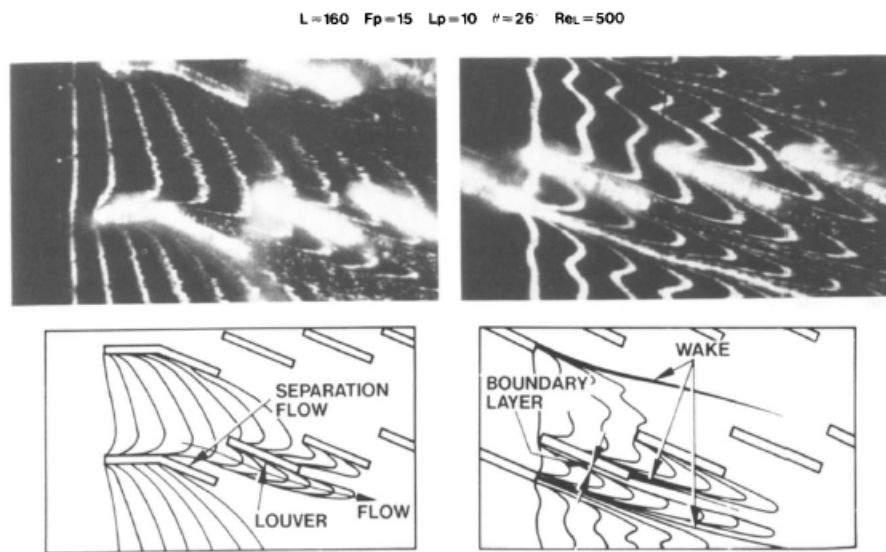


Figure 2.6: Visualization of flow in the louvered fin array (*Kajino and Hiramatsu [42]*)

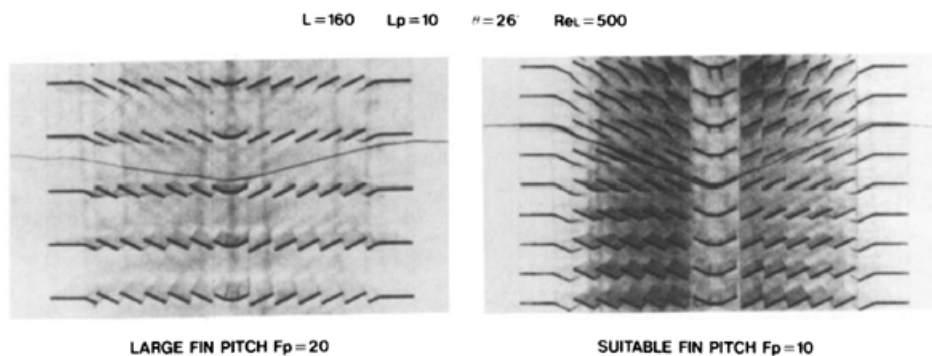


Figure 2.7: Streamlines in a model of the louvered fin array (*Kajino and Hiramatsu [42]*)

Sahnoun and Webb [43] developed a mathematical model for the louvered fin geometry and predicted the air side friction factors and air side heat transfer. Geometrical parameters of the louver

fin such as the number of louvers, louver width and length and the louver angle were considered and the equations of boundary layer and channel flow were utilized for developing the mathematical model. As in the study of Davenport, the model was validated by predicting the heat transfer coefficient and friction factor of 32 louver arrays. It was found that at the highest Reynolds numbers, all of the heat transfer coefficient were predicted within a maximum error of $-14/ + 25$ percent and a mean error of ± 8 percent. Also at the highest Reynolds numbers, all of the friction factors were predicted within a maximum error of $-22/ + 26$ percent and a mean error of ± 8 percent. The equation used to determine the air side heat transfer coefficient for louver fin has following form:

$$h_o = \frac{1}{\eta A_o [h_e A_e + \eta_l h_l A_l + \eta_{s1} h_{s1} A_{s1} + \eta_{s2} h_{s2} A_{s2}]} \quad (2.1)$$

where h_e , h_l , h_{s1} and h_{s2} are the heat transfer coefficient at the end region, louver, non-louvered inlet and exit fin regions and internal flow re-directional louver, respectively. A_e , A_l , A_{s1} and A_{s2} are the areas of the end region, louver, non-louvered inlet and exit fin regions and internal flow re-directional louver, respectively. η_l , η_{s1} and η_{s2} are the efficiencies of louver, non-louvered inlet and exit fin regions and internal flow re-directional louver, respectively. A_o is total air side surface area and η , the surface efficiency.

The equation used to determine the air side friction factor for louver fin has following form:

$$f = f_l \left(\frac{u_l}{u_c} \right)^2 \frac{A_l}{A_o} + f_{s1} \frac{A_{s1}}{A_o} + f_{s2} \frac{A_{s2}}{A_o} + f_e \frac{A_e}{A_o} + C_{DI} \frac{A_{DI}}{A_o} (1 + F_e) f_{app} \quad (2.2)$$

where f_e , f_l , f_{s1} and f_{s2} are friction factor at the end region, louver, non-louvered inlet and exit fin regions and internal flow re-directional louver, respectively. u_l and u_c are the flow velocities over the louver and at the minimum flow area flow, C_{DI} is the drag coefficient on the louvers, F_e is the flow efficiency, A_{DI} is the area on which profile drag occurs and f_{app} is a term accounting for the friction and momentum of the developing flow associated with the flow fraction that bypasses the louvers.

Webb and Wang [44] developed semi analytical heat transfer and friction correlations for the louver fin geometry, which predicted 91% of the friction data within $\pm 20\%$ and 95% of heat transfer coefficient data within $\pm 20\%$.

McLaughlin and Webb [45] reported that the heat transfer coefficient h_o given by Eq. 2.1 can be used in dry fin surfaces such those in condenser where condensate water film does not form on the surfaces. However, in the case of wet surfaces like those in the evaporator, where the temperature of refrigerant is very low, condensate forms on the surface of the heat exchangers. Therefore, for the louver fin geometries in heat exchangers like automotive evaporators, wet air side performance was investigated. The effect of the presence of condensate water film on the air side heat transfer and friction characteristics was examined experimentally in a wind tunnel. Wind tunnel tests were conducted with fully dry and fully wet air side surfaces for measuring the air side sensible heat transfer coefficient and pressure drop. It was found that the wet heat transfer coefficient suffers a significant reduction from the dry value, at a critical louver pitch at which bridging of the louvers occurs by the condensate. The fully wet heat transfer coefficient is given by following equation:

$$h_{o,w} = \left(\frac{c_{p,a}}{b_{w,m}h_o} + \frac{t_w}{k_w} \right)^{-1} \quad (2.3)$$

where h_o is the fully dry heat transfer coefficient given by Eq. 2.1, $c_{p,a}$ is the specific heat of air, t_w is the mean thickness of water film on the air side surface, k_w is the thermal conductivity of water film and $b_{w,m}$ is the slope of the air saturation curve at the mean water film temperature of the external surface.

Park and Jacobi [46, 47] formulated the air side heat transfer and friction correlations for dry and wet fin flat-tube louver fin heat exchangers based on a regression analysis of various experimental data points. j and f factors were developed to predict the air side performance from a most comprehensive experimental base consisting of their own data and data obtained from nine independent laboratories for 126 sample heat exchangers consisting of 1030 heat transfer and 1270 pressure drop measurements. The j and f factor correlations predicted the experimental data with errors of 11% and 16% respectively. For the wet surface louver fin geometry, correlations for the Colburn j and f factor are developed in terms of a wet surface multiplier. The wet surface multiplier correlations fit with 21.1% and 24.4% errors respectively. Also an alternative, stand alone j and f factor correlations resulted in residuals of 22% and 29% respectively.

2.4 Heat transfer correlations for boiling in small channels

Boiling heat transfer is a complicated phenomenon as it involves a two-phase flow process. Boiling is a liquid-to-vapour phase change process that occurs when the temperature of the liquid at a specific pressure is raised to the saturation temperature at that pressure. There are two types of boiling, namely, pool boiling and flow boiling. In pool boiling, liquid does not flow due to an external force, and heat transfer occurs due to the motion of molecules by external heat applied. The example of pool boiling is tea making. In flow boiling, the liquid flows in a channel due to an external force. In flow boiling, the liquid is forced to flow inside the tube, and heat is applied from outside the tube. As the liquid converts to vapour, the dryness fraction changes from $x = 0$ to 1. The steam formation in a flowing pipe, evaporation of a refrigerant in an evaporator are examples of flow boiling. Flow boiling inside a pipe shows different flow regimes as liquid converts to vapour. The heat transfer coefficient changes for different regimes. Fig. 2.8 shows the different flow regimes and the variation of the heat transfer coefficient for flow boiling in a tube. The main flow regimes are as follows: Bubbly flow, slug flow, annular flow, transition flow, mist flow. The heat transfer coefficient has a higher value at the transition flow regime and generally occurs at a dryness fraction between 0.7 to 0.8.

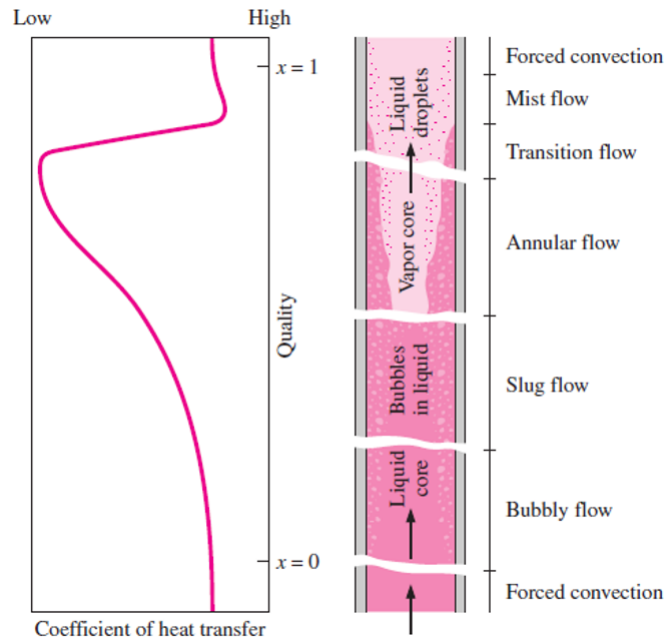


Figure 2.8: Different flow regimes encountered in flow boiling in a tube (*Cengel and Ghajar [140]*)

2.4.1 Classifications of channels

Classification of channels according to Kandlikar [59]:

- Conventional Channels: $D_h > 3$ mm
- Minichannels: $3 \text{ mm} \geq D_h > 0.2$ mm
- Microchannels: $0.2 \text{ mm} \geq D_h > 0.01$ mm

D_h is the hydraulic diameter of channel. This classification was used for flow of gases but can also be recommended for boiling and condensing flows.

Cheng and Wu [60] based on the magnitudes of gravity and surface tension effects proposed the classification:

- Microchannel, if $Bd < 0.5$ (negligible effect of gravity)
- Minichannels, if $0.5 < Bd < 3.0$ (both gravity and surface tension have significant effect)
- Macrochannel, if $Bd > 3.0$ (surface tension has negligible effect)

Kew and Cornwell [61] gave the following classification, based on their tests on heat transfer during boiling in tubes of diameter 1.39, 2.87, and 3.69 mm:

- Microchannel: $Bd < 4$
- Macro channel: $Bd > 4$

Brauner and Ullman [62] studied flow pattern transitions in gas-liquid flow in minichannels and proposed that the transition between mini and macro channel occurs at a Bond number of 1.6.

Li and Wu [63] have given a transition criterion based on their analysis of data for boiling heat transfer in minichannels.

Chen [68] formulated a boiling heat transfer correlation with net vapour generation to saturated, non metallic fluids in convective flow, with an additive mechanism of micro and macro convective heat transfer. In the study two dimensionless functions, an effective two-phase Reynolds number

function F and a bubble-growth suppression function S were taken into consideration for the purpose of the interaction of the two mechanisms. With empirical correlation of heat transfer data and a momentum analogy analysis, F was obtained as a function of the Martinelli parameter and S was obtained as an empirical function of the two-phase Reynolds number. Data available for water and organic compounds were used to test the correlation, which showed $\pm 12\%$ average deviation between calculated and measured boiling coefficients for all (over 600) the data points from ten experiments. Therefore the correlation resulted in good agreement between experimentally measured coefficients and calculated ones. The correlation thus appears to verify the postulated principle of interacting micro and macro convective contributions to boiling heat transfer in the annular flow regime. The function F is calculated by momentum transfer analogy. It was observed that if more data and better understanding of bubble dynamics was known, further improvement was possible for exact functional form of the correlation and the numerically determined values of F and S .

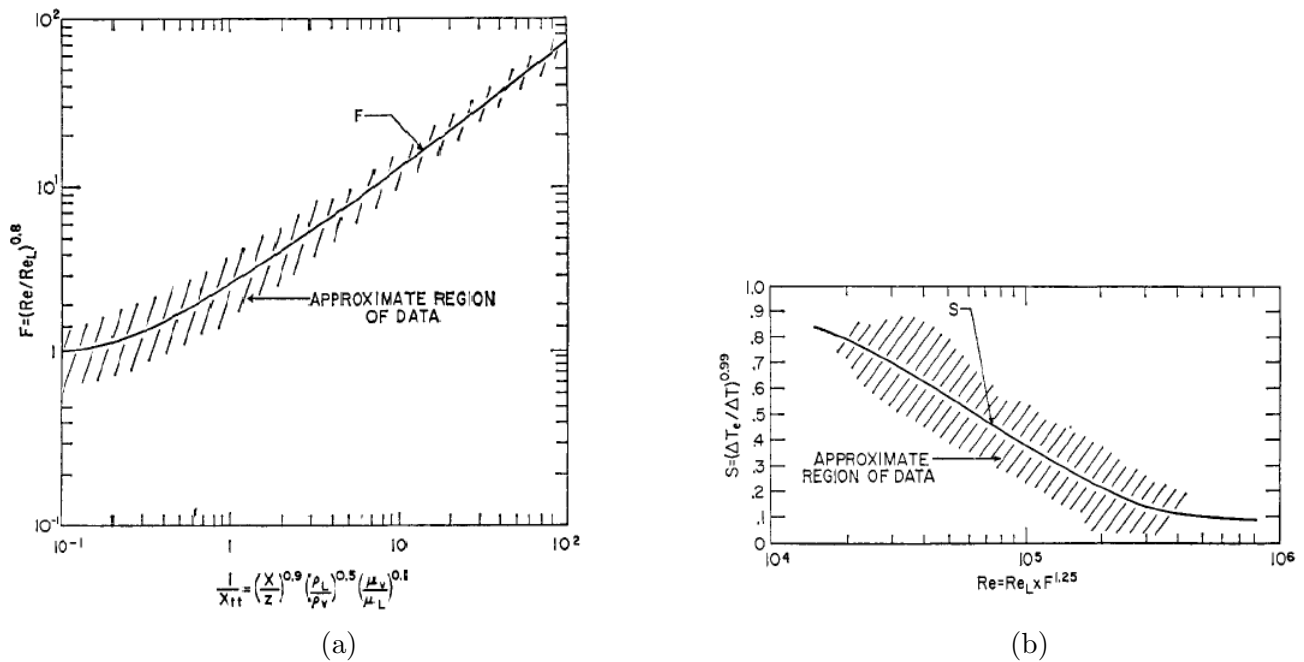


Figure 2.9: (a) Reynolds number factor, f (b) Suppression factor, S , Chen [68]

Shah [48] developed the chart correlation (graphical method) for heat transfer during boiling flow through pipes. Correlation obtained was based on 800 data points from 18 independent experimental studies which can be applicable for most of the common refrigerants and boiling water from 15 to 2500 psia pressure. The charts can be useful for all pipes materials, horizontal and vertical orientation,

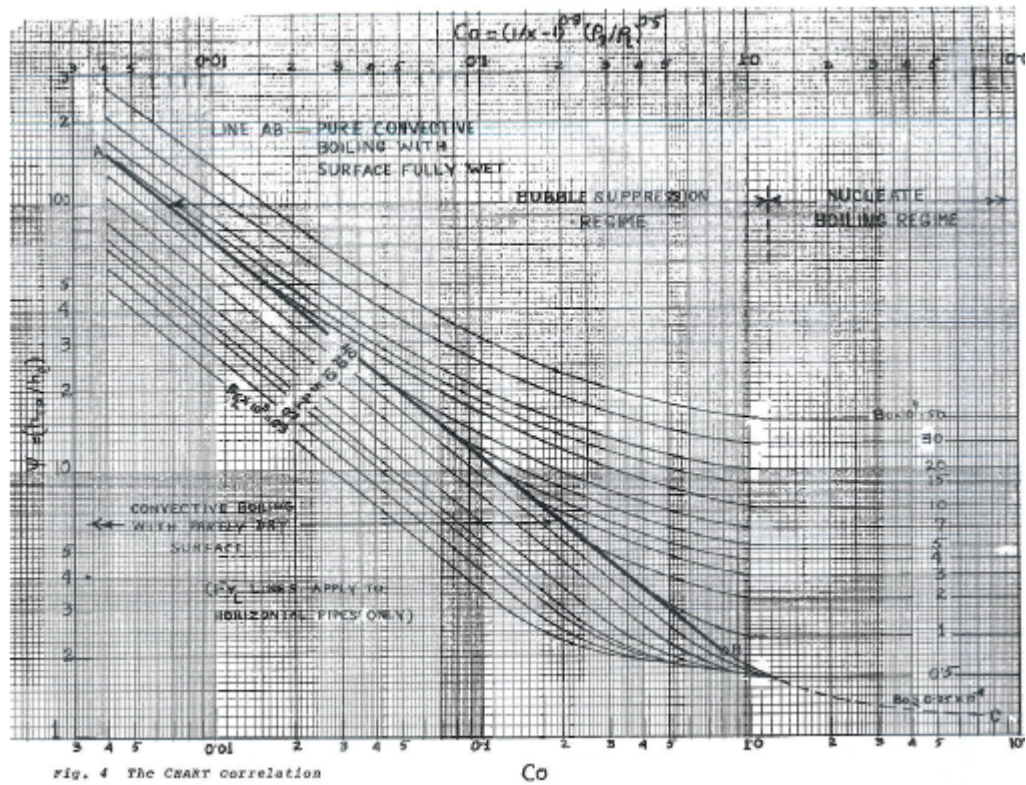


Figure 2.10: The chart correlations given in *Shah* [48]

circular and annular flow channels, upward and downward flow, and wide range of heat and mass flux. Also applicable for saturation boiling inside the pipes of all Newtonian fluids. It is stated that the charts can be useful for saturated boiling at sub-critical heat flux and liquid deficiency regions but not applicable for subcooled boiling and stable film boiling. Fig. 2.10 shows the chart correlation developed by Shah.

Shah [49] developed the mathematical equation for the chart correlation which was developed in [48] for heat transfer during boiling flow through pipes. The equations covered three regimes such as nucleate boiling, convective boiling in which bubble nucleation is negligible, and an intermediate bubble suppression regime in which both nucleate boiling and convective effects are significant. The equations are of simple form and covered wide range of refrigeration and steam generation applications. Also the equations can be easily programmed for computer calculations. The results obtained by equations were compared with other experimental results which showed good agreement for wide range of applications. It was claimed that the correlation was verified with 3000 data points for 12

fluids up to reduced pressure of 0.89, in a tubes up to 41 mm diameter and in annuli with gaps from 1.1 to 6.2 mm.

Shah [67] formulated a unified correlation for prediction of heat transfer coefficients during saturated boiling prior to critical heat flux in mini, micro and channels of conventional sizes in horizontal flow and vertical upward flow. It was proven and verified that the correlation is applicable for a wide range of parameters like- channels of various shapes (round, rectangle, triangle), fully or partially heated, horizontal and vertical down-flow, diameters 0.38 mm to 27.1 mm, 30 fluids (water, CO₂, ammonia, halocarbon refrigerants, organics, cryogenes), reduced pressure 0.0046 to 0.787, and mass flux 15 to 2437 kg m⁻²s⁻¹. It was also claimed that the 4852 data points from 137 data sets from 81 sources correlated with a mean absolute deviation of 18.6%. When compared with other correlations it was observed that the present correlation showed significantly lower deviations. The unified equation is given in the form:

$$h_{TP}/h_{Shah} = 2.1 - 0.008 We_{GT} - 110 B_o \geq 1 \quad (2.4)$$

For horizontal channels with $Fr_{LT} < 0.01$, $F = 1$, use of D_{HYD} in We_{GT} and Fr_{LT} is recommended while the use of D_{HP} is recommended in all other expressions. D_{HP} is the ratio of four times the flow area to the perimeter with heat transfer. $h_{Shah}=h_{TP}$ is the two phase heat transfer coefficient.

Klimenko [69] developed a generalized correlation for vertical and horizontal channels with a fully wetted perimeter for two-phase forced flow heat transfer (nucleate boiling and vaporization). The correlation shows 12.9% absolute deviation with experimental data obtained for nine fluids((water, freons, cryogenes). The correlation is applicable for a wide range of parameter: pressure 0.61-30.4 bar, mass flow rate 50-2690 kg.s⁻¹, vapour quality 0.017-1.00, channel diameters 1.63-41.3 mm. It was observed that vaporization heat transfer rate was dependent on the thermal conductivity of channel wall material.

Klimenko [70] developed a generalized correlation for vertical and horizontal channels with a fully wetted perimeter for two-phase forced flow heat transfer (nucleate boiling and vaporization). The correlation was applicable for experimental data for 21 different liquids (water, organic liquids, freons and cryogenics) in the following ranges of the main parameters: pressure, 0.61-196 bar; heat flux

density, $10 - 8 \times 10^6 \text{ Wm.w}^{-2}$; mass flow rate, $5.6-6240 \text{ kg.m}^{-1}.\text{s}^{-1}$; channel diameter, $0.47-74.7 \text{ mm}$ and showed mean absolute deviation of 14.4% . It was observed that thermal conductivity of the channel wall material affected the nucleate boiling and the vaporization heat transfer intensity. For four groups of fluids (water, organic liquids, freons and cryogens), it was demonstrated that nucleate boiling heat transfer was described by a single equation in dimensionless variables containing an individual constant. Also a single equation with a constant applicable for all the fluids was proposed.

Kandlikar [59] developed a correlation for vertical and horizontal tubes for predicting saturated flow boiling heat transfer coefficients. Correlation was based on contributions due to nucleate boiling and convective mechanisms in flow boiling and covered 5246 data points from 24 experimental investigations with ten fluids (water, R11, R12, R13-B1, R22, R113, R114, R152a, nitrogen, and neon). It was reported that correlation gives a mean deviation of 15.9 percent with water data, and 18.8 percent with all refrigerant data.

Wambsganss et al. [134] investigated the boiling heat transfer of R113 refrigerant in 2.92 mm diameter tube. The local heat transfer coefficients were measured from experiments and 10 correlations for heat transfer coefficients were developed for a heat flux range of $8.8 - 90.75 \text{ kW.m}^{-2}$, mass flux $50 - 300 \text{ kg.m}^{-2}.\text{s}^{-1}$, equilibrium mass quality $0 - 0.9$. High boiling number was observed at high heat flux and low mass flux in small channels. It was also observed that slug flow pattern was produced in small diameter channels. The results of these two, high boiling number and slug flow pattern lead to domination by nucleation mechanism. It was claimed that data obtained by the studies showed good agreement with other investigator's data and the results are applicable for compact heat exchangers.

2.5 Heat transfer correlations for condensation in small channels

Condensation occurs when the temperature of vapour is reduced below its saturation temperature. It is complicated vapour to liquid conversion process involving two phase phenomenon. There are two types of condensation namely, film condensation and dropwise condensation. The heat transfer coefficient and pressure drop during condensation in flow through the small channels are very essential

parameters in the refrigeration and air conditioning applications. The super-heated vapour from compressor is condensed in condenser to convert into sub-cooled liquid. To understand the flow patterns(different regimes) and heat transfer and pressure drop in condensation, numerous analytical and experimental studies were done in past years. The analytical studies involved modeling of physical condensation problem and experimental studies deals with measurement of heat transfer behavior of certain fluids.

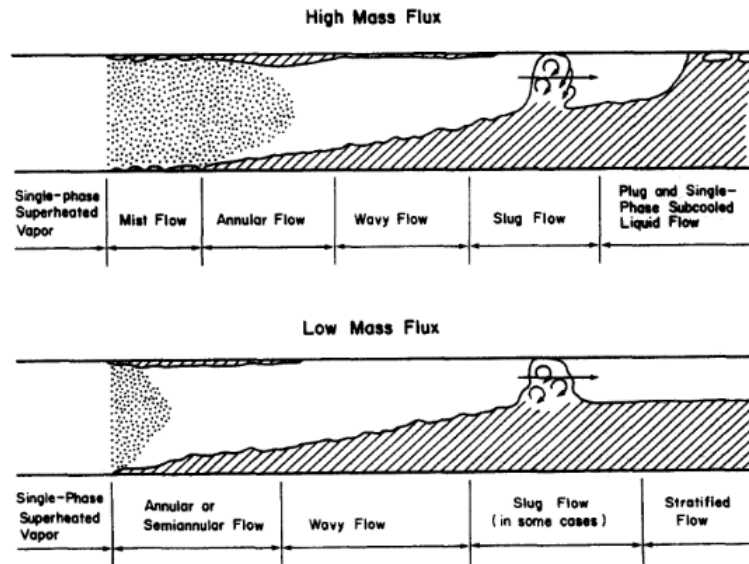


Figure 2.11: Flow patterns in condensation in horizontal tube, *Soliman* [86]

Baker [77] performed the experimental analysis to measure the pressure drops for oil and gas flow simultaneously in 4 to 10 inch diameter pipes. Flow regime chart was developed to predicting the type of flow pattern in the pipeline. Different flow regimes were observed from chart namely, bubble flow, plug flow, stratified flow, wavy flow, slug flow, annular flow, and spray flow. Lockhart and Martinelli method for designing two-phase pipeline was inadequate for larger diameter lines and also for some flow patterns. Therefore separate correlations were developed for each flow pattern by modifying the Lockhart and Martinelli method. It was observed that manifold increased the pressure drop when liquid was deliberately put into a gas pipeline due to the faster motion of gas then liquid(accumulated liquid reduce the area for gas flow). It was reported that pressure loss of a fluid flowing through a pipe is inversely proportional to the fifth power of the pipe diameter. A reduction of 20% area could

cause 3/4 increase in pressure drop and 60% reduction could increase pressure drop by one hundred times. For some gas-liquid ratio, many projections of liquid waves into the gas steams were observed.

Mandhane et al. [78] used a database of 5935 experimental data to develop a flow regime map similar to that of Baker [77]. In this map superficial gas velocity was taken as the abscissa and the superficial liquid velocity as the ordinate(Fig. 2.12) so that it can be easily read. It was observed that the map can correctly predict the flow regime for 68 percent of the observations in their database compared to 42% for the original Baker map. The boundaries of the map were constructed primarily for air-water data in larger tubes. Comparisons with recent data for refrigerants revealed systematic problems with the Mandhane map because of the much higher vapour densities of the refrigerants than air densities in the Mandhane data. The vapour density is considerably higher at condensation temperatures than at evaporation temperatures.

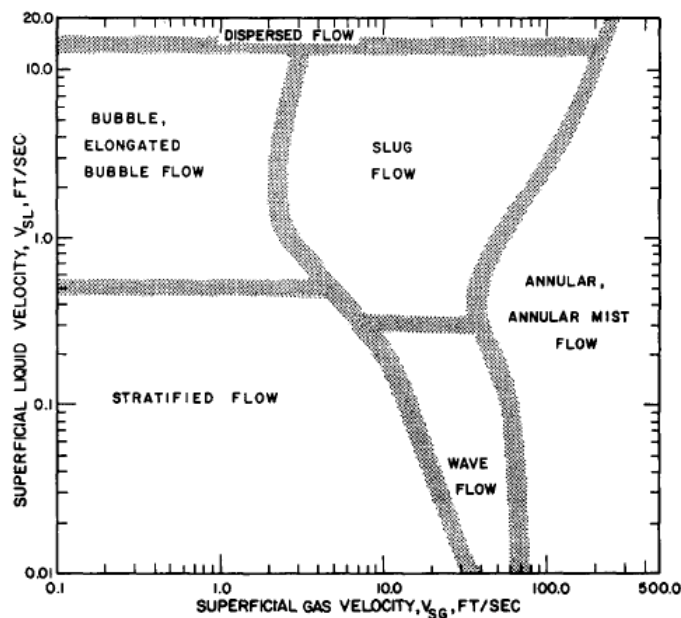


Figure 2.12: Flow pattern map, *Mandhane et al.* [78]

Taitel and Dukler [79] predicted the flow regimes for concurrent gas liquid flow in pipes from data covered for flow rates and fluid properties. The regimes map developed in a two-dimensional plot by locating transition boundaries between the regimes. This map includes five flow regimes such as stratified smooth, stratified wavy, annular, intermittent (plug and slug) and dispersed bubble. Proposed model predicted the relationship between the following variables at which flow regime

transitions take place: gas and liquid mass flow rates, properties of the fluids, pipe diameter, and angle of inclination to the horizontal.

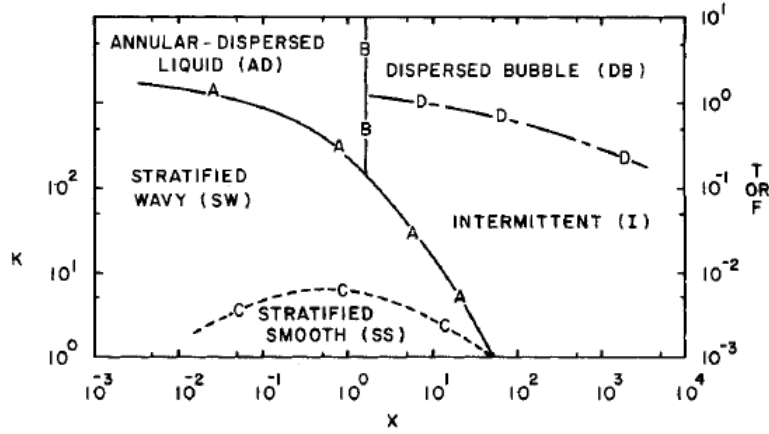


Figure 2.13: Flow pattern map, *Taitel and Dukler* [79]

In this study the map was developed for adiabatic flows but can also be used for diabatic flows investigated by others (Barnhart [120], Wattelet [121], Wattelet et al. [122]).

Butterworth [80] and Dukler and Hubbard [81] observed experimentally the transition of a stratified-wavy flow to an intermittent or annular flow. Wave growth on stratified-wavy flow which led to one of two effects were described in this study. One is the annular flow which is due to low liquid fractions at which the wave washed the liquid around the circumference of the tube and the second is the intermittent (slug or plug) flow at high liquid fractions at which the wave bridged the tube cross section. This transition based on a modification of the Kelvin-Helmholtz stability for an infinitesimal wave between two horizontal plates was predicted by Taitel and Dukler who also extended the theory to predict the stability of finite waves inside a tube. In dimensionless form, their result can be expressed as follows:

$$F_{td}^2 \left[\frac{1}{(1 - \tilde{h}_l)^2} \frac{\tilde{u}_g^2 \sqrt{1 - (2\tilde{h}_l - 1)^2}}{\tilde{A}_g} \right] \geq 1 \quad (2.5)$$

All terms in the bracketed portion of Eq.2.5 are exclusive functions of the Martinelli parameter, so the boundary is a function of only F_{td} and X_{tt} .

Soliman [82] investigated effect of tube diameter and fluid properties on the transition from annular to wavy and intermittent flow during condensation inside horizontal tubes for eight data sets covered with different tube diameters (diameter ratio of 3.3:1) and different test fluids (vapor density ratio of about 50:1). It was observed that transition shifted noticeably to higher superficial vapor velocities as the vapor density decreases, while the influence of tube diameter is minor. After comparison with other data it was claimed that approach suggested by Mandhane et al. [78] for property corrections failed in predicting the trends inherent in the data of R12 and R113. However, excellent agreement was possible with the data of condensing steam which is close in properties to air-water mixtures at low values of quality (lower than 0.4). Compared with Taitel and Dukler [79], correlation seems to lose accuracy at higher quality values corresponding to high equilibrium liquid levels for which the Kelvin-Helmholtz theory of stability of surface waves may not be applicable. Therefore modified correlation based on hypothesis that this transition occurs at a constant Froude number, F_r , irrespective of diameter or condensing fluid was developed which predicted the transition with more consistency and accuracy.

Soliman [83] developed the correlation based on a balance between destructive and stabilizing forces acting on the liquid film predicted flow pattern for the mist-annular transition during condensation. The correlation covered wide range of tube diameters and fluid properties. Flow investigation shown that in annular flow, some liquid droplets were entered in to vapour phase flow. The entering of liquid droplets lead to a transition into mist flow as the vapour velocity was increased. Pressure drop and heat transfer coefficient characteristics change was observed during the annular to mist-annular transition. A correlation was developed based on assumption that the stability of the liquid film depends on a balance between the destructive vapor inertia force and the stabilizing surface tension and liquid viscous forces. It was also claimed that the developed correlation shows good agreement with other data for wide range of application.

Soliman [86] investigated and developed the correlation for mist-annular transition on the heat transfer mechanism during condensation. The correlation of annular flow cannot be applicable for mist flow with great accuracy therefore new correlation developed for annular to mist transition which showed good agreement with data base for different fluids and tube orientations. The correlation

developed for annular flow in [83] cannot be used for heat transfer coefficients at high qualities and/or high mass fluxes. Therefore a new correlation for mist flow based on mixture-wall interaction and saturation to wall temperature difference was proposed which showed that a dimensionless parameter Weber number (W_e) had relevance to heat transfer and that $W_e = 30$ may serve as an upper limit for models based on the assumption of annular flow. It was reported that the new mist flow correlation cannot be applicable outside the mist region which may lead to errors outside the mist flow.

Dobson et al. [84] performed the experimental studies with four refrigerants namely, R12, R22, R134a and azeotropic blends of 50% - 50% and 60% - 40% mixture of R32 and R125 in smooth round horizontal tubes (for diameter 3.14 mm to 7.04 mm) for prediction of heat transfer and flow regimes during condensation. Stratified, wavy, wavy-annular, annular, annular-mist, and slug flows were observed with flow visualization at inlet and outlet of condensers and heat transfer data were collected. The flow regimes were divided into two categories, gravity-dominated and shear-dominated flow regimes and it was also reported that true mist flow without a stable wall film was not observed during investigation. It was observed that laminar film condensation was more dominant in gravity dominated flow regime and forced convective condensation was dominant in shear dominated flow. Therefore separate heat transfer correlations were developed for each of these flow regimes and claimed that these correlations agreed well with several of others data. To obtain the optimum diameter of tube the heat transfer correlations were combined with the pressure drop correlations as a simple model. An optimum diameter existed where condensing surface area was a minimum. It was observed that optimum diameter corresponded to a decrease in the inlet temperature difference of between 23% and 37%.

Nusselt [87] was the pioneer in the analytical studies of gravity-driven condensation of a pure component on a vertical plate. Nusselt derived the local and mean Nusselt numbers and the mean Nusselt number at $x = L$ is given by:

$$Nu_L = \frac{\bar{h}_L}{k_f} = 0.943 \left[\frac{g(\rho_l - \rho_g)i_{lg}L^3}{k_f \nu_l (T_{sat} - T_s)} \right]^{1/4} \quad (2.6)$$

The bracketed term in Eq. 2.6 can be expressed in dimensionless form as:

$$\bar{Nu}_L = 0.943 \left[\frac{Ga^* Pr_1}{Ja_1} \right]^{1/4} \quad (2.7)$$

Dhir and Lienhard [88] developed the expressions similar as Rohsenow-Nusselt expressions for condensate film thickness and the local Nusselt number on arbitrary axisymmetric bodies(vertical plates and cylinders). The expressions were based on effective gravity on the body. It was reported that radii of curvature greatly exceeded the film thickness, that Prandtl numbers were never substantially less than unity, and that the ratio of sensible to latent heats was not large. The equation is:

$$g_{\text{eff}} = \frac{x(gR)^{4/3}}{\int_0^x g^{1/3} R^{4/3} dx} \quad (2.8)$$

In Eq. 2.8, $R(x)$ is the local radius of curvature and $g(x)$ is the local gravity component in the x-direction. For the horizontal cylinder, the effective gravity can be evaluated numerically and averaged over the circumference of the tube, yielding:

$$Nu = 0.729 \left[\frac{Ga_D^* Pr_1}{Ja_1} \right] \quad (2.9)$$

The subscript in the Galileo number Ga_D indicates that the diameter is the length scale. Ja_1 is the liquid Jakob number.

Bromley and Rohsenow [89, 90] corrected for the assumption of a linear temperature profile based on integral analysis. It is like including the convective terms which were originally neglected in the energy equation. Cross flow terms were included by Bromley and both of them agreed that this effect could be corrected by replacing the latent heat in Eq. 2.6. The modified latent heat given by

$$i'_{lg} = i_{lg}(1 + 0.68Ja_1) \quad (2.10)$$

It was observed from present corrections that the assumption of a linear temperature profile in the original analysis is quite acceptable for Ja_1 much less than unity. It was shown that gravitational

forces (which tend to pull condensate down the tube wall) are much stronger than the vapour shear forces (which tend to pull the condensate in the direction of the mean flow) during condensation inside horizontal, smooth tubes at low vapour velocities. Therefore at the top of the tube a condensate film is formed and grows in thickness as it flows around the circumference. In the direction of the mean flow, bottom portion of the tube is filled with a liquid pool that transports the condensed liquid along the tube. This heat transfer mechanism is very similar to that in external falling-film condensation for which extensive theory has been developed.

Chato [72] studied stratified flows with low vapour velocities. A similarity solution for the condensate film was developed which was patterned after Chen analysis of falling film condensation outside of a horizontal cylinder. The solution region is the upper portion of the tube where falling-film condensation exists up to the liquid pool at the bottom. A model was developed based on open channel hydraulics to predict the depth of the liquid pool. It was found from the analytical model and experimental results for R113 that the depth of the liquid level was relatively constant. This allowed his heat transfer data to be approximated quite well by the following Nusselt type correlation:

$$Nu = \frac{\bar{h}_D}{k_l} = 0.555 \left[\frac{\rho_l(\rho_l - \rho_g)g'_{lg}D^3}{k_l\mu_l(T_{\text{sat}} - T_s)} \right]^{1/4} \quad (2.11)$$

The constant 0.555 is 76% of the value of 0.728 for external condensation on a cylinder. This decrease in heat transfer is due to the thickness of the liquid pool on the bottom of the tube which reduces the heat transfer to negligible amount.

Jaster and Kosky [91] performed the experimental work for condensation of steam with a horizontal pipe to determine a valid criterion for the flow transition from the initial annular regime to the final stratified regime. It was proposed that the flow regimes can be defined by stress ratio F (the axial shear forces/gravitational body forces). If $F > 29$ the flow is annular, for $29 > F > 5$ flow is transition and for $F < 5$ the flow is stratified. The values of F were measured at the boundaries of the transitional flow regime for steam/water. It was reported that dependency of L/D ratio on flow regimes was not indicated by performed experiments and not distinguishable between turbulent and laminar flow. The heat transfer in the mixed flow regime was correlated in terms of a Nusselt number computed as a linear function of the stress ratio (Fig. 2.14).

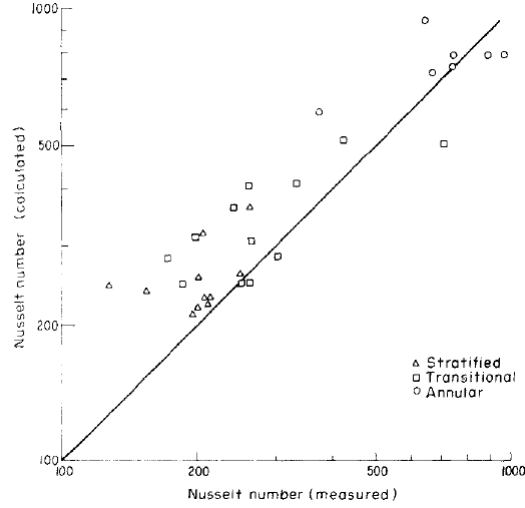


Figure 2.14: Comparison between computed and measured Nusselt numbers for stratified, transitional and annular flow, *Jaster and Kosky* [91]

Rosson and Myers [92] experimentally studied the intermittent flow regime which included stratified, wavy, and slug flows. The variation of heat transfer coefficient with angle around the tube was measured and was proven that the heat transfer coefficient continuously decreased from the top to the bottom of the tube. It was observed that at the top of the tube with superimposed effects of vapour shear, film wise condensation occurred. The constant in the Nusselt's solution was replaced with an empirically determined function of vapour Reynolds number. The equation is:

$$Nu_{\text{top}} = 0.31 Re_g^{0.12} \left[\frac{\rho_l(\rho_l - \rho_g) g i'_{lg} D^3}{k_l \mu_l (T_{\text{sat}} - T_s)} \right]^{1/4} \quad (2.12)$$

In the bottom of the tube forced-convective heat transfer was postulated. Using a heat and momentum transfer analogy, the recommended correlation is:

$$Nu_{\text{bot}} = \frac{\phi_{1,\text{lt}} \sqrt{8 Re_1}}{5 \left[1 + \frac{\ln(1 + 5 Pr_1)}{Pr_1} \right]} \quad (2.13)$$

where

$$\phi_{1,\text{lt}} = \sqrt{1 + \frac{1}{X_{\text{lt}}} + \frac{12}{X_{\text{lt}}^2}} \quad (2.14)$$

To represent the fraction of the tube perimeter over which film wise condensation occurred, the parameter β was defined as

$$\beta = Re_g^{0.1} \quad \text{if} \quad \frac{Re_g^{0.6} Re_1^{0.5}}{Ga} < 6.4 \times 10^{-5}$$

$$\beta = \frac{1.74 \times 10^{-5} Ga}{\sqrt{Re_g Re_1}} \quad \text{if} \quad \frac{Re_g^{0.6} Re_1^{0.5}}{Ga} > 6.4 \times 10^{-5}$$

The circumferentially averaged Nusselt number was given by

$$Nu = \beta Nu_{\text{top}} + (1 - \beta) Nu_{\text{bot}}$$

For acetone and methanol compounds Rosson and Myers [92] compared their predicted values with their own experimental data and it was found that the agreement was reasonable. A large amount of scatter was inherent due to inaccuracies in the experimental technique, so it was difficult to discern whether the deviations were due to experimental scatter or theoretical deficiencies.

Tien et al. [93] performed the analysis for gravity-driven condensation valid for stratified, wavy and slug flow. The analysis was similar to that of Rosson and Myers [92] and was more deeply rooted in conservation equations than empirically determined expressions. It predicts a single phase liquid Nusselt number for zero quality and reduces to the form of Rosson and Myers [92] for situations where stratified flow exists rather than slug flow. Six simultaneous nonlinear equations must be solved to use Tien's model. Although novel and well structured, the technique is rather involved for a practical design correlation.

Shah [8] developed a simple dimensionless correlation for condensation inside the pipes to determine the heat transfer coefficient for water, R11, R12, R22, R113, methanol, ethanol, benzene, toluene and trichloroethylene compounds. The correlation covered wide range of data including pipe diameter 7 to 40 mm, horizontal, vertical, and inclined orientations of pipes, reduced pressure from 0.002 to 0.44, saturation temperatures from 21 to 31°C, vapor velocities from 3 to 300 m/s, vapor qualities from 0 to 100%, mass flux 39000-758000 kg.m⁻²h⁻¹, heat flux from 158 to 1893000 W.m⁻², all liquid Reynolds numbers from 100 to 63000, and liquid Prandtl numbers from 1 to 13. It was observed that in the absence of nucleate boiling the mechanism of condensation and evaporation were

very similar. The convective component of Shah's flow boiling correlation was modified to form a two phase multiplier correlation for condensation as:

$$Nu = 0.023 Re_l^{0.8} Pr_l^{0.4} \left[1 + \frac{3.8}{P_{red}^{0.38}} \left(\frac{x}{1-x} \right)^{0.76} \right] \quad (2.15)$$

When quality x approaches 0 then the two-phase multiplier term approaches unity indicating that the single phase liquid heat transfer coefficient when only liquid is present. The properties of vapour and liquid become more alike when the reduced pressure increases and the two-phase multiplier decreases. Therefore qualitative behaviour is as expected from shah's correlation. When Shah compared the correlation with data from other sources for different fluids such as water, methanol, benzene, toluene, trichloroethylene and ethanol, he found that mean deviation between his correlation and the experimental data (474 points) was 17%. Although Shah's correlation was stated to be a generalized correlation and independent of flow regime, it is actually more appropriate for annular flow.

Shah [8] proposed the alternative comprehensive correlations for heat transfer during condensation which was applicable for conventional and mini/micro channels in all orientations. The correlations were developed from 136 data sets from 67 different sources and applicable for wide range of applications includes 33 fluids, hydraulic diameters of 0.1 mm to 49 mm, all orientations from vertically down to vertical up, reduced pressures of 0.0008 to 0.946, mass flux of 1.1 to 1400 kgm⁻²s⁻¹, various shapes (round, rectangular, triangular, etc.), and aspect ratio from 0.14 to 13.9. It was reported that the correlations showed good agreement when compared with others data.

Cavallini and Zecchin [97] deducted the dimensionless groups from the results of a theoretical annular flow analysis and used the same in an annular flow correlation. Later many groups were neglected by using regression analysis and such groups did not appear in the following empirically developed, two-phase multiplier type correlation:

$$Nu = 0.023 Re_l^{0.8} Pr_l^{0.33} \left\{ 2.64 \left[1 + \left(\frac{\rho_l}{\rho_g} \right)^{0.5} \left(\frac{x}{1-x} \right) \right] \right\}^{0.8} \quad (2.16)$$

The two-phase multiplier term is shown in brackets. In this study a comparison was made of the correlation with experimental data of six different studies with fluids like R113, R12 and R22. It was

found that standard deviation between their correlation and the experimental data sets varied from 8% to 47% and mean deviation of all the data combined was 30 percent, if each point was given equal weight, and 22%, if each set was given equal weight.

Cavallini et al. [142] performed the experimental analysis for the proposed correlation for local heat transfer coefficients during condensation of R1234yf and R134a at 40° saturation temperature in 0.96 mm diameter circular channel. The experiments were conducted for mass fluxes ranging between 200 and 1000 $\text{kg m}^{-2}\text{s}^{-1}$ to measure the heat transfer coefficient and pressure drop. It was observed that the R1234yf showed lower heat transfer coefficient than R134a at the same operating conditions (penalization from 15% at 200 $\text{kg m}^{-2}\text{s}^{-1}$ and 0.4 vapour quality to 30% at 800 $\text{kg m}^{-2}\text{s}^{-1}$ and 0.7 vapour quality). The comparison of heat transfer coefficient and pressure drop between R1234yf and R134a is shown in Fig. 2.15.

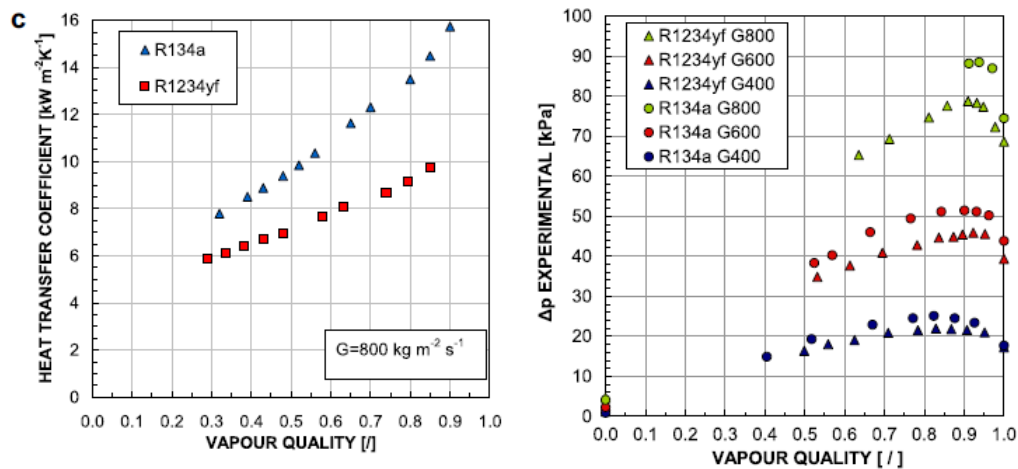


Figure 2.15: Comparison of heat transfer coefficient(left) and pressure drop(right) between R1234yf and R134a, *Cavallini et al.* [142]

Carpenter and Colburn [98] in their study used the shear based correlations for annular flow condensation and found that the resistance to heat transfer in the turbulent liquid flow was entirely inside the laminar sub-layer and that the wall shear stress was composed of additive components due to friction, acceleration and gravity.

Soliman et al. [99] developed a semi-empirical heat transfer correlation for annular flow by utilizing the framework of Carpenter and Colburn [98] and refining the same in several ways. The correlation was corrected for prediction of wall shear stress due to phase change but this component was normally

negligible in comparison to the frictional component except at low qualities. Also the correlation was improved for the friction pressure drop and new values of constants were presented in the correlation from the data of other researchers. Comparison was made for the predictions with data for steam, R113, R22, ethanol, methanol, toluene and trichloroethylene. However, the comparison revealed rather large deviations.

Chen et al. [100] developed the heat transfer correlation for annular-film condensation inside tubes on the basis of analytical and empirical results from the various literature data. Correlation incorporated the effects of interfacial shear stress, interfacial waviness, and turbulent transport in the condensate film. Two cases, cocurrent annular-film condensation inside vertical and horizontal tubes and countercurrent annular-film reflux condensation such as occurs inside the two-phase closed thermosyphon, were used to demonstrate this procedure. It was claimed that the correlations shown good agreement with others data.

2.6 Pressure drop in two phase flow through small channels

Zhang and Webb. [109] experimentally determined the pressure drop of refrigerants R134a, R22 and R404A in single phase flow as well as adiabatic two-phase flow. The geometries considered were a multichannel aluminium tube with an equivalent diameter of 2.13 mm and copper tubes of 3.25 mm and 6.25 inside diameter. The single phase friction factor correlated with Blasius formula with a margin of $\pm 10\%$. As the Fridel model (presented later) did not fit the two phase data adequately, particularly for higher reduced pressures, a new correlation across 119 data points was proposed with a mean deviation of 11.5%.

Lockhart and Martinelli [95] presented a method based on the two-phase multiplier for determining the pressure drop in two-phase flow. The two-phase multiplier depends upon the ratio of the pressure drops of the vapour and the liquid, called the Lockhart-Martinelli parameter X . In [95], the adiabatic two-phase flow data for air-water and oil-water mixtures was correlated in terms of X . Their results were presented in equation form by Chishholm [126].

$$\phi_1^2 = 1 + \frac{C}{X} + \frac{1}{X^2} \quad (2.17)$$

$$\phi_v^2 = 1 + CX + X^2 \quad (2.18)$$

where $\phi_l^2 = (dP_f/dz)/(dP_{f,l}/dz)$, $\phi_v^2 = (dP_f/dz)/(dP_{f,v}/dz)$ and C is a constant ranging from 5 to 20, based on whether the liquid and vapour phases are laminar or turbulent. Baroczy [127] represented his correlation graphically with a very complex behaviour of the multiplier correlation curves. Chisholm and Sutherland [128] provided an empirical function that fits the Baroczy [127] mass correlation terms. Friedel [129] developed a correlation with 25000 data points for both horizontal flow and vertical upflow, considering tube inner diameters down to 4 mm. The standard deviation of the correlation is 30% and is as follows:

$$\phi_{lo}^2 = C_{F1} + \frac{3.24C_{F2}}{Fr^{0.045}We^{0.035}} \quad (2.19)$$

where $\phi_{lo}^2 = (dP_f/dz)/(dP_{f,lo}/dz)$, and $C_{F1} = (1-x)^2 + x^2 \left(\frac{\rho_l}{\rho_v}\right) \left(\frac{f_{vo}}{f_{lo}}\right)$, $C_{F2} = x^{0.78}(1-x)^{0.24} + \left(\frac{\rho_l}{\rho_v}\right)^{0.91} \left(\frac{\mu_v}{\mu_l}\right)^{0.19} \left(1 - \frac{\mu_v}{\mu_l}\right)^{0.7}$, $We = \frac{G^2 D}{\rho_{tp} \sigma}$, $Fr = 1 - \frac{G^2}{gD\rho_{tp}^2}$, $rho_{tp} = \left(\frac{x}{\rho_v} + \frac{1-x}{\rho_l}\right)^{-1}$

Yang and Webb [130] experimentally determine pressure drop for single phase and two-phase flow in small diameter plain and micro-grooved flat extruded aluminum tubes with hydraulic diameters of 2.64 mm and 1.56 mm, respectively. Blasius equation based on hydraulic diameter is used to determine single phase friction factor data for the plain tube.

Wang et al. [131, 132, 133] investigated two-phase flow patterns and friction pressure drop of R134a, R22, and R407C in a 6.5 mm inside diameter plain round tube. It was observed that the flow pattern transition in small diameter tubes is different from that for large diameter tubes, which are better predicted by the Friedel [129] correlation.

Zhang and Webb [139] described the experimental and analytical work to develop a two-phase friction correlation for small hydraulic diameter tubes. Three tubes were tested to determine single phase and two phase pressure drop of refrigerants R134a, R22 and R404a. The two tubes were copper with inside diameters of 6.20 mm and 3.25 mm. The third tube was a multiport, flat extruded aluminum tube with a hydraulic diameter of 2.13 mm. The mass velocity ranges from 200-1000 kg/m²s and vapour quality from 0.2 to 0.89. The pressure drop was obtained in a horizontal tube

under adiabatic conditions so that the acceleration and gravity terms were not involved. The overall pressure drop consists of three components given as:

$$\Delta P_{\text{exp}} = \Delta P_f + \Delta P_i + \Delta P_e \quad (2.20)$$

The first and second terms in Eq. 2.20 are entrance and exit pressure losses respectively and are given by Collieras [7]:

$$\Delta P_i = \frac{G_2^2 v_f}{2} \left[\left(\frac{1}{C_c} - 1 \right)^2 + \left(1 - \frac{1}{\sigma^2} \right) \right] \left[1 + \left(\frac{v_{fg}}{v_f} \right) x \right] \quad (2.21)$$

$$\Delta P_e = G_1^2 \sigma (1 - \sigma) v_f \left[\frac{(1 - x)^2}{(1 - \alpha)} + \left(\frac{v_g}{v_f} \right) \frac{x^2}{\alpha} \right] \quad (2.22)$$

The details of the parameters in Eq. 2.21 and Eq. 2.22 are given by Collier [7].

2.7 Conclusions from the Literature review

Following conclusions are made from the literature review:

1. A number of alternative refrigerants have been proposed for the replacement of R134a but R1234yf is very much suitable and very much similar to R134a. Lee and Jung [15] have experimentally shown that the R1234yf has 4% less refrigeration capacity than R134a which proves that R134a can be replaced by R1234yf. Other sources of literature also suggest that in view of the low GWP value of R1234yf as compared to GWP of R134a, R1234yf is more suitable for Automotive Air Condition Systems (AACSS).
2. A number numerical and experimental studies have been done for AACSS with R134a and other refrigerants. However, not much numerical and experimental work was done with R1234yf. From the review of literature it is found that much work on thermal analysis remains to be done on AACSS with R1234yf as the refrigerant.

3. Thermodynamic and transport properties of R134a are available in many sources including Solvay Fluor manual [101]. The Solvay property correlations are based on experimental data and the values are found to match with Refprop data with 0.2% error. Cleland [102] also presented thermodynamic property correlation for R134a. On the other hand, work needs to be done in providing easily usable correlations for the thermodynamic and transport properties of R1234yf.
4. The mathematical models for swash plate compressor are available in many sources for both fixed plate and variable plate compressor. Most of the compressor work was performed with R134a. Compressor analysis with R1234yf is not available in the literature. Darr et al. [9] formulated various parameters for swash plate compressor based on experimental data with R134a. The actual volumetric efficiency is one of the important parameters for a compressor to determine the mass flow rate of refrigerant. However, there are only a few sources in which correlations for actual volumetric efficiency are presented, examples being Tian and Zhang [102], and Jabardo et al. [102].
5. Air side performance of condenser and evaporator involve heat transfer coefficient and friction factor correlations for dry and wet surface louver fin geometry. Sahnoun and Webb [43] formulations are based on the fundamental theory of boundary layer and flow through channels. The correlations are useful for dry fin surfaces and give accurate results. But Sahnoun and Webb [43] have not presented the analysis for wet fin surfaces. As far as wet surface heat transfer is concerned, McLaughlin and Webb [45] report the heat transfer for wet surface louver fin geometry. However, Park and Jacobi [46, 47] formulations are based on experimental data from various sources and equations are in simple form for both dry and wet fin geometry.
6. Refrigerant side calculations involve heat transfer coefficient and pressure drop for flow in small channels of condenser and evaporator. Boiling and condensation heat transfer in small channels are complicated processes. Large number of works have been done for boiling and condensation by various investigators. Effort was made since 1920's for studying boiling heat transfer process by experimental methods. The studies of flow regimes with the help of charts for different

regions in two phase boiling and condensation is very much helpful to predict the heat transfer coefficients. Shah [48, 49], Baker [77], Taitel and Dukler [79] and Mandhane et al. [78] developed and proposed the regime charts for different flow patterns. The disadvantage of charts is that they are in graphical form and not easy to use in computer simulations. The correlations of Chen [68], Shah [67], Klimenko [69, 70], Kandlikar [59], Wambsganss et al. [134] etc. are very useful for the predictions of boiling heat transfer. Soliman [82, 83, 86, 99], Dobson et al. [84], Dhir and Lienhard [88], Bromley and Rohsenow [89, 90], Chato [72], Shah [8], Cavallini et al. [97, 142] etc. have put in a great deal of efforts to develop heat transfer correlations with maximum accuracy and wide applicability for the condensation process.

Chapter 3

System Analysis and Numerical Calculations

In the present chapter, the mathematical models of various components of a small capacity AACCS are presented along with the property correlations of the refrigerants. The correlations for the thermodynamic and transport properties of the refrigerants including R134a and R1234yf and moist air are obtained from published literature. Properties for liquid and vapour saturation states and superheated state of both the refrigerants are required for making a complete mathematical model of the AACCS. The thermodynamic and transport properties for R134a are either taken from published sources or are calculated from the relevant formulations. However, the thermodynamic properties for R1234yf are generated from an equation of state formulation expressing the Helmholtz free energy in terms of temperature and density. Equations are required for the mass flow rate of refrigerant through the double-acting, five-cylinder, swash plate compressor, actual volumetric efficiency, isentropic work efficiency, heat lost from compressor body due to friction of internal rotating elements and compression power. The equations for actual volumetric, isentropic work efficiencies and heat lost from compressor are obtained from curve fits of experimental data taken from tests conducted on the experimental test rig. The data are obtained for different speeds of the compressor from 72 experiments. The compressor used is a fixed stroke swash plate compressor; therefore both the efficiencies and heat loss are functions of only the rotational speed of compressor. Mathematical models are also formulated for the condenser, evaporator and the thermostatic expansion valve. The

heat exchanger (condenser and evaporator) mathematical models entail two phase flow and liquid deficient/superheated regions and the calculation of heat transfer coefficient, pressure drop and heat capacities of condenser and evaporator. The required equations for the thermodynamic and transport properties of moist air also included in the formulation. The details of the mathematical model of the AACs are presented in the following sections.

3.1 Correlations for the thermodynamic and transport properties of R134a

The relation between saturation pressure and saturation temperature is obtained from Wagner type equation given in Solvay, [101]

$$\ln P_R = \frac{A_1(1 - T_R) + A_2(1 - T_R)^{B_1} + A_3(1 - T_R)^{B_2} + A_4(1 - T_R)^{B_3} + A_5(1 - T_R)^{B_4} + A_6}{T_R} \quad (3.1)$$

The Eq. 3.1 is applicable for the range of $0.60 < T_R < 0.96$. Here $P_R = P/P_c$ and $T_R = T/T_c$. The results obtained from Eq. 3.1 are found to closely match with Refprop software, the average error being 0.2 %. The constants, critical temperature and critical pressure values in Eq. 3.1 are given in Table 3.1.

Table 3.1: Constants in Eq. 3.1.

A_1	-7.7069	B_1	1.5158
A_2	2.4932	B_2	1.9907
A_3	-2.9212	B_3	4.3798
A_4	-3.8684	B_4	1.7461
A_5	4.6898E-01	T_c	374.21 K
A_6	-8.3360E-05	P_c	40.59 bar

3.1.1 Liquid properties

1. Specific liquid enthalpy (h_L) is given in Cleland [102]:

$$h_L = 200000 + 1335.29 T_L + 1.70650 T_L^2 + 7.6741 \times 10^{-3} T_L^3 \quad (3.2)$$

where T_L is the given temperature in °C at which liquid enthalpy is to be determined. Eq. 3.2 is applicable in the range $-40^\circ\text{C} \leq T_L \leq 70^\circ\text{C}$.

2. The liquid density (ρ_L) correlation is that reported in the Solvay Fluor manual [101].

$$\rho_L = \rho_c [1 + C_1(1 - T_R)^{1/3} + C_2(1 - T_R)^{2/3} + C_3(1 - T_R) + C_4(1 - T_R)^{4/3}] \quad (3.3)$$

where $T_R = T/T_c$ and T is the temperature in kelvins at which density is to be calculated. Eq. 3.3 is applicable in the range $0.6 \leq T_R \leq 0.96$.

The constants, critical density and critical temperature values in Eq. 3.3 are given in Table 3.2.

Table 3.2: Constants in Eq. 3.3.

C_1	C_2	C_3	C_4	ρ_c	T_c
1.732277	1.348322	-1.251446	1.056144	511.90	374.21
-	-	-	-	kg/m ³	K

3. The relation for the liquid specific heat at constant pressure (c_p) is taken from [101].

$$c_p = M_o + M_1(1 - T_R)^{1/9} + M_2(1 - T_R)^{2/9} + M_3(1 - T_R)^{3/9} + M_4(1 - T_R)^{6/9} \quad (3.4)$$

The constants appearing in Eq. 3.4 are given in Table 3.3. This equation is applicable in the range $0.6 \leq T_R \leq 0.96$.

Table 3.3: Constants in Eq. 3.4.

M_o	M_1	M_2	M_3	M_4
395.19033	-1588.637	2233.8111	-1120.361	81.256634
kJ/kg.K	kJ/kg.K	kJ/kg.K	kJ/kg.K	kJ/kg.K

4. Liquid dynamic viscosity (η') is given by [101]:

$$\ln \left(\frac{\eta'}{10^{-3}} \right) = H_o + H_1 t + H_2 t^2 + H_3 t^3 \quad (10^{-3} \text{ Pa.s}) \quad (3.5)$$

where t is the temperature in °C at which liquid dynamic viscosity is to be determined. Eq. 3.5 is applicable in the temperature range of -50°C to 60°C. The constants in Eq. 3.5 are given in Table 3.4.

Table 3.4: Constants in Eq. 3.5.

H_o	H_1	H_2	H_3
-1.29909	-0.0129286	4.9223×10^{-6}	-1.9860×10^{-7}
Pa.s	Pa.s/K	Pa.s/K ²	Pa.s/K ³

5. Liquid thermal conductivity (λ') is given by [101]:

$$\lambda' = J_o + J_1 t \quad (10^{-3} \text{ W/m.K}) \quad (3.6)$$

where t is temperature in °C at which liquid thermal conductivity is to be determined. $J_o = 94.21 \times 10^{-3} \text{ W/m.K}$ and $J_1 = -0.4284 \times 10^{-3} \text{ W/m.K}^2$. Eq. 3.6 is applicable in the temperature range of -50°C to 60°C.

3.1.2 Vapour properties

1. Vapour density (ρ_v) is given by [101]:

$$\rho_v = \frac{1}{z + b} \quad (3.7)$$

$$p = \frac{RT}{z} + \frac{E_1 + F_1T + G_1e^{-kT_R}}{z^2} + \frac{E_2 + F_2T + G_2e^{-kT_R}}{z^3} + \frac{E_3}{z^4} + \frac{E_4 + F_4T + G_4e^{-kT_R}}{z^5} \quad (3.8)$$

Eq. 3.7 is applicable for the range of $0.60 < T_R < 0.96$. Term z in Eq. 3.7 can be calculated by an iterative method for given pressure and temperature from Eq. 3.8. The constants and coefficients in Eq. 3.8 are given in Table 3.5.

Table 3.5: Constants in Eq. 3.1.

E_1	-1.40114E-03	F_2	-2.78860E-09
E_2	2.19433E-06	F_4	1.02574E-14
E_3	-6.73580E-10	G_1	-2.69555E-02
E_4	-4.66800E-12	G_2	2.67772E-05
F_1	1.63714E-06	G_4	1.69513E-10
b	2.99628E-04 m ³ /kg	K	5.475
R	8.14892E-04 bar.m ³ /(kg.K)		

2. Vapour enthalpy (h_v) is given by [101]:

$$h_v = h_0 + (pv - RT) + D_1T + D_2\frac{T^2}{2} + D_3\frac{T^3}{3} + D_4\frac{T^4}{4} + D_5\ln T + \frac{E_1}{z} + \frac{E_2}{2z^2} + \frac{E_3}{3z^3} + \frac{E_4}{4z^4} + e^{-kT_R} \cdot (1 + k \cdot T_R) \left(\frac{G_1}{z} + \frac{G_2}{2z} + \frac{G_4}{4z} \right) \quad (3.9)$$

Eq. 3.9 is applicable in the temperature range of -48 °C to 90 °C. h_0 is reference specific enthalpy taken as 295.57 kJ/kg and the constants and coefficients used in Eq. 3.9 are given in Table 3.6 and 3.5 .

3. Dynamic viscosity of vapour (η_v) is given by [101]:

$$\eta_v = \eta_o + \Delta\eta \quad (3.10)$$

where η_o is the ideal gas viscosity and $\Delta\eta$ is the residual contribution. Terms η_o and $\Delta\eta$ are given by:

$$\eta_o = 2.6696 \times 10^{-2} \times \frac{\sqrt{MT}}{\sigma^2 \Omega T^*} \quad (10^{-6} \text{ Pa.s}) \quad (3.11)$$

where $T^* = kT/\epsilon$ and

$$\begin{aligned} \Omega(T^*) = & \exp[0.45667 - 0.53955 \ln T^* + 0.187265(\ln T^*)^2 - 0.03629(\ln T^*)^3 \\ & + 0.00241(\ln T^*)^4] \end{aligned} \quad (3.12)$$

$$\Delta\eta = T_R^{2.2} [\ln(1.65 + \rho_{R0}^{0.8})]^{1.6} \left[e^{(1-\frac{0.78}{T_c})\rho_{R0}} - 1 \right] (F \cdot z_c \cdot \zeta)^{-1} \quad 10^{-6} \quad (3.13)$$

where $z_c = \frac{P_c V_c}{RT_c}$ and $\rho_{R0} = \frac{\rho - \rho_o}{\rho_c}$ and the values of the constants are as follows:

$F = 1$ for R134a

$R = 8314 \text{ J/kmol.K}$ (Universal gas constant)

$\rho_c = 515.30 \text{ kg/m}^3$ (Critical density)

$\rho_o = \text{Density at 1.013 bar and given temperature, kg/m}^3$

$\zeta = 39721 \text{ 1/Pa.s}$

$\sigma = 0.5067 \text{ nm}$

$\epsilon/k = 277.74 \text{ K}$

Eq. 3.10 is applicable in the range of $-50 \text{ }^\circ\text{C}$ to $90 \text{ }^\circ\text{C}$.

4. Thermal conductivity of vapour (λ'') is given by [101]:

$$\lambda'' = L_o + L_1 t + L_2 t \quad (10^{-3} \text{ W/m.K}) \quad (3.14)$$

where t is in °C, $L_0 = 11.804$, $L_1 = 0.0805$ and $L_2 = 1.33741 \times 10^{-4}$. Eq. 3.14 is applicable in the range of -50 °C to 90 °C.

5. Specific heat of vapour at constant pressure (c_p) is given by [101]:

$$c_p = D_1 + D_2T + D_3T^2 + D_4T^3 + D_5/T \quad (\text{kJ/kg.K}) \quad (3.15)$$

The constants appearing in Eq. 3.15 are given in Table 3.6.

Table 3.6: Constants in Eq. 3.15.

D_1	D_2	D_3	D_4	D_5
2.49202×10^{-1}	2.45251×10^{-3}	-1.65650×10^{-6}	8.91048×10^{-10}	-6.96764
kJ/kg.K	kJ/kg.K ²	kJ/kg.K ³	kJ/kg.k ⁴	kJ/kg

6. Enthalpy change in isentropic compression (Δh) when vapour is superheated at suction in compression process is given by (Cleland [102]):

$$\Delta h = \frac{c}{c-1} P_1 v_1 \left[\left(\frac{P_2}{P_1} \right)^{\frac{c-1}{c}} - 1 \right] \quad (3.16)$$

where P_1 , P_2 and v_1 are suction pressure, discharge pressure and suction specific volume respectively. Term c in Eq. 3.16 is represented by a curve fit equation and is given by:

$$c = c_{il} (1 + 1.1757 \times 10^{-3} \Delta T_s - 1.814 \times 10^{-5} \Delta T_s^2 + 4.121 \times 10^{-5} \Delta T_s \Delta T_{sat} - 8.093 \times 10^{-7} \Delta T_s^2 \Delta T_{sat}) \quad (3.17)$$

The quantity c_{il} is given by:

$$c_{il} = 1.06469 - 1.6907 \times 10^{-3} T_{sat1} - 8.560 \times 10^{-6} T_{sat1}^2 - 2.135 \times 10^{-5} T_{sat1} \Delta T_c - 6.1730 \times 10^{-7} T_{sat1}^2 \Delta T_c + 2.0740 \times 10^{-7} T_{sat1} \Delta T_c^2 + 7.720 \times 10^{-9} T_{sat1}^2 \Delta T_c^2 - 6.103 \times 10^{-4} \Delta T_c \quad (3.18)$$

where $\Delta T_c = T_{\text{sat}2} - T_{\text{sat}1}$, $T_{\text{sat}1}$ and $T_{\text{sat}2}$ are saturation temperatures at suction and discharge respectively.

3.2 Correlations for the thermodynamic and transport properties of R1234yf

The relation between saturation pressure and saturation temperature is (Tanaka and Higashi [104]):

$$T_r \log \left(\frac{P_s}{P_c} \right) = A\tau + B\tau^{1.5} + C\tau^{2.5} + D\tau^5 \quad (3.19)$$

where $\tau = 1 - T_r$ and $T_r = T/T_c$.

The value of the critical temperature is $T_c = 367.85$ K and that of the critical pressure is $P_c = 33.82$ bar. This equation is applicable in the range of 210 K to 360 K. The constants appearing in Eq. 3.19 are given in Table 3.7.

Table 3.7: Constants in Eq. 3.19.

<i>A</i>	<i>B</i>	<i>C</i>	<i>D</i>
7.42628	1.98692	-3.60052	6.45367

3.2.1 Liquid properties

1. The correlation for saturation liquid density (ρ_L) is taken from Leck [110]:

$$\rho_L = 478 \sum_{i=0}^4 d_i X^i \text{ (kg/m}^3\text{)} \quad (3.20)$$

$$X = \left(1 - \frac{T}{367.85} \right)^{\frac{1}{3}} - 0.3315471 \quad (3.21)$$

The constants d_i appearing in Eq. 3.20 are given in Table 3.8 and T is in K.

Table 3.8: Constants in Eq. 3.20.

d_0	d_1	d_2	d_3	d_4
1.667131	2.314933	1.032059	0.09413147	-0.8200684

Correlations for liquid specific enthalpy (h_L), specific heat at constant pressure (c_p) and specific heat at constant volume (c_v) are developed by curve fitting the Refprop software data for the working temperature range.

2. Liquid specific enthalpy (h_L):

$$h_L = 2 \times 10^{-7}T^4 - 1 \times 10^{-6}T^3 + 0.0012T^2 + 1.2988T + 200.22 \quad (\text{kJ/kg}) \quad (3.22)$$

This equation is applicable in the range of -40 °C to 70 °C. Here T is in °C.

3. Liquid specific heat at constant pressure (c_p)

$$c_p = 5 \times 10^{-10}T^5 - 2 \times 10^{-8}T^4 - 2 \times 10^{-6}T^3 + 5 \times 10^{-5}T^2 + 0.005T + 1.2801 \quad (\text{kJ/kg.K}) \quad (3.23)$$

where T is in °C and this equation is applicable in the range of -40 °C to 70 °C.

4. Liquid specific heat at constant volume (c_v)

$$c_v = 5 \times 10^{-11} T^5 - 2 \times 10^{-9} T^4 - 2 \times 10^{-7} T^3 + 1 \times 10^{-6}T^2 + 0.002T + 0.8653 \quad (\text{kJ/kg.K}) \quad (3.24)$$

This equation is applicable in the range of -40 °C to 70 °C. The temperature T is in °C.

5. Liquid dynamic viscosity (μ_L)

$$\mu_L = (7 \times 10^{-7}T^4 - 0.0002T^3 + 0.0217T^2 - 2.5487T + 208.65) \times 10^{-6}(\text{Pa.s}) \quad (3.25)$$

This equation is applicable in the range of -40 °C to 70 °C. The temperature T is in °C.

6. Liquid thermal conductivity (k_L)

$$k_L = (1 \times 10^{-10}T^6 - 1 \times 10^{-8}T^5 - 5 \times 10^{-7}T^4 + 3 \times 10^{-5}T^3 + 0.001T^2 - 0.3505T + 71.477) \times 10^{-3} \quad (\text{W/m.k}) \quad (3.26)$$

This equation is applicable in the range of -40 °C to 70 °C. The temperature T is in °C.

3.2.2 Vapour properties

Thermodynamic properties of R1234yf in saturation vapour and superheated vapour state are presented in this section. The equation of state in terms of density and temperature for Helmholtz free energy is presented by Richter and Lemmon [105, 111]. The equation of state is valid from $T = 220$ to 410 K and for pressures up to 30 MPa. The equation of state in terms of density and temperature reads as follows:

$$a(\rho, T) = a^0(\rho, T) + a^r(\rho, T) \quad (3.27)$$

where a is Helmholtz energy, $a^0(\rho, T)$ is ideal gas contribution to Helmholtz energy and $a^r(\rho, T)$ is the residual Helmholtz energy which accounts for the influence of intermolecular forces. All the thermodynamic properties can be calculated by taking the derivatives of dimensionless form of Helmholtz energy.

$$\alpha(\delta, \tau) = \alpha^0(\delta, \tau) + \alpha^r(\delta, \tau) \quad (3.28)$$

In Eq. 3.28, $\delta = \rho/\rho_c$ and $\tau = T_c/T$. The critical values of temperature, pressure and density are taken as $T_c=367.85$ K, $p_c=3382.2$ kPa, and $\rho_c = 475.55$ kg/m³ respectively. The ideal gas Helmholtz energy is:

$$\alpha^0 = \ln \delta \ln \tau + a_1 + a_2\tau + \sum_{i=3}^6 a_i \ln [1 - \exp(-b_i\tau)] \quad (3.29)$$

The constants appearing in Eq. 3.29 are given in Table 3.9. The residual fluid Helmholtz energy

Table 3.9: Constants in Eq. 3.29.

a_1	-4.970583	b_3	1.062478
a_2	4.29352	b_4	3.344237
a_3	3.043	b_5	5.363757
a_4	5.874	b_6	11.762957
a_5	9.337		
a_6	7.922		

is

$$\begin{aligned}
 \alpha^r(\delta, \tau) = & \sum_{k=1}^5 N_k \delta^{d_k} \tau^{t_k} + \sum_{k=6}^{11} N_k \delta^{d_k} \tau^{t_k} \exp(-\delta^{l_k}) \\
 & + \sum_{k=12}^{18} N_k \delta^{d_k} \tau^{t_k} \exp(-\eta_k(\delta - \epsilon_k)^2 - \beta_k(\tau - \gamma_k)^2)
 \end{aligned} \tag{3.30}$$

The constants appearing in Eq. 3.30 are given in Table 3.10.

Table 3.10: Constants in Eq. 3.30.

k	N_k	t_k	d_k	l_k	η_k	β_k	γ_k	ϵ_k
1	0.04592563	1.0	4					
2	1.546958	0.32	1					
3	-2.355237	0.929	1					
4	-0.4827835	0.94	2					
5	0.1758022	0.38	3					
6	-1.210006	2.28	1	2				
7	-0.6177084	1.76	3	2				
8	0.6805262	0.97	2	1				
9	-0.6968555	2.44	2	2				
10	-0.02695779	1.05	7	1				
11	1.389966	1.4	1		1.02	1.42	1.13	0.712
12	-0.4777136	3.0	1		1.336	2.31	0.67	0.910
13	-0.1975184	3.5	3		1.055	0.89	0.46	0.677
14	-1.147646	1.0	3		5.84	80.0	1.28	0.718
15	0.0003428741	3.5	2		16.2	108.0	1.20	1.640

The functions used for calculating vapour density, enthalpy, entropy and specific heat capacities are given below.

1. Vapour density (ρ_v)

$$\rho_v = \frac{p}{R T \left[1 + \delta \left(\frac{\partial \alpha^r}{\partial \delta} \right)_\tau \right]} \quad (\text{kg/m}^3) \quad (3.31)$$

2. Specific vapour enthalpy (h_v)

$$h_v = R T \tau \left[\left(\frac{\partial \alpha^o}{\partial \tau} \right)_\delta + \left(\frac{\partial \alpha^r}{\partial \tau} \right)_\delta \right] + \delta \left(\frac{\partial \alpha^o}{\partial \tau} \right)_\tau + R \quad (\text{J/kg}) \quad (3.32)$$

3. Isochoric specific heat capacity (c_v)

$$c_v = -R \tau^2 \left[\left(\frac{\partial^2 \alpha^o}{\partial \tau^2} \right)_\delta + \left(\frac{\partial^2 \alpha^r}{\partial \tau^2} \right)_\delta \right] \quad (\text{J/kg K}) \quad (3.33)$$

4. Isobaric specific heat capacity (c_p)

$$c_p = c_v + R \frac{\left[1 + \delta \left(\frac{\partial \alpha^r}{\partial \delta} \right)_\tau - \delta \tau \left(\frac{\partial^2 \alpha^r}{\partial \delta \partial \tau} \right) \right]^2}{\left[1 + 2\delta \left(\frac{\partial \alpha^r}{\partial \delta} \right)_\tau + \delta^2 \left(\frac{\partial^2 \alpha^r}{\partial \delta^2} \right)_\tau \right]} \quad (\text{J/kg.K}) \quad (3.34)$$

5. Specific entropy (s)

$$s = R \tau \left[\left(\frac{\partial \alpha^o}{\partial \tau} \right)_\delta + \left(\frac{\partial \alpha^r}{\partial \tau} \right)_\delta \right] - R \alpha^o - R \alpha^r \quad (\text{J/kg.K}) \quad (3.35)$$

where p is pressure in Pa and T is in K.

Equations for transport properties, viz., dynamic viscosity and thermal conductivity [107] [108] [112] are given below:

6. Dynamic viscosity $\eta(\rho, T)$ is expressed in (Dymond et al. [113]) as the sum of four independent contributions:

$$\eta(\rho, T) = \eta_o(T) + \eta_1(T)\rho + \Delta\eta(\rho, T) + \Delta\eta_c(\rho, T) \quad (3.36)$$

where ρ is molar density and T is the absolute temperature. The first term is the dilute gas limit viscosity, the second term is the second virial viscosity, the third term is the residual viscosity and the fourth is the critical enhancement viscosity. In the present study, since the region around the critical point is not encountered, the critical enhancement viscosity is not included in the formulation.

$$\eta_o(T) = \frac{5}{16} \left[\frac{\tilde{M}_w RT}{\pi} \right]^{1/2} \frac{1}{\sigma^2 \Omega^{(2,2)}} \quad (3.37)$$

$$\begin{aligned} \Omega^{(2,2)} = & 1.16145(T^*)^{-0.14874} + 0.52487e^{-0.77321T^*} + 2.16178e^{-2.43787T^*} \\ & - 6.435 \times 10^{-4}(T^*)^{0.14874} \sin[18.0323(T^*)^{-0.7683} - 7.27371] \end{aligned} \quad (3.38)$$

where $T^* = k_B T / \epsilon$ and:

$$\eta_1(T) = B_\eta(T) \eta_o(T) \quad (3.39)$$

$$B_\eta(T) = B_\eta^*(T^*) N_A \sigma^3 \quad (3.40)$$

$$B_\eta^*(T^*) = \sum_{i=0}^6 b_i (T^*)^{-0.25i} + b_7 (T^*)^{-2.5} + b_8 (T^*)^{-5.5} \quad (3.41)$$

$$\Delta\eta(\rho, T) = \rho_r^{2/3} T_r^{1/2} \left(c_0 + c_1 \rho_r + c_2 \rho_r^2 + \frac{c_3 \rho_r + c_4 \rho_r^6 + c_5 \rho_r T_r^2 + c_6 \rho_r^5 T_r}{c_7 T_r + c_8 \rho_r T_r} \right) \quad (3.42)$$

The constants appearing in Eq. 3.37, 3.38, 3.39, 3.40, 3.41, 3.42 are given in Table 3.11. These equations are applicable in the range of temperature 220 K to 410 K and for pressures up to 30 MPa.

Table 3.11: Constants in Eq.(3.37), (3.38), (3.39), (3.40), (3.41) and (3.42).

ϵ/k_B	275 K	b_0	-19.572881	c_0	-0.19425910
$M_w(\text{gmol}^{-1})$	114.0416	b_1	219.73999	c_1	-2.079577245
σ	0.531	b_2	-1015.3226	c_2	0
a_o	-836950	b_3	2471.0125	c_3	-43.47027288
a_1	6336.28	b_4	-3375.1717	c_4	0
a_2	-2.3544	b_5	2491.6597	c_5	0
a_3	0.0395563	b_6	-787.26086	c_6	0
a_4	39509.1	b_7	14.085455	c_7	-3.53882791
a_5	121.018	b_8	-0.34664158	c_8	1

7. Vapour thermal conductivity(λ) The vapour thermal conductivity is given in Ely and Hanley [114] is given below:

$$\lambda = \lambda^{\text{int}} + \lambda^* + \lambda^r + \lambda^{\text{crit}} \quad (\text{W/m.K}) \quad (3.43)$$

In Eq. 3.43, λ^{int} is thermal conductivity of internal modes of heat transfer due to internal motions of molecules.

$$\lambda^{\text{int}} = \frac{f_{\text{int}}\eta^*}{M} \left(C_p^* - \frac{5}{2}R \right) \quad (3.44)$$

where η^* is dilute gas viscosity in $\mu\text{Pa.s}$, C_p^* is ideal gas heat capacity in J/mol.K and $f_{\text{int}} = 1.32 \times 10^{-3}$. λ^* is the dilute gas conductivity given by:

$$\lambda^* = \frac{15 \times 10^{-3} R \eta^*}{4M} \quad (3.45)$$

The term λ^r in Eq. 3.43 is the residual and λ^{crit} is critical enhancement given by [107] [108] [112].

3.3 Mathematical model for the swash plate compressor

The swash-plate compressor in the present system has five cylinders and is a double acting, reciprocating type with fixed stroke. The mathematical model of swash plate compressor consists of the equations for the mass flow rate of refrigerant, actual volumetric efficiency, isentropic work efficiency,

heat loss due to friction and compressor power. Darr and Crawford [9] described the model for the swash plate compressor with isentropic volumetric efficiency, isentropic work efficiency and heat loss due to friction were determined from experimental data. In the present work also, these correlations are determined from the experiments conducted on the experimental facility from 72 data points including varying speed of compressor (600-1400 rpm), air inlet velocity at condenser (1.0 m/s and 1.5 m/s) and air inlet temperature at condenser (26 °C to 34 °C).

1. Correlation for mass flow rate (\dot{m}_r) of refrigerant:

$$\dot{m}_r = 2 n V_{\text{disp}} N \frac{\eta_{a,v}}{60 v_s} \quad (\text{kg/s}) \quad (3.46)$$

where

$$V_{\text{disp}} = \frac{\pi}{4} D_c^2 S_c \quad (3.47)$$

$$\eta_{a,v} = f(r_v) \eta_{cl} \quad (3.48)$$

$$\eta_{cl} = 1 - r \left[\frac{v_s}{v_{d,i}} - 1 \right] \quad (3.49)$$

$$r_v = 2.5642 \times 10^{-06} N^2 - 1.7016 \times 10^{-03} N + 2.3171 \quad (3.50)$$

$$f(r_v) = 0.17763 r_v + 0.022188 \quad (3.51)$$

Eqs. 3.50 and 3.51 are obtained by curve fitting 72 experimental data points covering the ranges of parameters mentioned earlier. Figs. 3.1 and 3.2 show the variation of compressor volume ratio with compressor speed and variation and efficiency ratio with volume ratio respectively for all experimental operating conditions.

For ready reference, the compressor-related nomenclature is as follows:

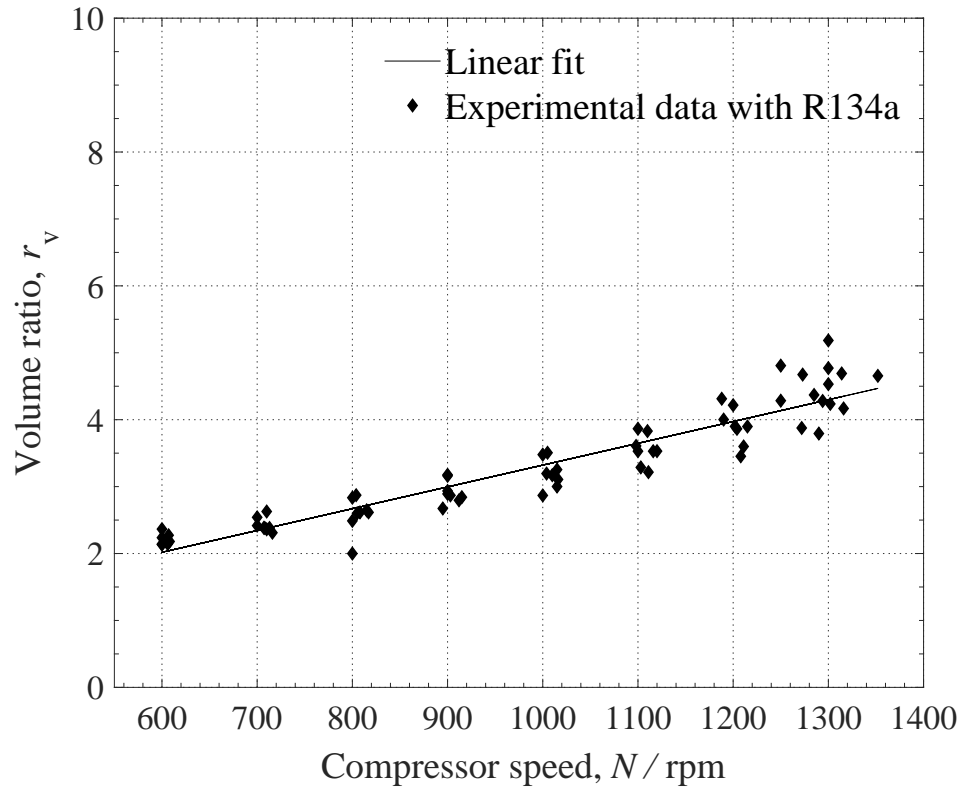


Figure 3.1: Variation of volume ratio with compressor speed for 72 data points.

n = number of cylinders

D_c = Diameter of cylinder (m)

S_c = cylinder stroke length (m)

N = Rotational speed of compressor (rpm)

V_{disp} = cylinder displacement volume

$\eta_{a,v}$ = actual volumetric efficiency

η_{cl} = clearance volumetric efficiency

r = clearance fraction

v_s = specific volume at compressor suction

$v_{d,i}$ = specific volume at compressor discharge for isentropic compression

2. Correlation for the isentropic work efficiency ($\eta_{w,i}$):

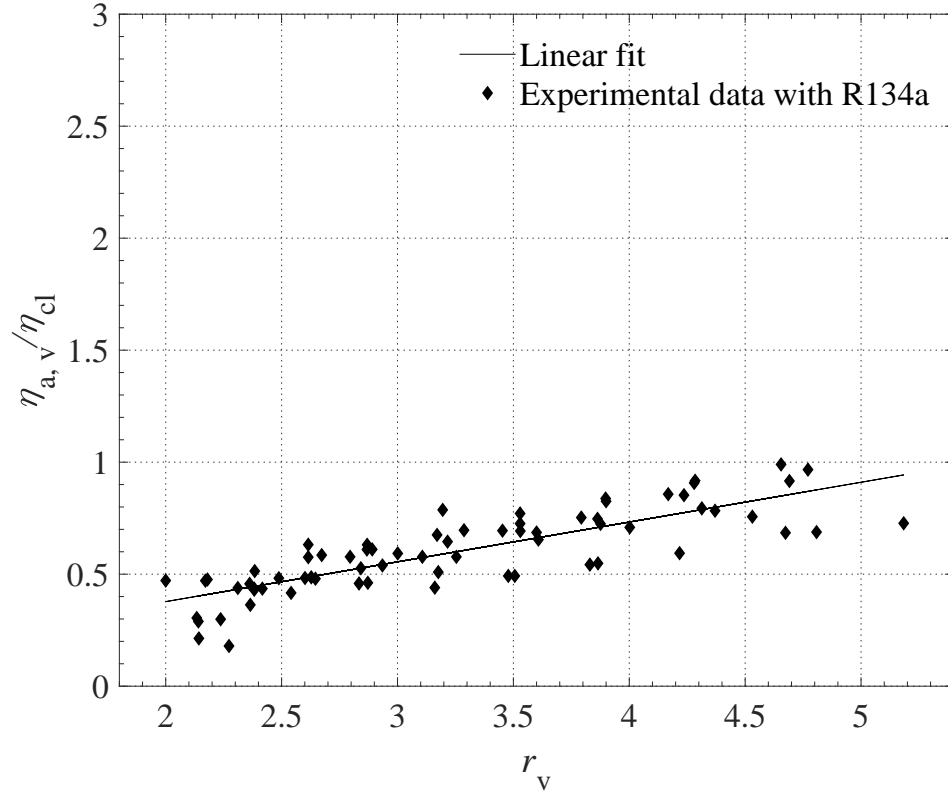


Figure 3.2: Variation of efficiency ratio with volume ratio for 72 data points.

Eq. 3.52 is also obtained by curve fitting the experimental data points. Fig. 3.3 shows the variation of isentropic work efficiency with compressor speed for all the experimental operating conditions.

$$\eta_{w,i} = 6.85142 \times 10^{-05} N + 0.88782 \quad (3.52)$$

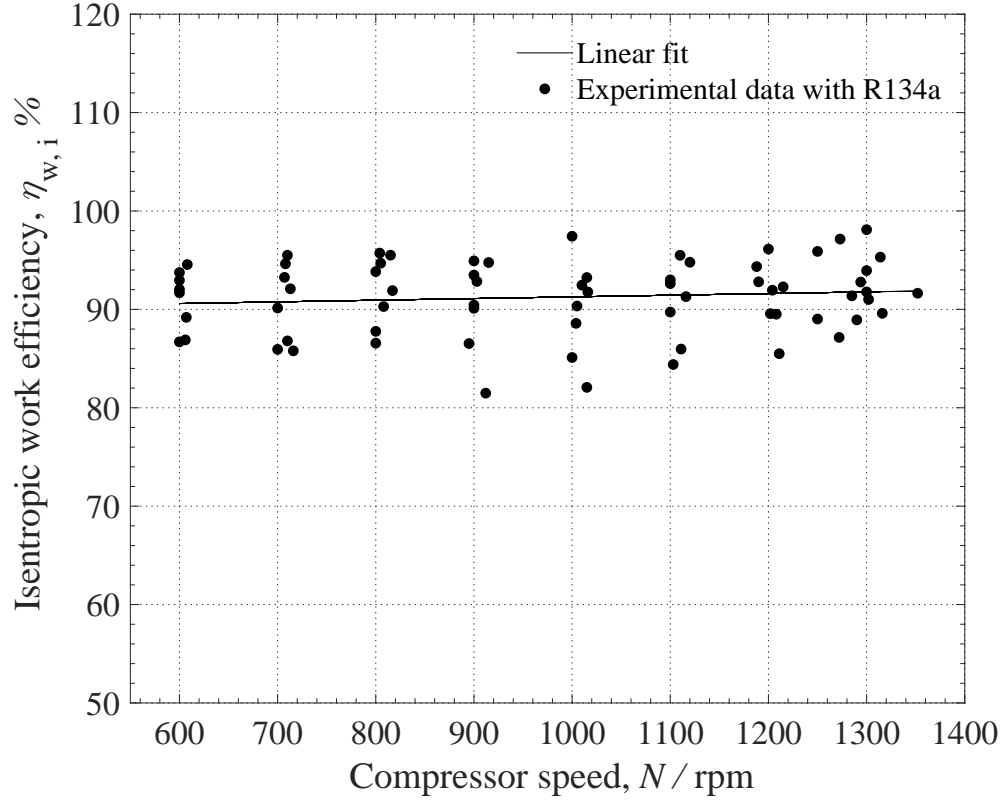


Figure 3.3: Variation of isentropic work efficiency with compressor speed for 72 data points.

3. Correlation for the heat loss from the compressor body due to friction (\dot{Q}_{loss}):

The heat lost from the compressor to the surrounding is due to friction of internal movement of parts including swash plate, pistons and bearings. The heat is lost by convection and radiation modes. To find this heat lost, the shell of compressor is considered as cylinder and the shell temperature is determined by measurement with thermocouples. The equations of heat transfer for combined natural convection and low-speed forced convection and radiation are used to find total heat loss. During the experiment it was found that total heat lost strongly depends on the speed of the compressor. Therefore following equation for heat lost is obtained as a function of compressors speed (N).

$$\dot{Q}_{\text{loss}} = 1.9728 \times 10^{-03} N + 38.2359 \quad (3.53)$$

Eq. 3.53 is obtained by curve fitting of experimental data. Fig. 3.4 shows the variation heat loss from compressor shell with compressor speed for all the experimental operating conditions.

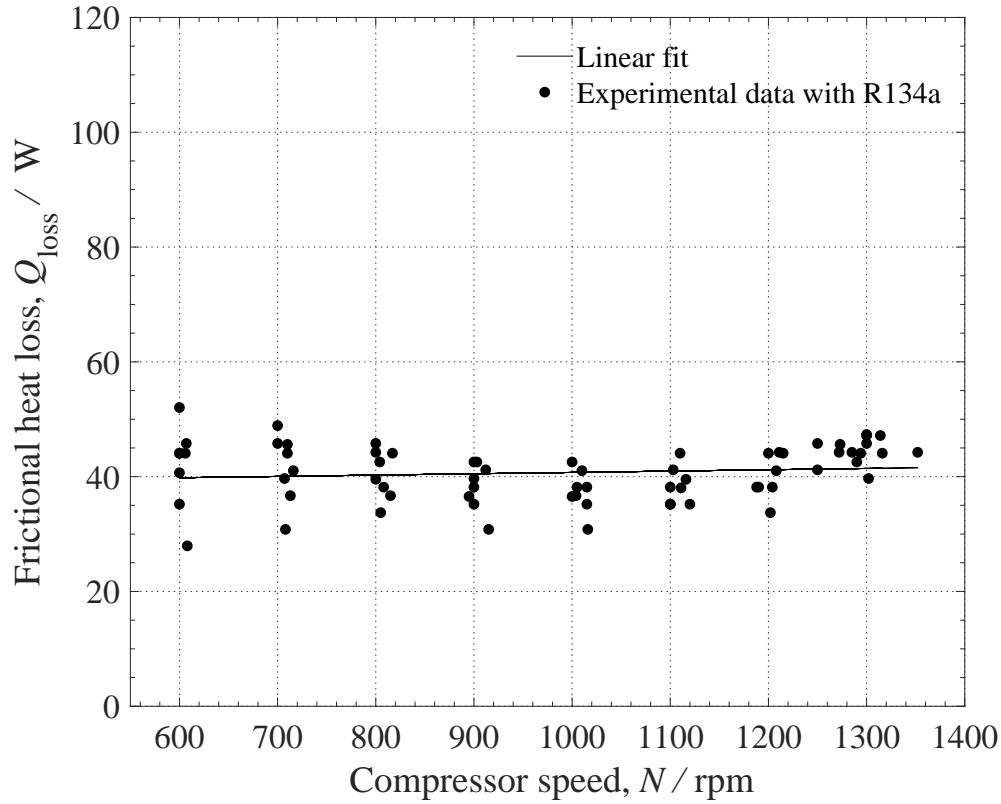


Figure 3.4: Variation of friction heat loss with compressor speed for 72 data points.

4. Correlation for compressor power (\dot{W}_c): The compressor used is not strictly a perfect adiabatic compressor because there is small heat loss to the surroundings from the compressor body. This is because due to the motion of the internal rotating parts, heat is generated due to friction and is delivered to the surrounding space by convection and radiation. The following equation gives the power consumed by the compressor:

$$\dot{W}_c = \dot{m}_r \frac{(i_d - i_s)}{\eta_{w,i}} + \dot{Q}_{\text{loss}} \quad (3.54)$$

where:

i_d = specific enthalpy of vapour at compressor discharge.

i_s = specific enthalpy of vapour at suction of compressor.

\dot{m}_r = mass flow rate refrigerant calculated from Eq. 3.46.

3.4 Correlations for flat-tube, louvered-fin condenser

There are two sides for flat-tube, louvered-fin condenser; one is the air side and other is the refrigerant side. The air side mathematical model involves dry surface heat transfer coefficient and friction factor. The refrigerant side consists of superheated vapour flow, two-phase flow and subcooled liquid flow. The mathematical model involves refrigerant side pressure drop and refrigerant side heat transfer coefficient for each region. The relevant correlations for various regions are described in this section. The condenser used in the experimental facility consists of 36 parallel tubes connected to inlet and outlet headers. The refrigerant enters into the inlet header and is divided into 36 tubes and is again collected in the outer header at the exit of the tubes. The louvered fins are attached between two tubes to form a fin array structure as shown in Fig. 3.5. In the present study, the condenser is discretized in the refrigerant flow direction. In the condenser, refrigerant flows in vertically downward direction inside the tubes. A condenser element consists of one fin and tube with length equal to fin pitch (F_p). Fig. 3.6 shows one element of the condenser. The air flows parallel to the fin surface, i.e., it is in crossflow with respect to the refrigerant flow. One element consists of half fin on either side of tube. Fig. 3.7 shows the various geometry-related quantities of the louvered-fin attached to the tube. Heat transfer area and other areas are formulated and are given in Table 3.12, which are required for calculations.

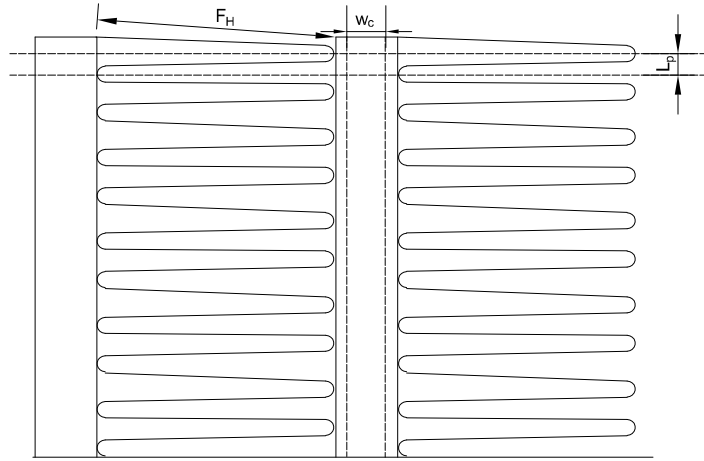


Figure 3.5: Fin arrays of condenser.

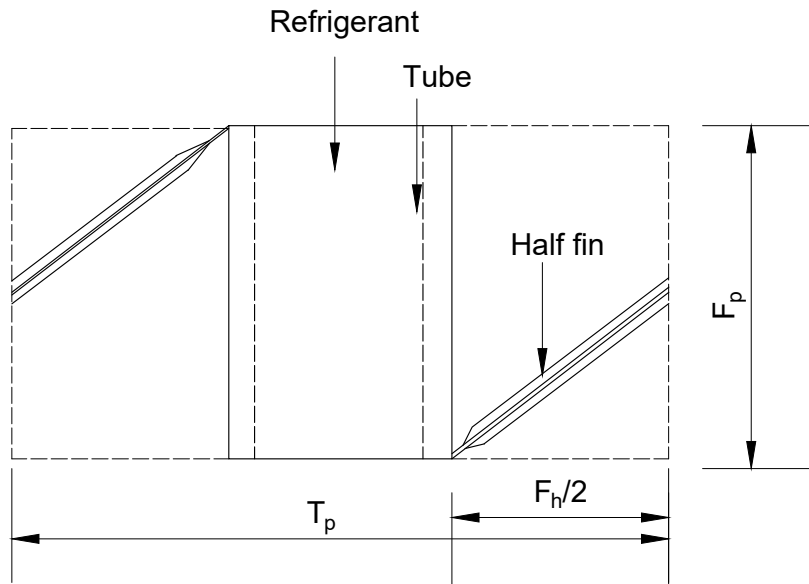


Figure 3.6: Condenser element with the tube and half fin on either side.

3.4.1 Air side correlations

1. Correlation for air side heat transfer coefficient (h_o) for dry finned surface

In the numerical calculation, the condenser is divided into a number of small elements along the refrigerant flow direction and the correlations are applied for each element. The refrigerant

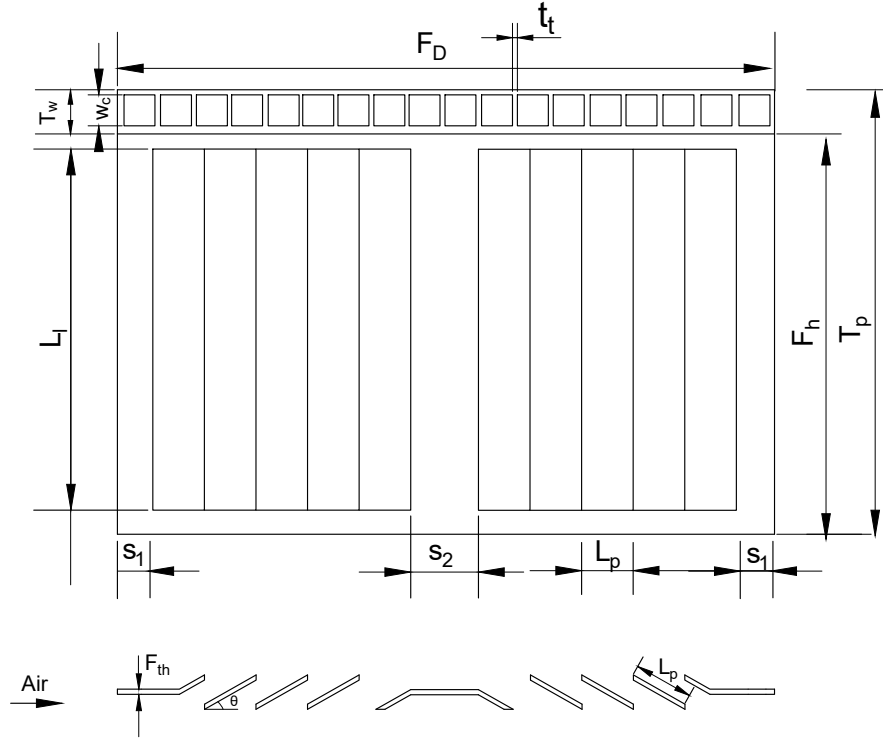


Figure 3.7: Condenser fin with louvers and tube channels.

Table 3.12: Various areas of condenser element.

Area of s1 region, $A_{s1} = 2 \times 2 F_h S_1$
Area of s2 region, $A_{s2} = 2 F_h S_2$
Area of louvers, $A_l = 2 L_l L_p N_l$
Area of end region for louvers, $A_{e,l} = 2(F_h - L_l)L_p N_l$
Area of end region for s1, $A_{e,s1} = 4(F_h - L_l)S_1$
Area of end region for s2, $A_{e,s2} = 6(F_h - L_l)S_2$
Area of unfinned region, $A_{u,fin} = 2 F_d [F_p - F_{th}]$
Area of fin, $A_{fin} = A_{s1} + A_{s2} + A_l + A_{e,l} + A_{e,s1} + A_{e,s2}$
Outer area, $A_o = A_{u,fin} + A_{fin}$
Internal area, $A_i = 2 N_c w_c F_p$
Mean tube area, $A_{t,m} = 2(w_c + 0.5t_t)F_p$
Air flow area, $A_{a,c} = T_p F_p$

flow inside the channels and the air flow through the interfin spaces results in a crossflow arrangement. Park and Jacobi [46] described the correlations for dry surface heat transfer coefficient and friction factor.

The air side heat transfer coefficient is given by:

$$h_o = \frac{j C_{p,a} G_c}{Pr_a^{2/3}} \quad (3.55)$$

where $G_c = \rho_a U_c$, j is the Colburn factor j -factor given by:

$$j = C_1 j_{Re} j_{low} j_{louver} \alpha^{C_2} N_{LB}^{C_3} \left(\frac{F_h}{L_p}\right)^{C_4} \left(\frac{F_d}{F_p}\right)^{C_5} \left(\frac{L_L}{F_L}\right)^{C_6} \left(\frac{F_h}{T_p}\right)^{C_7} \times \left(1 - \frac{F_{th}}{L_p}\right)^{C_8} \left(\frac{L_p}{F_p}\right)^{C_9} \quad (3.56)$$

$$j_{Re} = Re_{LP}^{[C_{10} + C_{11} \cosh(F_p/L_p - 1)]} \quad (3.57)$$

$$j_{low} = 1 - \sin\left(\frac{L_p}{F_p} \theta\right) \left[\cosh\left(C_{12} Re_{LP} - C_{13} \frac{F_d}{N_{LB} F_p}\right) \right]^{-1} \quad (3.58)$$

$$j_{louver} = 1 - C_{14} \tan \theta \left(\frac{F_d}{N_{LB} F_p}\right) \cos \left[2\pi \left(\frac{F_p}{L_p \tan \theta} - 1.8\right) \right] \quad (3.59)$$

2. Correlation for Fanning f -factor for dry finned surface

$$f = D_1 f_{Re} N_{LB}^{D_2} \left(\frac{F_p}{L_p}\right)^{D_3} \sin(\theta + D_4) \left(1 - \frac{F_h}{T_p}\right)^{D_5} \left(\frac{L_1}{F_1}\right)^{D_6} \times \left(\frac{F_{th}}{L_p}\right)^{D_7} \left(\frac{F_h}{F_p}\right)^{D_8} \quad (3.60)$$

$$f_{Re} = \left(Re_{LP} \frac{F_p}{L_p}\right)^{D_9} + D_{10} Re_{LP}^{[D_{11}(F_{th}/F_p)]} \quad (3.61)$$

The constants used to calculate the Colburn j - and Fanning f -factors are given in Table 3.13.

Table 3.13: Constants used to calculate the Colburn j - and Fanning f -factors in Eqs. 3.55 and 3.60.

C_1	0.872	D_1	3.69
C_2	0.219	D_2	-0.256
C_3	-0.0881	D_3	0.904
C_4	0.149	D_4	0.200
C_5	-0.259	D_5	0.733
C_6	0.540	D_6	0.648
C_7	-0.902	D_7	-0.647
C_8	2.62	D_8	0.799
C_9	0.301	D_9	-0.845
C_{10}	-0.458	D_{10}	0.00130
C_{11}	-0.00874	D_{11}	1.26
C_{12}	0.0490		
C_{13}	0.142		
C_{14}	-0.0065		

The ranges of validity of the dimensionless parameters in the Park and Jacobi [46] correlations are $Re_{Dh} = 0 - 2000$, $F_h/L_p = 2.5 - 7$, $F_d/F_p = 2.5 - 15$, $L_1/F_1 = 0.8 - 0.9$, $F_{th}/L_p = 0.01 - 0.07$ and $L_p/F_p = 1.4 - 2.5$.

3.4.2 Refrigerant side correlations

The refrigerant side calculations involve correlations for pressure drop and heat transfer coefficient for three different regions (in flow direction inside the flat tubes), namely, the superheated vapour, two-phase condensation and subcooled regions.

1. Correlations for the superheat region

(a) Pressure drop in superheat region:

The correlation for pressure drop for superheat region is presented by (Webb and Wu [2]):

$$\frac{dP}{dz} = f \frac{1}{D_h} \frac{G^2}{2\rho_v} \quad (\text{Pa/m}) \quad (3.62)$$

where the friction factor f can be calculated by the Petukhov equations for turbulent flow:

$$f = [1.58 \ln(Re_{D_h}) - 3.28]^{-2} \quad (3.63)$$

where G is the mass flow velocity in $\text{kg}/\text{m}^2 \cdot \text{s}$ and Re_{D_h} is Reynolds number for the hydraulic diameter of the condenser tube element.

(b) Heat transfer coefficient (h_r) in superheat region.

The correlation for heat transfer coefficient for superheat region is given by Petukhov equation for turbulent flow:

$$h_r = \frac{(f/2) Re_{D_h} Pr_v}{1.07 + 12.7(f/2)^{1/2} (Pr_v^{2/3} - 1)} \left(\frac{k_v}{D_h} \right) \quad (\text{W}/\text{m}^2\text{K}) \quad (3.64)$$

where f is the friction factor given in Eq. 3.63.

2. Correlations for two-phase region.

Correlations for two-phase region in condensation involves the pressure drop and heat transfer coefficient for the condenser element, as mentioned earlier.

(a) pressure drop for two-phase flow:

Pressure drop for two-phase flow (mixture of vapour and liquid) in small diameters tubes consists of three terms, namely, friction term, gravitational term and acceleration term.

The correlation given by Carey [5] is:

$$\left(\frac{dP}{dz} \right) = \left(\frac{dP}{dz} \right)_{fr} - [(1 - \alpha)\rho_l + \alpha\rho_v]g \sin \Omega - \frac{d}{dz} \left[\frac{G^2 x^2}{\alpha\rho_v} + \frac{G^2(1 - x)^2}{(1 - \alpha)\rho_l} \right] \quad (3.65)$$

Here α is the void fraction given by (Zivi [115]):

$$\alpha = \frac{1}{1 + \left(\frac{1-x}{x} \right) \left(\frac{\rho_v}{\rho_l} \right)^{2/3}} \quad (3.66)$$

Pressure drop due to friction in Eq. 3.65 is calculated using the relation (Zhang and Webb [109]):

$$\left(\frac{dP}{dz}\right)_{\text{fr}} = 2\frac{f_{\text{lo}}G^2}{\rho_1 D_h} \left[(1-x)^2 + 2.2x^2 \left(\frac{P}{P_c}\right)^{-0.94} + 2.6x^{0.8}(1-x)^{0.25} \left(\frac{P}{P_c}\right)^{-1.44} \right] \quad (3.67)$$

where $f_{\text{lo}} = 0.079Re_{\text{lo}}^{-0.25}$ and $Re_{\text{lo}} = GD_h/\mu_1$.

(b) Entry and exit pressure loss correlations for two phase.

The two phase pressure losses at the tube entrance and exit are calculated using the following correlations (Collier [7]):

$$\Delta P_{\text{exit}} = G^2 \sigma (1 - \sigma) \left[\frac{(1-x)^2}{\rho_1 (1-\alpha)} + \frac{x^2}{\rho_v \alpha} \right] \quad (3.68)$$

$$\Delta P_{\text{entry}} = \left(\frac{G}{C_c}\right)^2 (1-C_c) \left[\frac{(1+C_c) \left\{ \frac{x^3}{\rho_v^2 \alpha^2} + \frac{(1-x)^3}{\rho_1^2 (1-\alpha)^2} \right\}}{2[x/\rho_v + (1-x)/\rho_1]} - C_c \left\{ \frac{x^2}{\rho_v \alpha} + \frac{(1-x)^2}{\rho_1 (1-\alpha)} \right\} \right] \quad (3.69)$$

where σ is the ratio of tube cross-sectional area to the frontal area and C_c is the contraction coefficient.

(c) Heat transfer coefficient correlation for two phase flow condensation in small tubes.

Shah's correlations [8] are used to calculate the heat transfer coefficient for two-phase region. The equations are:

$$h_r = h_L \left[(1-x)^{0.8} + \frac{3.8x^{0.76}(1-x)^{0.04}}{p_r^{0.38}} \right] \quad (3.70)$$

where h_L is the heat transfer coefficient assuming all the mass flowing as liquid and given by Dittus-Boelter:

$$h_L = 0.023Re_L^{0.8}Pr_1^{0.4}k_1/D \quad (3.71)$$

3. Correlations for sub-liquid flow region.

(a) Correlation for pressure drop for liquid flow inside the tubes:

$$\left(\frac{dP}{dz}\right)_{\text{lo}} = 2 \frac{f_{\text{lo}} G^2}{\rho_1 D_{\text{h}}} \quad (3.72)$$

where $f_{\text{lo}} = 0.079 Re_{\text{lo}}^{-0.25}$ and $Re_{\text{lo}} = GD_{\text{h}}/\mu_1$.

(b) Correlation for heat transfer coefficient for liquid flow inside the tubes:

$$h_{\text{r}} = 0.023 Re_{\text{L}}^{0.8} Pr_1^{0.4} k_1 / D \quad (3.73)$$

4. Overall heat transfer coefficient (UA):

The total thermal resistance from the air to the refrigerant is formulated as in Eq. 3.74

$$\frac{1}{UA} = \frac{1}{h_{\text{r}} A_{\text{i}}} + \frac{2t}{k A_{\text{t,m}}} + \frac{1}{h_{\text{o}} A_{\text{o}} \eta_{\text{o}}} \quad (3.74)$$

$$\eta_{\text{o}} = 1 - A_{\text{fin}}(1 - \eta) / A_{\text{o}} \quad (3.75)$$

$$\eta = \frac{\tanh(m F_{\text{f}}/2)}{(m F_{\text{f}}/2)} \quad (3.76)$$

$$m^2 = \frac{2h_{\text{o}}}{F_{\text{th}} K_{\text{fin}}} \quad (3.77)$$

5. Total heat rejection rate of condenser (\dot{Q}_{cond}):

Heat transfer rate for an element in any of the three regions is calculated by:

$$\dot{Q}_{\text{ele}} = UA(T_{\text{r}} - T_{\text{a}}) \quad (3.78)$$

Eq. 3.78 is applicable for all the three regions. T_r and T_a are the average temperature of refrigerant and the average temperature of air for the element respectively.

The total heat rejection rate of condenser is the summation of the elemental heat rejection rates (\dot{Q}_{ele}) in the superheat, two-phase and subcooled regions, i.e., over the entire length of the tubes in the condenser.

$$\dot{Q}_{\text{cond}} = N_{\text{tubes}} \left(\sum \dot{Q}_{\text{cond,sh}} + \sum \dot{Q}_{\text{cond,TP}} + \sum \dot{Q}_{\text{cond,sc}} \right) \quad (3.79)$$

$N_{\text{tubes}}=36$ number of tubes.

3.5 Calculations for thermostatic expansion valve(TXV)

The expansion process of the refrigerant in the thermostatic expansion valve(TXV) is considered as isenthalpic. At the inlet of thermostatic expansion valve the refrigerant may be in the subcooled or two-phase state depending on the heat rejection rate in the condenser. The dryness fraction (x) of the refrigerant at the outlet of the thermostatic expansion valve is calculated by considering constant enthalpy at inlet and outlet. The equations are:

1. Dryness fraction of refrigerant at outlet of TXV if inlet state of refrigerant is two-phase:

$$x_{\text{out,txv}} = \frac{h_{f,\text{in,txv}}(1 - x_{\text{in,txv}}) + h_{g,\text{in,txv}}x_{\text{in,txv}} - h_{f,\text{out,txv}}}{h_{g,\text{out,txv}} - h_{f,\text{out,txv}}} \quad (3.80)$$

where

$x_{\text{out,txv}}$ = dryness fraction at the outlet of TXV.

$x_{\text{in,txv}}$ = dryness fraction at the inlet of TXV.

$h_{f,\text{in,txv}}$ = specific enthalpy of liquid refrigerant at the inlet of TXV.

$h_{g,\text{in,txv}}$ = specific enthalpy of vapour refrigerant at the inlet of TXV.

$h_{f,\text{out,txv}}$ = specific enthalpy of liquid refrigerant at the outlet of TXV.

$h_{g,\text{out,txv}}$ = specific enthalpy of vapour refrigerant at the outlet of TXV.

2. Dryness fraction of refrigerant at outlet of TXV if inlet state of refrigerant is subcooled liquid:

$$x_{\text{out,txv}} = \frac{h_{f,\text{in,txv}} - h_{f,\text{out,txv}}}{h_{g,\text{out,txv}} - h_{f,\text{out,txv}}} \quad (3.81)$$

3.6 Correlations for flat-tube, louvered-fin evaporator

In respect of the geometry and structure, the condenser and evaporator elements are similar but the working of evaporator is opposite to condenser. In condenser heat is rejected from refrigerant to surrounding air and the condenser is working under high pressure side of compressor and the temperature of refrigerant inside the tubes is always greater than the dew point of surrounding moist air into which the condenser is rejecting heat. Therefore the outer finned surfaces of condenser remain dry and no condensate water film will form on it. Evaporator works on the low pressure side and the refrigerant and outer wall temperatures are usually less than the dew point temperature of surrounding moist air inside the space where the cooling effect is required. Therefore condensed water film will form on the outer surfaces of evaporator due to condensation of water vapour present in the moist air. In the present study the mathematical model of evaporator consists of the correlations for three flow regions namely two-phase flow, liquid deficient and superheated vapour flow region. Wu and Webb [2] predicted the performance parameters of brazed aluminium evaporator for three regions. The correlation involved the pressure drop, wetted surface heat transfer coefficient and cooling capacity of evaporator. The evaporator is discretized into a number of small elements each of length equal to the fin pitch in the refrigerant flow direction. Each element consists of half fin on either side of the tube. Fig. 3.8 shows the single element of the evaporator. The water film is present on both surfaces of tube and on both the half portions of the fin. The tube channels and fin structure are shown in Fig. 3.9. The various areas of the evaporator element are given in Table 3.14.

Kuehn, Ramsey and Threlkeld [6] described the procedure to calculate the heat transfer coefficient for wetted surfaces. The refrigerant inside the tube has low temperature and therefore the outside tube surface is usually at a temperature less than the dew point temperature of moist air. The air

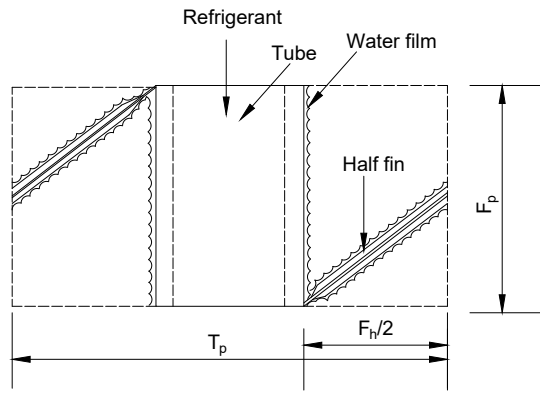


Figure 3.8: Evaporator element cell shows wet surface and water film formation.

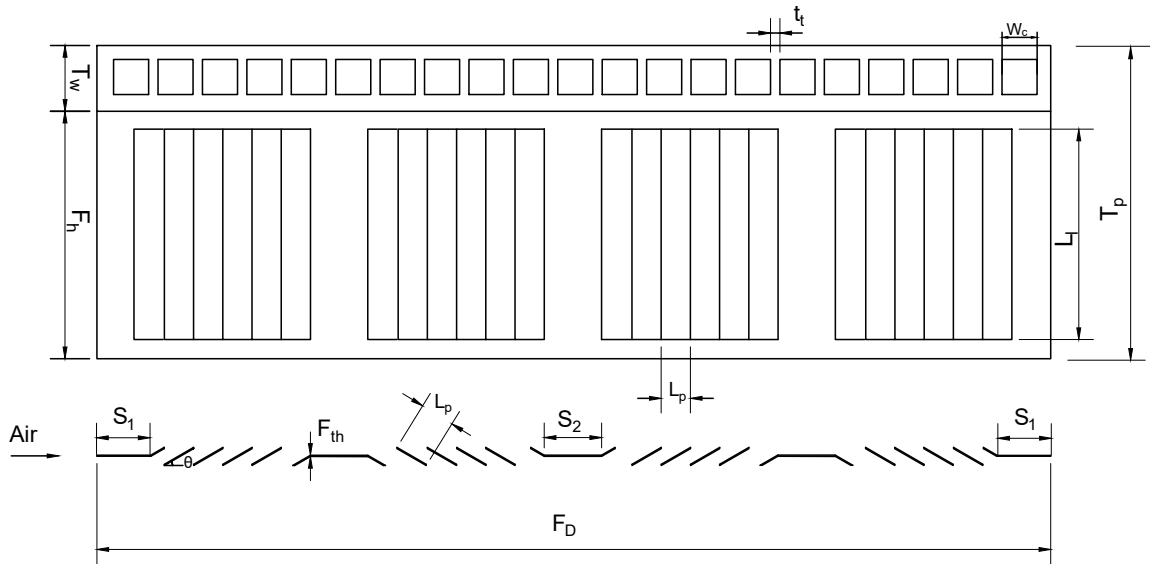


Figure 3.9: Evaporator fin shows louvers and tube channels.

flow is in a crossflow direction with respect to that of the refrigerant. The thickness of water film is very small. Following [6], a constant value is taken.

1. Correlations for slope of air saturation curve and enthalpy of air

To calculate the heat transfer coefficient and thereby the overall heat transfer coefficient for a wetted finned surface, the slope of air saturation curve is required. The equations for saturation

Table 3.14: Various areas of evaporator element.

Area of s1 region, $A_{s1} = 2 \times 2 F_h S_1$
Area of s2 region, $A_{s2} = 2 \times 3 F_h S_2$
Area of louvers, $A_l = 2 L_1 L_p N_l$
Area of end region for louvers, $A_{e,l} = 2(F_h - L_1)L_p N_l$
Area of end region for s1, $A_{e,s1} = 4(F_h - L_1)S_1$
Area of end region for s2, $A_{e,s2} = 6(F_h - L_1)S_2$
Area of unfin region, $A_{u,fin} = 2 F_d[F_p - F_{th}]$
Area of fin, $A_{fin} = A_{s1} + A_{s2} + A_l + A_{e,l} + A_{e,s1} + A_{e,s2}$
Outer area, $A_o = A_{u,fin} + A_{fin}$
Internal area, $A_i = 2N_c w_c F_p$
Mean tube area, $A_{t,m} = 2(w_c + 0.5t_t)F_p$
air flow area, $A_{a,c} = T_p F_p$

air enthalpy and slope of saturation air curve are given by the cubic curve fit and its derivative in the range of 2° to 30° saturation air temperatures:

$$h_{if} = aT_{if}^3 + bT_{if}^2 + cT_{if} + d \quad (3.82)$$

and

$$b = \frac{dh_{if}}{dT_{if}} = 3aT_{if}^2 + 2bT_{if} + c \quad (3.83)$$

where $a = 0.98855 \times 10^{-3}$, $b = 0.1135 \times 10^{-1}$, $c = 1.7861$ and $d = 9.3625$. Eq. 3.82 is used to calculate the air enthalpy and Eq. 3.83, for calculate the slope of air saturation curve, respectively.

2. Correlation for air side heat transfer coefficient for wetted fined surface ($h_{o,w}$):

The evaporator surfaces are assumed to be fully wet by the condensate and the enthalpy driving potential method is used to calculate the heat transfer coefficient and heat transfer rate. Park and Jacobi [47] considered the wet surface heat transfer in a comprehensive manner. The air side wet surface heat transfer coefficient is derived as:

$$h_{o,w} = \frac{h_o b_f}{cp_{ma}} \quad (3.84)$$

$$h_o = \frac{j_w c p_{ma} G_c}{Pr_{ma}^{2/3}} \quad (3.85)$$

$$j_w = a_1 Re_{Lp}^{a_2} \left(\frac{L_p}{F_p}\right)^{a_3} \sin(\theta)^{a_4} \left(\frac{L_l}{F_h}\right)^{a_5} \left(\frac{F_d}{F_p}\right)^{a_6} \left(\frac{F_h}{T_p}\right)^{a_7} \quad (3.86)$$

$$b_f = \frac{h_{ma, T_{f, tip}} - h_{ma, T_{t, o}}}{T_{f, tip} - T_{t, o}} \quad (3.87)$$

where $h_{ma, T_{f, tip}}$ is the enthalpy of saturation air at the fin tip temperature, $h_{ma, T_{t, o}}$ is the enthalpy of saturation air at the tube outer surface temperature, $T_{f, tip}$ is the fin tip temperature, $T_{t, o}$ is the tube outer temperature and $G_c = \rho_{ma} U_c$.

3. Correlation for wetted surface efficiency ($\eta_{o, w}$)

$$\eta_{o, w} = 1 - A_{fin}(1 - \eta_{fin, w})/A_o \quad (3.88)$$

$$\eta_{fin, w} = \frac{\tanh(m_w F_f/2)}{(m_w F_f/2)} \quad (3.89)$$

$$m^2 = \frac{2h_o}{K_{fin} F_{th}} \quad (3.90)$$

$$m_w^2 = \frac{m^2 b_f}{c p_{ma}} \quad (3.91)$$

4. Correlation for wetted surface friction factor (f_w)

$$f_w = b_1 + b_1 Re_{Lp}^{b_3} \left(\frac{L_p}{F_p}\right)^{b_4} \sin(\theta)^{b_5} \left(\frac{F_h}{T_p}\right)^{b_6} \quad (3.92)$$

The constants used to calculate wet fin Colburn- j and Fanning f factors in Eq. 3.86 and 3.92 are given in Table 3.15.

Table 3.15: Constants to calculate the wet Colburn j - and Fanning f -factors in Eqs. 3.86 and 3.92.

a_1	0.4260	b_1	0.07400
a_2	-0.3149	b_2	152.7
a_3	0.6705	b_3	-1.116
a_4	0.3489	b_4	2.242
a_5	0.5123	b_5	0.9680
a_6	-0.2698	b_6	1.716
a_7	-0.2845		

5. Correlations for two phase flow boiling in evaporator.

(a) Correlations for pressure drop

The pressure drop relations for flow boiling in the evaporator are the same as those of intube condensation in the condenser, except that in the evaporator we do not encounter the subcooled region.

Pressure drop for two-phase flow (mixture of vapour and liquid) in small diameter tubes consists of three terms, namely, the friction term, gravitational term and the acceleration term. Correlation is given by (Carey [5]):

$$\left(\frac{dP}{dz}\right) = \left(\frac{dP}{dz}\right)_{\text{fr}} - [(1 - \alpha)\rho_l + \alpha\rho_v]g \sin \Omega - \frac{d}{dz} \left[\frac{G^2 x^2}{\alpha\rho_v} + \frac{G^2(1 - x)^2}{(1 - \alpha)\rho_l} \right] \quad (3.93)$$

here α is the void fraction given by (Zivi [115]):

$$\alpha = \frac{1}{1 + \left(\frac{1-x}{x}\right) \left(\frac{\rho_v}{\rho_l}\right)^{2/3}} \quad (3.94)$$

Pressure drop due to friction in Eq. 3.93 is calculated using (Zhang and Webb [109]):

$$\left(\frac{dP}{dz}\right)_{\text{fr}} = 2 \frac{f_{\text{lo}} G^2}{\rho_l D_h} \left[(1 - x)^2 + 2.2x^2 \left(\frac{P}{P_c}\right)^{-0.94} + 2.6x^{0.8}(1 - x)^{0.25} \left(\frac{P}{P_c}\right)^{-1.44} \right] \quad (3.95)$$

where $f_{\text{lo}} = 0.079 Re_{\text{lo}}^{-0.25}$ and $Re_{\text{lo}} = GD_h/\mu_l$.

(b) Entry and exit pressure loss correlations for two phase.

The two phase pressure losses at the tube entrance and exit are calculated using the correlations in (Collier [7]):

$$\Delta P_{\text{exit}} = G^2 \sigma (1 - \sigma) \left[\frac{(1 - x)^2}{\rho_l (1 - \alpha)} + \frac{x^2}{\rho_v \alpha} \right] \quad (3.96)$$

$$\Delta P_{\text{entry}} = \left(\frac{G}{C_c} \right)^2 (1 - C_c) \left[\frac{(1 + C_c) \left\{ \frac{x^3}{\rho_v^2 \alpha^2} + \frac{(1-x)^3}{\rho_l^2 (1-\alpha)^2} \right\}}{2[x/\rho_v + (1-x)/\rho_l]} - C_c \left\{ \frac{x^2}{\rho_v \alpha} + \frac{(1-x)^2}{\rho_l (1-\alpha)} \right\} \right] \quad (3.97)$$

where σ is the ratio of tube cross-section area to the frontal area, C_c is the contraction coefficient.

(c) Correlation for heat transfer coefficient:

The heat transfer coefficient is calculated by correlations described by (Shah [48, 49]):

$$h_r = h_{r1} \Psi_s = f(C_o, B_o, Fr_{le}) \quad (3.98)$$

C_o , B_o and Fr_{le} are the convection, boiling and Froude numbers respectively, defined by:

$$C_o = \left(\frac{1-x}{x} \right)^{0.8} \left(\frac{\rho_v}{\rho_l} \right)^{0.5} \quad (3.99)$$

$$B_o = \frac{\ddot{q}}{Gi_{lv}} \quad (3.100)$$

$$Fr_{le} = \frac{G^2}{\rho_l^2 g D_h} \quad (3.101)$$

The value of Ψ_s in Eq. 3.98 is:

$$\Psi_{cb} = 1.8/C_o^{0.8} \quad (3.102)$$

for $C_o > 1$ if $B_o > 0.3 \times 10^{-4}$.

$$\Psi_{nb} = 230 \quad (3.103)$$

for $B_o < 0.3 \times 10^{-4}$.

$$\Psi_{nb} = 1 + 46B_o^{0.5} \quad (3.104)$$

Then the value of Ψ_s is the greater of Ψ_{cb} and Ψ_{nb} , Ψ_{cb} is for convective boiling, and Ψ_{nb} for nucleate boiling.

For $0.1 < C_o \leq 1$

$$\Psi_{bs} = FB_o^{0.5} \exp(2.74C_o^{-0.5}) \quad (3.105)$$

and for $o \leq 0.1$

$$\Psi_{bs} = FB_o^{0.5} \exp(2.47C_o^{-0.15}) \quad (3.106)$$

Then the value of Ψ_s is the greater of Ψ_{bs} and Ψ_{cb} , Ψ_{bs} is for bubble suppression. The $F=15.43$ for $B_o < 11 \times 10^{-4}$ and $F=14.7$ for $B_o > 11 \times 10^{-4}$, h_{rl} is the single phase heat transfer coefficient for the liquid flowing alone in the tube given by Dittus-Boelter relation, $h_{rl} = 0.023Re_1^{0.8}Pr_1^{0.4}(k_l/D_h)$.

6. Correlations for superheat region in the evaporator

The pressure drop and heat transfer in the superheated region of the evaporator are calculated in a manner similar to the superheated region of the condenser.

(a) Correlation for pressure drop and heat transfer coefficient.

Webb and Wu [2] described the correlation for pressure drop for superheat region:

$$\frac{dP}{dz} = f \frac{1}{D_h} \frac{G^2}{2\rho_v} \quad (\text{Pa/m}) \quad (3.107)$$

$$h_r = \frac{(f/2)Re_{Dh}Pr_v}{1.07 + 12.7(f/2)^{1/2}(Pr_v^{2/3} - 1)} \left(\frac{k_v}{D_h} \right) \quad (\text{W/m}^2\text{K}) \quad (3.108)$$

where friction factor f can be calculated by Petukhov equations for turbulent flow:

$$f = [1.58 \ln(Re_{Dh}) - 3.28]^{-2} \quad (3.109)$$

where G is mass flow velocity in $\text{kg/m}^2.\text{s}$ and Re_{Dh} is Reynold's number for hydraulic diameter of condenser tube element.

7. Correlation for overall heat transfer coefficient (UA) for wet surface

$$\frac{1}{UA} = \frac{b'_i}{h_r A_i} + \frac{b'_i t}{k_t A_{t,m}} + \frac{cp_{ma}}{\eta_{o,w} h_{o,w} A_o} \quad (3.110)$$

The term b'_i in Eq. 3.110 is the slope of the air saturation curve at the mean inner tube surface temperature ($T_{t,i}$) as suggested by Park and Jacobi [46].

8. Heat transfer rate for a single element (\dot{Q}_{ele})

The heat transfer rate for two phase and super heat region for every element is:

$$\dot{Q}_{ele} = UA(h_{ma} - h_{ma,T_r}) \quad (3.111)$$

9. Total heat transfer rate in the evaporator (\dot{Q}_{evp}):

The total heat transfer rate in the evaporator is the summation of the heat transfer rates in the two-phase region and the superheat region, i.e., over the entire length of evaporator tube.

$$\dot{Q}_{evp} = \sum \dot{Q}_{evp,TP} + \sum \dot{Q}_{evp,sh} \quad (3.112)$$

10. Outlet moist air temperature from evaporator ($T_{a,o}$)

The outlet moist air temperature from the evaporator ($T_{a,o}$) can be calculated by the following equation:

$$T_{a,o} = \frac{(\dot{m}_{da}c_{p,da} - 0.5h_oA_o) + 0.5h_o(A_fT_{f,av} + A_{u,fin}T_{t,o})}{(\dot{m}_{da}c_{p,da} - 0.5h_oA_o)} \quad (3.113)$$

where h_o is the air side dry heat transfer coefficient, m_a is the air mass flow rate through element and $c_{p,da}$ is the specific heat of dry air. $T_{f,av}$ is average fin temperature given as:

$$T_{f,av} = \left(h_{ma} - \frac{(h_{ma} - h_{ma,F,t,o})}{0.5F_h m_w} \right) \frac{(\sinh(0.5F_h m_w) - \tanh(0.5F_h m_w))}{\cosh(0.5F_h m_w) + \tanh(0.5F_h m_w) - a'_t/b'_t} \quad (3.114)$$

11. Outlet moist air humidity from evaporator($W_{a,o}$):

The outlet moist air humidity from the evaporator ($W_{a,o}$) can be calculated by following equation:

$$W_{a,o} = \frac{h_{a,o} - c_{p,da}T_{a,o}}{h_{fg,o} + c_{p,wv}T_{a,o}} \quad (3.115)$$

where $h_{a,o}$ specific enthalpy of air at the evaporator element outlet.

3.7 Moist air thermodynamic and transport property relations

The equations for thermodynamic and transport properties of moist air are presented in this section. The dry bulb temperature (T_D) and wet bulb temperature (T_W) are required to calculate the thermodynamic properties of moist air. To calculate the transport properties, dry bulb temperature and humidity ratio are required. The value of the atmospheric pressure (P_{atm}) is considered at the elevation (Z) from mean sea level of the particular location where the study is conducted. In the present study the value is $P_{atm}=0.893$ bar. Tsay and Lin [116] have presented property correlations of moist air in their work. The properties water vapour and dry air are taken from [117].

3.7.1 Thermodynamic properties

1. Humidity ratio (W):

$$W = \frac{[h_{fg,o} - (c_{p,lw} - c_{p,wv})T_W] W^* - c_{p,da}(T_D - T_W)}{h_{fg,o} + c_{p,wv}T_D - c_{p,lw}T_W} \quad (3.116)$$

where $h_{fg,o}=2501.6$ kJ/kg, $c_{p,lw}=4.1868$ kJ/kg.K, $c_{p,wv}=1.868$ kJ/kg.K, $c_{p,da}=1.005$ kJ/kg.K and W^* is the saturation air humidity ratio given by the following equation:

$$W^* = 0.62198 \frac{P^*}{P_{atm} - P^*} \quad (3.117)$$

Equation for P^* is taken from Tsay and Lin [126].

$$P^* = (221.2 \times 10^2) 10^{q_s} \quad (3.118)$$

$$q_s = -[3.13223 + 3.116 \times 10^{-6}(210 + T_W)^{2.066}] \left(\frac{647.3}{T_W + 273.15} - 1 \right) \quad (3.119)$$

where P^* is the saturation pressure in kPa, P_{atm} is surrounding pressure, T_D is dry bulb temperature in °C and T_W is wet bulb temperature in °C.

2. Relative humidity (ϕ):

$$\phi = \frac{P_{wv}}{P_{wv,s}} \quad (3.120)$$

where

$$P_{wv,s} = (221.2 \times 10^2) 10^{q_s} \quad (3.121)$$

$$q_s = -[3.13223 + 3.116 \times 10^{-6}(210 + T_W)^{2.066}] \left(\frac{647.3}{T_W + 273.15} - 1 \right) \quad (3.122)$$

$$P_{wv} = \frac{W P_{atm}}{W + 0.62198} \quad (3.123)$$

where W is humidity ratio calculate by Eq. 3.116.

3. Enthalpy of moist air (h_{ma}):

$$h_{ma} = c_{p,da}T_D + W(h_{fg,o} + c_{p,wv}T_D) \quad (\text{kJ/kg}) \quad (3.124)$$

4. The density of moist air on moist air basis ($\rho_{ma,1}$):

$$\rho_{ma,1} = \frac{P_{atm}}{T_D R \left[\frac{x_{wv}}{R_{wv}} + \frac{(1 - x_{wv})}{R_{da}} \right]} \quad (\text{kg/m}^3) \quad (3.125)$$

5. The density of moist air on dry air basis ($\rho_{ma,2}$):

$$\rho_{ma,2} = \frac{(P_{atm} - P_{wv})R_{da}}{R.T_D} \quad (\text{kg/m}^3) \quad (3.126)$$

where $x_{wv} = W/(1 + W)$, $R=8.314$ kJ/kmole.k, $R_{da}=28.9645$, $R_{wv}=18.0527$.

6. The specific heat at constant pressure of moist air per kg of moist air ($c_{p,ma1}$):

$$c_{p,ma1} = x_{wv}c_{p,wv} + (1 - x_{wv})c_{p,da} \quad (\text{kJ/kg.K}) \quad (3.127)$$

7. The specific heat at constant pressure of moist air per kg of dry air ($c_{p,ma2}$):

$$c_{p,ma2} = c_{p,da} + W c_{p,wv} \quad (\text{kJ/kg.K}) \quad (3.128)$$

where

$$c_{p,wv} = 1.89208 - 5.40671 \times 10^{-04}T_D + 1.74476 \times 10^{-06}T_D^2 - 8.38480 \times 10^{-10}T_D^3 \quad (3.129)$$

$$c_{p,\text{da}} = 1.02252 - 1.75903 \times 10^{-04}T_{\text{D}} + 4.02136 \times 10^{-07}T_{\text{D}}^2 - 4.86946 \times 10^{-11}T_{\text{D}}^3 \quad (3.130)$$

3.7.2 Transport properties

1. Dynamic viscosity of moist air (μ_{ma}):

$$\mu_{\text{ma}} = \frac{\mu_{\text{wv}}}{1 + \frac{y_{\text{da}}}{y_{\text{wv}}}\Phi_{i,j}} + \frac{\mu_{\text{da}}}{1 + \frac{y_{\text{wv}}}{y_{\text{da}}}\Phi_{j,i}} \quad (3.131)$$

where

$$\mu_{\text{wv}} = 8.02 + 0.0407(T_{\text{D}} - 273.16) \times 10^{-06} \quad (3.132)$$

$$\mu_{\text{da}} = \frac{1.4888 \times 10^{-06}T_{\text{D}}^{1.5}}{118 + T_{\text{D}}} \quad (3.133)$$

$$T_{\text{D}} \text{ is in Kelvin, } y_{\text{wv}} = \frac{x_{\text{wv}}}{M_{\text{wv}}} \times \frac{1}{\left[\frac{x_{\text{wv}}}{M_{\text{wv}}} + \frac{(1 - x_{\text{wv}})}{M_{\text{da}}} \right]}, \quad y_{\text{da}} = 1 - y_{\text{wv}}.$$

$$\Phi_{i,j} = \frac{\left(1 + \sqrt{\frac{\mu_i}{\mu_j}} \left(\frac{M_j}{M_i} \right)^{0.25} \right)^2}{\sqrt{8 \left(1 + \frac{M_i}{M_j} \right)}} \quad (3.134)$$

The subscripts i and j are used for dry air (da) and water vapour (wv).

2. The thermal conductivity of moist air (k_{ma}):

$$k_{\text{ma}} = \frac{k_{\text{wv}}}{1 + \frac{y_{\text{da}}}{y_{\text{wv}}}A_{i,j}} + \frac{k_{\text{da}}}{1 + \frac{y_{\text{wv}}}{y_{\text{da}}}A_{j,i}} \quad \text{W/m.K} \quad (3.135)$$

where $A_{i,j} = \frac{1}{4} \left[1 + \sqrt{\frac{\mu_i}{\mu_j} \left(\frac{M_j}{M_i} \right)^{0.75} \frac{1 + S_i/T_D}{1 + S_j/T_D}} \right]^2 \frac{1 + S_{i,j}/T_D}{1 + S_{j,i}/T_D}$, $S_{wv}=559.5$, $S_{da}=115.5$, $S_{i,j} = 0.733\sqrt{S_i S_j}$. i and j alternately used for dry air (da) and water vapour (wv).

$$k_{wv} = [1.87 + 1.65 \times 10^{-03}(T_D - 273.16)^{9/7} + 5.7 \times 10^{-13}(T_D - 273.16)^{5.1}] \times 10^{-02} \quad (3.136)$$

$$k_{da} = \frac{1.195 \times 10^{-03} T_D^{1.6}}{118 + T_D} \quad (3.137)$$

NOTE: wv is water vapour and da is dry air.

3.8 Heat load estimation for small AAC system

Heat load calculations are an essential part of the thermal design of the AACs. The refrigeration effect and the the cooling capacity of evaporator should be known with sufficient accuracy for the selection of system components like compressor, condenser and most importantatly, the evaporator (cooling coil). The heat load estimation has a direct bearing on the system performance, cost and maintenance of system. Therefore the air conditioning system should be designed on the basis of heat load encountered under comfort conditions. The COP of system is the ratio of the refrigeration effect (cooling capacity of evaporator) to the work (power required) of the compressor. The total heat load estimation for AACs should take into account various individual heat load components acting. The heat gain by the vehicle consists of the solar heat gain by direct and diffuse radiation, metabolic rate of the occupants in the cabin, heat inleak from the engine, convection heat load by transmission of heat from surroundings to vehicle, reflected radiation from heated road, ventilation load, etc. The total heat load is the summation of all heat gains mentioned. In the present study calculations have been done to find the individual heat loads gained by a small car (five seater) for the summer condition at Bangalore city (which is the capital of Karnataka state) and also for the other major cities of India. Fig. 3.10 shows the different heat loads gained by a typical small capacity vehicle.

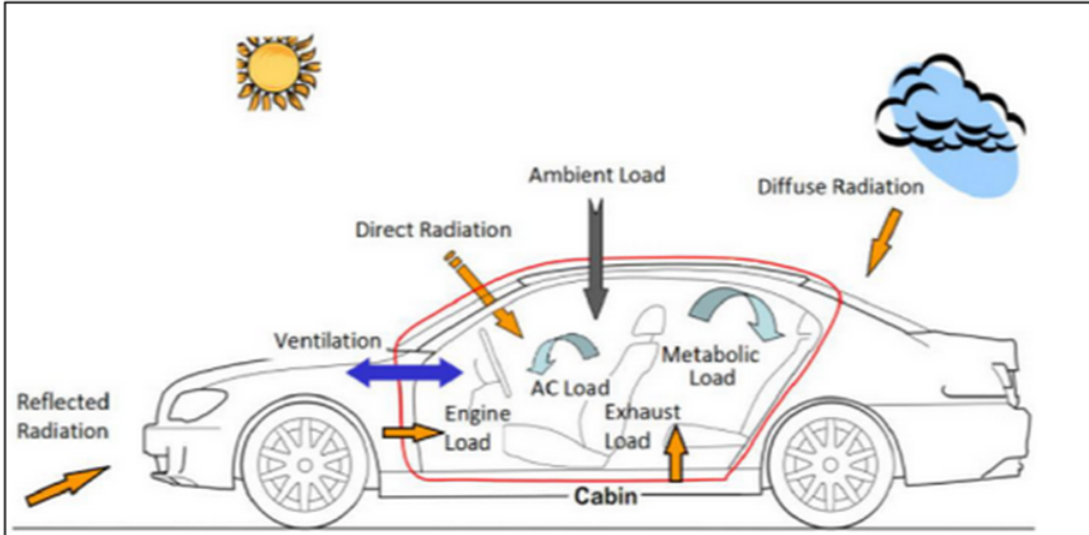


Figure 3.10: Different types of heat loads gained by automotive

From the present studies it has been observed that the solar direct and diffuse radiation and metabolic heat load of passengers oads have a major contribution in the total heat. The procedures for calculating the heat gains are given below:

1. To calculate the solar global radiation on 21st April at Bangalore:

Latitude of Bangalore, $\phi = 13^\circ$

Elevation of Bangalore from mean sea level, $Z = 920$ m

Day number on 21st April, $N=111$

Hour angle at 2 PM on 21st April, $\omega = -30^\circ$

Declination angle δ for the given day is

$$\delta = 23.45 \sin \frac{360(N - 80)}{370} \quad (3.138)$$

Zenith angle θ_z is

$$\theta_z = \sin \phi \sin \delta + \cos \phi \cos \delta \cos \omega \quad (3.139)$$

According to ASHRAE clear sky model the normal solar direct radiation is:

$$I_{bn} = A \exp \left(- \exp(-1.184 \times 10^{-4} Z \frac{B}{\cos \theta_z}) \right) \quad (3.140)$$

The beam radiation on a horizontal surface is:

$$H_b = I_{bn} \cos \theta_z \quad (3.141)$$

The diffuse radiation is

$$H_d = C I_{bn} \quad (3.142)$$

Total solar radiation is the sum of direct and diffuse radiations:

$$H_g = H_b + H_d \quad (\text{W/m}^2) \quad (3.143)$$

where A , B and C are the constants with values $A = 1164$, $B = 0.164$ and $C = 0.120$. H_b and H_d are the direct and diffuse solar radiations respectively.

2. To calculate the outer air side heat transfer coefficient h_o for the vehicle:

The Reynolds number for the air flow about the vehicle is:

$$Re = \frac{\rho U_o L_{top}}{\mu} \quad (3.144)$$

where ρ is density of air, U_o is the velocity of air flowing over the top of the vehicle (i.e. the relative velocity of air with respect to the vehicle), L_{top} is the length of the vehicle and μ is the dynamic viscosity of air.

The top of the vehicle is considered as a horizontal plate and the Nusselt number considered is:

For laminar flow i.e. $Re < 5 \times 10^5$

$$Nu = 0.664Re^{0.5}Pr^{0.333} \quad (3.145)$$

For Turbulent flow i.e. $Re > 5 \times 10^5$

$$Nu = 0.037Re^{0.8}Pr^{0.333} \quad (3.146)$$

The heat transfer coefficient is

$$h_o = \frac{Nuk}{L_{top}} \quad (\text{W/m}^2\text{K}) \quad (3.147)$$

where k is thermal conductivity of air.

3. To calculate the inner side heat transfer coefficient h_i of the vehicle

The procedure to calculate the inner side heat transfer coefficient is similar to that of the outer surface. The same equations are used with different inner cabin conditions. The Reynolds number for the given inner cabin conditions for the vehicle is:

$$Re = \frac{\rho U_i L_{top}}{\mu} \quad (3.148)$$

where ρ is density of air, U_i is the velocity of air circulating inside the cabin over the inner surfaces, L_{in} is the length of the inner surface of the vehicle and μ is the dynamic viscosity of air.

The inner surfaces of the vehicle are considered as a flat plate and the Nusselt number is calculated in a similar manner.

4. To calculate the transmission heat by radiation and convection through the metal body of vehicle: The outer surface temperature of metal body of vehicle can be determined by solving

the following function by Newton- Raphson method. The function is

$$function = \sigma \epsilon_m A_{top} T_{o,s}^4 + \left[h_o A_{dir} + \frac{k_m A_{dir}}{t_{cov} \left(\frac{k_{cov}}{t_{cov} h_i} + 1 \right)} \right] T_{o,s} - QTY \quad (3.149)$$

where QTY is

$$QTY = \frac{A_{dir} T_i k_{cov}}{t_{cov}} + (1 - \rho) H_g A_{dir} + \sigma \epsilon_m A_{top} T_{sky}^4 + h_o A_{dir} T_o \quad (3.150)$$

where:

$\sigma = 5.67 \times 10^{-8} \text{ W/m}^2\text{K}^4$ (Stefan Boltzmann constant)

ϵ_m = Emissivity of metal body of vehicle.

A_{top} = Area of top surface of vehicle.

$T_{s,o}$ = Temperature of outer top surface of roof of vehicle.

A_{dir} = Area of vehicle exposed to direct radiation.

k_{cov} = thermal conductivity of interior covers.

t_{cov} = thickness of interior covers.

T_i = Temperature of air inner cabin.

ρ = Reflectivity of metal body.

k_m = thermal conductivity of metal body.

T_o = Temperature of air at outer surrounding condition.

T_{sky} = Temperature of Sky = $T_o - 6$

t_m = thickness of metal body.

The heat transmission or gain is:

$$Q_{tran,metal} = T_{o,s} \frac{k_{cov} A_{dir}}{\left[\frac{k_{cov}}{t_{cov} h_i} + 1 \right] t_{cov}} - \frac{A_{dir} T_i k_{cov}}{t_{cov}} \quad (3.151)$$

5. To calculate the heat transmission by radiation and convection through the glass areas of the vehicle: The heat load gained by glass surfaces of vehicle by convection and radiation is:

$$Q_{\text{tran, glass}} = A_{\text{glass}} H_g \left[\left(\frac{1}{\frac{1}{h_o} + \frac{1}{h_i} + \frac{t_{\text{glass}}}{k_{\text{glass}}}} \right) \frac{\alpha}{h_o} \right] + \left(\frac{1}{\frac{1}{h_o} + \frac{1}{h_i} + \frac{t_{\text{glass}}}{k_{\text{glass}}}} \right) A_{\text{glass}} (T_o - T_i) \quad (3.152)$$

where

A_{glass} = Area of glass surfaces through which solar radiation enters the vehicle.

k_{glass} = thermal conductivity of glass.

α = Absorptivity of glass.

τ = Transmissivity of glass.

6. Sensible and latent heat gain from passengers in the vehicle:

$$Q_p = (S_g + L_g) N_p \quad (\text{W}) \quad (3.153)$$

where S_g and L_g are the sensible and latent heat gains per person respectively. N_p is the number of people in vehicle.

7. Heat gained by reflected radiation between road and bottom surfaces of vehicle

Fig. 3.11 shows the reflection of solar radiation from road surface.

The Reynolds number for the given conditions between road surface and bottom surface of the vehicle is

$$Re = \frac{\rho U_o L_{\text{bot}}}{\mu} \quad (3.154)$$

For laminar flow i.e $Re < 5 \times 10^5$

$$Nu = 0.664 Re^{0.5} Pr^{0.333} \quad (3.155)$$

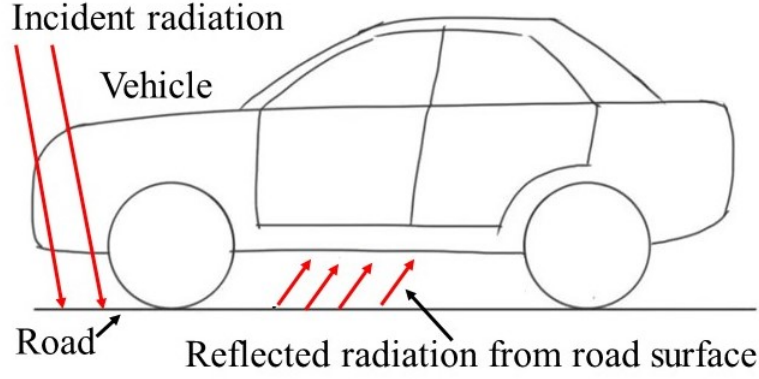


Figure 3.11: Reflected solar radiation from road surface.

For Turbulent flow i.e $Re > 5 \times 10^5$

$$Nu = 0.037Re^{0.8}Pr^{0.333} \quad (3.156)$$

Then the heat transfer coefficient is

$$h_{bot} = \frac{Nuk}{L_{bot}} \quad (\text{W/m}^2\text{K}) \quad (3.157)$$

where k is thermal conductivity of air.

The heat gained by reflected radiation from road can be determined by using Newton-Raphson method to solve the following function:

$$function = 3.15\sigma T_{bot}^4 + 3.5 \times 0.5h_{bot} - 3.5h_{bot} - \frac{28000}{1 + 266.66 \left[1 + \frac{105}{3.5h_i} \right]} T_{bot} + QTY \quad (3.158)$$

$$QTY = 3.5 \times 0.5T_{road} + 3.5 \times 0.9\sigma T_{road}^4 + \frac{28000T_i}{1 + 266.66 \left(1 + \frac{105}{3.5h_i} \right)} \quad (3.159)$$

$$Q_{ref} = \frac{28000}{1 + 266.66 \left[1 + \frac{105}{3.5h_i} \right]} T_{bot} - \frac{28000}{1 + 266.66 \left[1 + \frac{105}{3.5h_i} \right]} T_i \quad (3.160)$$

where

\dot{Q}_{ref} = heat gained by reflected radiation.

T_{bot} = Temperature of bottom surface of vehicle exposed to road reflection.

T_{road} = Temperature of road.

h_{bot} = heat transfer coefficient between road and vehicle.

L_{bot} = length of bottom surface of vehicle exposed to road.

The total heat gained is determined by the summation of the various components and considering that 25% of total heat gain by three component transmission of metal, transmission of glass and reflection of road as an additional heat gain from sources like engine and ventilation air.

$$Q_{\text{load}} = (Q_{\text{tran,metal}} + Q_{\text{tran,glass}} + Q_{\text{ref}}) + 0.25 \times (Q_{\text{tran,metal}} + Q_{\text{tran,glass}} + Q_{\text{ref}}) \quad (3.161)$$

A computer code has been developed to determine the total heat gain by the vehicle at different locations, weather conditions and times of the year and of the day. The code was run for a latitude of 13° for Bangalore city for 21 April. The data required to run the code are:

$\phi = 13^\circ$ (Latitude angle of Bangalore).

$Z = 920$ m (Elevation from mean sea level).

$N = 111$ (day number on 21st April).

$U_o = 15$ m/s (Velocity of air flowing over vehicle).

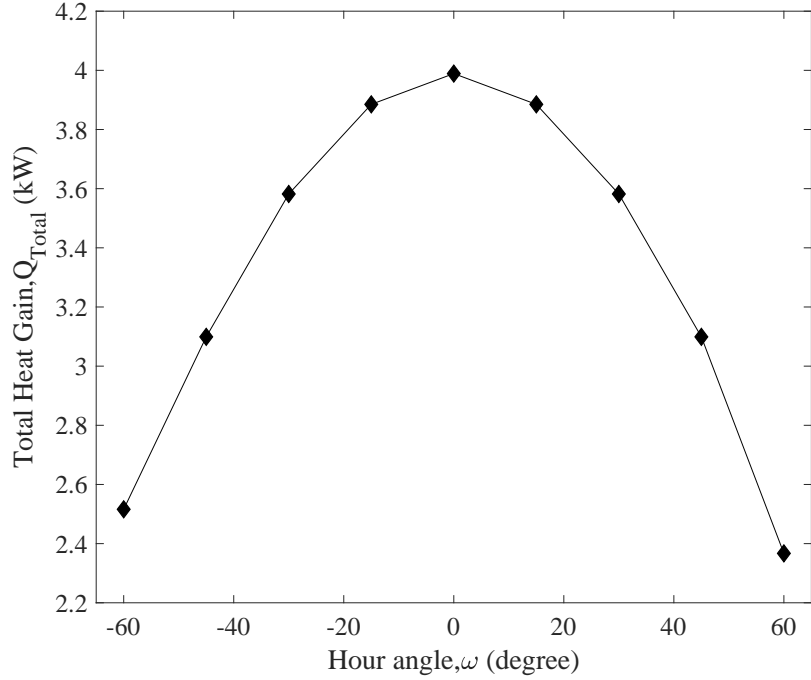
$T_o = 45$ °C (Temperature of surrounding air).

$T_i = 45$ °C (Temperature of cabin air).

$A_{\text{dir}} = 2.9$ m² (Area of vehicle exposed to direct solar radiation).

$A_{\text{top}} = 1.437$ m² (Area of top surface of the vehicle).

$A_{\text{glass}} = 2.38$ m² (Area of glass surface of the vehicle).



H

Figure 3.12: Variation of total heat gained by the vehicle at different hour angles at $\phi = 13^\circ$, on 21 April

$$L_{\text{top}} = 1.58 \text{ m}^2 \text{ (length of top surface of the vehicle.)}$$

$$t_{\text{glas}} = 5 \text{ m (Thickness of glass).}$$

$$t_{\text{m}} = 2 \text{ m (Thickness of metal body).}$$

Fig. 3.12 shows the variation of total heat gained by the vehicle calculated by Eq. 3.161 with respect to the hour angle. From the plot it can be observed that the total heat gained has less value at 60° hour angle (morning 8 AM) and becomes a maximum at zero hour angle (at 12 noon when Sun is overhead) and again becomes less at -60° (evening 4 PM).

The total heat gained for 21 April (day number $N = 111$) by the vehicle is also determined for different hour angles for five major state capitals of India. The latitudes and elevations of the cities are taken from standard sources. The calculations are made for 45°C surrounding air temperature for each case and an air velocity of 15 m/s. Fig. 3.13 shows the values of total heat gain at different hour angles for five major state capitals of India.

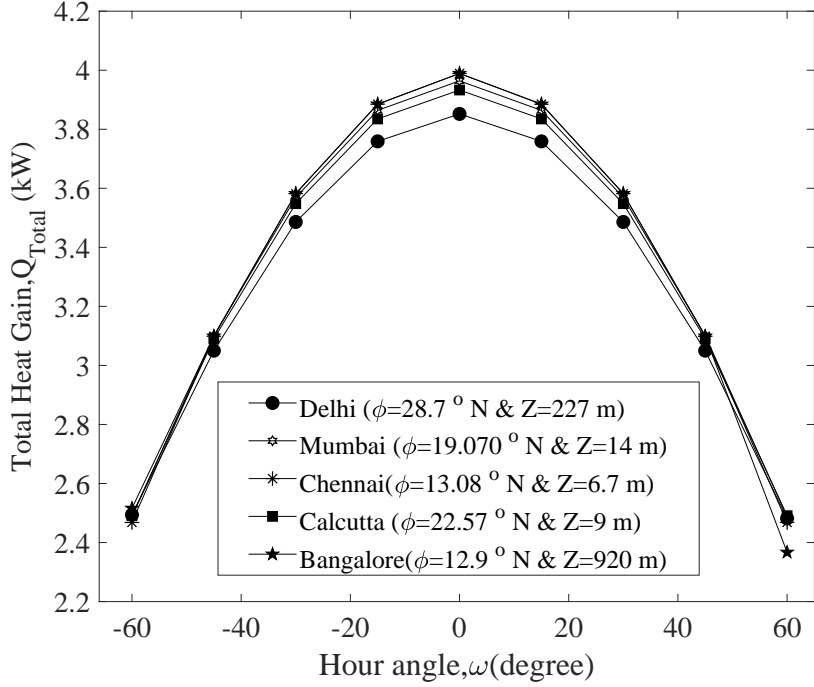
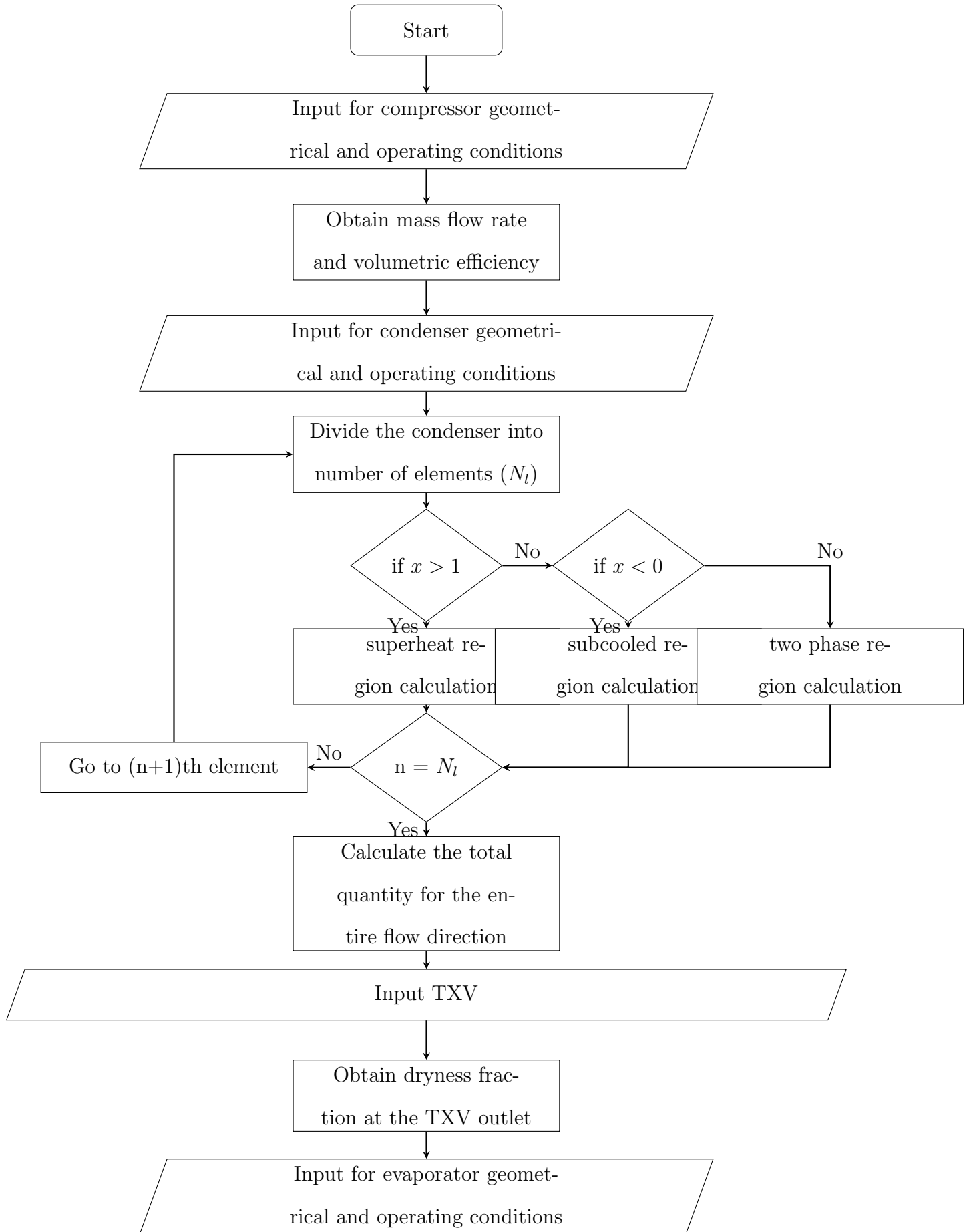


Figure 3.13: Variation of total heat gained by the vehicle at different hour angles for different capitals of India on 21 April, $T_o = 45^\circ C$, $U_o = 15m/s$

3.9 Algorithm for computer code and geometrical data

A computer code is developed for the performance prediction of the AACCS. The code consists of several routines related to the mathematical equations for each component of the system, namely, the compressor, condenser, expansion valve and evaporator, thermodynamic and transport properties of the refrigerants, geometrical data related to compressor, condenser, TXV and evaporator and operating conditions like air temperature, air humidity, air velocities, compressor pressure ratio, compressor suction pressure, speed of the compressor, degree of superheat at the outlet of the evaporator, etc. For given geometrical and operating conditions the code solves the equations for properties of refrigerants and the performance of the system. The properties of the refrigerants are calculated by building subroutines into the main program. Fig. 3.14 shows the flow chart of the computer code. The calculations begin with the compressor and proceed to condenser, TXV and evaporator. For evaporator calculations, the water film temperature and the mean tube temperature are first guessed to obtain the pressure drop and heat transfer rate and then recalculated by an iterative process until convergence. For condenser and evaporator the length in the flow direction of the refrigerant is

divided into a number of identical elements of the same geometrical configuration and dimensions. The flow of refrigerant inside the tubes is divided into three regions, superheated, two phase and subcooled, in the case of the condenser and into two regions, two phase and superheated in the case of the evaporator. At a given pressure of the refrigerant at the inlet of the condenser, that is at the inlet of the first element, pressure drop is calculated which gives the pressure at the outlet of the element and the heat transfer rate. This is done by carrying out the required number of iterations over the same element. With these quantities determined, the control goes to the next element, for which the same procedure is repeated. In this manner, calculations are done for all the elements in the condenser and evaporator. The total heat transfer rate is determined by a summation over all the elements.



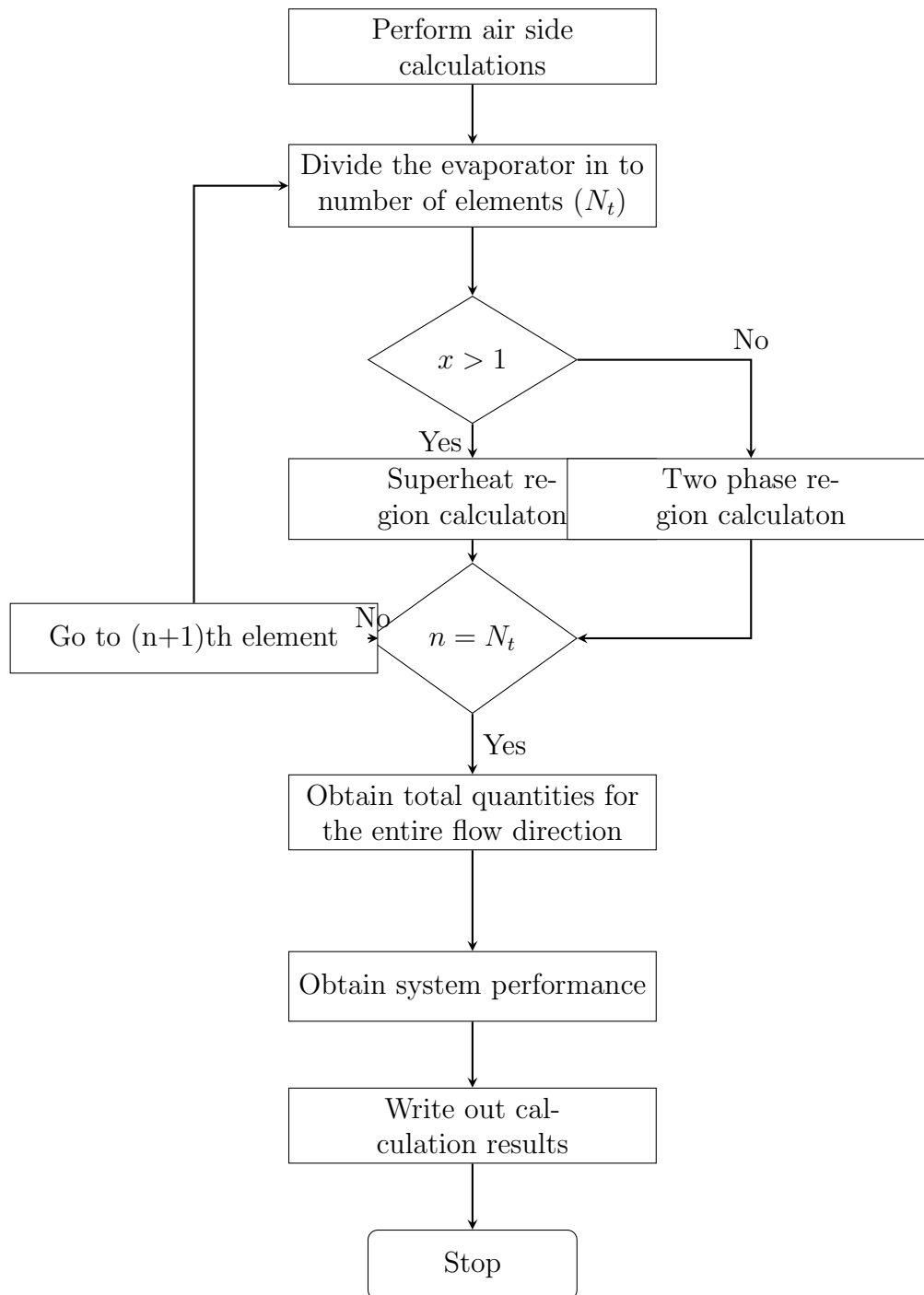


Figure 3.14: Flow chart for the numerical code for AACs

3.10 Geometrical and operating data required for the computer code

The geometrical and operating data of the components is as follows:

3.10.1 Swash plate compressor.

Geometrical data:

Following data of swash plate compressor are required:

1. Number of Cylinder(n)= 5
2. Stoke length of cylinder (S_c)= 17 mm
3. Diameter of cylinder (D_c)= 25 mm
4. Clearance fraction (r)= 1%

Operating data:

1. Rotational speed of compressor (N)= 600-1400 rpm
2. Compression ratio (ϵ)= $\frac{P_{\text{dis}}}{P_{\text{suc}}} = 2$ to 10
3. Suction pressure $p_{\text{suc}} = 1.2$ to 4.0 bar
4. Degree of superheat at suction (T_{deg})= 5 °C

3.10.2 Flat-tube louvered fin condenser.

Geometrical data:

1. Length of condenser (H_{cond})= 34 cm
2. Width of condenser (W_{cond})= 34 cm
3. Depth of condenser (D_{cond})= 16 mm

4. Louver length (L_1)=7 mm
5. Louver pitch (L_p) = 1 mm
6. Number of louver (N_1)= 10
7. Louver angle (θ)= 30 °C
8. Non-louver inlet and exit fin regions (S_1)= 2.4 mm
9. Re-direction length (S_2) = 2.0 mm
10. Fin pitch (F_p) = 1.5 mm
11. Fin height (F_D)=(F_h) = 16 mm
12. Fin thickness (t_f)=(F_{th}) = 0.17 mm
13. Tube pitch (T_p)= 10 mm
14. Tube width (T_w)=(D_{min})= 1.75 mm
15. Number of parallel tubes = 36
16. Channel height (w_w)= 0.6 mm
17. Channel width (w_c)= 0.9 mm
18. Number of channel (N_c)= 19
19. Tube wall thickness (t_t)= 0.4 mm
20. Hydraulic diameter (D_h)= 0.72 mm
21. Element length in flow direction (dz)= 1.5 mm

Operating data:

1. Temperature of air at element inlet ($T_{a, cn, in}$)= 26 °C to 34 °C;
2. Atmospheric pressure (P_{atm})= 98.3 kPa
3. Relative humidity of air (ϕ_r)= 0.5 to 0.9
4. Specific heat of air ($c_{p, air}$)= 1007 J/kg.K
5. Specific heat of water vapour ($c_{p, wv}$)= 1868 J/kg.K
6. Frontal velocity air at condenser inlet (u_{fr})= 1.0 m/s and 1.5 m/s
7. Thermal conductivity of fin and tube (k_{fin})= 200 W/m.K

3.10.3 Flat tube louvered fin evaporator.

Geometrical data:

1. Length of Evaporator (H_{evp}) = 25 cm
2. Width of Evaporator (W_{evp})= 18 cm
3. Depth of Evaporator (D_{evp})= 85 mm
4. Louver length (L_1)= 18 mm
5. Louver pitch (L_p)= 2.5 mm
6. Number of louver (N_1)= 24
7. Louver angle (θ)= 30 °
8. Nonlouver inlet and exit fin regions (S_1)= 5 mm
9. Re-direction length (S_2)= 15 mm
10. Fin pitch (F_p)= 1.5 mm

11. Fin height (F_D)= (F_h) = 21 mm
12. Fin thickness (t_f)= (F_{th}) = 0.1 mm
13. Tube pitch (T_p)= 26 mm
14. Tube width (T_w)= (D_{min}) = 5.2 mm
15. Channel width (w_c)=2.9 mm
16. Number of channel (N_c)= 21
17. Tube wall thickness (t_t)= 0.8 mm
18. Hydraulic diameter (D_h)= 2.9 mm
19. Element length in flow direction (dz)=1.5 mm

Operating data:

1. Temperature of air at element inlet ($T_{air,cond,in}$)= 25 °C to 35 °C
2. Atmospheric pressure (P_{atm})= 98.3 kPa
3. Relative humidity of air (ϕ_r) = 0.5 to 0.9
4. Specific heat of air ($c_{p,air}$) = 1007 J/kg.K
5. Specific heat of water vapour ($c_{p,wv}$)= 1868 J/kg.K
6. Frontal velocity air at evaporator inlet (u_{fr})= 2 m/s
7. Thermal conductivity of fin and tube (k_{fin}) = 200 W/m.K

Chapter 4

Experimental Facility and Procedures

4.1 Introduction

The experimental work consists in the development of a test rig for small capacity automotive air conditioning system (typically that of a five seater small passenger car with about 3.5 kW cooling capacity). The test rig is designed and fabricated in a such way that it can operate at different parametric conditions. An automotive air conditioning system operates under various speeds, temperatures and humidity ratios of air at different time zones and locations. The test rig is designed keeping this in mind and consists of two main parts; first the main air conditioning system and second, the instrumentation to measure the performance of system. The main system is fixed on a frame along with air carrying ducts and other instruments. The system is driven by electrical motor which is also placed on the main frame. The frame is made of steel channels that can withstand the weight and provide support to the system at various running conditions of system. The physical quantities such as temperatures, velocities, humidities etc., can be measured by locating sensors and instruments at different points within the system and inside the air ducts. A control panel is provided near the frame and all the parameters are controlled from that control panel.

Fig. 4.1 shows the schematic of the experimental facility of the AACS used in the present study. The core AACS consists of a swash plate compressor, an evaporator, a condenser, a thermostatic expansion valve, a dryer and aluminium circular pipe fittings, which form a closed system. A three-phase induction AC motor is used to drive the compressor with variable frequency to control the speed of

compressor. An energy meter is electrically connected to the motor for measuring the power input in kWh. The pulleys of the motor and compressor are connected by a rubber V-belt. A three-phase AC supply is required for the working of the motor. The evaporator is fixed inside the rectangular transparent plastic duct along with two heat loads (electric bulbs approximately 400 W each plus atmospheric heat inleak load), two air circulation fans and three air control valves as shown. The evaporator duct has two passages such that fresh air and recirculation air can flow through the evaporator and is also provided with ports for placing different sensors at the inlet and outlet of the evaporator. By closing and opening the three air control valves, an arrangement is made to direct completely fresh air or recirculated air through the duct. The condenser is fixed inside the single straight transparent plastic rectangular duct as shown. A variable heat load (electric heater) and a variable speed air flow fan are provided in the condenser duct. A rheostat is used to control the heater and an electrical controller is used to control the speed of condenser fan. Various digital and analogue measuring instruments are used in AACS set up, of which some instruments like pressure gauges, thermocouple and differential pressure sensor, etc., are directly connected to system and the others such as digital tachometer are used when required to measure the quantities.

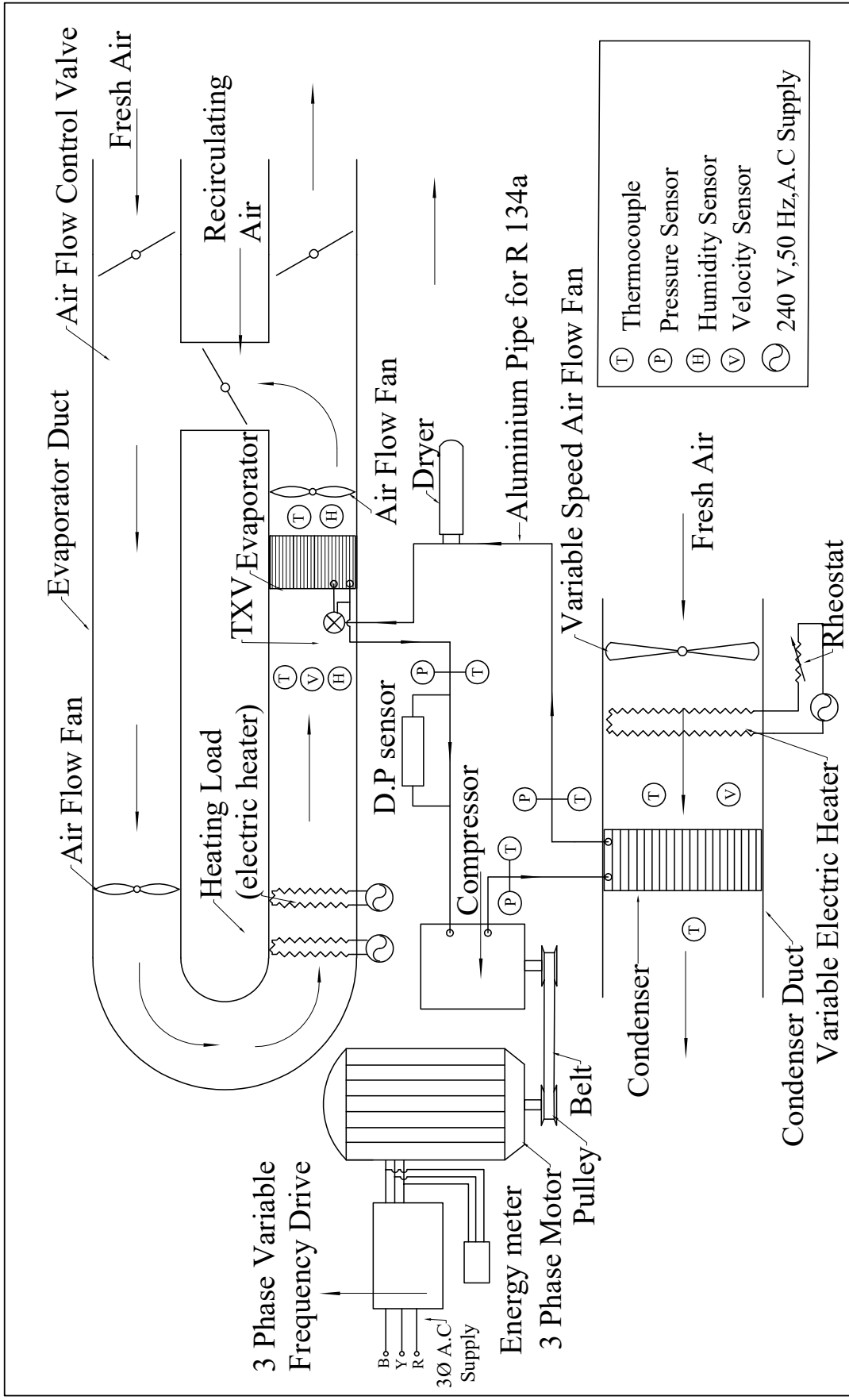


Figure 4.1: Schematic of the experimental setup of the automotive AC system.

4.2 Core automotive AC system

The following are the main components of the system:

1. Swash plate compressor
2. Evaporator
3. Condenser
4. Thermostatic expansion valve(TXV)
5. Dryer or Receiver
6. Connecting pipes and fittings

4.2.1 Swash plate compressor

The compressor is the heart of any vapour compression system. Swash plate reciprocating compressors are used in automobiles because they can be run from the engine shaft, are compact and have higher performance. The compressor in the system is a five cylinder, double acting, swash plate, reciprocating compressor. Fig. 4.2 shows the actual compressor and its cut portion revealing the five cylinders. The bore of each cylinder is 25 mm and the stroke is 17 mm. The cylinders are attached to the swash plate through smooth ball-an-socket bearings which give a smooth motion for the swash plate. Two ports, namely, in port and out port are there for suction and discharge of compressed vapour. The vapour is aspirated from the in port and is delivered with high pressure through the out port. The compression ratio is the ratio of compressed pressure to suction pressure. The flow of refrigerant inside the swash plate compressor is very complicated because refrigerant vapour enters from suction manifold and passes through many passages and valves. The entry manifold is divided into two pipes so that the refrigerant vapour is equally directed to both sides of the compressor cylinders. Similarly the exit manifold is divided into two pipes to collect the refrigerant from both the sides of cylinders and deliver to the discharge side. Fig. 4.3 shows the suction and discharge valve geometries. These valves are circular thin discs bored with holes and provided with a poppet-like valve. The suction and

discharge discs, face to face, are placed at both the sides of the compressor cylinders. These valves open and close by pressure differences inside the compressor and the manifolds and act alternately according to the swash plate motion.

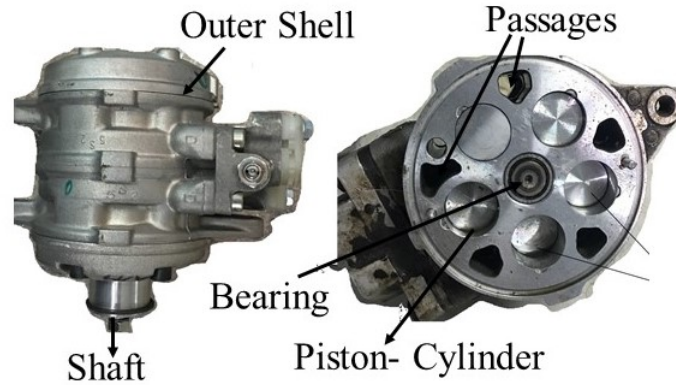


Figure 4.2: Swash plate compressor(top view and cut view)

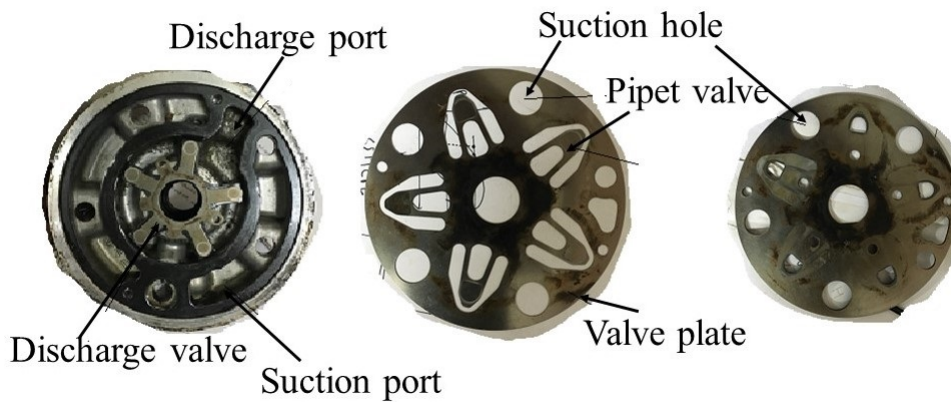


Figure 4.3: Suction and discharge valve plates of compressor

4.2.2 Evaporator

The evaporator or cooling coil is an important part of the system and its function is to extract heat from required space and provide comfort to the passengers. In the present system, the evaporator is a flat tube, louvered fin, brazed aluminium type of evaporator which gives high performance and has lower weight and higher compactness. Fig. 4.4 shows the evaporator used in the experimental setup. The front view shows the flat tube and fins arrangement and the top view shows the inlet port, outlet port and the thermostatic expansion (TXV) valve. The louvered fins can be observed in the top view.

The flat rectangular tube of the evaporator carrying the refrigerant contains multiple channels inside. These channels are very small in size as can be seen in Fig. 4.5. Fig. 4.6 shows the fin structure and the arrangement of louvers in the fins. The evaporator is placed inside the rectangular duct along with heating load (electric bulbs) and an air flow fan.

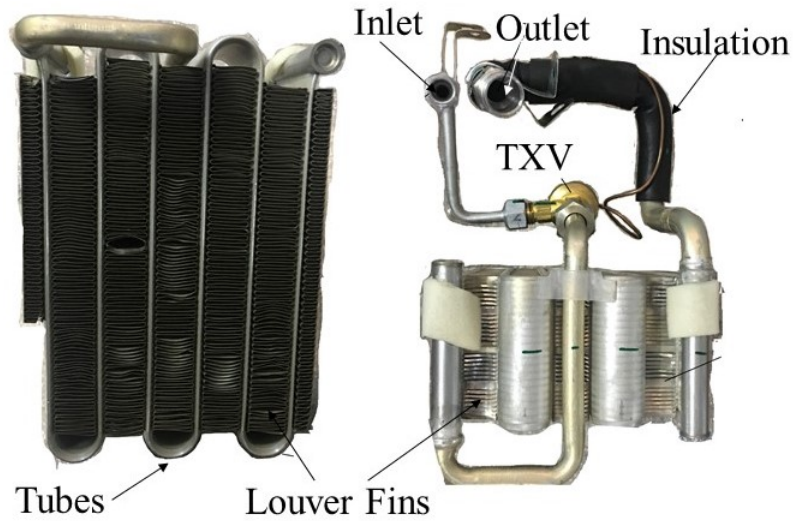


Figure 4.4: Evaporator front view and top view

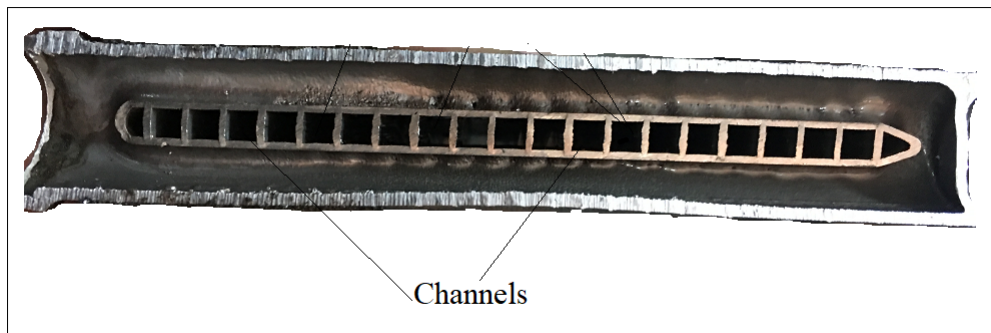


Figure 4.5: Evaporator tube cross section

4.2.3 Condenser

The condenser used is an aluminium, brazed, flat-tube, louvered fin type as shown in Fig. 4.7. The cross-sectional area of the tube is shown in Fig. 4.8. The channels of condenser tube are smaller than those of the evaporator tube and the size of the fins is also smaller than that of evaporator fins. The tube of the evaporator is a continuous and serpentine tube from inlet to outlet. The flow

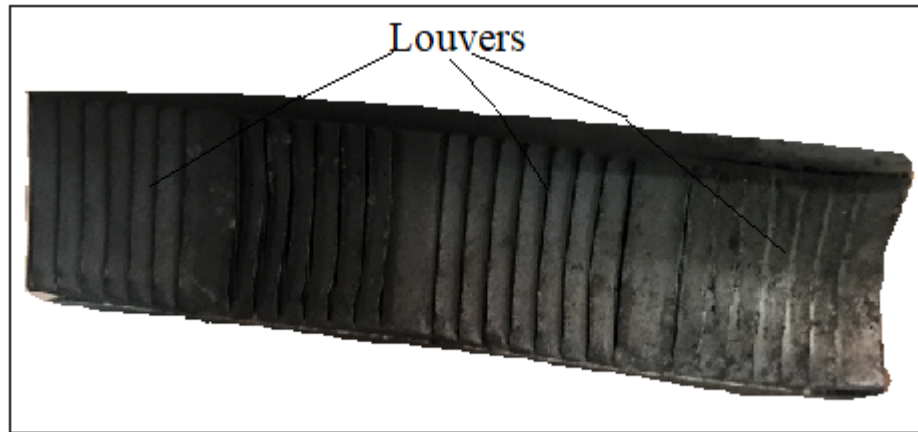


Figure 4.6: Evaporator fin structure showing louvers

of refrigerant is continuous without dividing from header to parallel tubes. But in the condenser, parallel tubes are connected to headers and the flow of refrigerant is divided into these tubes. The condenser is placed inside the condenser duct along with fan and variable load electric heater.

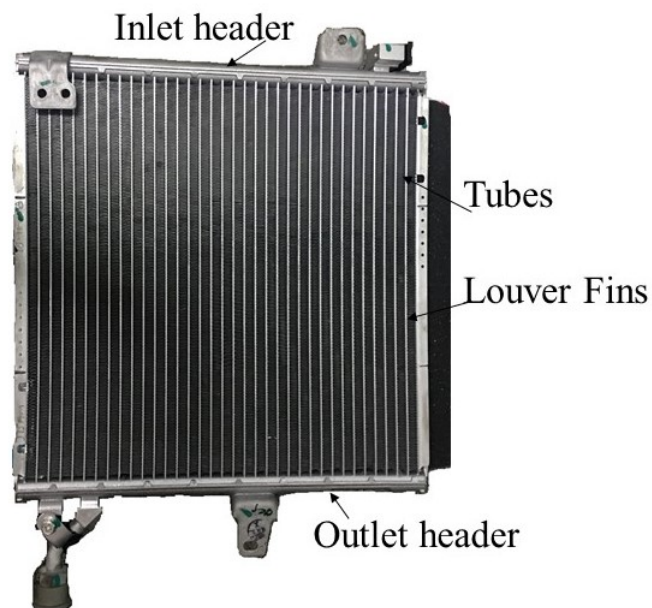


Figure 4.7: Condenser used in experiment set-up

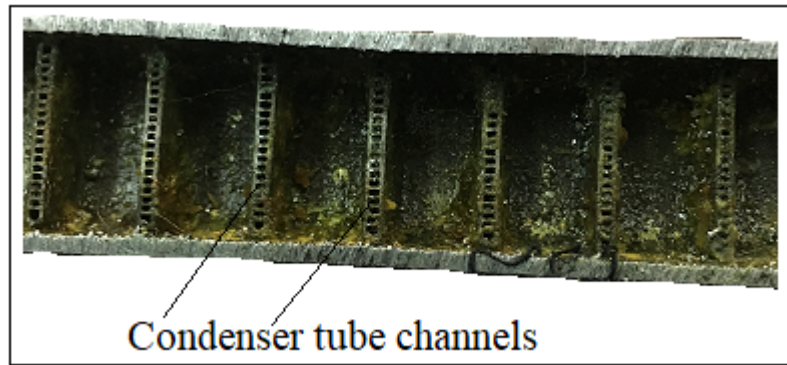


Figure 4.8: Cross section of parallel tubes showing small channels in condenser.

4.2.4 Thermostatic expansion valve (TXV)

The thermostatic expansion valve (TXV) used in present study is shown in Fig. 4.9. The function of TXV is to deliver refrigerant at high pressure from condenser to the evaporator at low pressure and to control the mass flow rate according to the heat load on the evaporator. A feeler bulb or phial is placed at the evaporator pipe outlet. This senses the temperature of the superheated vapour and controls the opening and closing of TXV to control the degree of superheat and hence the mass flow rate of refrigerant. The feeler bulb and the TXV are connected by a small diameter copper tube which is filled with the same refrigerant as that used in the system.

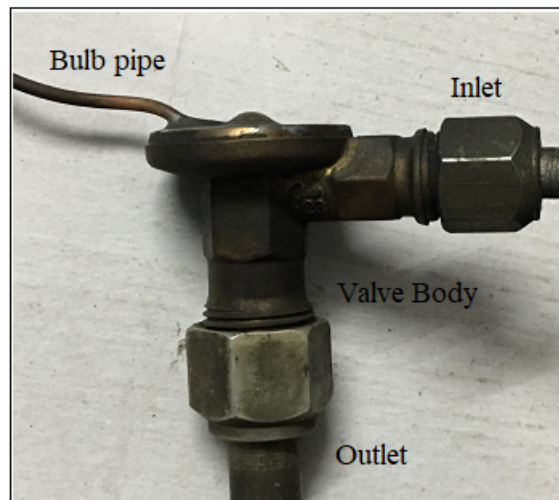


Figure 4.9: Thermostatic expansion valve used in experiment set-up

4.2.5 Dryer or Receiver:

A receiver or dryer (or receiver-dryer) is an important part of AAC system and is placed between the condenser and the TXV. The function of the dryer is to absorb the refrigerant vapour leaving from condenser due to incomplete condensation and maintain mass continuity in system. Fig. 4.10 shows the dryer used in the experimental setup. It acts as a temporary storage container for oil and refrigerant when neither are needed for system operation (such as during periods of low cooling demand). This is the 'receiver' function of the receiver/dryer. Most receiver/dryers contain a filter that can trap debris that may be present inside the system. Receiver/dryers contain a material called desiccant. The desiccant is used to absorb moisture (water) that may have gotten inside the AC system during manufacture, assembly or service. Moisture can get into the AC components from humidity in the air. This is the 'drier' function of the receiver/drier. Damage can occur if there is excessive moisture inside an AC system. It can cause corrosion, as well as possibly degrade the performance of the compressor lubricating oil.

The receiver/drier should be replaced any time the system is opened for service and most compressor warranties require it. The desiccant is only capable of absorbing a certain amount of moisture and when the inside of the system and/or the receiver/drier are/is exposed to the atmosphere, the desiccant can become very quickly saturated with humidity in the air. If this occurs, the desiccant is no longer effective and will not provide future protection. Additionally, the filter inside the receiver/dryer could be restricted by debris that may have been inside the system. This could diminish refrigerant and oil flow.



Figure 4.10: Receiver or Dryer

4.2.6 Pipes and Fittings

The components of the AACCS are interconnected by smooth aluminium round pipes as shown in Fig. 4.11. Different diameter pipes are used in system because the flow inside the pipes are vapour, two-phase or liquid. The flow from the evaporator outlet to condenser inlet is vapour flow and therefore larger diameter pipe (11 mm internal diameter) is required. The flow from condenser outlet to TXV inlet is liquid and hence small diameter pipe is enough. K-type thermocouples and pressure gauges are mounted on aluminium blocks and connected to pipes by TIG welding. The differential pressure sensor is mounted on the pipe between the evaporator and the compressor at the lower pressure side. There are two ports provided on pipes for charging the system with refrigerant, one on high pressure side and the other on low pressure side. In case of repair and damage which requires dismantling of the system, fittings are provided on the pipes with nuts and bolts. By opening these nuts and bolts we can assemble and disassemble the system and carry out any repair.



Figure 4.11: Aluminium pipes and fittings.

4.3 Measuring instruments and electrical equipments

Other than the AACS proper, there are other parts of the experimental facility. The system is driven by electrical motor and important parameters are measured with the help of different instruments.

The following are the two categories of supporting components:

Electrical equipments

Measuring instruments

4.3.1 Electrical equipments

The following is the electrical equipments used in the experimental setup:

1. Electric motor.
2. Frequency converter.
3. Heating coils.
4. Air flow fans.
5. Rheostat.

Electric motor

As mentioned before, the compressor is driven by electrical an motor. The three-phase AC induction motor is used in the experimental setup is shown in Fig. 4.12. The following are the specifications of motor:

1. Manufacturer: Integrated Electrical Co.(P) Ltd., Bangalore (India)
2. Type: 3-phase induction with star connection
3. Capacity: 1.1 kW
4. Voltage: 415 V

5. Ampere: 2.8 A
6. RPM: 1410
7. Frequency: 50 Hz
8. Efficiency: 75%

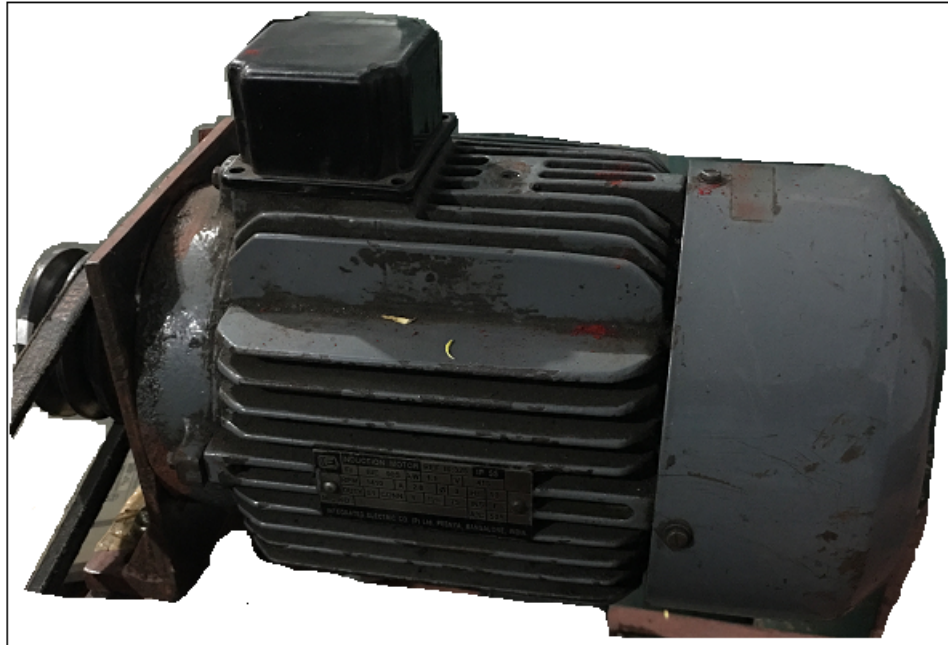


Figure 4.12: Three-phase AC electric motor used in the experimental setup

Frequency converter drive

The rotational speed of motor in the experiment setup is changed by a variable frequency converter. The drive is directly connected to the motor and controls its speed electrically by changing the current and voltage supply to motor. Fig. 4.13 shows the variable frequency converter drive. The front portion of drive consists of display screen and control buttons. The three phase wire connections can be made as per the instructions given in the manual provided by manufacturer. The speed variation in the present study is from 500 - 1400 rpm with a minimum difference of 5 rpm.



Figure 4.13: Variable frequency converter drive.

Heating coil and heating bulbs

The main function of heating coil and heating bulbs in the experiment setup is to provide heating load on the evaporator and condenser. There are two electrical heating coils (heaters) and two bulbs of 200 W each are used. Two bulbs are provided for evaporator and one coil with variable heat for the condenser. The coils are fixed in the ducts and are operated by switches fixed on the control panel board. The bulbs of 400 W are fixed in the evaporator duct and function to provide warmer air to the evaporator. The heating coil of capacity 1.2 kW is fixed in the condenser duct and is controlled by a rheostat to vary the temperature of air at the inlet to the condenser. Fig. 4.14 shows the heating coil and bulbs used in the experimental setup.

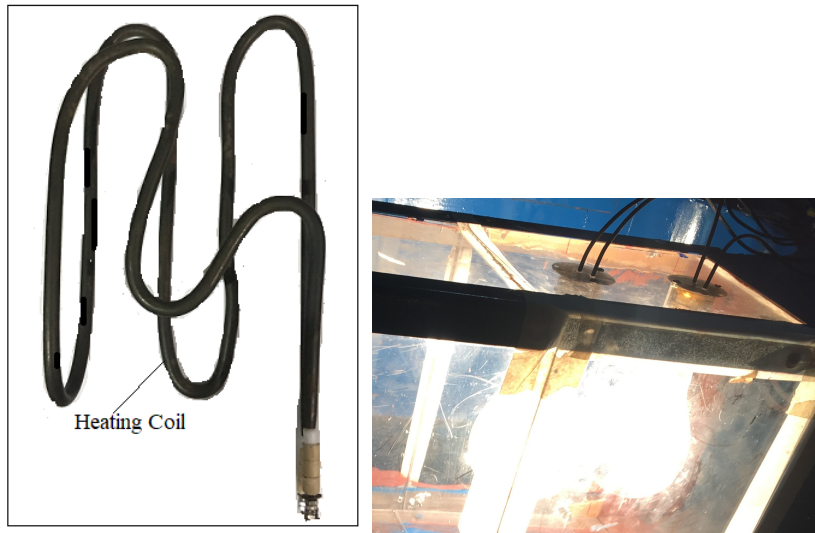


Figure 4.14: Electric heating load coil and bulbs.

Air flow fans

The function of the fans is to circulate the air inside the ducts. The fans are fixed at the inlets of the evaporator and the condenser. Fig. 4.15 shows the condenser and evaporator fans used in experimental setup. The condenser fan is a variable speed fan and the evaporator fan is a constant speed fan. The range of air speed provided by the condenser fan is 1 m/s to 2 m/s and air speed provided by the evaporator fan is approximately 2 m/s. The fans are operated on 230 V and 50 Hz AC power supply.

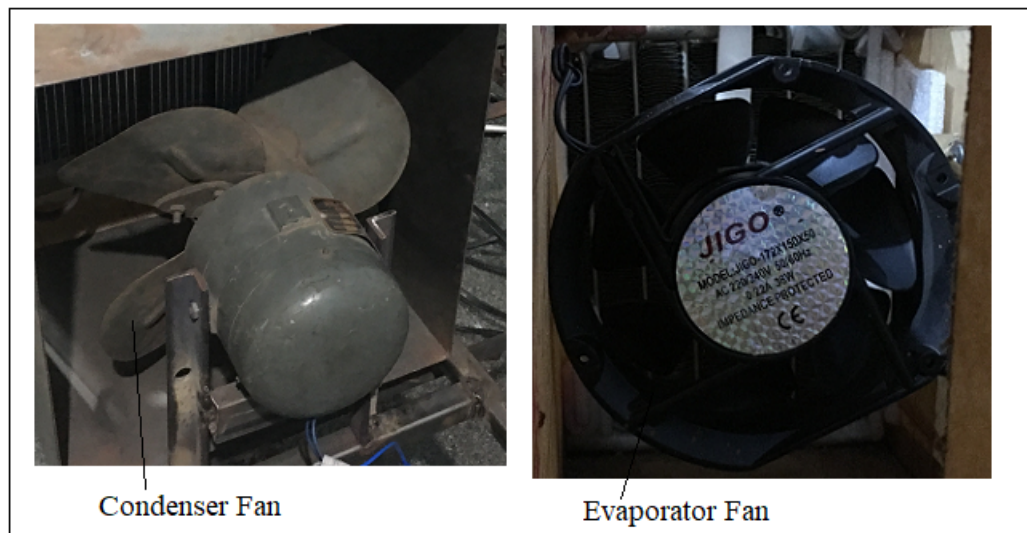


Figure 4.15: Electric fans used in condenser and evaporator.

Rheostat

The rheostat is electrically connected to the condenser heater and its function is to provide variable resistance to heater for controlling the temperature of the coil. Fig. 4.16 shows the rheostat. The rheostat is fixed on a control board and the resistance is changed by a controlling knob. The range of air temperature obtained is 26°C to 35°C.

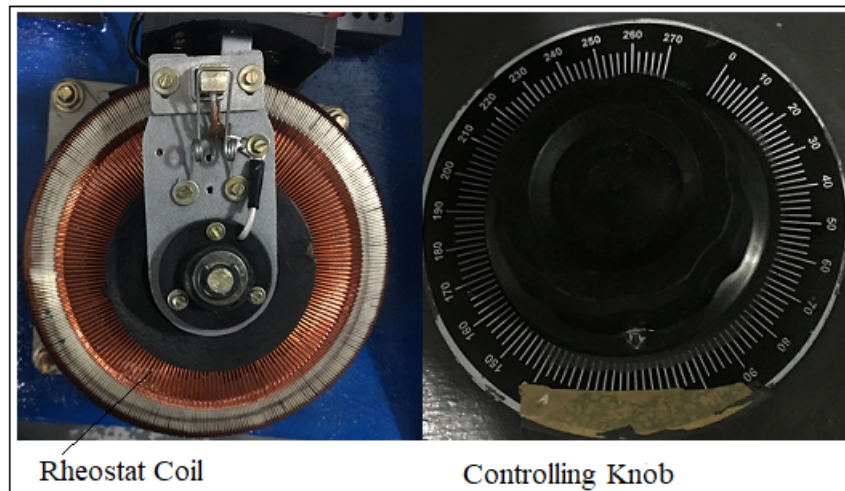


Figure 4.16: Variable resistant coil (Rheostat).

4.3.2 Measuring instruments

Following are the measuring instruments used in the experimental facility.

1. Thermocouples
2. Pressure gauges.
3. Differential pressure sensor.
4. Tachometer
5. Energy meter
6. Anemometer
7. Air temperature and humidity sensor

Thermocouples

Thermocouples used in the present work are K type (Nickel-Chromium, Nickel-Alumel, i.e., Chromel-Alumel). The thermocouple has two metal wires with red and yellow insulations. The red insulated wire is made of Nickel aluminium alloy and has magnetic properties while the yellow insulated wire is made of chromium nickel alloy which is non-magnetic. The diameter of both the wires is 1.5 mm and can be used to measure temperatures in the range of $-180\text{ }^{\circ}\text{C}$ to $1350\text{ }^{\circ}\text{C}$ with an accuracy of $\pm 0.1\text{ }^{\circ}\text{C}$ and resolution of $1\text{ }^{\circ}\text{C}$. The thermocouples are calibrated by the manufacturing company and are provided with a display unit. The thermocouples are fixed at desired locations in system to measure the refrigerant temperature inside the tubes. The aluminium blocks are welded to the main pipe line of the system and the pressure gauges and the thermocouples are fixed to the block such that measurement can be made of the refrigerant temperature and pressure without any leak of the refrigerant from the system. Fig. 4.17 shows the K type thermocouple and its display unit. As shown in the figure, both the wires form a common junction and this junction tip is placed in the location where temperature is to be measured. The other ends of the wires are connected to display unit.

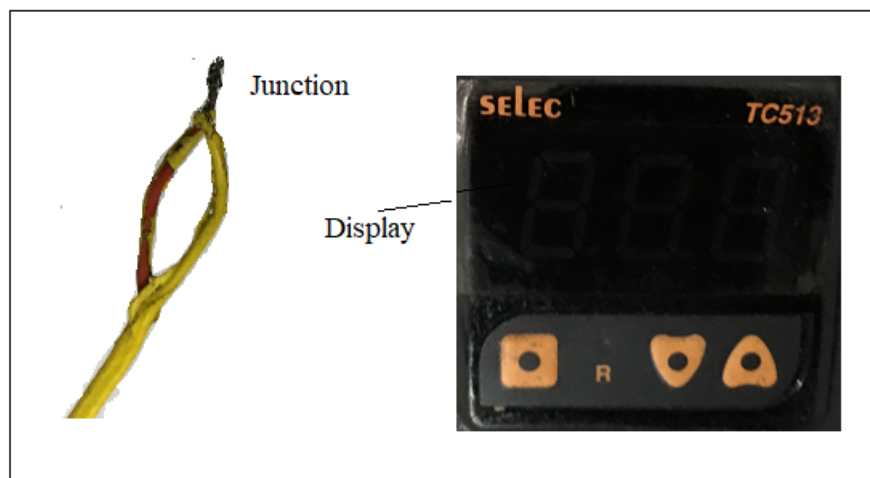


Figure 4.17: K type thermocouple and display unit.

Pressure gauges

The pressure gauges are mechanical dial gauges and the function of these is to measure the refrigerant pressure. The gauges are fixed on an aluminium block. The aluminium block is 25 mm square in cross-section into which holes are made from side and top. The side holes are made to weld the

main refrigerant pipe line and the top holes are internally threaded to fix the pressure gauges and thermocouples. Fig. 4.18 shows the pressure gauge along with the aluminium block. The range of pressure gauge is 0 - 21 kgf/cm² gauge pressure, with a resolution of 0.5 kg/cm². Three pressure gauges are used in the setup to indicate the pressures at the compressor inlet, compressor outlet and the condenser outlet.

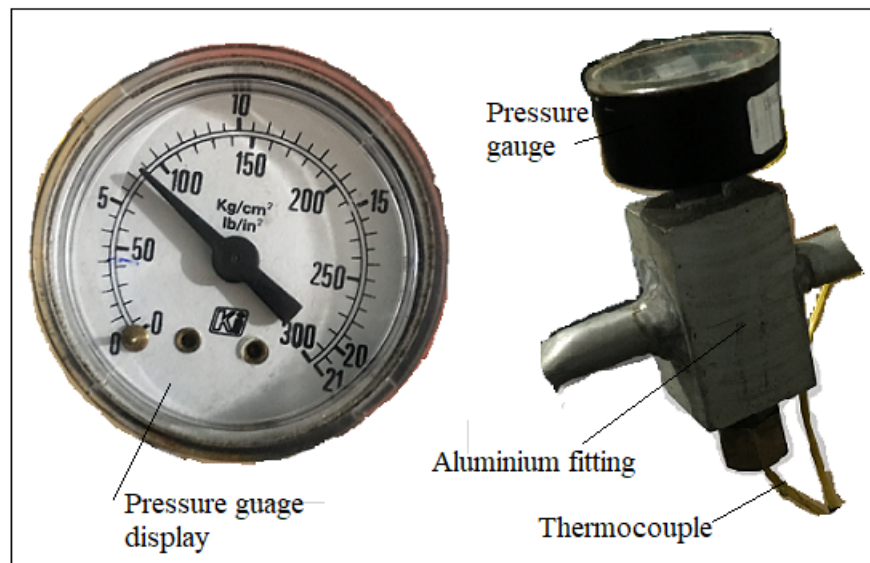


Figure 4.18: Pressure gauge and its position on aluminium block.

Differential pressure sensor

The mass flow rate of refrigerant is one of the desired quantities in calculating the performance of the air conditioning system. The actual mass flow rate can be found by placing the mass flow meter in the main system pipe line. There are several mass flow meters available in the market but suitable ones for the measurement of the small flow rates of refrigerants R134a or R1234yf are not easily available at reasonable prices. Hence a differential pressure gauge is used to calculate the mass flow rate of the refrigerant by utilizing the pressure difference in the mass flow rate relation. The differential pressure sensor is fixed between the evaporator and compressor in the low pressure side. The low pressure refrigerant vapour flows from the evaporator to compressor. Two holes are made 6 inches apart on the pipe between the evaporator and the compressor and from these two holes bypass pipes are provided to connect the differential gauge. Flow does not take place through the gauge. Rather the fluid exerts its pressure on the sensing element of the differential gauge from both sides. The

sensing element indicates the difference of pressure between the two holes which are 6 inches apart. Fig. 4.19 shows the differential pressure gauge and the display unit. The differential pressure gauge is designed to work under a maximum line pressure of 5 bar. The range of differential pressure gauge is from 0 Pa to 1000 Pa with an accuracy of 0.1 Pa and resolution of 1 Pa. When the experiments were in progress, it was discovered that the differential pressure sensor was not calibrated accurately for the experimental conditions encountered. Therefore the mass flow rate of refrigerant had to be obtained indirectly from an energy balance on the evaporator between the air and refrigerant sides.

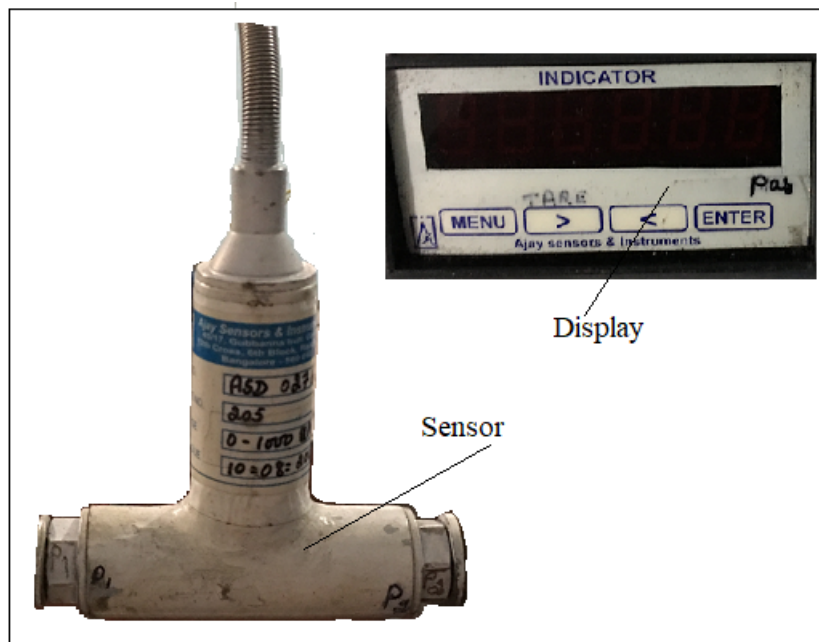


Figure 4.19: Differential Pressure Sensor.

Digital tachometer

To measure the rotational speed of motor and compressor, a digital tachometer is employed. This is an optical type non-contact device and works on the reflective scanning method. A light reflecting foil is attached to the shaft of the compressor; it rotates at the same speed of the shaft. The light reflected from the foil is incident on the light sensor of the tachometer gun. The frequency of the reflected light is calibrated in terms of the rotational speed of the shaft. Fig 4.20 shows the digital tachometer used for the rotational speed measurement. It has a red switch to point the laser on to the sensor and display screen to display the speed. The following are the specifications of tachometer:

Supplier: System Digital Tachometer (India).

Range: 60 to 100000 rpm.

Accuracy: ± 0.05 %.

Resolution: 0.1 rpm up to 999.9 rpm and 1 rpm above 1000 rpm.

Display: 5 digits, 7 segment bright red LED.

Operating temperature: 0 to 60 °C.



Figure 4.20: Digital tachometer.

Energy meter

The energy meter is used to determine the electrical power input to the motor. The coefficient of performance (COP) of system is the ratio of the cooling capacity to the power consumed by compressor. By connecting the energy meter to the motor, power input to the motor can be determined. Using this reading and the transmission efficiency between the motor and the compressor, it is possible to determine the power consumed by compressor. The energy meter used in the experimental setup is supplied by Techno Ltd.(India). This is of good quality and can be used for both single phase as well as three phase motors. The meter is a single unit and comes with an analogue display which indicates the electrical energy consumed in kWh. The average electrical power is found by dividing the energy meter reading by time. Fig 4.21 shows the picture of the energy meter. The meter is placed on the control panel board. The resolution of meter is 0.1 kWh.



Figure 4.21: Three phase energy meter.

Anemometer

The function of the anemometer is to measure the velocity of air flowing in evaporator and condenser ducts. The velocity of air is required to calculate the capacity of the evaporator and the condenser from the air side. The anemometer is a digital type instrument and is capable of accurately measuring the velocity of air. Fig. 4.22 shows the digital anemometer used in the setup. The instrument consists of two parts; a wind sensing fan and a display unit. The fan is made of plastic material and therefore is light in weight and can be handled easily. The fan should be placed in position in the air current such that air flow is perpendicular to the fan and facing the upstream. The air stream applies a force to rotate the fan and the rotations of the fan are calibrated to measure the linear velocity of air. The instrument can measure the velocity of air in different units i.e. m/s, ft/min, knots, km/h and Mph. The following are the specifications of anemometer:

Supplier: Digital Instrumentation (India).

Range: 0 - 140 km/h.

Accuracy: $\pm 3\%$.

Resolution: 0.3.

Display: LED display screen.

Operating temperature: -10 to 50 °C and 40% to 85% Humidity.

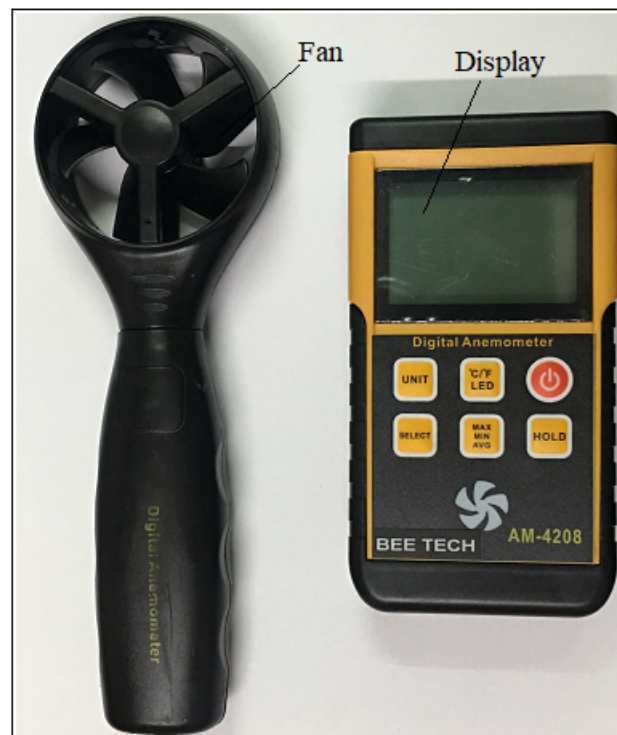


Figure 4.22: Anemometer.

Air temperature and humidity sensor

To measure the dry bulb and wet bulb temperatures of moist air, two parallel K-type thermocouples are fixed on a plastic base to form a sensor. One thermocouple is wound with cotton wick to measure the wet bulb temperature and the other one without wick measures the dry bulb temperature. Fig. 4.23 shows the device as described above. The output of these thermocouples are electrical signals, which are given to display unit made for K-type thermocouple. The signals are processed in the unit and give the output in degrees Celsius. The calibration is done by manufacturer. The device gives DBT and WBT of moist air. The humidity of air can be calculated by these DBT and WBT by using the standard Eq. 3.116 presented in chapter 3. In the wet bulb sensor the bead is surrounded by a cotton wick moistened with distilled water.

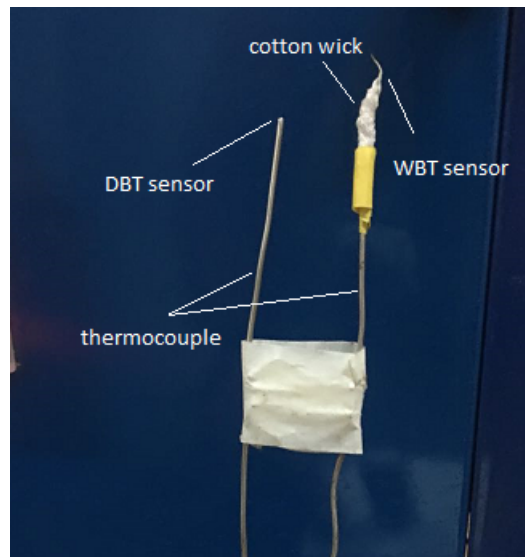


Figure 4.23: Air temperature and humidity sensor.

4.4 Construction of the experimental test facility

The components of the automotive air conditioning system, namely, the compressor, condenser, receiver, TXV and the evaporator are mounted on a frame made of steel channels. The frame gives support to all the components and also absorbs vibrations. The electrical control board is also mounted on the main frame which is shown in Fig. 4.24. The frame is made of steel channels with L-shaped cross-section (each limb 15 mm in length and 2 mm in thickness). These steel channels are cut into different segments and are welded to form the frame. The ducts and other components are fixed on this frame along with control panel board. The evaporator and condenser ducts are mounted on the frame with 4 inch screws as shown in Fig. 4.24. The condenser duct is 36 cm \times 40 cm in cross section and 91 cm in length. The condenser, variable load heater and fan is placed inside the condenser duct and this duct is open to surroundings from both the ends. The air is forced to move by the fan into the condenser from one end and is released into the surroundings from the other end. This is a simple open type duct without any recirculation of air. The second one is the evaporator duct which is a recirculation type of duct. The size of the duct is 19 cm \times 27 cm in cross-section and 130 cm in length. The evaporator attached with thermostatic expansion valve (TXV) as a single unit is placed inside this duct along with electrical heating coils and fan. This duct has two similar

and parallel ducts of 130 cm length joined by U-bends and a connecting passage Fig. 4.24. There are three air control valves fixed in the evaporator duct to make the arrangement for recirculation of air. Two valves are fixed at each end of the duct and the third valve is fixed in the connecting passage. By closing and opening of these three valves to different degrees, recirculation air at the evaporator can be obtained with different percentages of fresh air.

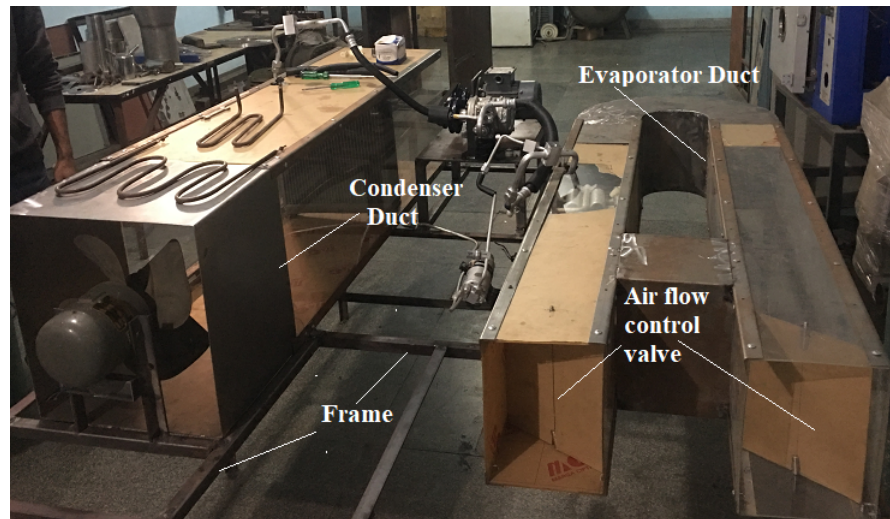


Figure 4.24: Evaporator and condenser ducts are mounted on frame.

4.5 Charging of the AAC System with refrigerant

Before beginning the experimental runs, the automotive air conditioning system is charged with R134a. The quantity of refrigerant charged inside the system can be found by taking the difference of mass of the refrigerant bottle before and after charging on a weight balance machine. Fig. 4.25 shows the measurement of mass of refrigerant (R134a) on weighing machine. It is observed that the mass of bottle before and after charging the system is 20.58 kg and 20.38 kg, respectively; therefore the charge is 200 grams ($20.58 - 20.38 = 0.2$ kg). The charging process will now be described in detail. The charging of the system requires the charging kit and a vacuum pump. The kit consists of flexible pipes, pressure gauges and connecting ports. First the entire system is charged with an inert gas (organ in the present case) up to 5 bar pressure and any leakage of the inert gas from the system is checked by applying soap solution from out side at different joints. If there is any leakage, then soap bubbles will form at the leakage points. In addition it is ensured that the system filled with the

inert gas stays at 5 bar for several hours. Any pressure loss indicates leakage of the inert gas. After the leak check the inert gas is completely removed by pressing the non-return valve of the charging port of system. Then the vacuum pump is connected to the system with the kit. There are two ports on the system, one on the low pressure side and the other on the high pressure side. The kit has three pipes, coloured red, blue and yellow as can be seen in Fig . 4.26. The red pipe is connected to the higher pressure port, blue is connected to the lower pressure port and the yellow pipe required for connecting the refrigerant bottle and vacuum pump. After making proper connections on the pump and creating the vacuum inside the system up to -50 cm of Hg (indicated on vacuum gauge by green colour in Fig. 4.26). The purpose of evacuating the system is to remove all the moisture and other contaminants from inside the system. After evacuation of system, both the valves of the kit are closed, the yellow pipe is disconnected from the pump and is connected to the refrigerant bottle. The valves of the kit are then slowly opened, the refrigerant is allowed to flow into the system and the compressor is run at full speed. Fig. 4.27 shows the charging of system with R134a. The compressor should be run until the desired pressures are obtained at the lower and higher sides of the system. In the present case the higher pressure is 12 psi (0.827 Bar) and lower pressure is 2.5 psi (0.172 Bar) for a completely charged system.



Figure 4.25: Refrigerant bottle and weigh balance device.

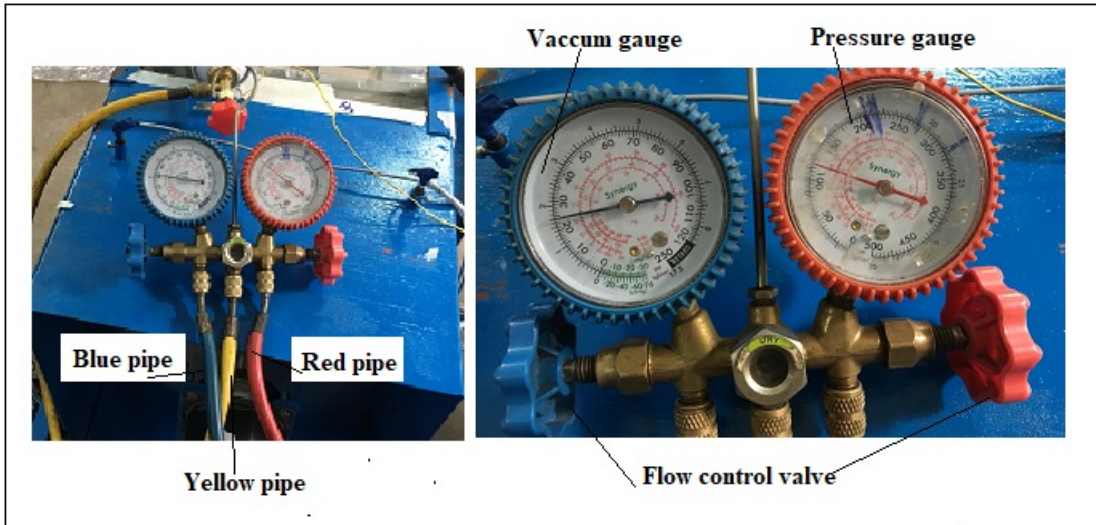


Figure 4.26: Refrigerant charging Kit.

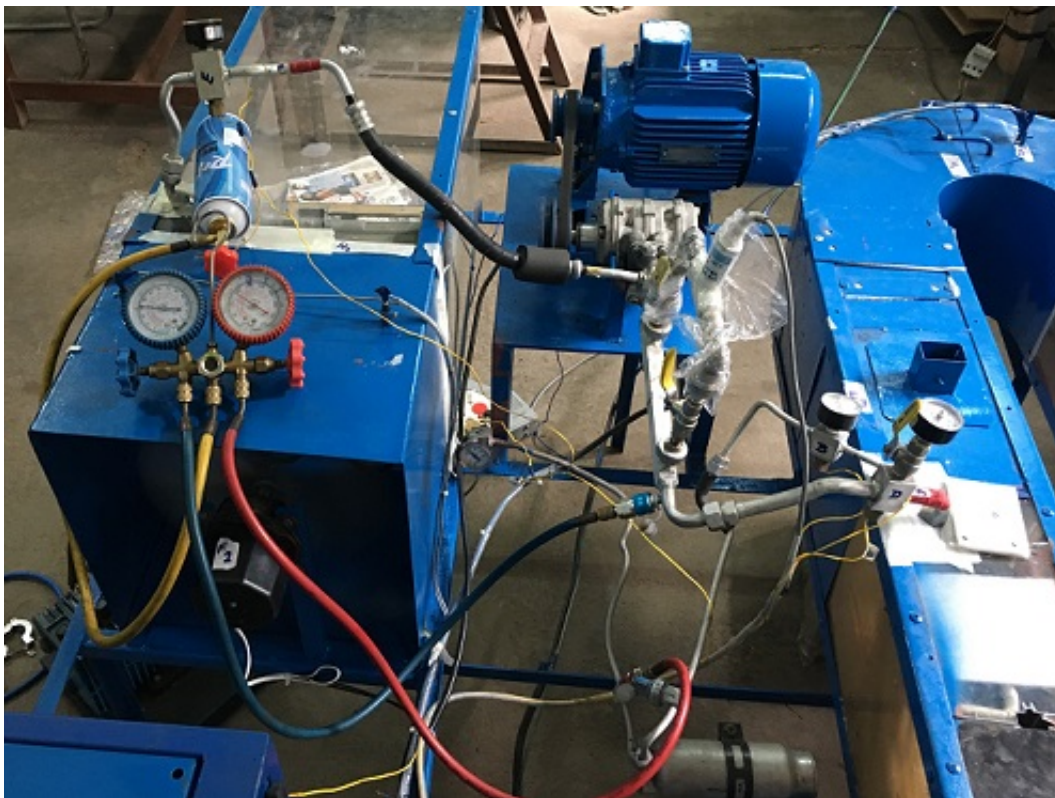


Figure 4.27: Charging of system with R134a.

4.6 Experimental procedure

The experimental procedure to conduct a typical run is as follows:

- The wet bulb, dry bulb temperatures and the total pressure of the ambient air in the laboratory are measured.
- The condenser and evaporator fans are switched on.
- The electric heater placed in the condenser duct and the electric bulbs placed in the evaporator duct (for the purpose of applying the load) are switched on.
- The compressor is switched on and the rotational speed is set at the desired value with the help of the frequency converter. The compressor speed is measured by a digital tachometer.
- The system is allowed to run for sufficient time (about 20 minutes) to attain steady state.
- The refrigerant side pressures and temperatures as well as the air side dry bulb and wet bulb temperatures at condenser and evaporator inlets and outlets are recorded. The air velocity at evaporator and condenser inlets are measured with a vane anemometer.
- The readings are arranged in the required format for carryint out further calculations as illustrated in the next chapter.
- The same procedure is repeated for other operating conditions.

Chapter 5

Results and Discussion

5.1 Method of calculation of various quantities

The operating variables are speed of compressor, air inlet velocity at the condenser and the air temperature at the inlet of the condenser. Most experiments are conducted for 100% fresh air condition and constant heat load on evaporator (400 W plus transmission load through the duct walls). This is because attempts to use larger recirculation resulted in frosting of the evaporator and to avoid frosting, more heat load had to be applied, but the dissipation of the heater bulbs was limited to 400 W in the experimental setup. The velocity of air is kept constant in the evaporator duct at 2 m/s for all the experiments.

The equations which are required to calculate the performance parameters of AAC system with experimental values are given here.

The performance parameters of the AACs are the evaporator capacity, condenser heat rejection rate, compressor power, coefficient of performance, mass flow rate of the refrigerant, actual volumetric efficiency of the compressor, isentropic work efficiency of compressor, heat loss rate from the compressor body (shell) and the temperature and humidity ratio at the evaporator outlet. The following section presents the equations of performance parameters.

5.1.1 Evaporator capacity (\dot{Q}_{evp})

The evaporator capacity is calculated as follows:

$$\dot{Q}_{\text{evp}} = \frac{V_{\text{a,evp,avg}} A_{\text{evp,duct}}}{v_{\text{a,evp,o}}} (h_{\text{a,evp,in}} - h_{\text{a,evp,o}}) \quad (5.1)$$

where $V_{\text{a,evp,avg}}$ is the average air velocity in the evaporator duct, $A_{\text{evp,duct}}$ is the cross-sectional area of the evaporator duct, $v_{\text{a,evp,o}}$ is air specific volume at the evaporator outlet, $h_{\text{a,evp,in}}$ is the air specific enthalpy at the evaporator inlet and $h_{\text{a,evp,o}}$ is air specific enthalpy at the evaporator outlet.

5.1.2 Refrigerant mass flow rate (\dot{m}_{r})

The refrigerant mass flow rate is given by:

$$\dot{m}_{\text{r}} = \frac{\dot{Q}_{\text{evp}}}{(h_{\text{r,evp,o}} - h_{\text{r,evp,in}})} \quad (\text{kg/s}) \quad (5.2)$$

where $h_{\text{r,evp,in}}$ is the refrigerant specific enthalpy at the evaporator inlet and $h_{\text{r,evp,o}}$ is the refrigerant specific enthalpy at the evaporator outlet.

5.1.3 Condenser capacity (\dot{Q}_{cond})

The condenser capacity is calculated as follows:

$$\dot{Q}_{\text{cond}} = \rho_{\text{a,cond,in}} V_{\text{a,cond,avg}} A_{\text{cond,duct}} c_{\text{p,a,cond,in}} (T_{\text{a,cond,o}} - T_{\text{a,cond,in}}) \quad (5.3)$$

where $\rho_{\text{a,cond,in}}$ is air density at the condenser inlet, $V_{\text{a,cond,avg}}$ is the average air velocity at the condenser, $A_{\text{cond,duct}}$ is the area of condenser duct, $c_{\text{p,a,cond,in}}$ is the air specific heat at the condenser inlet, $T_{\text{a,cond,in}}$ is the air temperature at the condenser inlet and $T_{\text{a,cond,o}}$ is the air temperature at the condenser outlet.

5.1.4 Compressor power (\dot{W}_{comp})

The compressor power is calculated from the electrical energy given to the motor by considering a motor efficiency of 75% and belt transmission efficiency 90%.

$$\dot{W}_{\text{comp}} = \frac{\Delta E}{t} \eta_{\text{motor}} \eta_{\text{tran}} + \dot{Q}_{\text{loss}} \quad (\text{kW}) \quad (5.4)$$

where ΔE is the electrical power in kWh, t is time in hours, η_{motor} is the motor efficiency and η_{tran} is the transmission efficiency of the belt and pulley system. \dot{Q}_{loss} calculated from Eq. 5.24 is the heat loss from compressor shell due to friction.

5.1.5 Actual volumetric efficiency ($\eta_{\text{a,v}}$)

To actual volumetric efficiency is calculated from the following relation:

$$\eta_{\text{a,v}} = \frac{\dot{V}_{\text{s}}}{\dot{V}_{\text{disp}}} \quad (5.5)$$

where \dot{V}_{s} is the actual volume flow rate and \dot{V}_{disp} is the displacement volume flow rate of the compressor operating at the same speed. The clearance fraction r is calculated to be 1%, the bore and stroke of the compressor being 25 mm and 17 mm, respectively. The actual volumetric flow rate of the reciprocating compressor is less than the ideal isentropic flow rate due to pressure losses in suction and discharge valves, degree of superheat and leakage from compressor. Fig. 5.1 shows the actual suction and delivery of vapour on a pressure-volume diagram.

$$\dot{V}_{\text{s}} = \dot{m}_{\text{r}} v_{\text{s}} \quad (5.6)$$

$$\dot{V}_{\text{disp}} = V_{\text{disp}} \frac{N}{60} \quad (5.7)$$

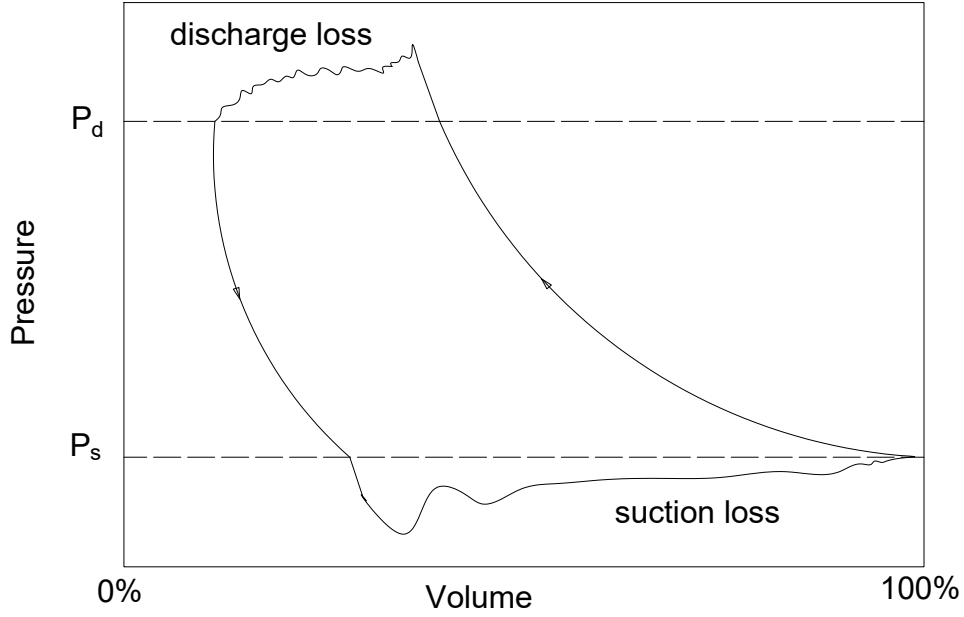


Figure 5.1: Actual pressure-volume diagram with pressure drop at the suction and discharge valves of compressor.

where N is the rotational speed in rpm and V_{disp} is the displacement volume given by:

$$V_{\text{disp}} = 2n \frac{\pi}{4} D_c^2 S_c \quad (5.8)$$

In the above relation n is the number of cylinders, D_c is the bore and S_c is the stroke.

The clearance volumetric efficiency is defined by:

$$\eta_{\text{cl}} = 1 - r \left[\frac{v_s}{v_{d,i}} - 1 \right] \quad (5.9)$$

where v_s is the specific volume at the suction and $v_{d,i}$ is the specific volume at discharge for an isentropic compression. The quantity f_v is the ratio of the actual volumetric efficiency to the clearance volumetric efficiency.

$$f(r_v) = \frac{\eta_{a,v}}{\eta_{\text{cl}}} \quad (5.10)$$

In the experimental procedure, the volume ratio r_v ($= v_s/v_d$, where v_d is the actual discharge specific volume) is obtained as the function of compressor speed N by a quadratic curve fit. Fig. 5.2 shows the experimental data in a graph of volume ratio versus compressor speed. The ratio of actual volumetric efficiency and clearance volumetric efficiency is obtained as a function of volume ratio by a linear curve fit from 72 experimental data points as shown in Fig. 5.3. The equations are as follows:

$$r_v = 2.5642 \times 10^{-06} N^2 - 1.7016 \times 10^{-03} N + 2.3171 \quad (5.11)$$

$$f(r_v) = 0.17763 r_v + 0.022188 \quad (5.12)$$

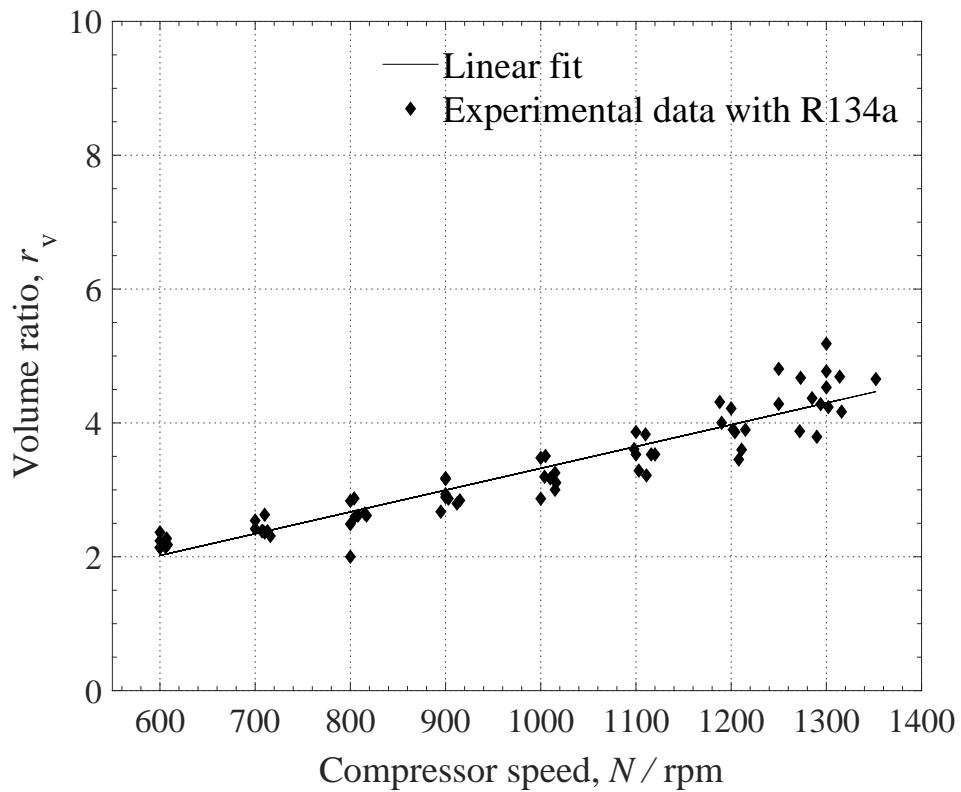


Figure 5.2: Volume ratio verse compressor speed.

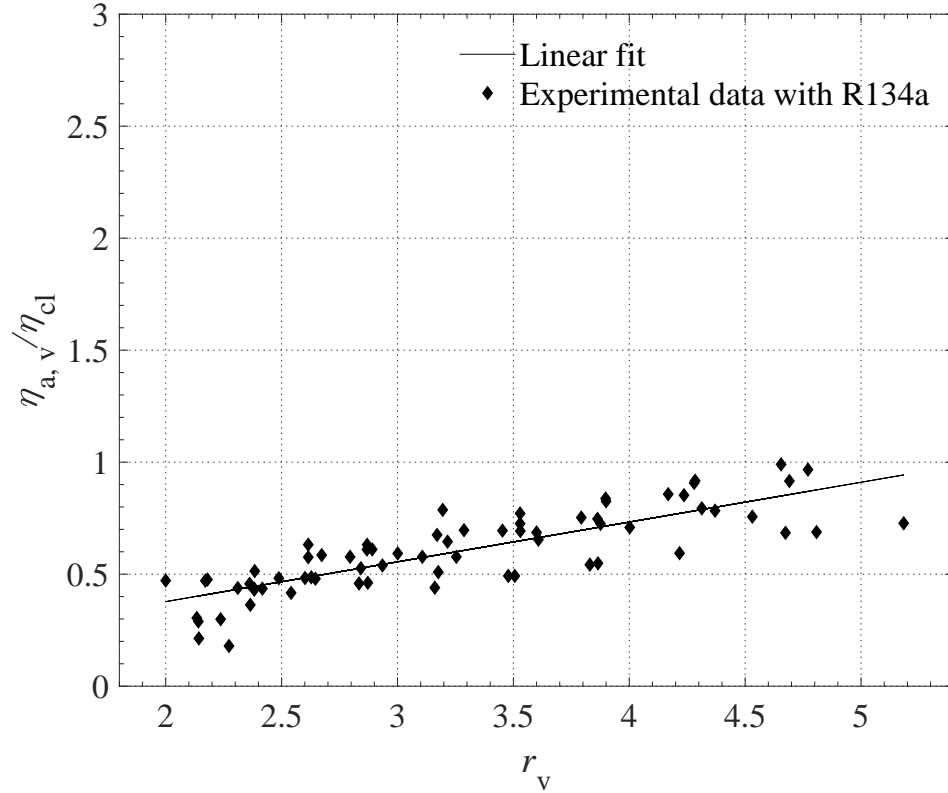


Figure 5.3: Efficiency ratio versus volume ratio.

5.1.6 Isentropic work efficiency ($\eta_{i,w}$)

The isentropic work efficiency is given by:

$$\eta_{i,w} = \frac{\Delta h_i}{\Delta h} \quad (5.13)$$

where Δh_i is the isentropic refrigerant enthalpy change and Δh is the actual enthalpy change across the compressor.

5.1.7 Heat loss from the compressor body due to friction (\dot{Q}_{loss})

Heat is generated due to friction in the ball bearings of the swash plate compressor. This heat is dissipated by mixed (i.e. combined natural and forced) convection and radiation heat transfer from the outer surface of the compressor into the surroundings. The compressor placed in the experimental facility is subjected to an air flow with a small velocity of 0.2 m/s in a vertically downward direction.

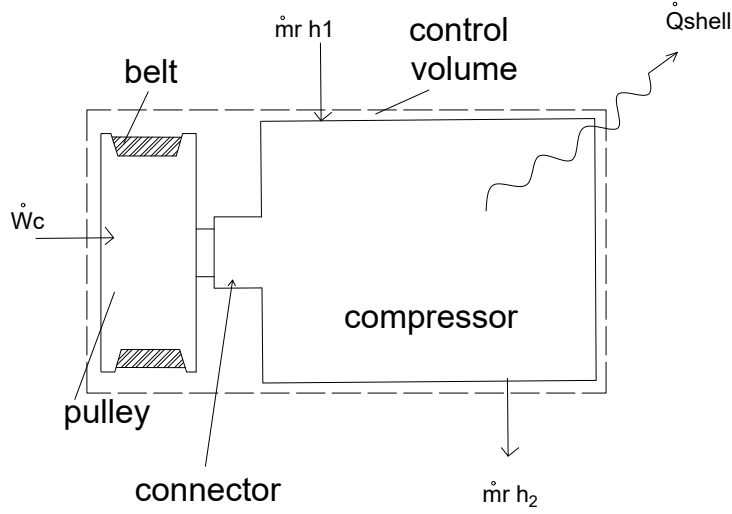


Figure 5.4: Energy balance for compressor.

However natural convection creates air motion in the upward direction. This may be called opposing mixed convection. The correlation of Chen and Armary [118] is used to find the mixed convection heat transfer for opposing flow. Fig. 5.4 shows the energy balance for compressor. \dot{W}_c is the actual work given to compressor and \dot{Q}_{loss} is the heat loss due to friction given out to surrounding. The area of heat transfer (A_{comp}) from compressor to the surroundings is the sum of the areas of the compressor cylinder, cylinder faces and the areas of pulley faces. The total area is calculated as:

$$A_{\text{comp}} = \pi D_{\text{comp}} L_{\text{comp}} + \frac{\pi}{4} D_{\text{comp}}^2 + \left[\frac{\pi}{4} D_{\text{comp}}^2 - \frac{\pi}{4} d_s^2 \right] + \pi d_s l_s + \frac{\pi}{2} D_{\text{pull}}^2 \quad (5.14)$$

where D_{comp} is the compressor diameter, L_{comp} is the compressor length, d_s diameter of connector, l_s is the length of connector and D_{pull} is the diameter of pulley.

For opposing flow, according to Chen and Armary's mixed convection Nusselt number based on the diameter of compressor is:

$$\left[\frac{Nu_d}{Nu_{dF}} \right]^{2.5} = 1 - \Omega^{2.5} \quad \text{if } \Omega < 0.7 \quad (5.15)$$

and

$$\frac{Nu_d}{Nu_{dF}} = 1.2 - \Omega - 0.2 \quad \text{if } \Omega > 0.7 \quad (5.16)$$

where

$$\Omega = \left[\frac{Gr_d}{Re_d^2} \right]^{1/4} \quad (5.17)$$

Nu_{dF} is the Nusselt number for forced convection given by:

$$Nu_{dF} = 0.464Re_d^2 + 0.0004Re_d \quad (5.18)$$

Gr_d is the Grashof number based on diameter given by:

$$Gr_d = \frac{g\beta(T_s - T_o)d^3}{\nu^2} \quad (5.19)$$

Re_d is the Reynolds number based on diameter given by:

$$Re_d = \frac{u d}{\nu} \quad (5.20)$$

The heat transfer coefficient for mixed convection is

$$h_{\text{mix}} = \frac{Nu_d k_a}{d} \quad (5.21)$$

The heat lost due to mixed convection is

$$\dot{Q}_{\text{mix}} = h_{\text{mix}} A_{\text{comp}} (T_s - T_o) \quad (5.22)$$

Heat lost by radiation from compressor to surrounding surfaces (assumed to be at T_o) is:

$$\dot{Q}_{\text{rad}} = \sigma \epsilon A_{\text{comp}} (T_s^4 - T_o^4) \quad (5.23)$$

The total heat lost is

$$\dot{Q}_{\text{loss}} = \dot{Q}_{\text{mix}} + \dot{Q}_{\text{rad}} \quad (5.24)$$

The tests are conducted for different operating conditions. The three operating parameters considered here are the inlet air temperature of condenser $T_{a,cond,in}$, inlet air velocity of condenser $V_{a,cond,in}$ and compressor rotational speed N . The operating conditions are given in Table 5.1.

Table 5.1: Range of operating variable

Operating Variable	Range	Step
N	600 rpm to 1400 rpm	100 rpm
$T_{a,cond,in}$	26°C to 34°C	2°C
$V_{a,cond,in}$	1 m/s to 1.5 m/s	0.1 m/s

After changing any operating variable, the system was run for several minutes (more than 15 minutes) to attain steady state. A total of 72 tests are conducted to cover the required parametric space. The results of experiments and simulation are shown in tabular form in Appendix A. The following are the results obtained for different conditions in graphical form. The plots shows the comparison between experimental and simulated data for R134a and R1234yf. Simulation results of both R134a and R1234yf showed that the performance variable of AACCS were different values. The difference in these variable are occurs due to different thermodynamic and transport properties values. Also the latent heat of vaporization of R1234yf is lesser than that of R134a. The percentage difference between the experimental and simulation results is defined as:

$$\text{Percentage difference} = \frac{\text{Experimental value} - \text{Numerical value}}{\text{Experimental value}} \times 100 \quad (5.25)$$

5.2 Volume ratio (r_v)

The volume ratio is the ratio of specific volumes at the compressor inlet and outlet. The variation of volume ratio with compressor speed at different air temperatures and velocities are plotted. Figs. 5.5, 5.6, 5.7 and Fig. 5.8 show the variation of volume ratio (r_v) with compressor speed (N) at different air temperatures and velocities. It is observed in each plot that the volume ratio increases with compressor speed and that this is true both in the case of experimental and simulated data. As compared with experimental values, the simulation values for R134a show a minimum of 0.03% and a maximum of 1.5% deviation and for R1234yf these figures are a minimum of 0.02% and a

maximum of 6%. The comparison of simulation data with R134a and R1234yf shows a maximum of 5% deviation. It is observed that at higher values of N there is more deviation. At higher speeds there will be more frictional heat due to the motion of the pistons in the cylinders. The higher deviation at higher speeds could be due to higher heating due to frictional heat, of the suction vapour reaching the suction of valve of the compressor. The values of percentage difference are presented in Table A.23 in the Appendix A .

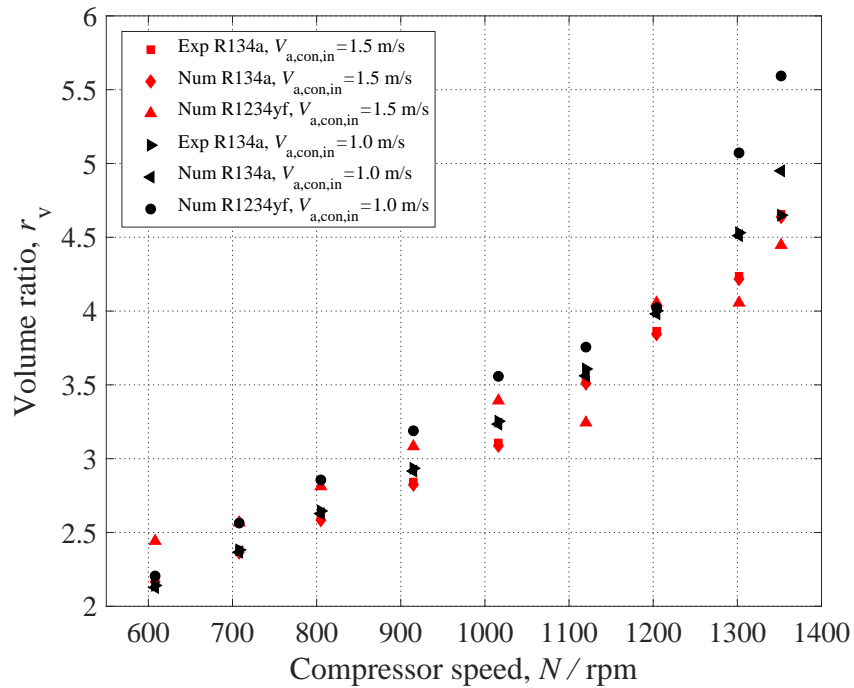


Figure 5.5: Variation of volume ratio with compressor speed for $T_{a,cond,in} = 26$ °C

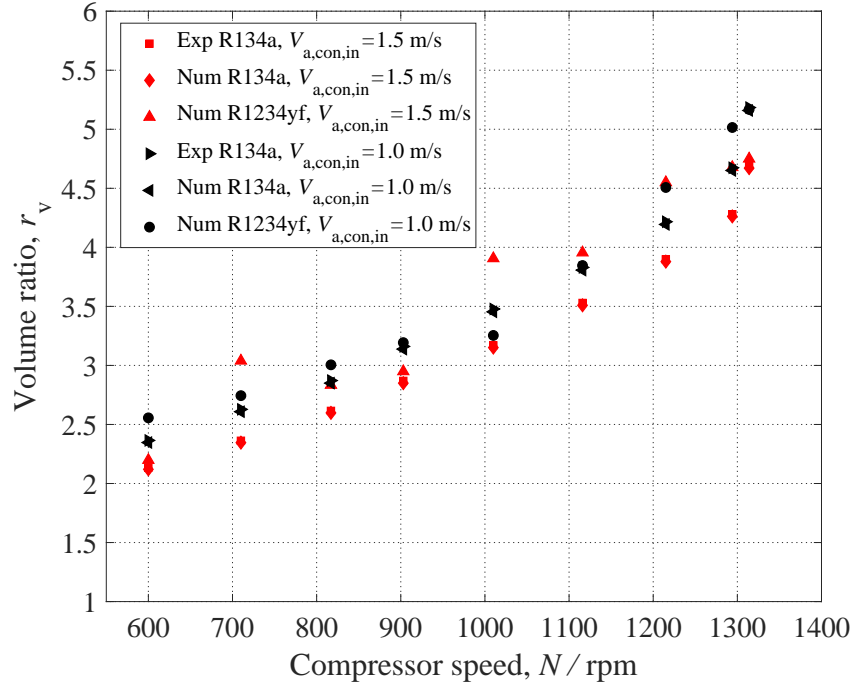


Figure 5.6: Variation of volume ratio with compressor speed for $T_{a,cond,in} = 28\text{ °C}$

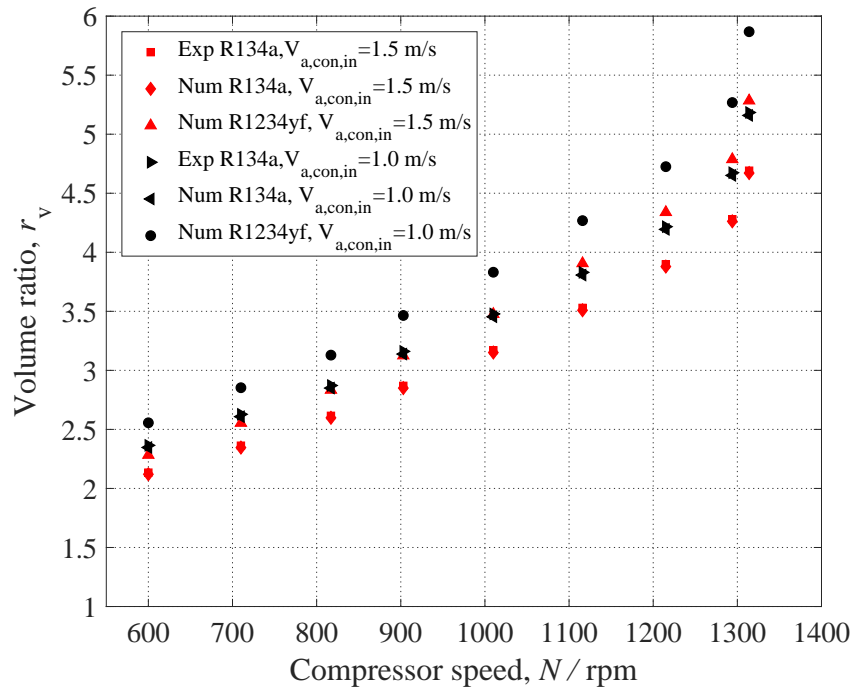


Figure 5.7: Variation of volume ratio with compressor speed for $T_{a,cond,in} = 30\text{ °C}$

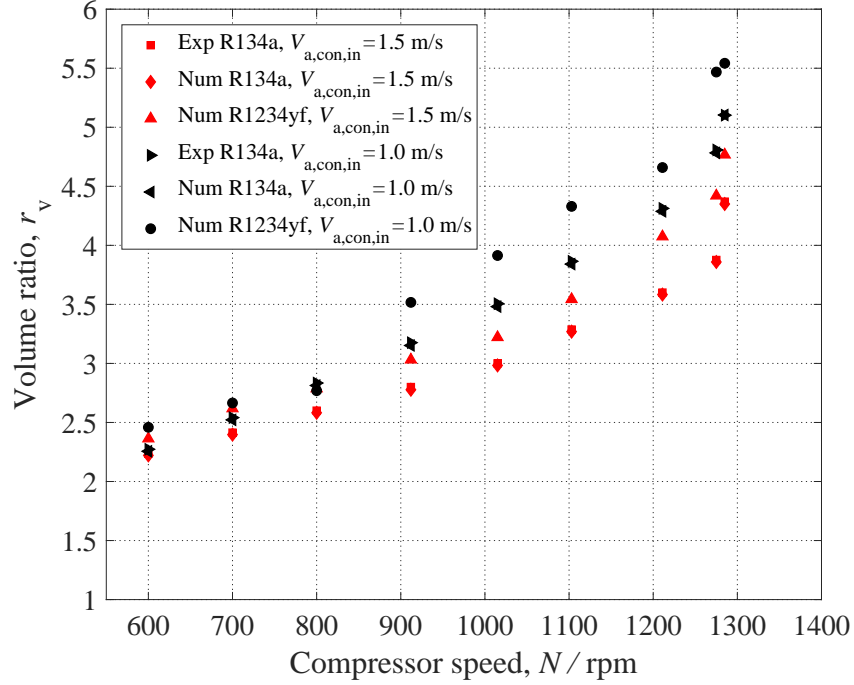


Figure 5.8: Variation of volume ratio with compressor speed for $T_{a,cond,in} = 34$ °C

5.3 Pressure ratio (r_p)

The pressure ratio is the ratio of the absolute pressure at compressor outlet to that at the inlet. Figs. 5.9, 5.10, 5.11 and Fig. 5.12 show the variation of pressure ratio (r_p) with compressor speed (N) at different condenser air temperatures and velocities. It is observed in each plot that the pressure ratio increases with compressor speed both in the case of experiment and simulation. As compared with experimental values, the simulation values for R134a show a maximum of 1% deviation. For R1234yf the maximum deviation is 5%. Comparison between of the simulation data with R134a and R1234yf shows a minimum of 1% and a maximum of 8% deviation. As in the case of volume ratio, at higher value of N , the deviation is higher.

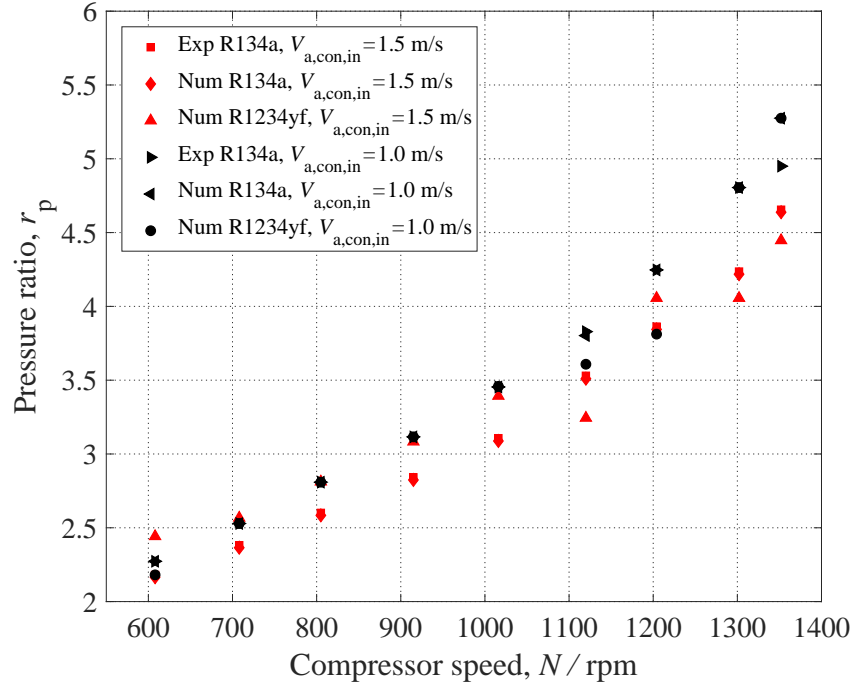


Figure 5.9: Variation of pressure ratio with compressor speed for $T_{a,cond,in} = 26 \text{ }^\circ\text{C}$

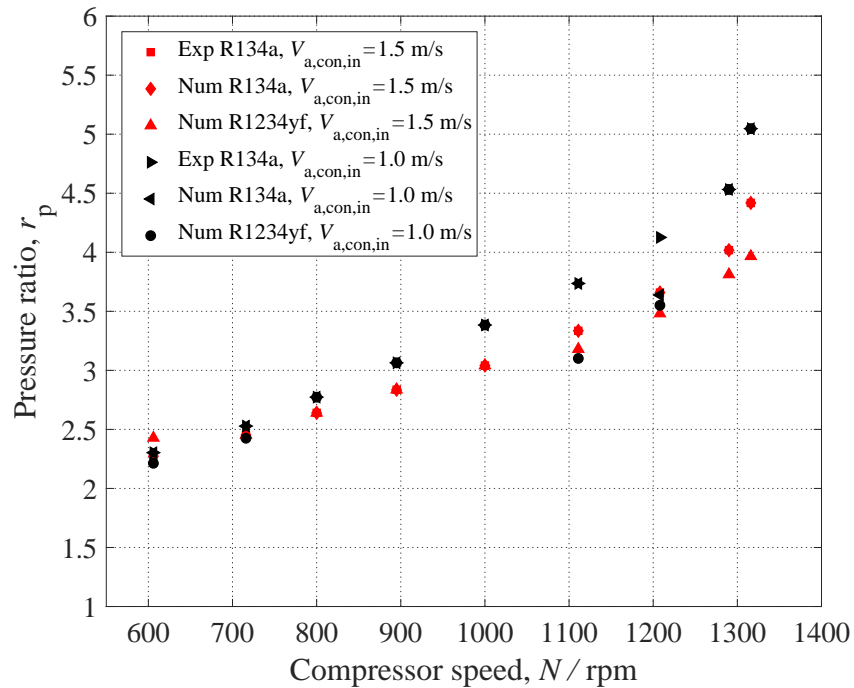


Figure 5.10: Variation of pressure ratio with compressor speed for $T_{a,cond,in} = 28 \text{ }^\circ\text{C}$

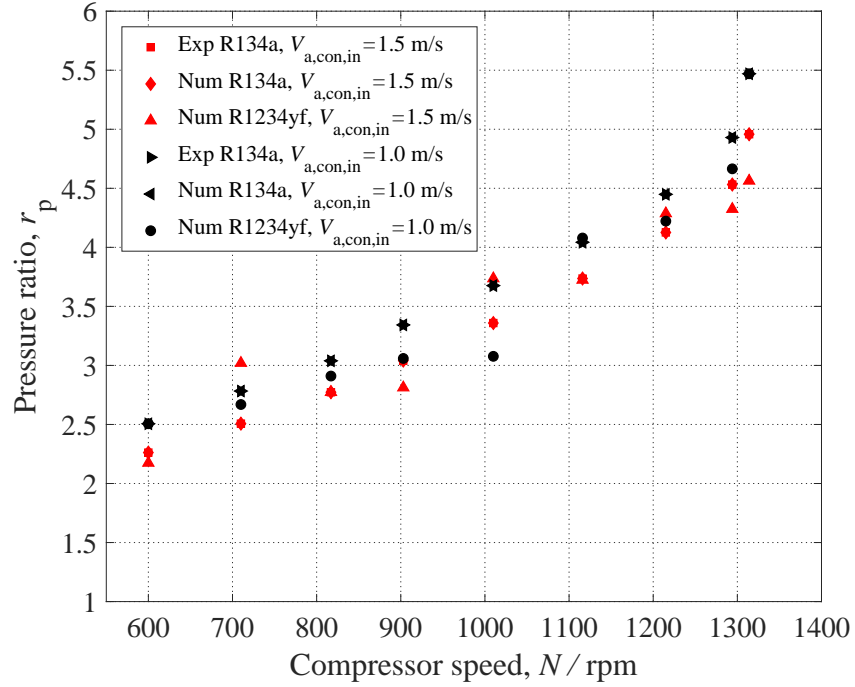


Figure 5.11: Variation of pressure ratio with compressor speed for $T_{a,cond,in} = 30$ °C

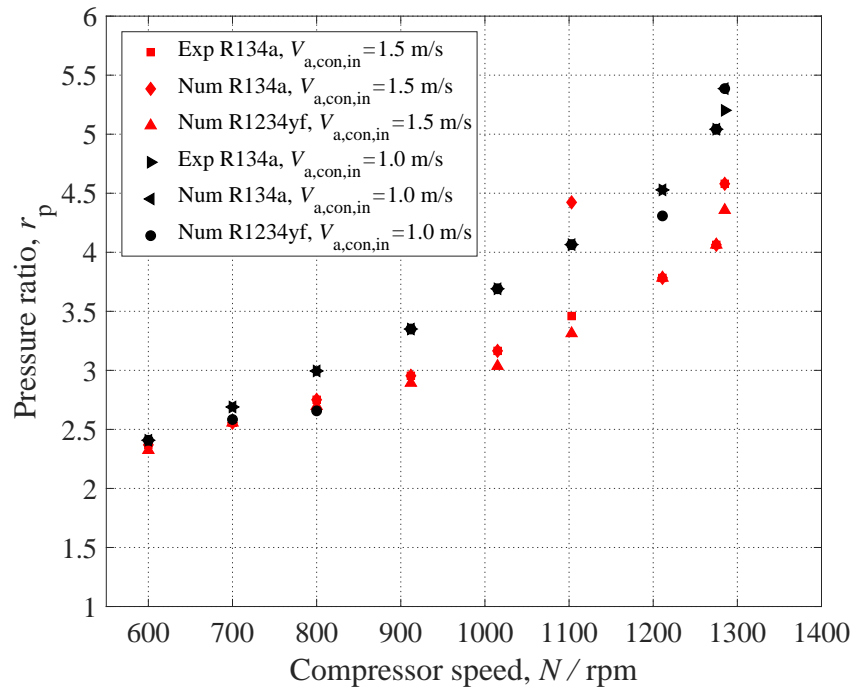


Figure 5.12: Variation of pressure ratio with compressor speed for $T_{a,cond,in} = 34$ °C

5.4 Refrigerant mass flow rate (\dot{m}_r)

The variation of mass flow rate (\dot{m}_r) with compressor speed at different condenser air temperatures and velocities is shown in Figs. 5.13, 5.14, 5.15 and Fig. 5.16. It is observed that mass flow rate increases with compressor speed in the experiments and simulation calculations. Compared with the experimental values, the simulation values for R134a show deviations in the range 0.2% to 10%. For R1234yf the deviations are in the range of 1.% to 17%. Comparison between R134a and R1234yf simulation data reveals a minimum of 1% and a maximum of 10% deviation. It is observed that at lower values of N there is less deviation between experiment and numerical results as compared to higher values of N .

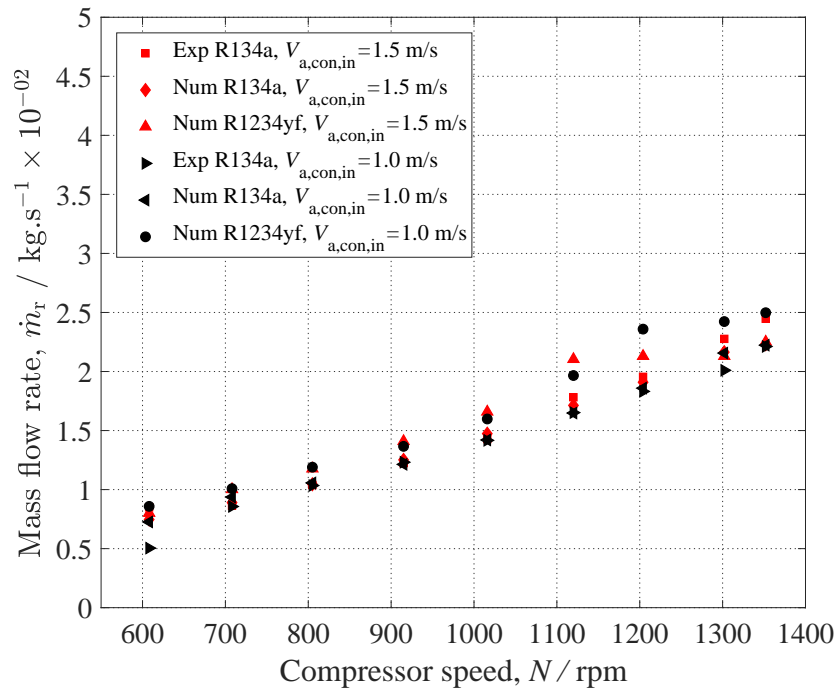


Figure 5.13: Variation of refrigerant mass flow rate with compressor speed for $T_{a,\text{cond},\text{in}} = 26 \text{ }^\circ\text{C}$

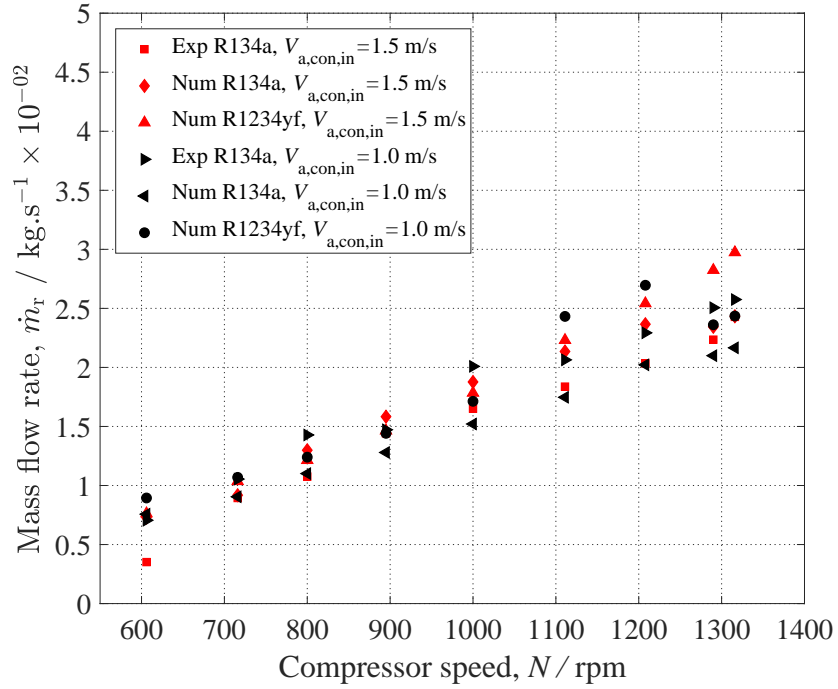


Figure 5.14: Variation of refrigerant mass flow rate with compressor speed for $T_{a,\text{cond},\text{in}} = 28 \text{ }^\circ\text{C}$

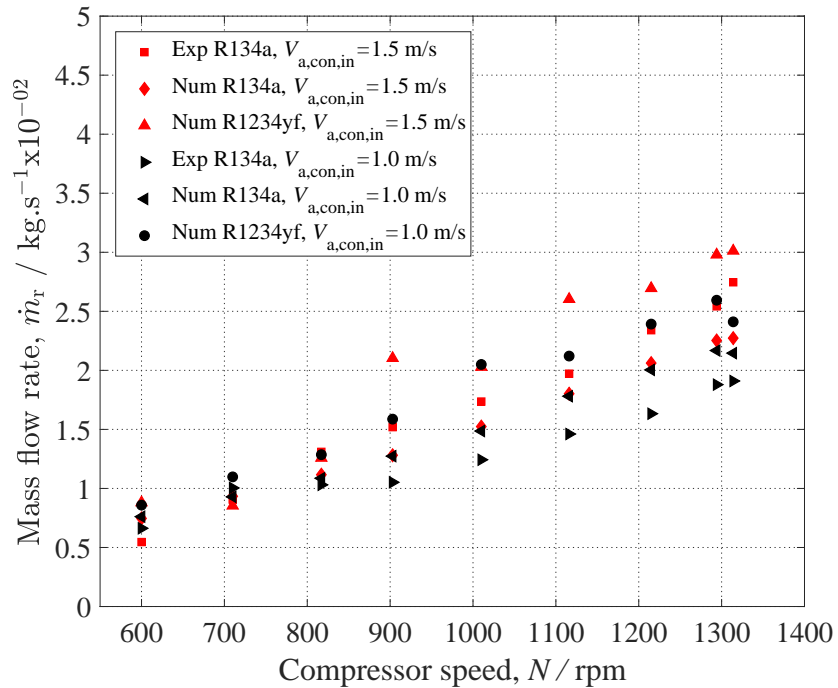


Figure 5.15: Variation of refrigerant mass flow rate with compressor speed for $T_{a,\text{cond},\text{in}} = 30 \text{ }^\circ\text{C}$

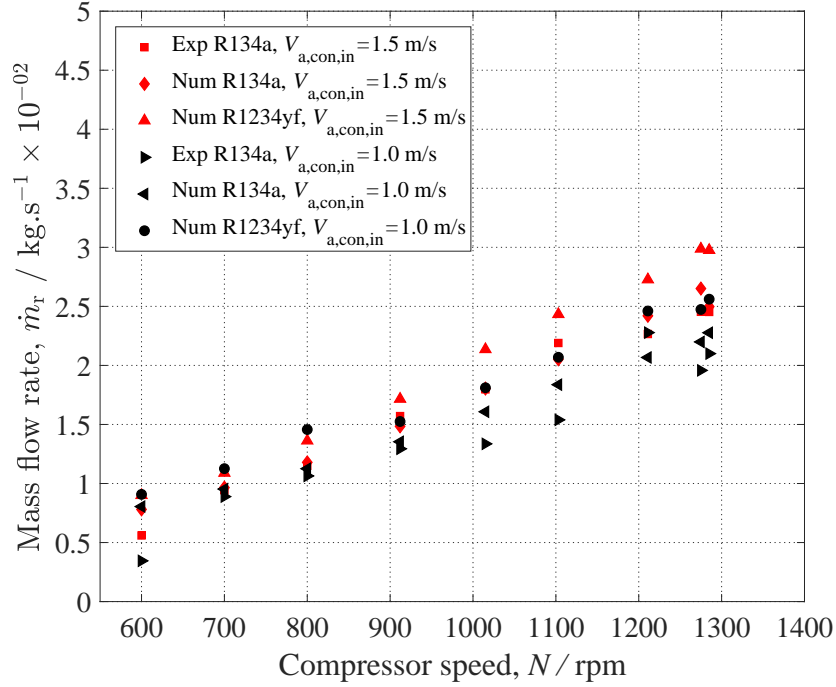


Figure 5.16: Variation of refrigerant mass flow rate with compressor speed for $T_{a,cond,in} = 34$ °C

5.5 Actual volumetric efficiency ($\eta_{a,v}$)

The variation of actual volumetric efficiency ($\eta_{a,v}$) with compressor speed at different air temperature and velocity are plot here. Fig. 5.17, 5.18, 5.19 and Fig. 5.20 are shows the variation of actual volumetric efficiency, ($\eta_{a,v}$) with compressor speed (N) at different air temperature and velocity. It is observed in each plot that actual volumetric efficiency is increase with compressor speed in experiment and simulation calculations. As compared with experimental values the simulation values for R134a shows minimum 0.1 % & maximum 10 % deviation and for R1234yf shows minimum 2 % & maximum 9 % deviation. The comparison between both simulation with R134a and R1234yf data shows minimum 1 % & maximum 10 % deviation. It is observed that at lower values of N shows less deviation between experiment and numerical results as compared to higher values of N .

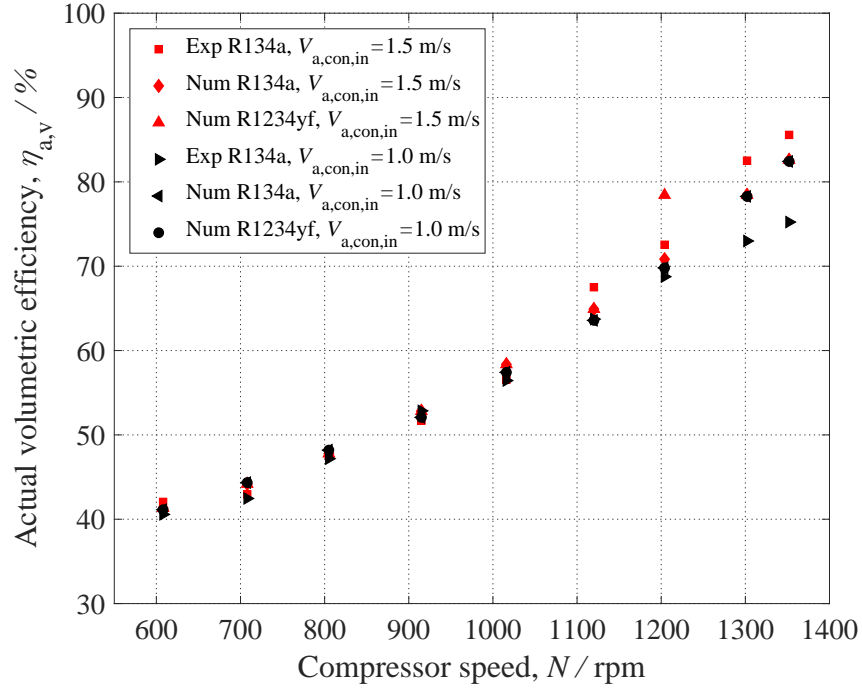


Figure 5.17: Variation of actual volumetric efficiency with compressor speed for $T_{a,cond,in} = 26$ °C

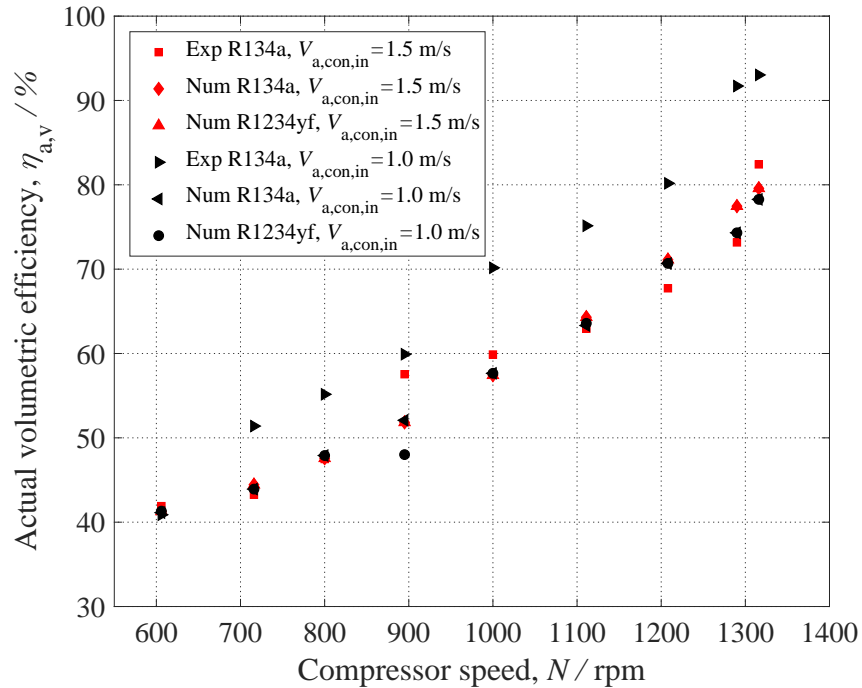


Figure 5.18: Variation of actual volumetric efficiency with compressor speed for $T_{a,cond,in} = 28$ °C

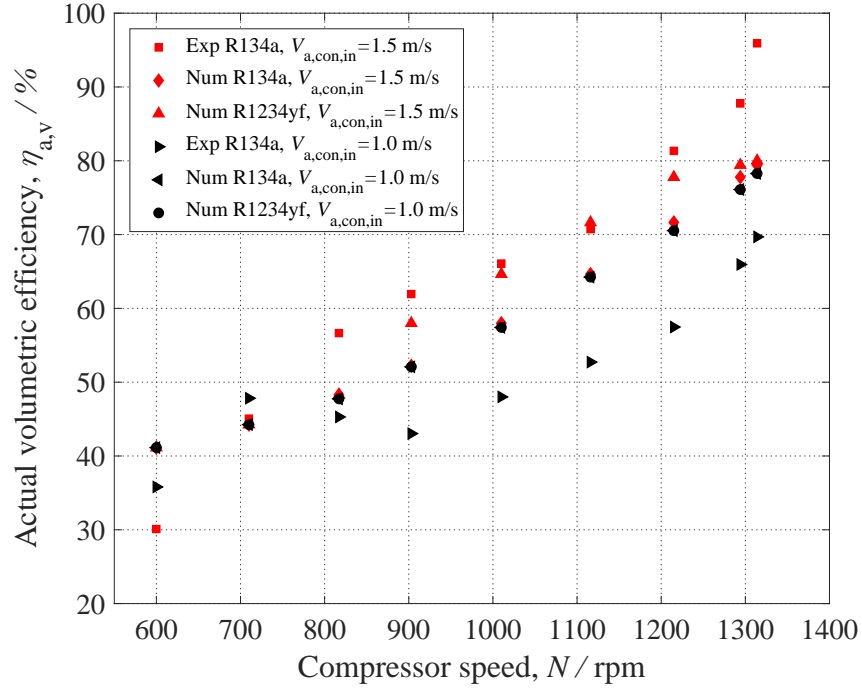


Figure 5.19: Variation of actual volumetric efficiency with compressor speed for $T_{a,cond,in} = 30\text{ }^\circ\text{C}$

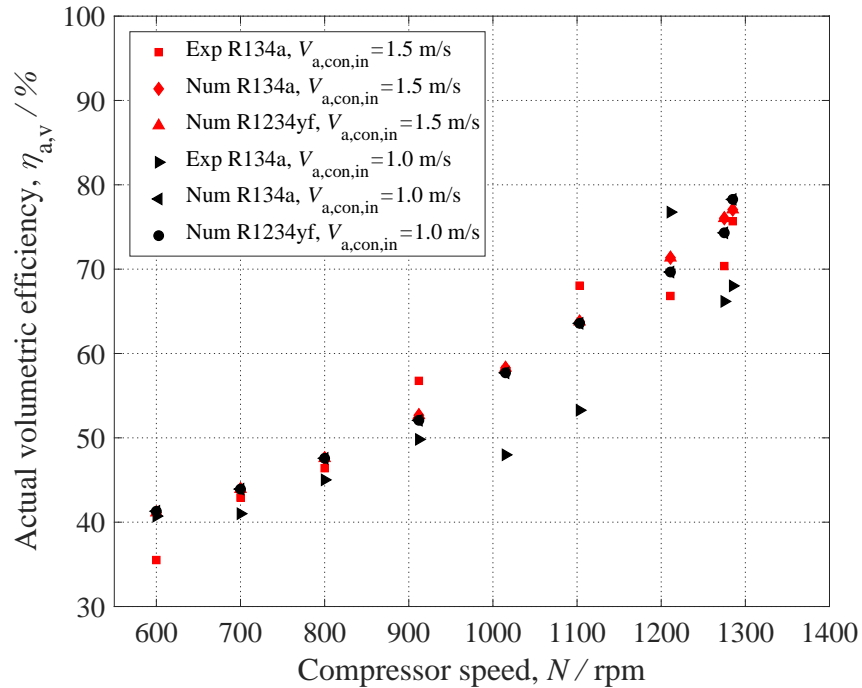


Figure 5.20: Variation of actual volumetric efficiency with compressor speed for $T_{a,cond,in} = 34\text{ }^\circ\text{C}$

5.6 Isentropic work efficiency ($\eta_{i,w}$)

The variation of isentropic work efficiency ($\eta_{i,w}$) with compressor speed is plotted in Figs. 5.21, 5.22, 5.23 and Fig. 5.24. It is observed that actual volumetric efficiency is not very much sensitive to compressor speed and this is true both in the case of experimental and simulation results. The values are in the range of 90% to 95% for almost all the operating conditions. As compared with experimental values the simulation values for R134a show a maximum of 6% deviation and those for R1234yf also show a maximum of 6% deviation. The comparison between both simulation data with R134a and R1234yf data shows a maximum of 2% deviation.

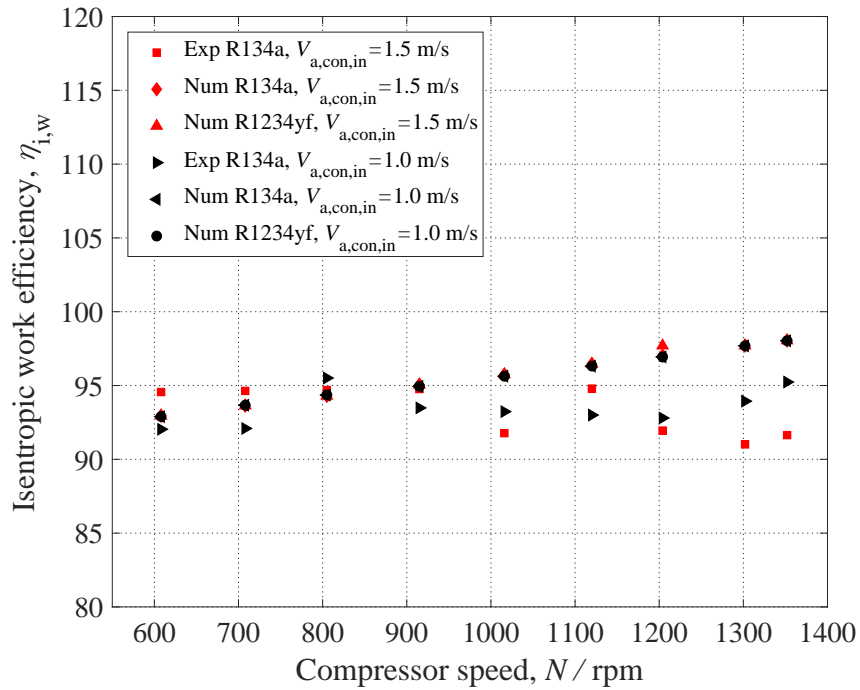


Figure 5.21: Variation of Isentropic work efficiency with compressor speed for $T_{a,cond,in} = 26$ °C

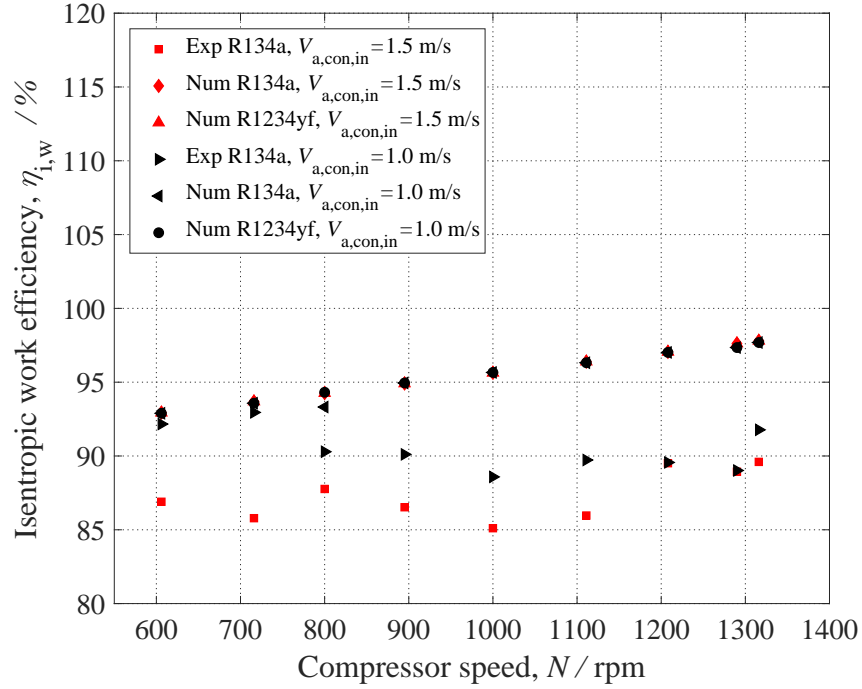


Figure 5.22: Variation of Isentropic work efficiency with compressor speed for $T_{a,cond,in} = 28 \text{ }^\circ\text{C}$

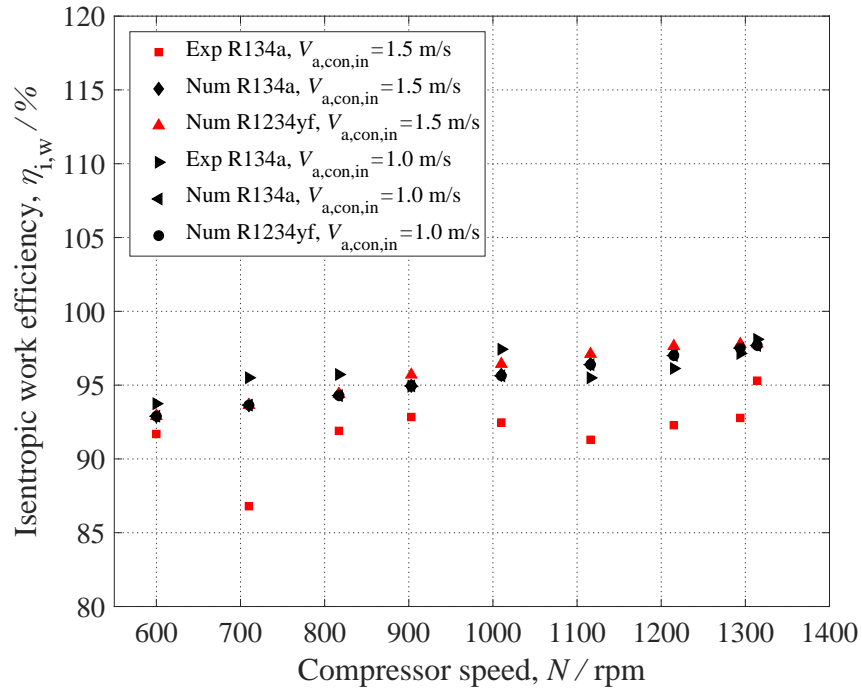


Figure 5.23: Variation of Isentropic work efficiency with compressor speed for $T_{a,cond,in} = 30 \text{ }^\circ\text{C}$

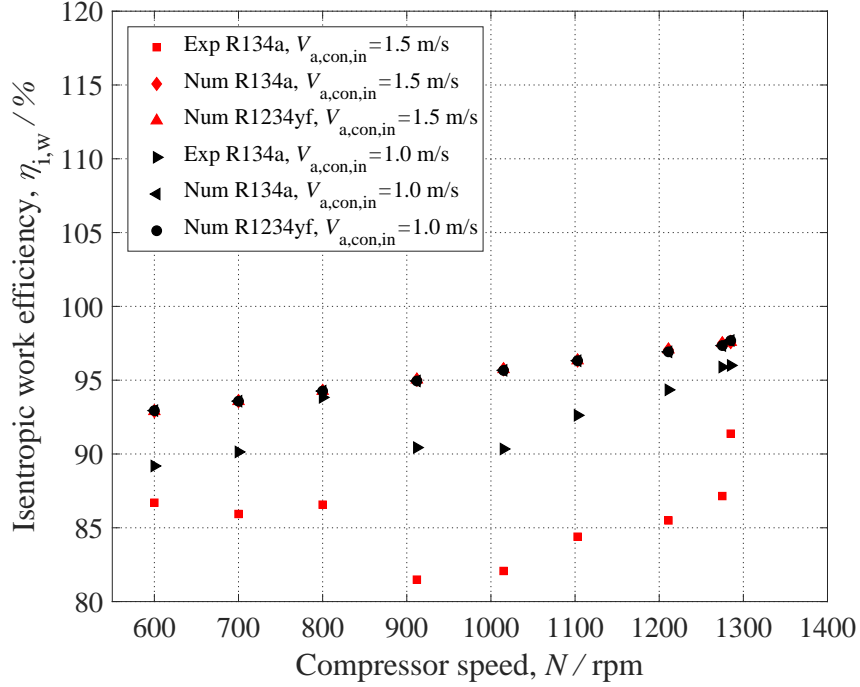


Figure 5.24: Variation of Isentropic work efficiency with compressor speed for $T_{a,cond,in} = 34$ °C

5.7 Compressor heat loss (\dot{Q}_{loss})

There is small amount of heat loss to surrounding from the compressor body. In the present work, the compressor is a small capacity component designed for 82 cc. It is observed that due to internal friction between piston, cylinder and other moving parts of compressor, heat is dissipated from the compressor body to the surroundings. The variation of compressor heat loss (\dot{Q}_{loss}) with compressor speed at different condenser air temperatures and velocities is shown in Figs. 5.25, 5.26, 5.27 and Fig. 5.28. It is seen in experimental and simulation results that compressor heat loss shows a small rise with compressor speed. The values are in the range of 30 W to 40 W. As compared with experimental values the simulation values for R134a show a minimum of 0.1% and a maximum of 10% deviation and for R1234yf, the deviation is in the range 0.1% to 10% deviation. The comparison between simulations with R134a and R1234yf shows a maximum of 2% deviation.

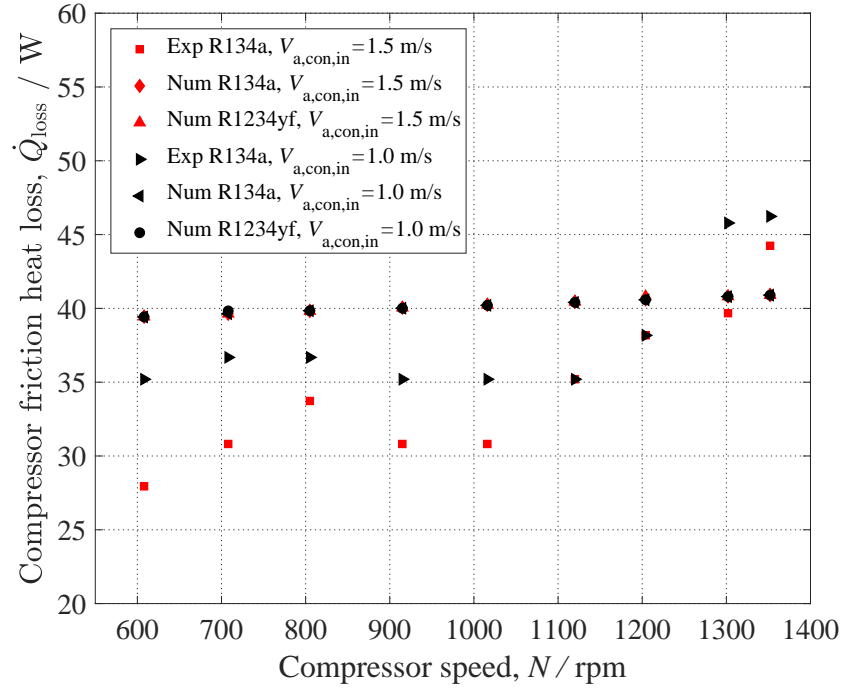


Figure 5.25: Variation of compressor friction loss with compressor speed for $T_{a,\text{cond},\text{in}} = 26$ °C

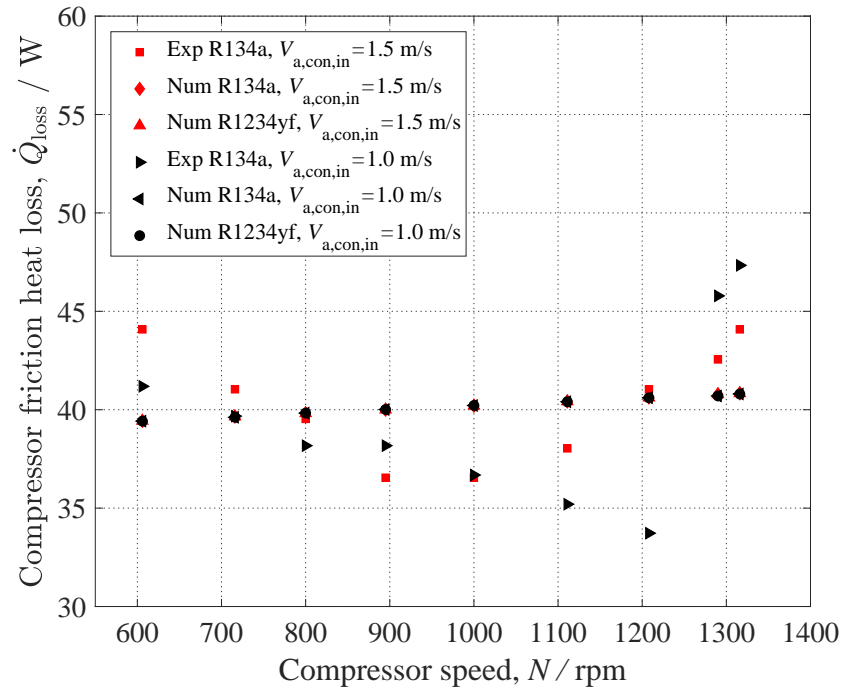


Figure 5.26: Variation of compressor friction loss with compressor speed for $T_{a,\text{cond},\text{in}} = 28$ °C

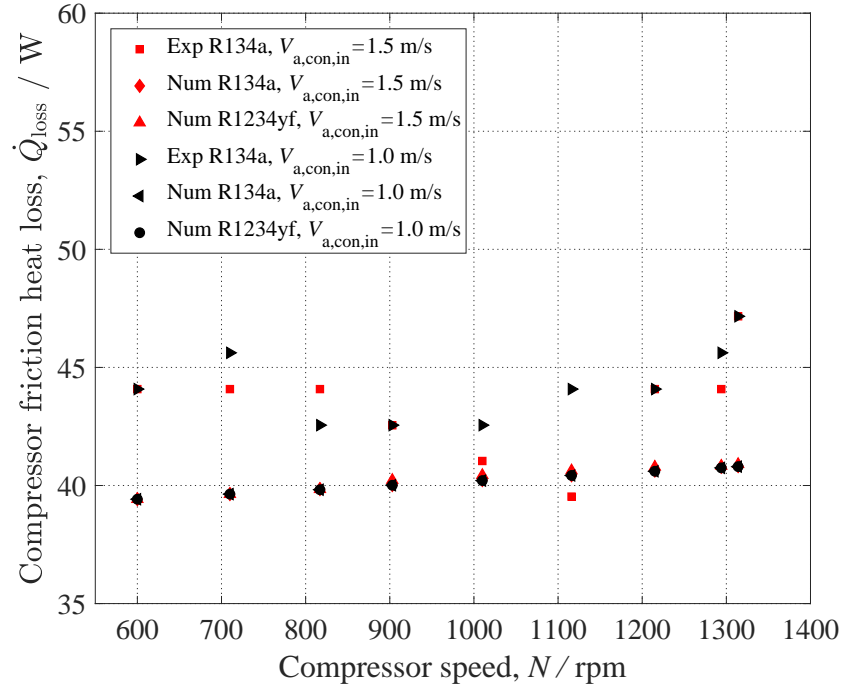


Figure 5.27: Variation of compressor friction loss with compressor speed for $T_{a,cond,in} = 30 \text{ }^\circ\text{C}$

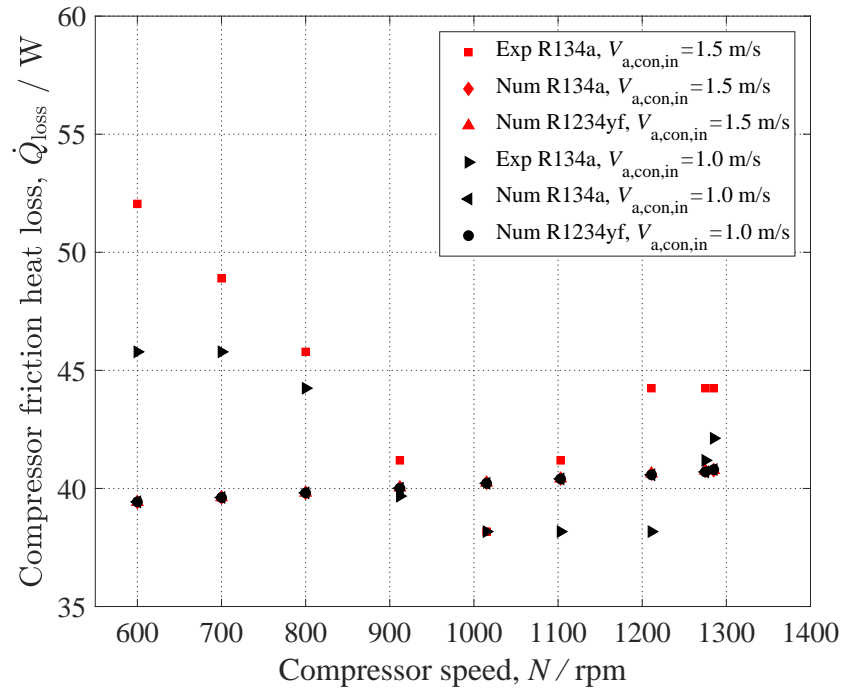


Figure 5.28: Variation of compressor friction loss with compressor speed for $T_{a,cond,in} = 34 \text{ }^\circ\text{C}$

5.8 Compressor work(\dot{W}_{comp})

The variation of compressor work (\dot{W}_{comp}) with compressor speed for various condenser inlet air temperatures and velocities is shown in Figs. 5.29, 5.30, 5.31, 5.32 and Fig. 5.33. From these graphs it is observed that compressor work is not much dependent on condenser air velocity and temperature but shows major variation with compressor speed. It increases with compressor speed in the case of experiments as well as numerical calculations. At lower compressor speed, the numerical values of compressor work are very close to the experiment values. At higher values of compressor speed, the numerical values of compressor work show a slight variation with experimental values. Compared with experimental values, the simulation values differ by 4-28% for R134a and 5-30% for R1234yf. Simulation results of R134a and R1234yf show minimum 1-10% deviation.

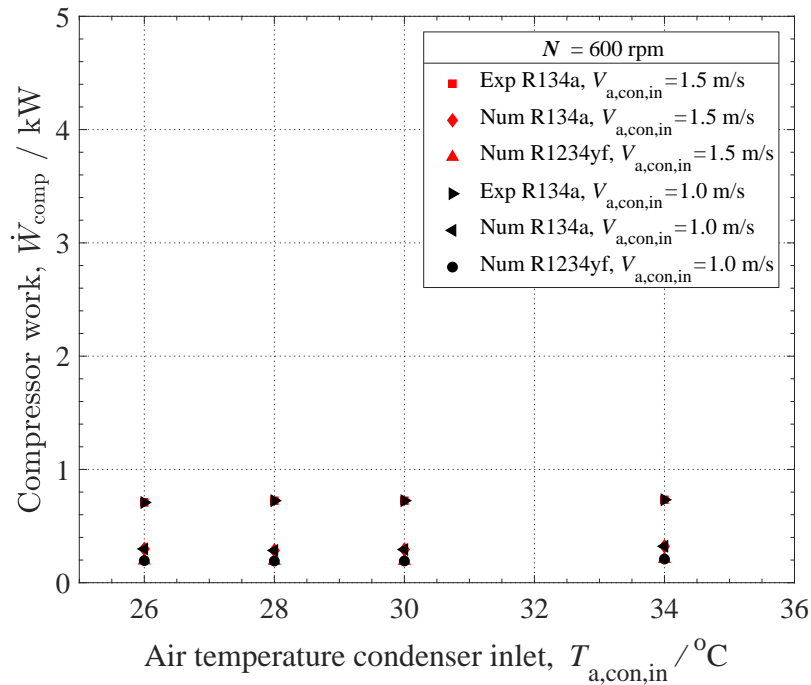


Figure 5.29: Variation of compressor work with air temperature condenser inlet for $N = 600 \text{ rpm}$

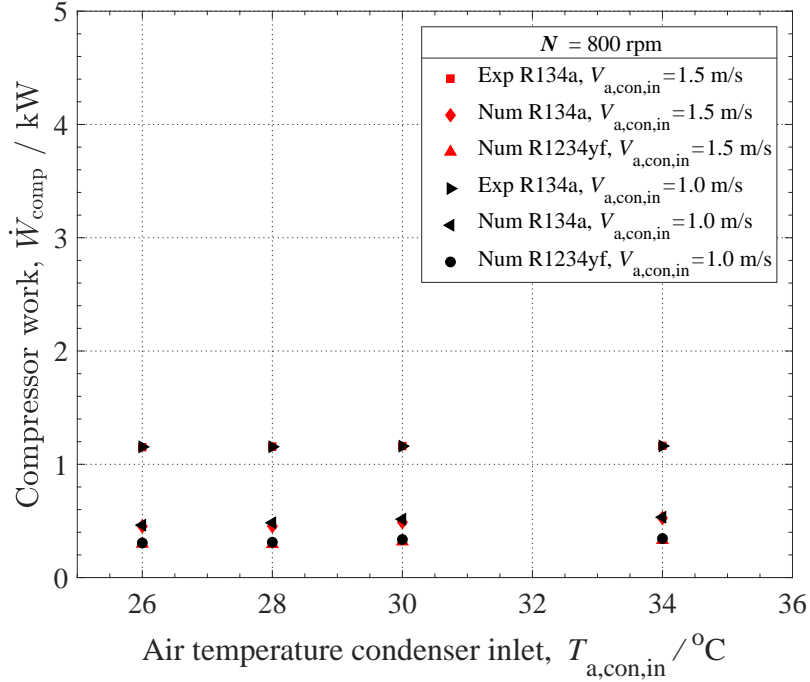


Figure 5.30: Variation of compressor work with air temperature condenser inlet for $N = 800$ rpm

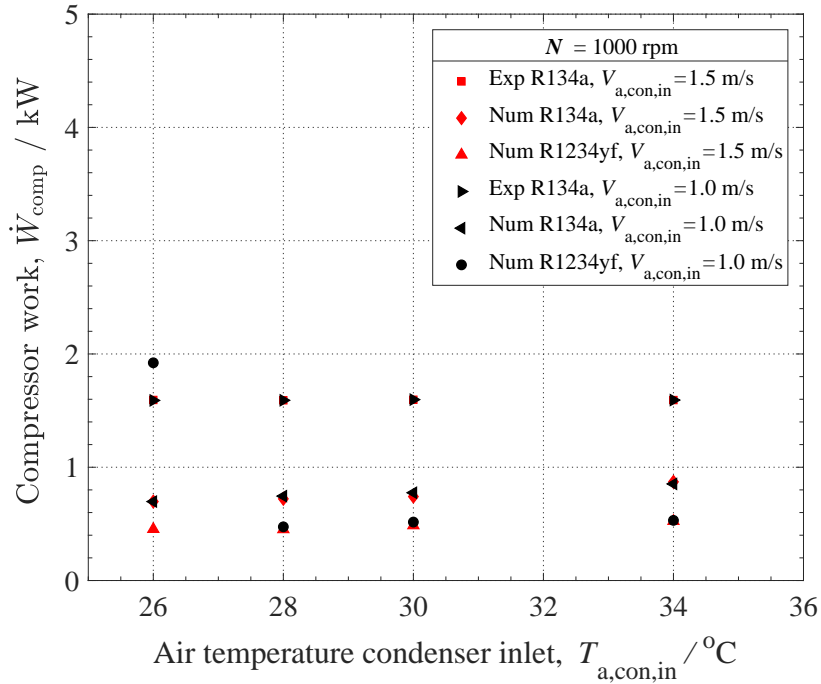


Figure 5.31: Variation of compressor work with air temperature condenser inlet for $N = 1000$ rpm

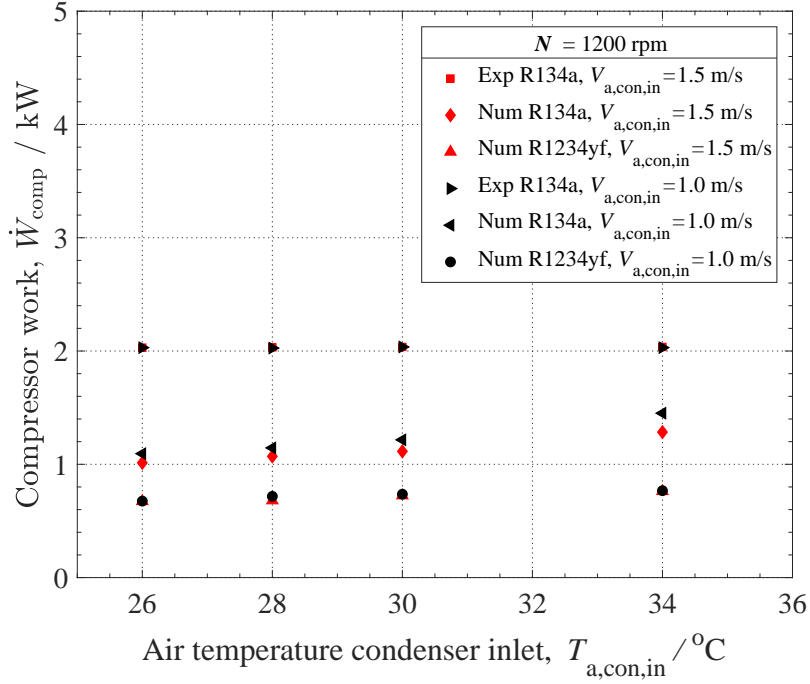


Figure 5.32: Variation of compressor work with air temperature condenser inlet for $N = 1200$ rpm

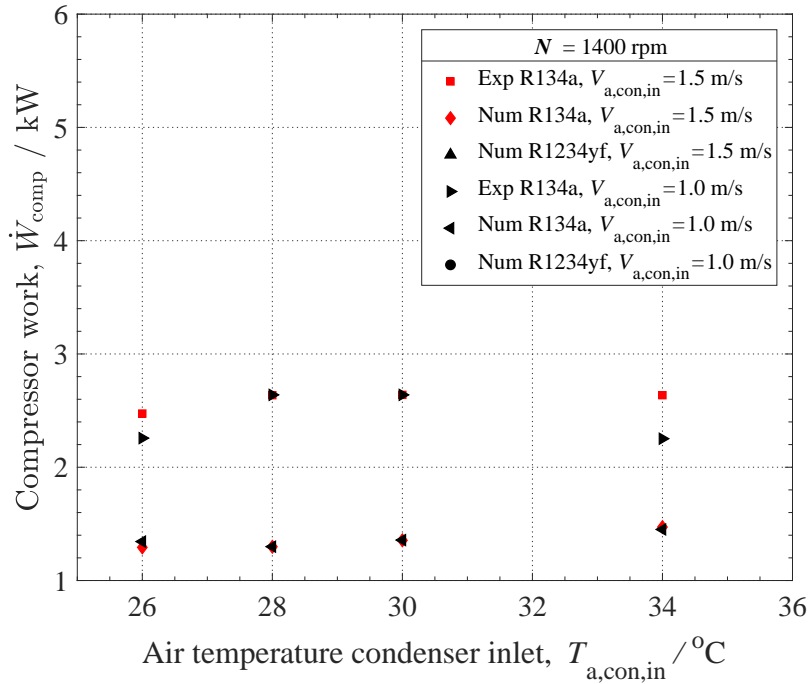


Figure 5.33: Variation of compressor work with air temperature condenser inlet for $N = 1400$ rpm

5.9 Condenser capacity (\dot{Q}_{cond})

The variation of condenser capacity (\dot{Q}_{cond}) with compressor speed is depicted in Figs. 5.34, 5.35, 5.36, 5.37 and Fig. 5.38. The condenser capacity is dependent on air velocity and inlet air temperature but shows a major variation with compressor speed due to change in mass flow rate of the refrigerant. It is observed that condenser capacity is higher at 1.5 m/s velocity and lower at 1.0 m/s in the case of both numerical and experimental results. Also at lower compressor speed, the comparison between the experimental and numerical results is more favourable as compared to higher speeds. As compared with experimental values the simulation values for R134a show a minimum of 4% and a maximum of 25% deviation and for R1234yf, the deviation is a minimum of 5% and a maximum of 30%. The comparison between simulations with R134a and R1234yf shows 1-10% deviation.

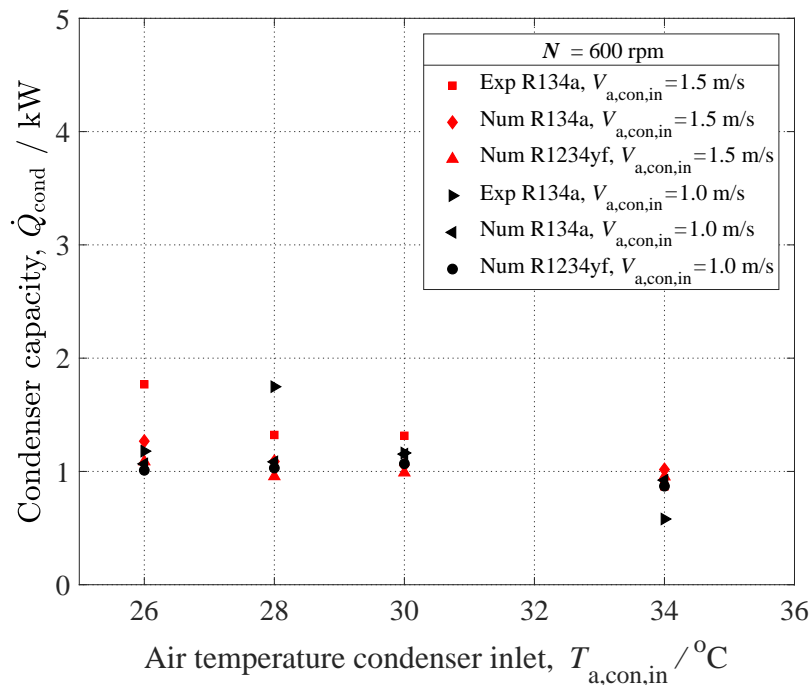


Figure 5.34: Variation of condenser capacity with air temperature condenser inlet for $N = 600$ rpm

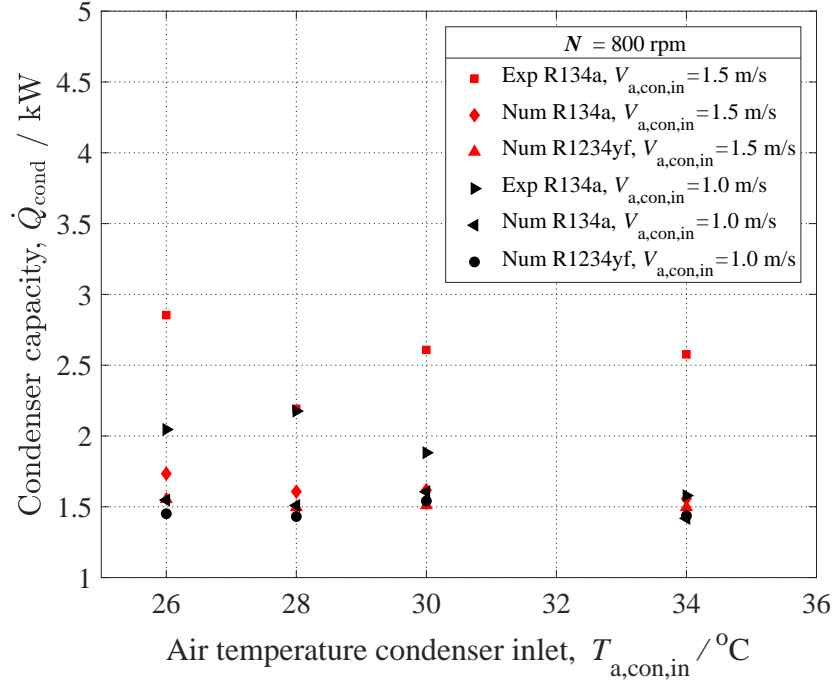


Figure 5.35: Variation of condenser capacity with air temperature condenser inlet for $N = 800$ rpm

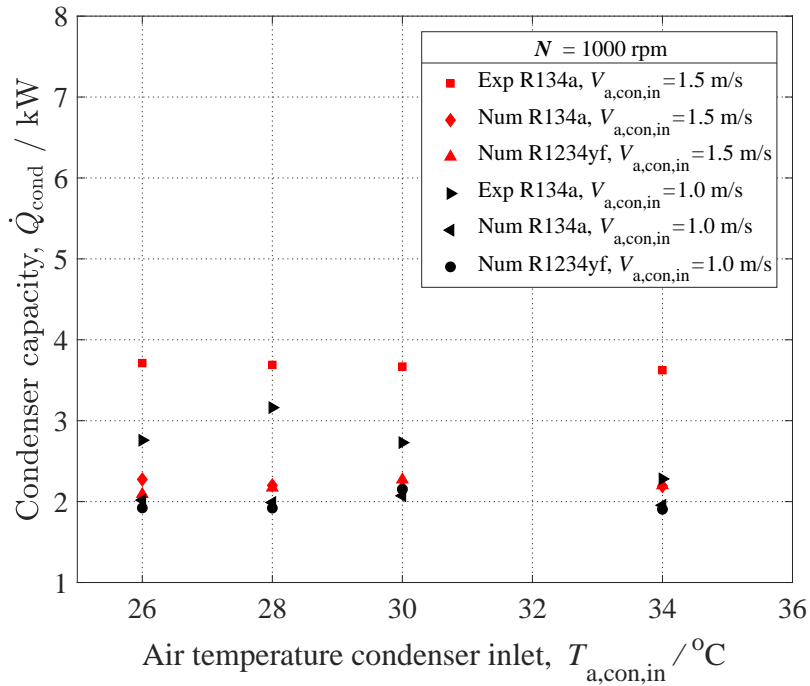


Figure 5.36: Variation of condenser capacity with air temperature condenser inlet for $N = 1000$ rpm

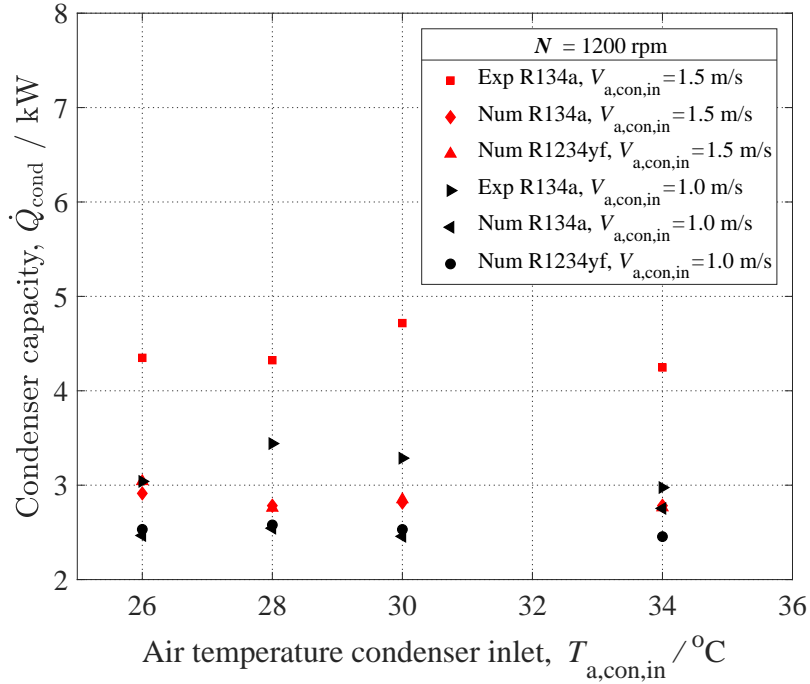


Figure 5.37: Variation of condenser capacity with air temperature condenser inlet for $N = 1200$ rpm

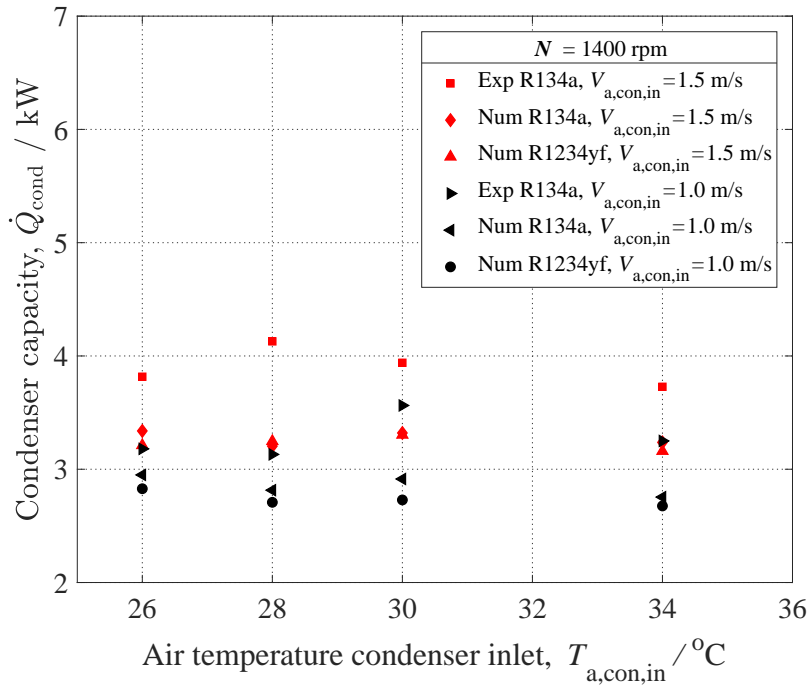


Figure 5.38: Variation of condenser capacity with air temperature condenser inlet for $N = 1400$ rpm

5.10 Evaporator capacity (\dot{Q}_{evp})

The variation of evaporator capacity (\dot{Q}_{evp}) with compressor speed at various condenser air velocities and air inlet temperatures is presented in Figs. 5.39, 5.40, 5.41, 5.42 and Fig. 5.43. It is observed that evaporator capacity decreases with increasing condenser air inlet temperature and increases with condenser air velocity. Compressor speed has a major effect on evaporator capacity due to change in the mass flow rate of refrigerant. It can be seen that the condenser capacity is higher at 1.5 m/s velocity and lower at 1.0 m/s for both numerical and experiment calculations. At lower compressor speed, the agreement between experimental and numerical results is better as compared to higher speeds. Experimental R134a results found to deviate by 3-30% compared to simulation results. Similarly the deviation between experimental and simulated results in the case of R1234yf is in the range of 4-35%. The comparison between simulations with R134a and R1234yf shows a minimum of 1% and a maximum of 10% deviation.

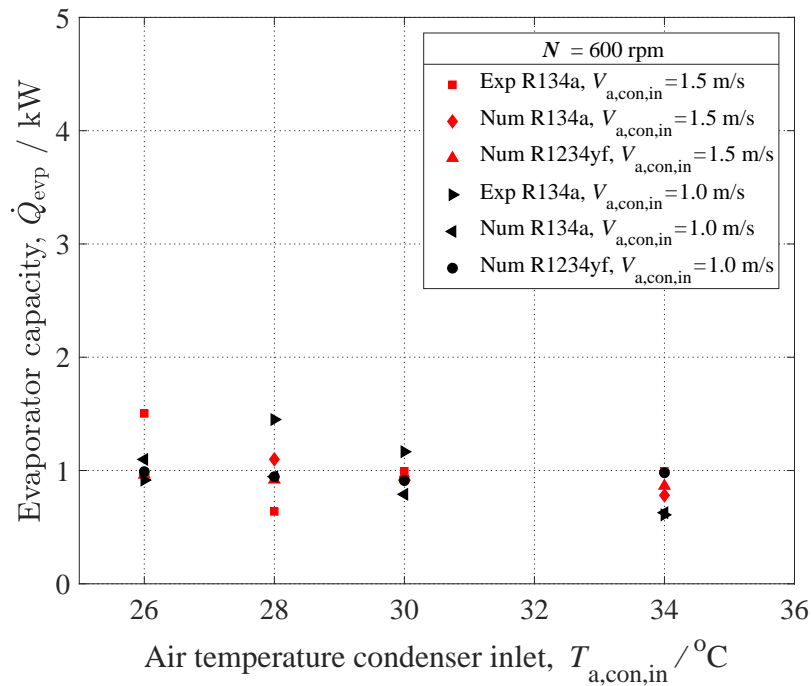


Figure 5.39: Variation of evaporator capacity with air temperature condenser inlet for $N = 600$ rpm

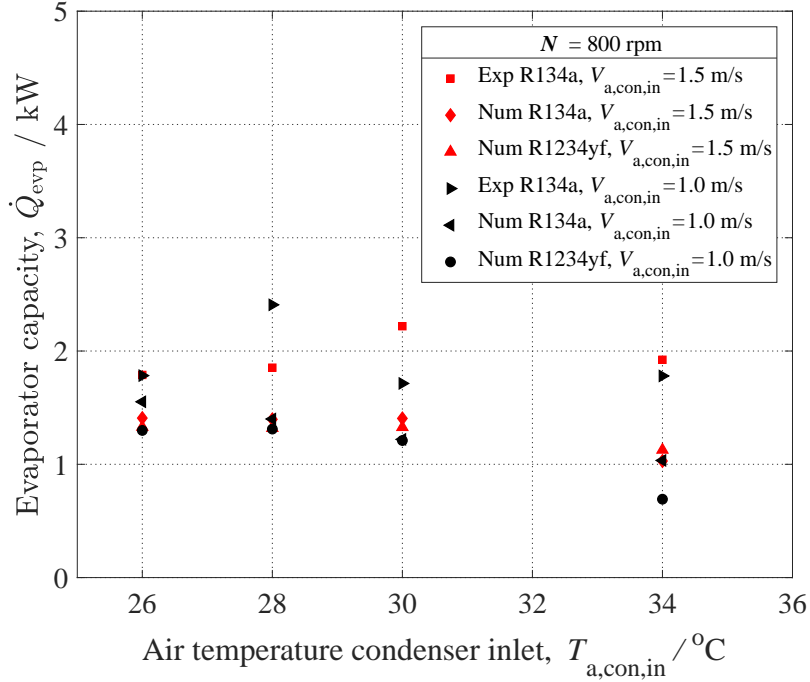


Figure 5.40: Variation of evaporator capacity with air temperature condenser inlet for $N = 800$ rpm

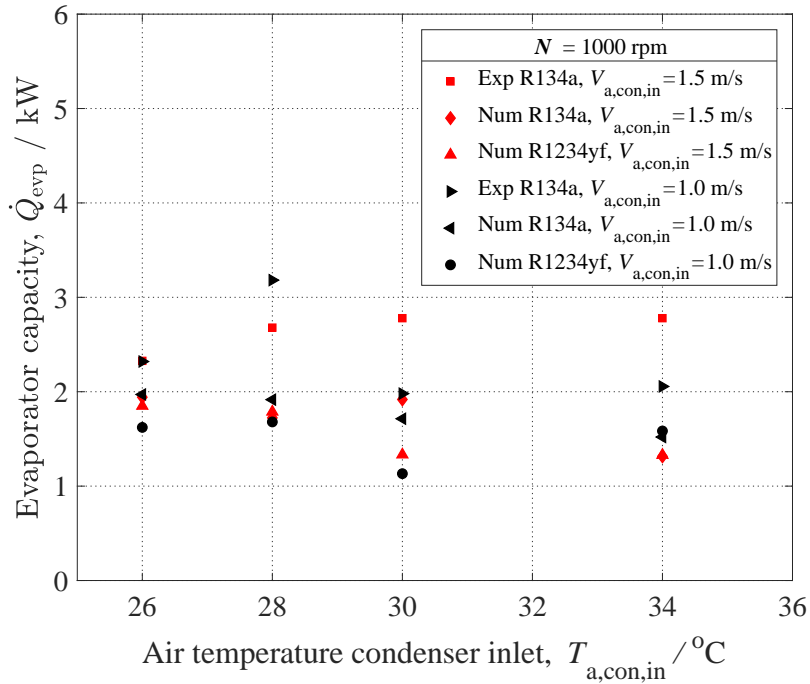


Figure 5.41: Variation of evaporator capacity with air temperature condenser inlet for $N = 1000$ rpm

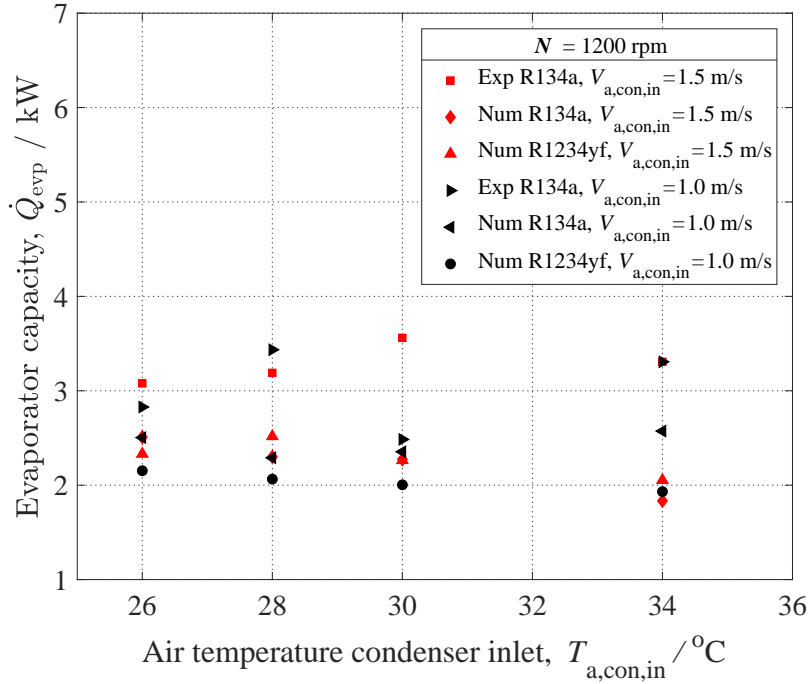


Figure 5.42: Variation of evaporator capacity with air temperature condenser inlet for $N = 1200$ rpm

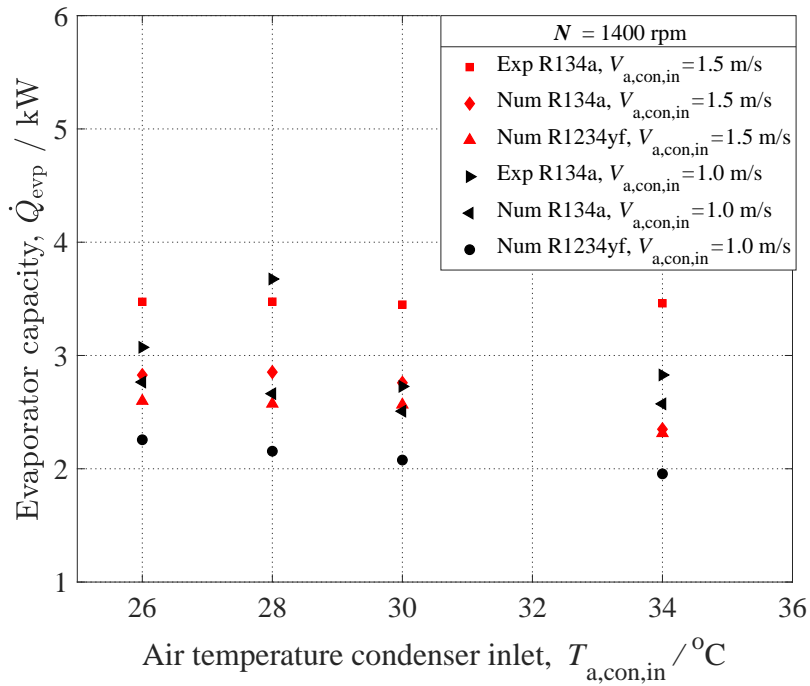


Figure 5.43: Variation of evaporator capacity with air temperature condenser inlet for $N = 1400$ rpm

5.11 Coefficient of performance (COP)

Fig. 5.44, 5.45, 5.46, 5.47 and Fig. 5.48 show the variation of the Coefficient of performance (COP) with condenser air inlet temperature ($T_{a,cond,in}$) at different compressor speeds and air velocities at the condenser inlet. It is observed that the COP is higher at 1.5 m/s velocity and lower at 1.0 m/s for in the case of both numerical and experimental results. The COP decreases with increase in condenser air inlet temperature. Higher speeds result in higher COP s. Experimental R134a results found to deviate by 2-25% compared to simulation results. Similarly the deviation between experimental and simulated results in the case of R1234yf is in the range of 5-35%. The comparison between simulations with R134a and R1234yf shows a minimum of 1% and a maximum of 10% deviation

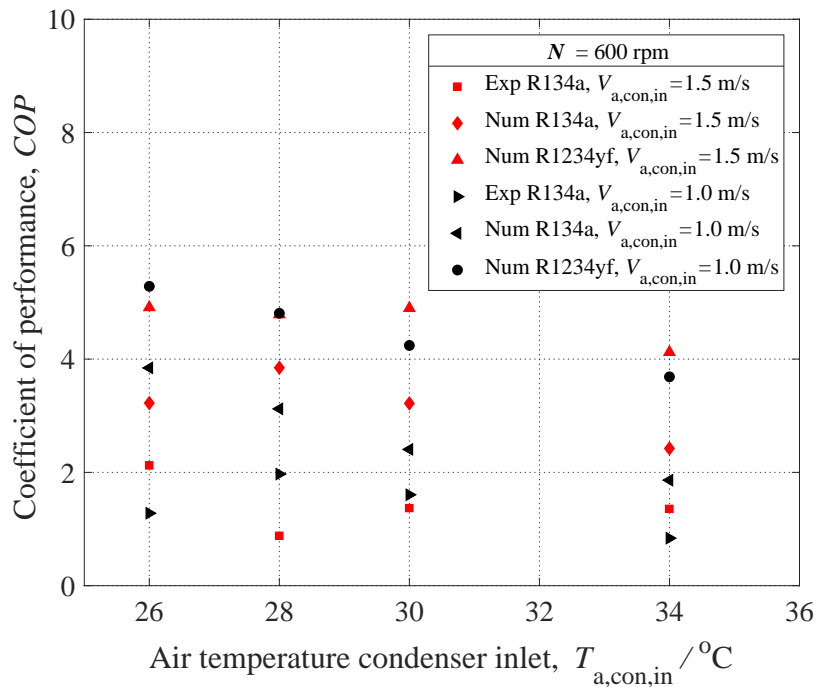


Figure 5.44: Variation of coefficient of performance with air temperature condenser inlet for $N = 600$ rpm

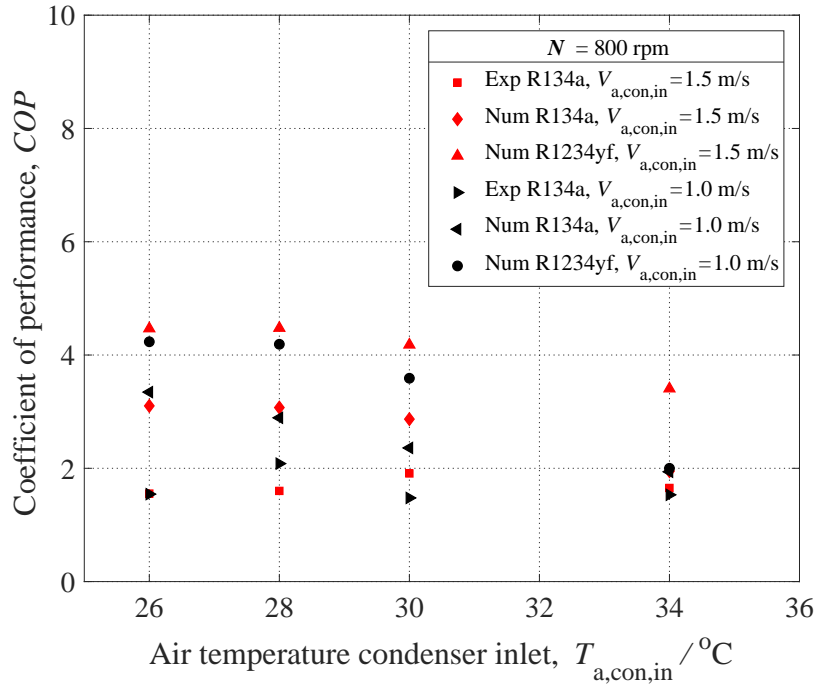


Figure 5.45: Variation of coefficient of performance with air temperature condenser inlet for $N = 800$ rpm

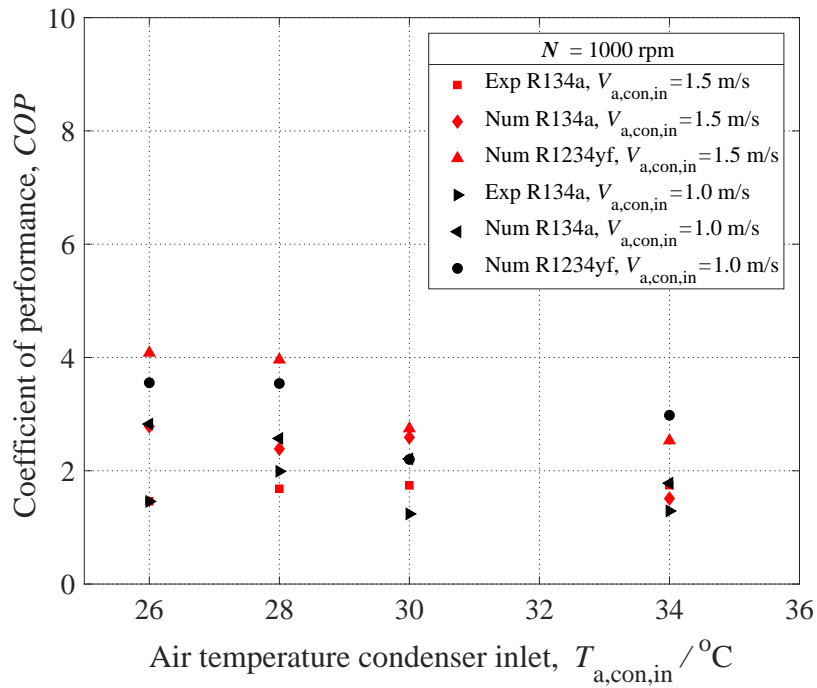


Figure 5.46: Variation of coefficient of performance with air temperature condenser inlet for $N = 1000$ rpm

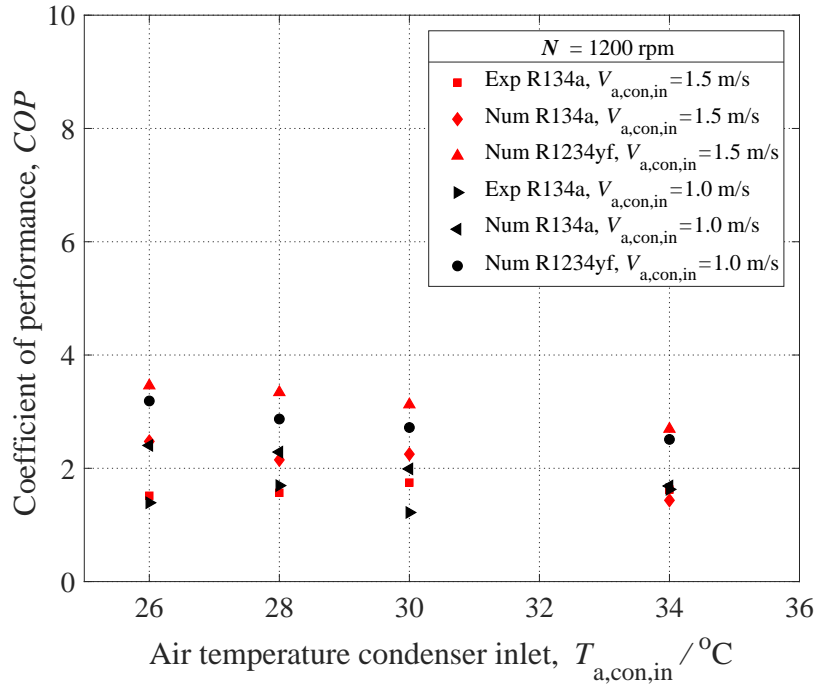


Figure 5.47: Variation of coefficient of performance with air temperature condenser inlet for $N = 1200$ rpm

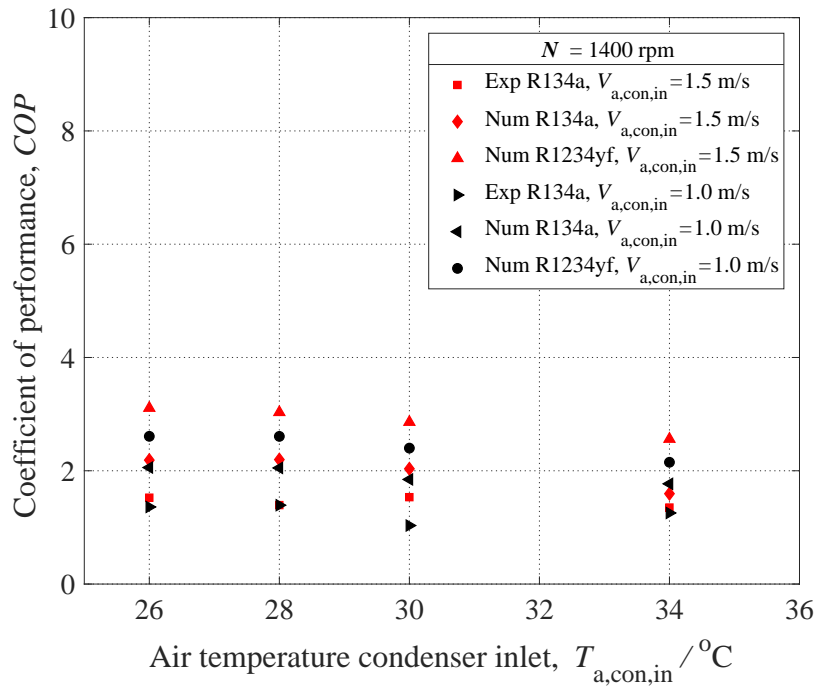


Figure 5.48: Variation of coefficient of performance with air temperature condenser inlet for $N = 1400$ rpm

5.12 Air temperature at evaporator outlet ($T_{a, \text{evp}, o}$)

Figs. 5.49, 5.50, 5.51, 5.52 and Fig. 5.53 show the variation of the air temperature at evaporator outlet ($T_{a, \text{evp}, o}$) with condenser air inlet temperature ($T_{a, \text{cond}, \text{in}}$) at different compressor speeds and air velocities at the condenser inlet. There is a slight increase in the air temperature at the evaporator outlet with increase in condenser air velocity as well as condenser air inlet temperature. With increase in compressor speed, there is a decrease in the evaporator outlet temperature due to the increase in refrigerant mass flow rate. There is also an increase in the evaporator capacity. At higher speeds, the state of the moist air at the outlet of the evaporator approaches saturation condition, i.e., the dry bulb temperature tends to reach the wet bulb temperature. It is observed from the plots that the experimental and numerical result are very close at higher compressor speed for both R134a and R1234yf. As compared with experimental values the simulation values for R134a show a minimum of 1% and a maximum of 20% deviation and for R1234yf the minimum deviation is 1% and the maximum deviation is 20%. The comparison between the simulation results with R134a and R1234yf shows 1-10% deviation.

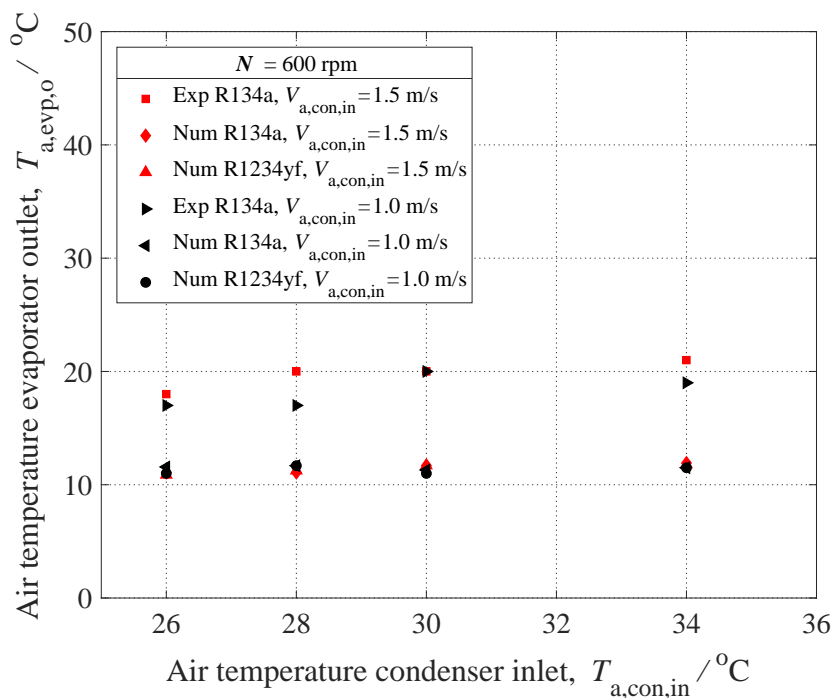


Figure 5.49: Variation of air temperature evaporator outlet with air temperature condenser inlet for $N = 600$ rpm

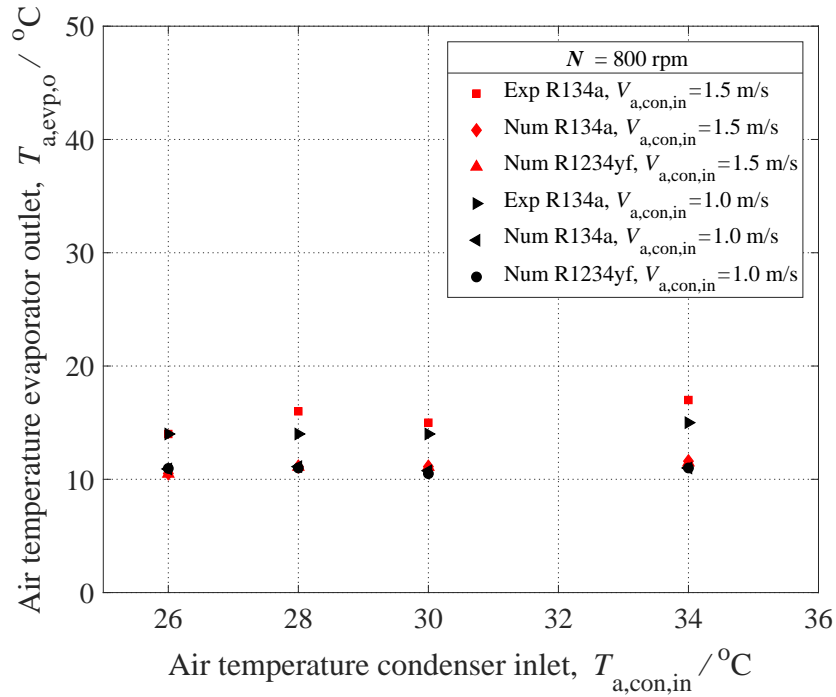


Figure 5.50: Variation of air temperature evaporator outlet with air temperature condenser inlet for $N = 800$ rpm

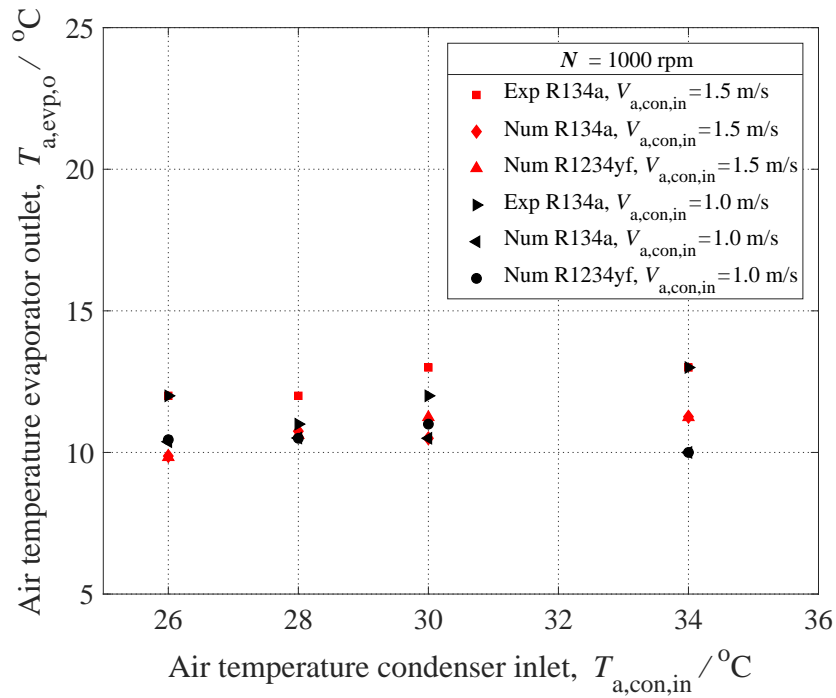


Figure 5.51: Variation of air temperature evaporator outlet with air temperature condenser inlet for $N = 1000$ rpm

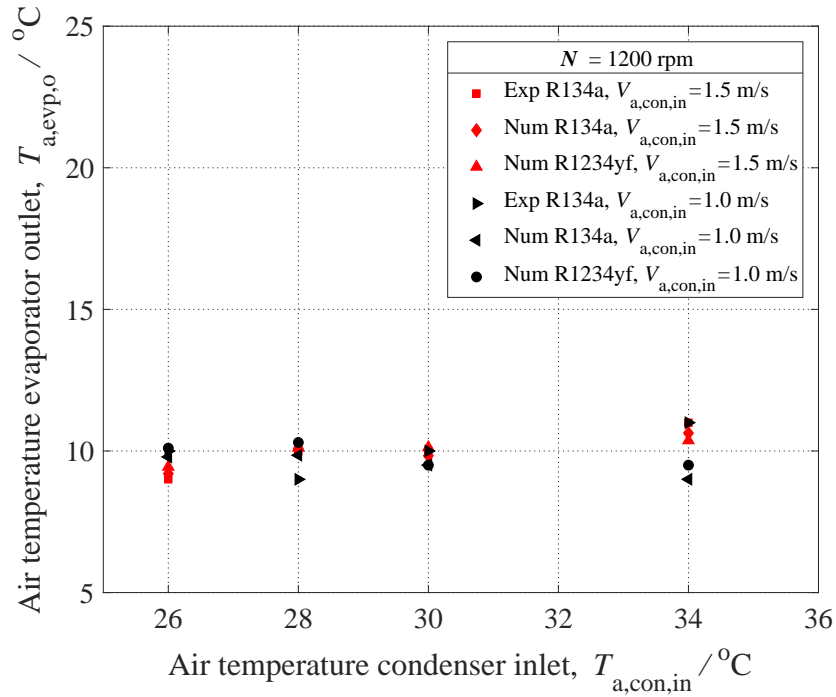


Figure 5.52: Variation of air temperature evaporator outlet with air temperature condenser inlet for $N = 1200$ rpm

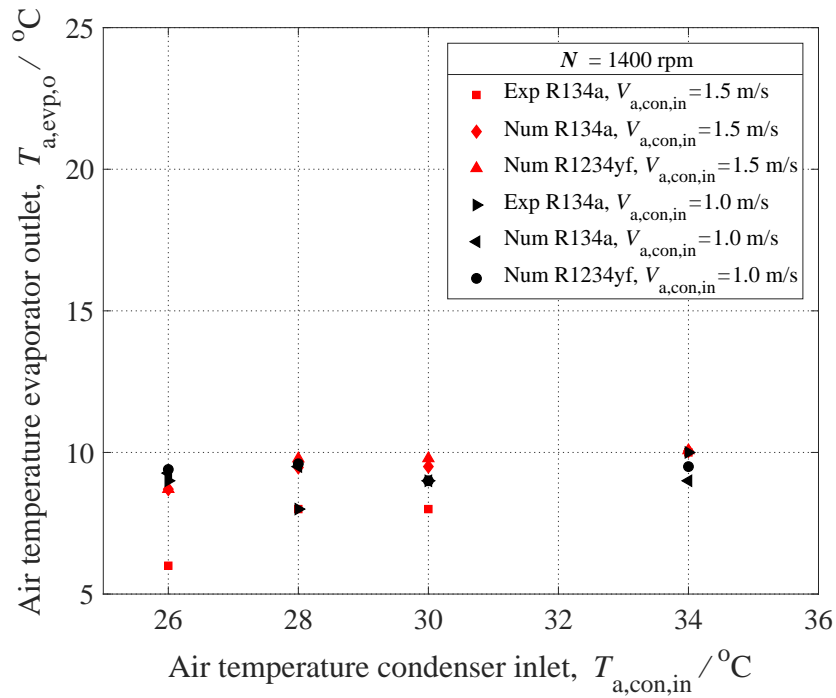


Figure 5.53: Variation of air temperature evaporator outlet with air temperature condenser inlet for $N = 1400$ rpm

5.13 Humidity ratio at evaporator outlet ($W_{a, \text{evp}, o}$)

The variation of air humidity ratio at the evaporator outlet ($W_{a, \text{evp}, o}$) is shown in Figs. 5.54, 5.55, 5.56, 5.57 and Fig. 5.58. As the process in the evaporator is cooling and dehumidification, air gets cooled and loses water vapour when it passes through the evaporator. As compared with experimental values the simulation values for R134a show a minimum of 2% and a maximum of 20% deviation, while for R1234yf the deviation is in the range of 1-20%. Comparison of the simulation results with R134a and R1234yf shows 1-10% deviation.

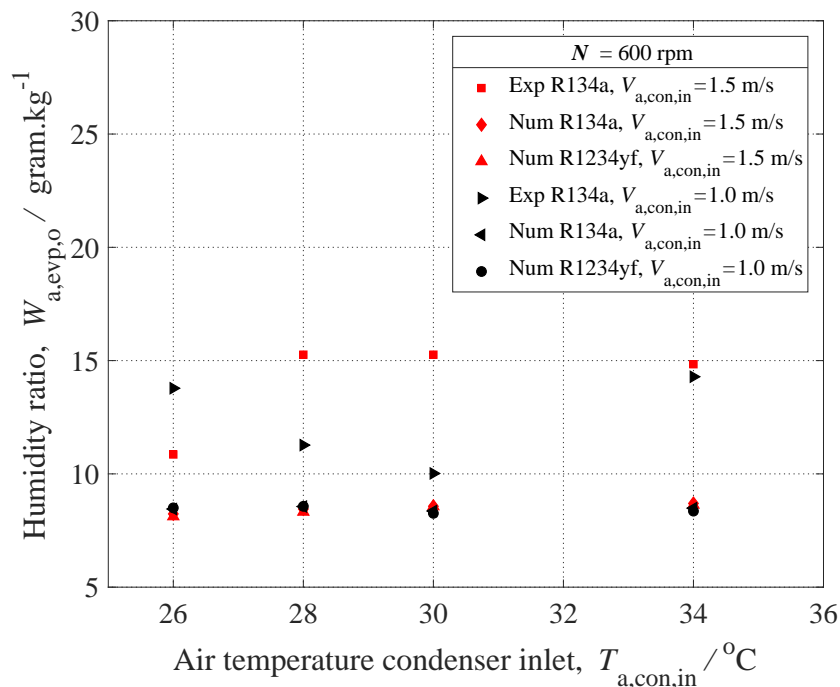


Figure 5.54: Variation of humidity ratio with air temperature condenser inlet for $N = 600$ rpm

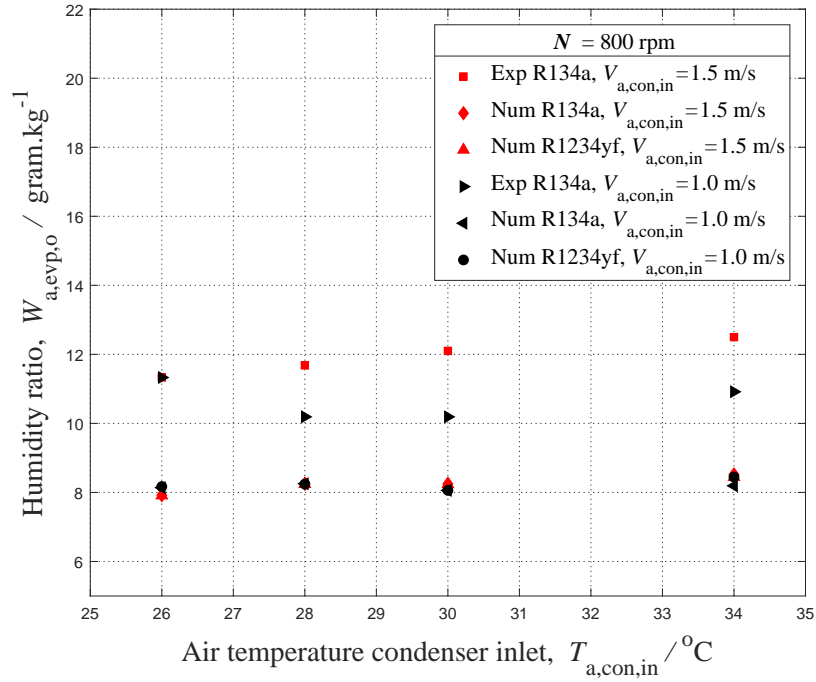


Figure 5.55: Variation of humidity ratio with air temperature condenser inlet for $N = 800$ rpm

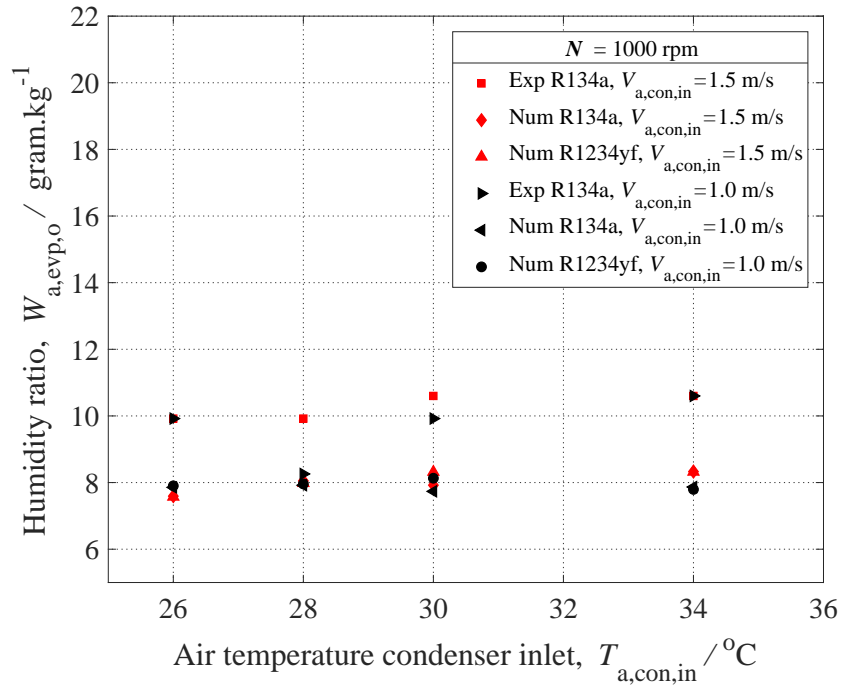


Figure 5.56: Variation of humidity ratio with air temperature condenser inlet for $N = 1000$ rpm

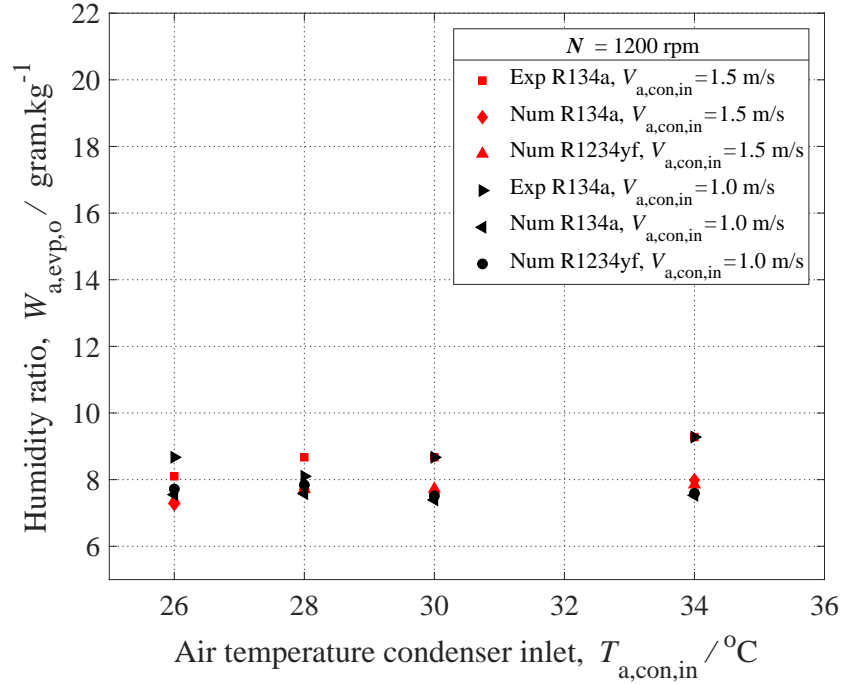


Figure 5.57: Variation of humidity ratio with air temperature condenser inlet for $N = 1200$ rpm

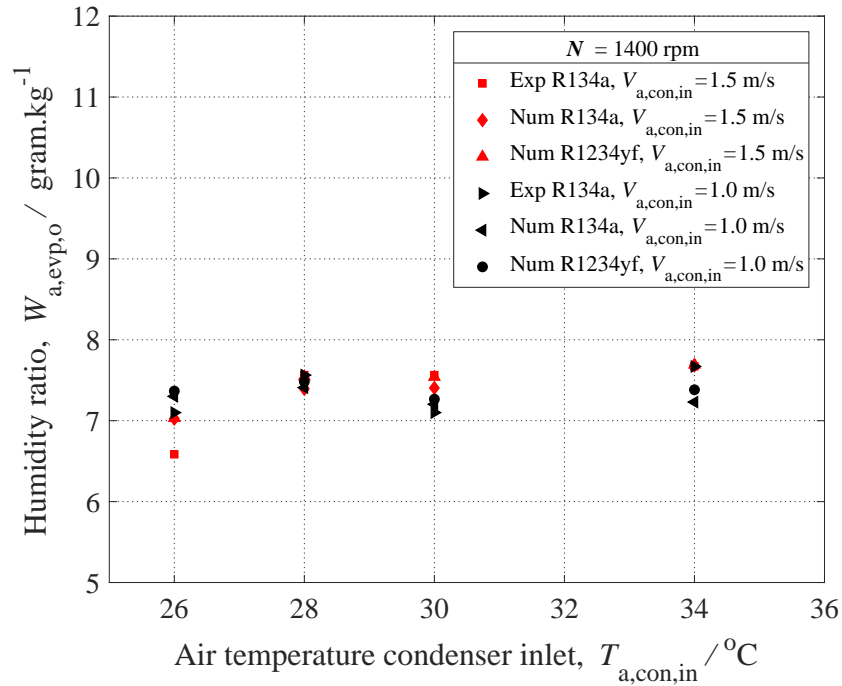


Figure 5.58: Variation of humidity ratio with air temperature condenser inlet for $N = 1400$ rpm

5.14 Relative humidity at evaporator outlet ($\phi_{a, \text{evp}, o}$)

The variation of air relative humidity at the evaporator outlet ($\phi_{a, \text{evp}, o}$) is shown in Figs. 5.59. It is shown that at higher compressor speed the experimental values of relative humidity are 100 % i.e the air get saturated at evaporator outlet. At lower compressor speed the experimental and numerical values are shows the variation in the range of 80 % to 90 %.

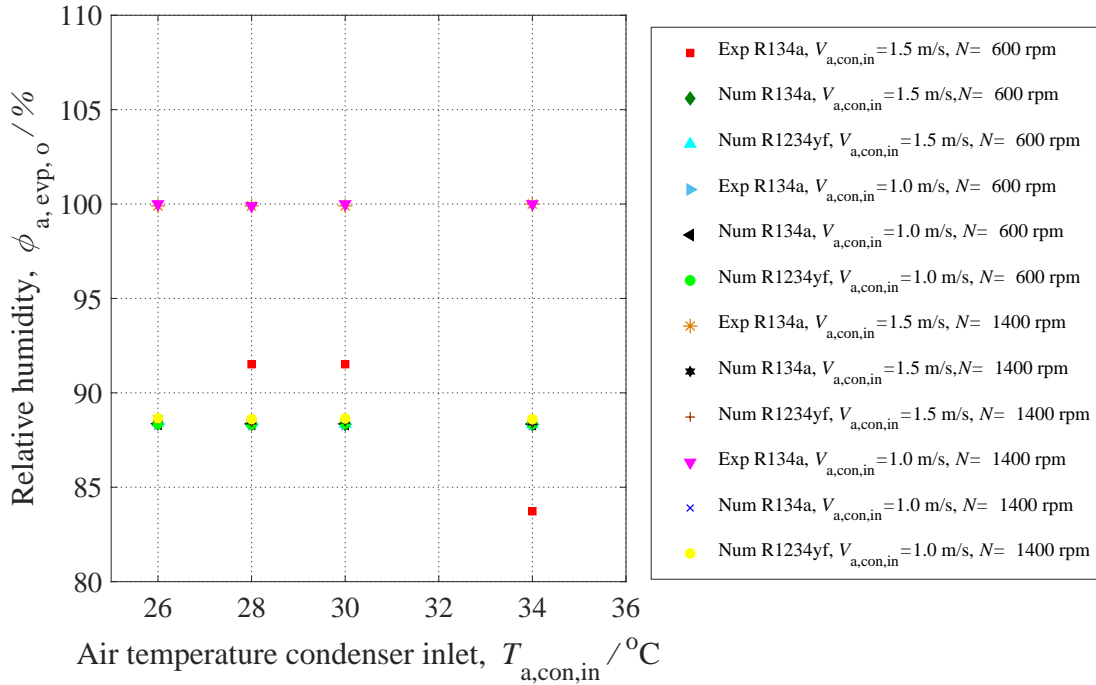


Figure 5.59: Variation of relative humidity with air temperature condenser inlet for $N = 600$ rpm and $N = 1400$ rpm

5.15 Air side dry and wet surface heat transfer coefficient (h_o) and ($h_{o,w}$)

Variations of the heat transfer coefficients (dry and wet in the case of the evaporator and dry in the case of condenser) with air velocity and air temperature are plotted in Fig. 5.60. The wet surface heat transfer coefficient is greater than the dry surface heat transfer coefficient due to the formation of a thin condensate water layer on the evaporator surface. It can be seen that h_o and $h_{o,w}$ are

greater at 1.5 m/s condenser air velocity than at 1.0 m/s. The effect of air temperature is not that significant on both h_o and $h_{o,w}$.

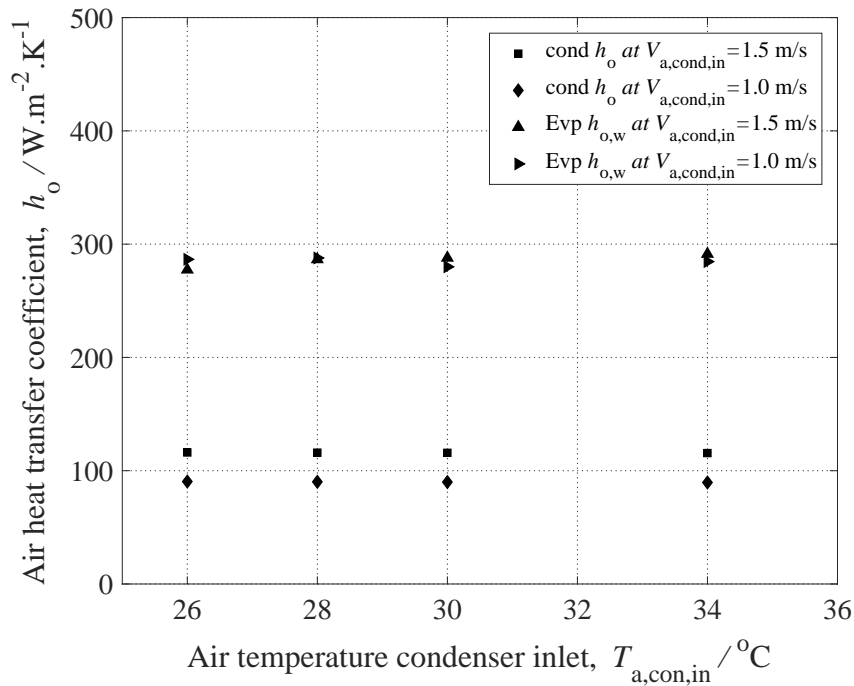


Figure 5.60: Variation of air side heat transfer coefficient for dry and wet surface with air temperature condenser inlet

5.16 Air side dry and wet surface friction factor (f_o) and ($f_{o,w}$)

Variations of the friction factor (both dry and wet friction factors in the case of evaporator and the dry friction factor in the case of the condenser) with air velocity and air temperature are plotted in Fig. 5.61. The friction factor for the wet surface is greater than that of the dry surface. Values of f_o and $f_{o,w}$ are higher at 1.5 m/s compared to those at 1.0 m/s. The effect of air temperature is not that significant on both f_o and $f_{o,w}$.

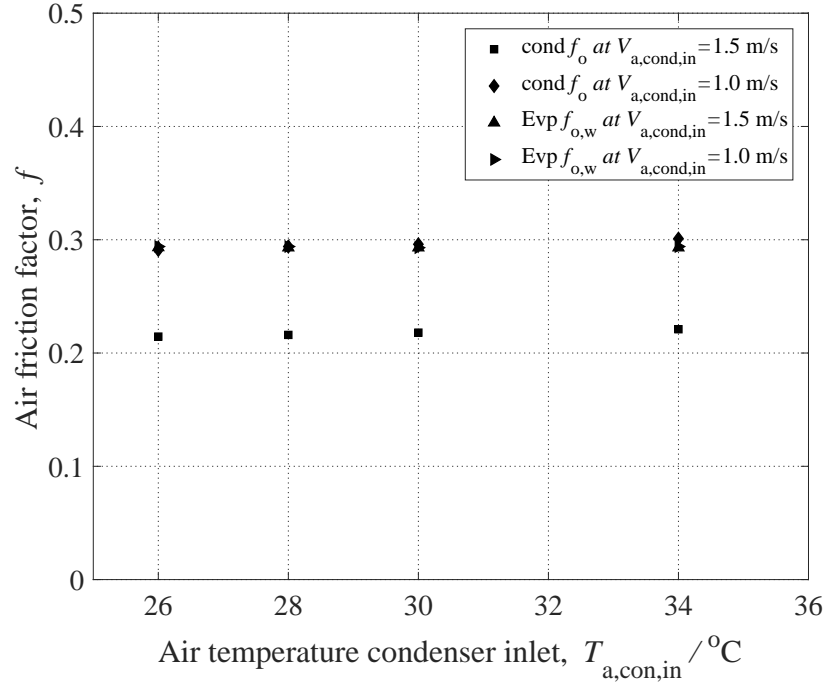


Figure 5.61: Variation of air side friction factor for dry and wet surface with air temperature condenser inlet

5.17 Air side dry and wet finned-surface efficiency (η_o) and ($\eta_{o,w}$)

:

Variations of the finned-surface efficiency (both dry and wet friction factors in the case of evaporator and the dry friction factor in the case of the condenser) with air velocity and air temperature are plotted in Fig. 5.62. The finned-surface efficiency for the wet surface is greater than that of the dry surface. Values of η_o and $\eta_{o,w}$ are higher at 1.5 m/s compared to those at 1.0 m/s. The effect of air temperature is not that significant on both η_o and $\eta_{o,w}$.

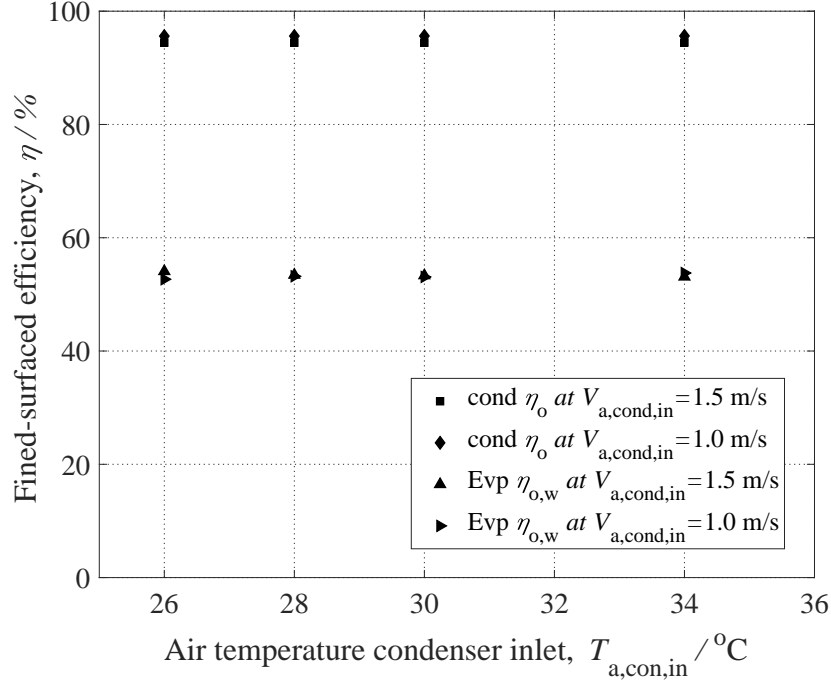


Figure 5.62: Variation of fined-surface efficiency for dry and wet surface with air temperature condenser inlet

5.18 Experimental repeatability tests and error bars

:

The experiments are repeated several times at each compressor speed to examine the repeatability of the results. and to plot error bars for several quantities of interest. Fig. 5.63 shows the error bars for evaporator capacity, condenser heat rejection rate, refrigerant mass flow rate and COP. Different investigators show different types of error bars like standard deviation based, standard error based and confidence intervals based. The error bars shown here are based on the standard deviation (i.e. $\sigma = \sqrt{[(x_i - \mu)^2]/[N - 1]}$, where x_i are the individual observations, μ is the mean and N is the number of observations). The error bars are shown for all the above quantities at compressor speeds of 600, 800, 1000, 1200 and 1400 rpm. From Fig. 5.63, it can be seen that the experimental runs have reasonably good repeatability.

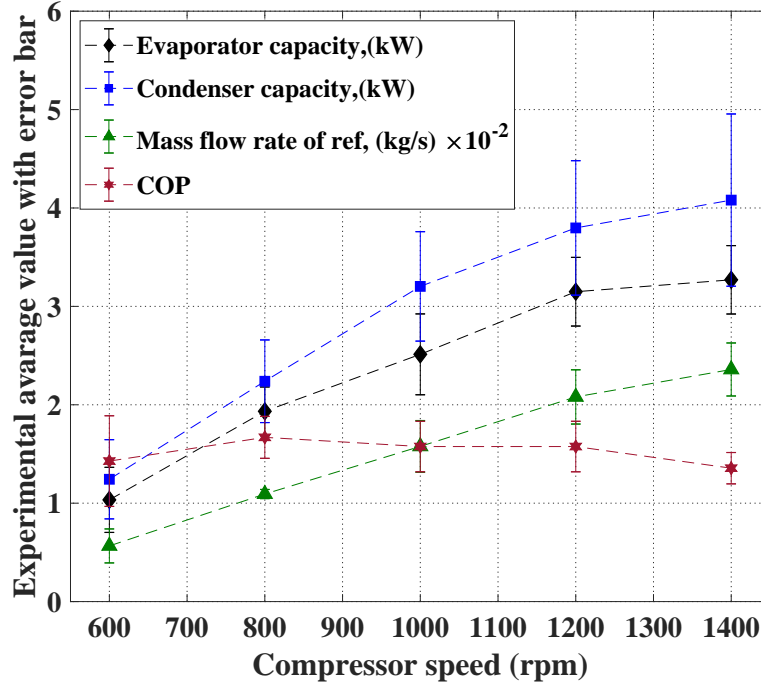


Figure 5.63: Experimental average values of evaporator capacity, condenser capacity, refrigerant mass flow rate and COP for various compressor speed and condensing air conditions with error bars.

5.19 Conclusions

The following conclusions are reached upon carrying out an experimental and numerical study of an AACS.

- The results from the mathematical model of the AACS and the experimental results obtained show a fair agreement with each other, with most of the results like mass flow rate, evaporator capacity, coefficient of performance, condenser capacity and compressor work showing a relative difference below 20%.
- Most of the numerical simulation results of the system with refrigerants R134a and R1234yf show a difference of typically below 10%.
- It is concluded that R1234yf is a very good alternative refrigerant for AACS in place of R134a. The results also show that R1234yf can be directly charged in an AACS which is running with R134a without any major design modifications.

- The performance of AACS with R1234yf is less than that of R134a because of the lower latent heat of R1234yf. The refrigerating effect and COP with R1234yf are 2% to 5% less than those with R134a. But from the global warming point of view R1234yf is much better than R134a with a small percentage reduction (about 5-10%) in the performance.

5.20 Suggestions for further work

- In the present work experiments are conducted with R134a in view of the difficulty in the availability of R1234yf and its higher cost. However, numerical analysis is carried out with both R134a and R1234yf. Once R1234yf becomes widely available at lower cost, experimental work can be conducted with R1234yf.
- In the experimental facility variation of humidity ratio can be done by injecting the water vapour inside the evaporator duct.
- At present it is difficult find mass flow meters for very small refrigerant flow rates; their cost also tends to be high. However, the experimental setup can be improved by including in the refrigeration circuit, a suitable and accurate mass flow rate meter.

Appendix A

$$P_E=P_{r,comp,o}, P_D=P_{r,comp,in}, T_E=T_{r,comp,o}, T_D=T_{r,comp,in}, T_C=T_{r,cond,o}, T_A=T_{r,evp,in}, T_F=T_{a,d,evp,in},$$

$$T_G=T_{a,w,evp,in}, T_H=T_{a,d,evp,o}, T_I=T_{a,w,evp,o}, T_J=T_{a,cond,in}, T_K=T_{a,cond,o}, V_A=V_{a,cond,in}$$

Surrounding condition:DBT=26 °C, WBT=18 °C and Pressure=893 kPa.

Table A.1: Experimental data for $V_A=1.5$ m/s and $T_J=26$ °C

N	P_E	P_D	T_E	T_D	T_C	T_A	T_F	T_G	T_H	T_I	T_J	T_K	T_s	ΔE	t	V_A
rpm	$\frac{kg}{cm^2}$	$\frac{kg}{cm^2}$	°C	kWh	min	m/s										
608	10	3.8	64	23	34	14	30	20	18	15	26	34	48	0.0520	5	1.5
708	10.5	3.6	66	22	35	13	30	20	15	15	26	36	50	0.0620	5	1.5
805	11.0	3.4	68	21	36	12	30	20	14	14	26	39	52	0.0733	5	1.5
915	11.5	3.2	70	20	38	11	30	20	13	13	26	42	50	0.0861	5	1.5
1016	12.0	3.0	72	17	40	11	30	20	12	12	26	43	50	0.102	5	1.5
1120	13.0	2.8	74	16	42	10	30	20	10	10	26	44	53	0.124	5	1.5
1204	13.5	2.6	77	14	42	7	30	20	9	9	26	46	55	0.1468	5	1.5
1302	14.0	2.4	79	12	42	6	30	20	7	7	26	44	56	0.1648	5	1.5
1352	14.5	2.2	80	10	42	5	30	20	6	6	26	45	59	0.1785	5	1.5

Table A.2: Experimental data for $V_A=1.5$ m/s and $T_J=28$ °C

Surrounding condition:DBT=25 °C, WBT=18 °C and Pressure=893 kPa.

N rpm	P_E $\frac{\text{kg}}{\text{cm}^2}$	P_D $\frac{\text{kg}}{\text{cm}^2}$	T_E °C	T_D °C	T_C °C	T_A °C	T_F °C	T_G °C	T_H °C	T_I °C	T_J °C	T_K °C	T_s °C	ΔE kWh	t min	V_A m/s
606	9.8	3.8	70	27	33	14	31	21	20	19	28	34	58	0.0520	5	1.5
716	10.4	3.7	71	24	36	14	31	21	18	16	28	37	56	0.0620	5	1.5
800	11	3.6	72	23	37	13	31	21	16	15	28	38	55	0.0733	5	1.5
895	11.6	3.5	73	20	39	12	31	21	14	13	28	43	53	0.0861	5	1.5
1000	12.2	3.4	75	18	41	11	31	21	12	12	28	45	53	0.102	5	1.5
1111	12.8	3.2	77	17	42	10	31	21	11	11	28	46	54	0.124	5	1.5
1208	13.4	3.0	78	17	44	10	31	21	10	10	28	48	56	0.1468	5	1.5
1290	14.0	2.8	80	15	45	8	31	21	9	9	28	51	57	0.1648	5	1.5
1316	14.6	2.6	82	14	46	7	31	21	8	8	28	52	58	0.1785	5	1.5

Table A.3: Experimental Data for $V_A=1.5$ m/s and $T_J=30$ °C

Surrounding condition:DBT=25 °C, WBT=18 °C and Pressure=893 kPa.

N rpm	P_E $\frac{\text{kg}}{\text{cm}^2}$	P_D $\frac{\text{kg}}{\text{cm}^2}$	T_E °C	T_D °C	T_C °C	T_A °C	T_F °C	T_G °C	T_H °C	T_I °C	T_J °C	T_K °C	T_s °C	ΔE kWh	t min	V_A m/s
600	10.2	4.0	70	29	34	15	32	22	20	20	30	36	58	0.0520	5	1.5
710	10.9	3.8	71	23	38	14	32	22	17	17	30	40	58	0.0620	5	1.5
817	11.6	3.6	72	23	39	13	32	22	15	15	30	42	58	0.0733	5	1.5
903	12.2	3.4	73	21	41	13	32	22	14	14	30	45	57	0.0861	5	1.5
1010	12.9	3.2	75	19	43	12	32	22	13	13	30	47	56	0.102	5	1.5
1116	13.7	3.0	77	16	45	11	32	22	12	12	30	49	55	0.124	5	1.5
1215	14.4	2.8	79	15	46	9	32	22	10	10	30	52	58	0.1468	5	1.5
1294	15.0	2.6	81	14	47	9	32	22	9	9	30	52	58	0.1648	5	1.5
1314	16.0	2.5	82	13	48	9	32	22	8	8	30	53	60	0.1785	5	1.5

Table A.4: Experimental Data for $V_A=1.5$ m/s and $T_J=34$ °C

Surrounding condition:DBT=26 °C, WBT=19 °C and Pressure=893 kPa.

N rpm	P_E $\frac{\text{kg}}{\text{cm}^2}$	P_D $\frac{\text{kg}}{\text{cm}^2}$	T_E °C	T_D °C	T_C °C	T_A °C	T_F °C	T_G °C	T_H °C	T_I °C	T_J °C	T_K °C	T_s °C	ΔE kWh	t min	V_A m/s
600	11.2	4.2	75	29	37	16	32	21	26	19	34	38	64	0.0520	5	1.5
700	11.9	4.1	76	26	39	15	32	21	19	17	34	43	62	0.0620	5	1.5
800	12.6	4.0	77	24	41	14	32	21	17	16	34	46	60	0.0733	5	1.5
912	13.3	3.9	80	20	44	13	32	21	14	14	34	48	57	0.0861	5	1.5
1015	14.0	3.8	81	18	46	13	32	21	13	13	34	51	55	0.102	5	1.5
1103	14.7	3.6	82	17	48	12	32	21	12	11	34	53	57	0.124	5	1.5
1211	15.4	3.4	83	15	50	11	32	21	11	11	34	54	59	0.1468	5	1.5
1272	16.2	3.3	84	14	50	10	32	21	10	10	34	56	59	0.1648	5	1.5
1285	17.0	2.0	85	15	52	10	32	21	10	10	34	56	59	0.1785	5	1.5

Table A.5: Experimental Data for $V_A=1.0$ m/s and $T_J=26$ °C

Surrounding condition:DBT=26 °C, WBT=18 °C and Pressure=893 kPa.

N rpm	P_E $\frac{\text{kg}}{\text{cm}^2}$	P_D $\frac{\text{kg}}{\text{cm}^2}$	T_E °C	T_D °C	T_C °C	T_A °C	T_F °C	T_G °C	T_H °C	T_I °C	T_J °C	T_K °C	T_s °C	ΔE kWh	t min	V_A m/s
600	9.8	3.8	66	25	32	14	32	20	17	17	26	34	53	0.0520	5	1.0
713	10.5	3.6	68	23	35	12	32	20	15	15	26	37	54	0.0620	5	1.0
815	11.2	3.4	70	23	37	11	32	20	14	14	26	40	54	0.0733	5	1.0
900	11.9	3.2	72	20	39	11	32	20	13	13	26	43	53	0.0861	5	1.0
1015	12.6	3.0	74	18	40	11	32	20	12	12	26	45	53	0.102	5	1.0
1100	13.3	2.8	76	16	44	9	32	20	11	11	26	47	54	0.124	5	1.0
1190	14.0	2.6	78	14	44	8	32	20	10	10	26	50	55	0.1468	5	1.0
1300	15.0	2.4	80	12	48	7	32	20	9	9	26	48	60	0.1648	5	1.0

Table A.6: Experimental Data for $V_A=1.0$ m/s and $T_J=28$ °C

Surrounding condition:DBT=26 °C, WBT=18 °C and Pressure=893 kPa.

N rpm	P_E $\frac{\text{kg}}{\text{cm}^2}$	P_D $\frac{\text{kg}}{\text{cm}^2}$	T_E °C	T_D °C	T_C °C	T_A °C	T_F °C	T_G °C	T_H °C	T_I °C	T_J °C	T_K °C	T_s °C	ΔE kWh	t min	V_A m/s
607	10.4	4.0	68	26	34	15	31	21	21	16	28	36	57	0.0520	5	1.0
707	11.0	3.8	70	25	36	14	31	21	17	15	28	40	56	0.0620	5	1.0
808	11.6	3.6	72	22	39	12	31	21	14	13	28	43	55	0.0733	5	1.0
900	12.3	3.4	74	20	41	12	31	21	13	13	28	45	55	0.0861	5	1.0
1004	13.0	3.2	76	17	43	10	31	21	11	10	28	50	54	0.102	5	1.0
1100	13.7	3.0	78	16	45	11	31	21	10	10	28	50	53	0.124	5	1.0
1202	14.4	2.8	80	14	47	8	31	21	9	9	28	52	59	0.1468	5	1.0
1250	15.0	2.6	82	12	48	8	31	21	8	8	28	54	60	0.1648	5	1.0
1300	15.8	2.4	83	11	50	7	31	21	8	8	28	57	61	0.1785	5	1.0

Table A.7: Experimental Data for $V_A=1.0$ m/s and $T_J=30$ °C

Surrounding condition:DBT=25 °C, WBT=17 °C and Pressure=893 kPa.

N rpm	P_E $\frac{\text{kg}}{\text{cm}^2}$	P_D $\frac{\text{kg}}{\text{cm}^2}$	T_E °C	T_D °C	T_C °C	T_A °C	T_F °C	T_G °C	T_H °C	T_I °C	T_J °C	T_K °C	T_s °C	ΔE kWh	t min	V_A m/s
600	11.4	4.0	70	25	36	16	32	19	20	15	30	38	58	0.0520	5	1.0
710	12.2	3.8	72	24	39	15	32	19	16	13	30	42	59	0.0620	5	1.0
804	12.8	3.6	74	23	41	13	32	19	14	13	30	43	57	0.0733	5	1.0
900	13.5	3.4	76	21	42	13	32	19	13	13	30	47	57	0.0861	5	1.0
1000	14.2	3.2	77	20	44	12	32	19	12	12	30	49	57	0.102	5	1.0
1110	14.9	3.0	78	16	46	11	32	19	11	11	30	51	58	0.124	5	1.0
1200	15.6	2.8	80	15	49	9	32	19	10	10	30	53	58	0.1468	5	1.0
1273	16.4	2.6	82	14	50	10	32	19	9	9	30	55	59	0.1648	5	1.0
1300	17.2	2.4	84	13	51	10	32	19	9	9	30	55	60	0.1785	5	1.0

Table A.8: Experimental Data for $V_A=1.0$ m/s and $T_J=34$ °C

Surrounding condition:DBT=26 °C, WBT=17 °C and Pressure=893 kPa.

N rpm	P_E $\frac{\text{kg}}{\text{cm}^2}$	P_D $\frac{\text{kg}}{\text{cm}^2}$	T_E °C	T_D °C	T_C °C	T_A °C	T_F °C	T_G °C	T_H °C	T_I °C	T_J °C	T_K °C	T_s °C	ΔE kWh	t min	V_A m/s
607	11.4	4.2	72	26	36	15	32	20	19	18	34	38	60	0.0520	5	1.0
700	12.3	4.0	74	24	40	15	32	20	16	15	34	43	60	0.0620	5	1.0
800	13.2	3.8	76	24	41	14	32	20	15	14	34	45	59	0.0733	5	1.0
900	14.2	3.6	78	20	44	13	32	20	14	13	34	48	56	0.0861	5	1.0
1005	15.0	3.4	80	19	46	13	32	20	13	13	34	50	55	0.102	5	1.0
1100	15.8	3.2	82	17	48	12	32	20	12	12	34	54	55	0.124	5	1.0
1188	16.8	3.0	84	16	51	10	32	20	11	10	34	55	56	0.1468	5	1.0
1250	17.8	2.8	86	15	51	10	32	20	10	10	34	57	57	0.1648	5	1.0

Table A.9: Experimental performance variables for R134a

N rpm	T_J °C	r_v	$\eta_{i,v}$	$\eta_{i,w}$	$\dot{m}_r \times 10^{-2}$ kg/s	\dot{Q}_{evp} kW	\dot{Q}_{cond} kW	\dot{W}_{comp} kW	COP	\dot{Q}_{loss} W
608	26	2.180	47.057	94.558	0.8503	1.503	1.769	0.708	2.122	27.944
708	26	2.529	42.936	94.633	0.8646	1.509	2.205	0.9299	1.622	30.814
805	26	2.601	47.510	94.694	1.0392	1.789	2.854	1.151	1.554	33.726
915	26	2.842	51.687	94.761	1.2245	2.062	3.498	1.359	1.517	30.814
1016	26	3.107	55.550	91.773	1.4282	2.327	3.712	1.594	1.459	30.814
1120	26	3.530	67.509	94.790	1.7819	2.835	3.925	1.809	1.567	35.198
1204	26	3.863	72.545	91.947	1.9551	3.079	4.349	2.030	1.516	38.173
1302	26	4.236	82.516	91.010	2.2765	3.548	4.560	2.250	1.576	39.675
1352	26	4.655	90.510	91.640	2.4468	3.774	4.771	2.474	1.525	44.243
606	28	2.143	19.903	86.899	0.3514	0.638	1.322	0.724	0.881	44.082
716	28	2.311	43.256	85.768	0.894	1.561	1.975	0.940	1.661	41.038
800	28	2.488	47.488	87.765	1.0752	1.853	2.192	1.157	1.601	39.531
895	28	2.673	57.542	86.527	1.4424	2.408	3.265	1.364	1.764	36.546
1000	28	2.868	59.878	85.107	1.6514	2.679	3.690	1.591	1.683	38.034
1111	28	3.147	62.934	85.966	1.8370	2.938	3.902	1.881	1.621	38.034
1208	28	3.453	67.730	89.511	2.033	3.190	4.324	2.033	1.568	41.038
1290	28	3.793	73.170	88.933	2.235	3.435	4.953	2.253	1.524	42.555
1316	28	4.168	82.423	89.60	2.428	3.675	5.161	2.636	1.394	44.082
600	30	2.134	30.104	91.690	0.5461	0.993	1.315	0.724	1.370	44.082
710	30	2.362	45.062	86.797	0.9508	1.624	2.179	0.943	1.722	44.082
817	30	2.615	56.653	91.906	1.310	2.219	2.608	1.161	1.909	44.82
903	30	2.869	61.941	92.839	1.5196	2.503	3.246	1.370	1.825	42.555
1010	30	3.170	66.076	91.296	1.7364	2.779	3.669	1.596	1.741	41.038

Table A.10: Continue experimental performance variables for R134a

1116	30	3.529	70.735	92.287	1.972	3.047	4.090	1.813	1.680	39.531
1215	30	3.898	81.342	92.778	2.340	3.561	4.717	2.036	1.748	44.082
1294	30	4.28	87.767	92.778	2.542	3.808	4.717	2.255	1.688	44.082
1314	30	4.691	95.920	95.309	2.746	4.049	4.925	2.639	1.534	47.165
600	34	2.237	29.512	86.699	0.5599	0.993	0.868	0.732	1.356	52.049
700	34	2.414	42.925	85.935	0.9432	1.621	1.939	0.947	1.710	48.898
800	34	2.60	46.401	86.566	1.1505	1.923	2.576	1.163	1.653	45.785
912	34	2.795	55.737	81.487	1.571	2.503	2.997	1.369	1.827	41.188
1015	34	3.001	58.072	82.074	1.7975	2.779	3.624	1.593	1.744	38.173
1103	34	3.287	68.043	84.396	2.19	3.3	4.040	1.815	1.818	41.188
1211	34	3.6	66.822	85.496	2.266	3.307	4.247	2.036	1.624	44.243
1274	34	3.876	70.366	87.149	2.4540	3.561	4.660	2.255	1.579	44.243
1300	34	4.370	75.683	91.377	2.4538	3.561	4.660	2.636	1.351	44.243
600	26	2.141	28.575	92.036	0.5044	0.915	1.179	0.715	1.279	35.198
713	26	2.382	42.465	92.092	0.8569	1.502	1.614	0.935	1.605	36.681
815	26	2.644	47.181	93.198	1.0345	1.783	2.046	1.154	1.544	36.681
900	26	2.935	52.856	95.508	1.231	2.056	2.474	1.365	1.507	35.198
1015	26	3.254	63.728	93.232	1.416	2.321	2.758	1.590	1.459	35.198
1100	26	3.608	63.728	92.999	1.6520	2.579	3.040	1.809	1.425	35.198
1190	26	4.002	68.762	92.8	1.8316	2.829	3.040	2.030	1.392	38.173
1300	26	4.531	72.991	93.942	2.010	3.073	3.180	1.392	1.361	45.785
607	28	2.171	46.601	92.164	0.8679	1.556	1.172	0.721	2.157	41.188
707	28	2.384	50.683	92.952	1.0543	1.851	1.748	0.938	1.971	39.675
808	28	2.615	62.162	90.289	1.4286	2.408	2.176	1.155	2.083	38.173
900	28	2.891	59.913	90.109	1.4722	2.413	2.460	1.366	1.765	38.173
1004	28	3.195	76.161	88.583	2.009	3.184	3.162	1.591	1.999	36.681

Table A.11: Continue experimental performance variables for R134a

1100	28	3.529	75.141	89.728	2.0647	2.0647	3.162	1.809	1.763	35.198
1202	28	3.90	80.175	89.563	2.2935	3.437	3.441	2.026	1.695	33.726
1250	28	4.284	88.697	89.018	2.5061	3.675	3.718	2.257	1.628	45.785
1300	28	4.771	93.028	91.773	2.575	3.675	4.131	2.639	1.392	47.336
600	30	2.365	35.8	93.744	0.6625	1.163	1.166	0.724	1.605	44.082
710	30	2.628	37.823	95.502	1.004	1.709	1.740	0.944	1.809	45.619
804	30	2.872	41.288	95.720	1.0205	1.715	1.882	1.160	1.477	42.555
900	30	3.161	43.036	94.925	1.0523	1.718	2.448	1.370	1.252	42.555
1000	30	3.478	48.008	97.430	1.243	1.981	2.729	1.597	1.239	42.555
1110	30	3.830	52.723	95.494	1.461	2.237	3.008	1.817	1.230	44.082
1200	30	4.217	57.474	96.128	1.633	2.485	3.286	2.036	1.220	44.082
1273	30	4.674	65.948	97.144	1.879	2.728	3.563	2.256	1.208	45.619
1300	30	5.184	69.689	98.1	1.910	2.728	3.563	2.639	1.033	47.165
607	34	2.273	17.718	89.785	0.3452	0.608	0.580	0.726	0.838	45.785
700	34	2.541	41.007	90.140	0.8896	1.501	1.295	0.944	1.588	45.785
800	34	2.834	45.018	93.834	1.064	1.781	1.579	1.162	1.532	44.243
900	34	3.176	49.816	90.435	1.294	2.056	2.002	1.368	1.5	39.675
1005	34	3.506	47.987	90.339	1.3368	2.056	2.281	1.593	1.29	38.173
1100	34	3.865	53.271	92.619	1.539	2.321	2.837	1.812	1.28	38.173
1188	34	4.313	76.76	94.346	2.278	3.307	2.975	1.628	1.628	38.173
1250	34	4.808	66.175	95.891	1.958	2.829	3.25	2.252	1.255	41.188

Table A.12: Numerical simulation performance variables for R134a

N rpm	T_J °C	V_A m/s	r_v	r_p	$\eta_{a,v}$ %	$\eta_{i,w}$ %	$\dot{m}_r \times 10^{-2}$ kg/s	\dot{Q}_{loss} W
608	26	1.5	2.165	2.165	41.322	92.947	0.7466	39.435
708	26	1.5	2.365	2.365	44.182	93.632	0.8897	39.632
805	26	1.5	2.584	2.584	47.780	94.297	1.0450	39.824
915	26	1.5	2.824	2.824	52.827	95.051	1.2515	40.041
1016	26	1.5	3.088	3.088	58.351	95.743	1.4736	40.240
1120	26	1.5	3.510	3.510	64.908	96.455	1.7132	40.445
1204	26	1.5	3.844	3.844	70.833	97.031	1.9092	40.611
1302	26	1.5	4.218	4.218	78.435	97.702	2.1639	40.804
1352	26	1.5	4.638	4.638	82.593	98.045	2.2312	40.901
600	28	1.5	2.121	2.273	41.274	92.933	0.7288	39.431
710	28	1.5	2.346	2.453	44.442	93.687	0.9183	39.648
817	28	1.5	2.598	2.642	47.572	94.262	1.2992	39.812
903	28	1.5	2.852	2.836	51.832	94.915	1.5832	40.010
1010	28	1.5	3.151	3.041	57.423	95.633	1.8772	40.202
1116	28	1.5	3.509	3.335	64.302	96.39	2.1353	40.422
1215	28	1.5	3.879	3.659	71.122	97.052	2.3662	40.619
1294	28	1.5	4.262	4.018	77.465	97.622	2.3441	40.780
1314	28	1.5	4.671	4.418	79.582	97.798	2.4331	40.832
600	30	1.5	2.120	2.262	41.131	92.898	0.7461	39.419
710	30	1.5	2.346	2.507	44.249	93.646	0.9336	39.636
817	30	1.5	2.598	2.773	48.281	94.379	1.1164	39.847
903	30	1.5	2.850	3.041	52.223	94.962	1.2812	40.017
1010	30	1.5	3.151	3.359	57.992	95.70	1.5242	40.228
1116	30	1.5	3.509	3.736	64.642	96.428	1.8022	40.432

Table A.13: Continue numerical simulation performance variables for R134a

N rpm	T_J °C	V_A m/s	r_v	r_p	$\eta_{a,v}$ %	$\eta_{i,w}$ %	$\dot{m}_r \times 10^{-2}$ kg/s	\dot{Q}_{loss} W
1215	30	1.5	3.879	4.126	71.649	97.105	2.0616	40.631
1294	30	1.5	4.262	4.532	77.782	97.642	2.2532	40.788
1314	30	1.5	4.671	4.958	79.415	97.782	2.2731	40.822
600	34	1.5	2.221	2.369	41.132	92.898	0.7804	39.419
700	34	1.5	2.397	2.556	43.925	93.577	0.9651	39.616
800	34	1.5	2.582	2.751	47.572	94.263	1.1792	39.814
912	34	1.5	2.777	2.954	52.676	95.035	1.4842	40.035
1015	34	1.5	2.983	3.165	58.292	95.736	1.8042	40.238
1103	34	1.5	3.269	4.423	63.777	96.332	2.0521	40.411
1211	34	1.5	3.583	3.783	71.353	97.073	2.4201	40.624
1275	34	1.5	4.859	4.063	76.032	97.492	2.6513	40.745
1285	34	1.5	4.351	4.582	77.062	97.583	2.4983	0.774
600	26	1.0	2.127	2.273	41.131	92.892	0.7261	39.419
700	26	1.0	2.366	2.529	44.348	93.667	0.9366	39.642
800	26	1.0	2.628	2.809	48.197	94.356	1.0568	39.843
912	26	1.0	2.916	3.116	52.079	94.948	1.2136	40.011
1015	26	1.0	3.234	3.454	57.420	95.633	1.4203	40.208
1103	26	1.0	3.561	3.802	63.579	96.318	1.6482	40.405
1211	26	1.0	3.981	4.247	69.807	96.935	1.8591	40.583
1275	26	1.0	4.511	4.805	78.279	97.688	2.1561	40.800
1285	26	1.0	4.950	5.275	82.423	98.031	2.2232	40.899
600	28	1.0	2.347	2.303	41.131	92.892	0.7572	39.419
700	28	1.0	2.608	2.528	43.922	93.577	0.9046	39.616

Table A.14: Continue numerical simulation performance Variables for R134a

800	28	1.0	2.850	2.773	47.904	93.317	1.1012	39.829
912	28	1.0	3.138	3.064	52.078	94.948	1.2797	40.012
1015	28	1.0	3.454	3.384	57.651	95.66	1.5212	40.216
1103	28	1.0	3.807	3.736	63.318	96.318	1.7471	40.405
1211	28	1.0	4.194	3.638	70.685	97.017	2.0221	40.607
1275	28	1.0	4.651	4.532	74.310	97.346	2.0996	40.701
1285	28	1.0	5.159	5.047	78.272	97.688	2.1661	40.810
600	30	1.0	2.347	2.506	41.131	92.892	0.7612	39.419
700	30	1.0	2.608	2.783	44.249	93.646	0.9291	39.636
800	30	1.0	2.850	3.039	47.739	94.290	1.0863	39.822
912	30	1.0	3.138	3.343	52.079	94.948	1.2734	40.011
1015	30	1.0	3.454	3.676	57.420	95.633	1.4862	40.208
1103	30	1.0	3.807	4.043	64.240	96.387	1.7812	40.425
1211	30	1.0	4.194	4.449	70.538	97.003	2.0042	40.603
1275	30	1.0	4.651	4.930	76.109	97.503	2.1683	40.747
1285	30	1.0	5.159	5.470	78.272	97.688	2.1458	40.800
600	34	1.0	2.256	2.408	41.298	92.940	0.8047	39.433
700	34	1.0	2.522	2.690	43.922	93.577	0.9529	39.616
800	34	1.0	2.813	2.995	47.575	94.263	1.1254	39.814
912	34	1.0	3.152	3.352	52.079	94.948	1.3536	40.011
1015	34	1.0	3.481	3.691	57.709	95.667	1.6077	40.218
1103	34	1.0	3.841	4.065	63.579	96.318	1.8372	40.405
1211	34	1.0	4.288	4.528	69.661	96.921	2.0673	40.579
1275	34	1.0	4.783	5.042	74.312	97.346	2.1992	40.701
1285	34	1.0	5.104	5.386	78.272	97.688	2.2773	40.821

Table A.15: Numerical simulation performance variables for R134a

N rpm	T_J °C	V_A m/s	\dot{Q}_{evp} kW	\dot{Q}_{cond} kW	\dot{W}_{comp} kW	COP	$T_{\text{a,evp,o}}$ °C	$W_{\text{a,evp,o}}$ gram/kg
600	26	1.5	0.961	1.267	0.2981	3.224	11.08	8.233
600	28	1.5	1.099	1.088	0.285	3.848	11.08	8.449
600	30	1.5	0.944	1.056	0.293	3.218	11.69	8.572
600	34	1.5	0.781	1.017	0.322	2.423	11.91	8.695
600	26	1.0	1.098	1.067	0.298	3.845	11.57	8.451
600	28	1.0	0.946	1.085	0.285	3.122	11.68	8.562
600	30	1.0	0.790	1.153	0.293	2.406	11.31	8.361
600	34	1.0	0.628	0.923	0.322	1.863	11.52	8.487
800	26	1.5	1.408	1.734	0.453	3.072	10.51	7.921
800	28	1.5	1.397	1.607	0.454	2.868	11.12	8.251
800	30	1.5	1.405	1.617	0.489	1.952	11.12	8.252
800	34	1.5	1.029	1.558	0.526	3.345	11.61	8.521
800	26	1.0	1.552	1.548	0.463	2.892	10.91	8.139
800	28	1.0	1.423	1.509	0.484	2.362	11.12	8.253
800	30	1.0	1.222	1.606	0.515	1.939	10.76	8.058
800	34	1.0	1.034	1.418	0.533	2.784	11.10	8.192
1000	26	1.5	1.942	2.274	0.697	2.387	9.87	7.592
1000	28	1.5	1.723	2.201	0.721	2.589	10.75	8.052
1000	30	1.5	1.971	2.171	0.741	1.511	10.51	7.922
1000	34	1.5	1.918	2.192	0.871	2.824	11.26	8.329
1000	26	1.0	1.315	2.018	0.697	2.571	10.38	7.856
1000	28	1.0	1.916	1.989	0.745	2.212	10.51	7.922
1000	30	1.0	1.714	2.072	0.775	1.781	10.51	7.736
1000	34	1.0	1.520	1.955	0.853	2.475	10.20	7.867

Table A.16: continue numerical simulation performance variables for R134a

N rpm	T_J °C	V_A m/s	\dot{Q}_{evp} kW	\dot{Q}_{cond} kW	\dot{W}_{comp} kW	COP	$T_{\text{a, evp, o}}$ °C	$W_{\text{a, evp, o}}$ gram/kg
1200	26	1.5	2.509	2.913	1.013	2.149	9.2	7.262
1200	28	1.5	2.321	2.783	1.070	2.252	10.09	7.707
1200	30	1.5	2.274	2.816	1.114	1.435	9.83	7.572
1200	34	1.5	1.834	2.783	1.284	2.404	10.63	7.986
1200	26	1.0	2.504	2.467	1.094	2.287	9.79	7.551
1200	28	1.0	2.290	2.544	1.145	1.991	9.85	7.582
1200	30	1.0	2.354	2.458	1.216	1.688	9.5	7.393
1200	34	1.0	2.573	2.754	1.451	2.187	9.0	7.532
1400	26	1.5	2.827	3.338	1.292	2.197	8.70	7.025
1400	28	1.5	2.853	3.204	1.298	2.035	9.47	7.393
1400	30	1.5	2.759	3.321	1.355	1.595	9.5	7.405
1400	34	1.5	2.349	3.237	1.472	2.057	10.05	7.682
1400	26	1.0	2.765	2.950	1.344	2.051	9.27	7.301
1400	28	1.0	2.663	2.815	1.299	1.847	9.5	7.409
1400	30	1.0	2.508	2.914	1.357	1.771	9	7.203
1400	34	1.0	2.573	2.754	1.451	1.892	9.0	7.232

Table A.17: Numerical simulation performance variables for R1234yf

N rpm	T_J °C	V_A m/s	r_v	r_p	$\eta_{a,v}$ %	$\eta_{i,w}$ %	$\dot{m}_r \times 10^{-2}$ kg/s	\dot{Q}_{loss} W
608	26	1.5	2.442	2.442	41.322	92.947	0.8014	39.435
708	26	1.5	2.567	2.567	44.182	93.632	1.0022	39.632
805	26	1.5	2.812	2.812	47.78	94.297	1.1772	39.824
915	26	1.5	3.083	3.083	52.827	95.051	1.4093	40.041
1016	26	1.5	3.393	3.393	58.351	95.744	1.6587	40.241
1120	26	1.5	3.244	3.244	64.908	96.455	2.4042	40.445
1204	26	1.5	4.056	4.056	78.435	97.70	2.9302	40.804
1302	26	1.5	4.056	4.056	78.435	97.70	2.9302	40.804
1352	26	1.5	4.447	4.447	82.593	98.045	3.0512	40.903
600	28	1.5	2.198	2.428	41.274	92.932	0.7629	39.431
710	28	1.5	3.039	2.453	44.442	93.687	1.0356	39.648
817	28	1.5	2.834	2.642	47.575	94.263	1.2141	39.814
903	28	1.5	2.949	2.836	51.834	94.912	1.4641	40.010
1010	28	1.5	3.906	3.041	57.422	95.631	1.7841	40.202
1116	28	1.5	3.955	3.182	64.302	96.392	2.2311	40.422
1215	28	1.5	4.553	3.481	71.122	97.051	2.5412	40.612
1294	28	1.5	4.678	3.812	77.465	97.622	2.8214	40.782
1314	28	1.5	4.752	3.966	79.58	97.798	2.9714	40.836
600	30	1.5	2.283	2.174	41.131	92.892	0.8807	39.419
710	30	1.5	2.554	3.022	44.242	93.642	0.8534	39.631
817	30	1.5	2.834	2.773	48.282	94.379	1.2581	39.841
903	30	1.5	3.125	2.812	57.992	95.701	2.1031	40.228
1010	30	1.5	3.476	3.736	64.642	96.428	2.0281	40.437
1116	30	1.5	3.906	3.724	71.649	97.106	2.6028	40.632

Table A.18: Continue numerical simulation performance Variables for R1234yf

1215	30	1.5	4.339	4.287	77.782	97.642	2.6951	40.788
1294	30	1.5	4.787	4.324	79.416	97.782	2.9792	40.828
1314	30	1.5	5.284	4.563	80.012	97.823	3.0125	40.912
600	34	1.5	2.363	2.324	41.132	92.892	0.9005	39.419
700	34	1.5	2.618	2.556	43.921	93.572	1.0892	39.616
800	34	1.5	2.787	2.696	47.575	94.263	1.3622	39.814
912	34	1.5	3.031	2.893	52.676	95.032	1.7156	40.035
1015	34	1.5	3.221	3.036	58.292	95.736	2.1361	40.238
1103	34	1.5	3.543	3.313	63.772	96.332	2.4331	40.411
1211	34	1.5	4.074	3.783	71.351	97.072	2.7271	40.624
1275	34	1.5	4.420	4.063	76.032	97.497	2.9872	40.745
1285	34	1.5	4.767	4.357	77.062	97.582	2.9762	40.772
600	26	1.0	2.205	2.181	41.131	92.898	0.8581	39.419
700	26	1.0	2.564	2.529	44.348	93.667	1.0082	39.830
800	26	1.0	2.856	2.809	48.197	94.365	1.1902	39.843
912	26	1.0	3.189	3.116	52.079	94.948	1.3662	40.011
1015	26	1.0	3.558	3.458	57.42	95.633	1.5982	40.208
1103	26	1.0	3.756	3.608	63.579	96.318	1.9662	40.405
1211	26	1.0	4.023	3.812	69.807	96.935	2.3591	40.583
1275	26	1.0	5.072	4.805	78.272	97.688	2.4232	40.800
1285	26	1.0	5.593	5.275	82.423	98.031	2.4982	40.899
600	28	1.0	2.556	2.213	41.312	92.892	0.8943	39.419
700	28	1.0	2.744	2.425	43.922	93.577	1.0691	39.616
800	28	1.0	3.005	2.773	47.904	94.317	1.2402	39.829
912	28	1.0	3.193	3.064	48.011	94.948	1.4418	40.011
1015	28	1.0	3.254	3.384	57.651	95.662	1.7134	40.216

Table A.19: Continue numerical simulation performance Variables for R1234yf

1103	28	1.0	3.846	3.101	63.579	96.318	2.4326	40.405
1211	28	1.0	4.507	3.551	70.685	97.017	2.6959	40.607
1275	28	1.0	5.015	4.532	74.312	97.346	2.3612	40.701
1285	28	1.0	5.168	5.047	78.272	97.688	2.4353	40.8
600	30	1.0	2.556	2.506	41.136	92.892	0.8586	39.419
700	30	1.0	2.853	2.669	44.252	93.646	1.0982	39.636
800	30	1.0	3.129	2.912	47.739	94.290	1.2862	39.822
912	30	1.0	3.465	3.059	52.079	94.948	1.5872	40.011
1015	30	1.0	3.831	3.077	57.422	95.633	2.0521	40.208
1103	30	1.0	4.268	4.079	64.242	96.387	2.1213	40.425
1211	30	1.0	4.725	4.222	70.53	97.003	2.3922	40.603
1275	30	1.0	5.268	4.665	76.109	97.503	2.5943	40.747
1285	30	1.0	5.868	5.470	78.272	97.688	2.4112	40.800
600	34	1.0	2.459	2.408	41.298	92.942	0.9082	39.433
700	34	1.0	2.665	2.584	43.922	93.577	1.1258	39.616
800	34	1.0	2.769	2.657	47.575	94.263	1.4572	39.814
912	34	1.0	3.517	3.352	52.079	94.948	1.5252	40.012
1015	34	1.0	3.914	3.691	57.709	95.662	1.8112	40.218
1103	34	1.0	4.332	4.065	63.579	96.318	2.0692	40.405
1211	34	1.0	4.659	4.308	69.662	96.921	2.4612	40.579
1275	34	1.0	5.467	5.042	74.310	97.346	2.4742	40.701
1285	34	1.0	5.542	5.386	78.272	97.688	2.5612	40.802

Table A.20: Numerical simulation performance variables for R1234yf

N rpm	T_J °C	V_A m/s	\dot{Q}_{evp} kW	\dot{Q}_{cond} kW	\dot{W}_{comp} kW	COP	$T_{\text{a,evp,o}}$ °C	$W_{\text{a,evp,o}}$ gram/kg
600	26	1.5	0.962	1.087	0.195	4.913	10.87	8.117
600	28	1.5	0.918	0.956	0.191	4.787	11.23	8.321
600	30	1.5	0.943	0.989	0.192	4.898	11.69	8.562
600	34	1.5	0.864	0.954	0.209	4.122	11.79	8.631
600	26	1.0	0.990	1.010	0.195	5.285	11	8.502
600	28	1.0	0.945	1.030	0.191	4.809	11.68	8.568
600	30	1.0	0.911	1.068	0.192	4.241	11	8.259
600	34	1.0	0.982	0.870	0.209	3.687	11.5	8.356
800	26	1.5	1.329	1.553	0.297	4.467	10.47	7.908
600	28	1.5	1.319	1.496	0.294	4.476	11.09	8.239
800	30	1.5	1.327	1.512	0.317	4.18	11.08	8.235
800	34	1.5	1.127	1.497	0.332	3.406	11.47	8.442
800	26	1.0	1.299	1.451	0.306	4.234	10.96	8.172
800	28	1.0	1.311	1.431	0.312	4.192	11	8.242
800	30	1.0	1.212	1.541	0.336	3.592	10.5	8.062
800	34	1.0	0.692	1.437	0.345	2.220	11.0	8.447
1000	26	1.5	1.849	2.091	0.4531	4.081	9.83	7.572
1000	28	1.5	1.787	2.171	0.451	3.962	10.61	7.982
1000	30	1.5	1.333	2.271	0.485	2.745	11.24	8.318
1000	34	1.5	1.329	2.199	0.524	2.533	11.24	8.322
1000	26	1.0	1.622	1.922	1.922	3.554	10.45	7.902
1000	28	1.0	1.682	1.922	0.474	3.541	10.5	7.962
1000	30	1.0	1.132	2.152	0.516	2.221	11	8.132
1000	34	1.0	1.584	1.905	0.531	2.982	10	7.795

Table A.21: continue numerical simulation performance variables for R1234yf

N rpm	T_J °C	V_A m/s	\dot{Q}_{evp} kW	\dot{Q}_{cond} kW	\dot{W}_{comp} kW	COP	$T_{\text{a, evp, o}}$ °C	$W_{\text{a, evp, o}}$ gram/kg
1200	26	1.5	2.331	3.041	0.673	3.460	9.43	7.374
1200	28	1.5	2.517	2.759	0.682	3.341	10.11	7.712
1200	30	1.5	2.264	2.849	0.724	3.125	10.12	7.721
1200	34	1.5	2.053	2.763	0.762	2.694	10.37	7.852
1200	26	1.0	2.153	2.532	0.675	3.189	10.10	7.718
1200	28	1.0	2.064	2.579	0.717	2.872	10.3	7.842
1200	30	1.0	2.004	2.531	0.736	2.722	9.5	7.512
1200	34	1.0	1.932	2.455	0.767	2.512	9.5	7.592
1400	26	1.5	2.598	3.211	0.836	3.107	8.70	7.031
1400	28	1.5	2.573	3.247	0.848	3.032	9.78	7.546
1400	30	1.5	2.565	3.303	0.897	2.859	9.78	7.542
1400	34	1.5	2.313	3.160	0.903	2.562	10.07	7.692
1400	26	1.0	2.256	2.828	0.865	2.608	9.4	7.366
1400	28	1.0	2.155	2.708	0.826	2.607	9.6	7.483
1400	30	1.0	2.077	2.729	0.865	2.421	9.0	7.266
1400	34	1.0	1.955	2.729	0.907	2.152	9.5	7.382

Table A.22: Numerical simulation performance variables for air side

T_J °C	V_A m/s	h_o W/m ² K	$h_{o,w}$ W/m ² K	η_o %	$\eta_{o,w}$ %	f_o	$f_{o,w}$
26	1.5	116.08	277.39	94.448	54.067	0.214	0.293
28	1.5	115.94	286.49	94.452	53.433	0.216	0.293
30	1.5	115.79	287.88	94.442	53.332	0.218	0.293
34	1.5	115.56	291.32	94.472	53.102	0.221	0.293
26	1.0	90.41	286.60	95.632	52.671	0.291	0.294
28	1.0	90.16	287.80	95.611	53.195	0.294	0.294
30	1.0	89.97	280	95.623	53.082	0.296	0.293
34	1.0	89.57	284.58	95.632	53.772	0.301	0.294

Table A.23: Comparison between experimental and numerical simulation results.

Parameter	Minimum and Maximum Difference,%		
	Exp and R134a	Exp and R1234yf	R134a and R1234yf
Volume ratio , r_v	0.03 - 1.5	0.02 - 6	0 - 5
Pressure ratio, r_v	0 - 1	0 - 5	1 - 8
Mass flow rate, \dot{m}_r	0.2 - 10	1.2 - 17	1 - 10
Actual volumetric efficiency, $\eta_{a,v}$	0.1 - 10	0.2 - 9	1 - 10
Isentropic work efficiency, $\eta_{i,w}$	0.02 - 6	0.02 - 6	0- 2
Friction heat lost, Q_{lost}	0.1 - 10	0.1 - 10	0 - 2
Evaporator capacity, Q_{evp}	3 - 30	4 - 35	1 - 10
Condenser capacity, Q_{cond}	2 - 25	5 - 30	1 - 10
Compressor power, W_{comp}	4 - 28	5 - 30	1 - 15
Coefficient of performance, COP	2 - 25	5 - 35	1 - 10
Air temperature evaporator outlet, $T_{a,evp,o}$	0 - 20	1 - 20	1 - 10
Humidity ratio evaporator outlet, $W_{a,evp,o}$	2 - 20	1 - 20	1 - 10

Table A.24: Comparison of formulated R134a saturation properties with REFPROP data.

	$T / ^\circ \text{C}$	-20	- 10	0	10	20	30	40
Ref	P / Bar	1.33	2.01	2.93	4.15	5.72	7.70	10.17
Num	P / Bar	1.32	2.00	2.92	4.14	5.71	7.69	10.15
Ref	$\rho_l / \text{kg/m}^3$	1358.30	1327.10	1294.80	1261.00	1225.30	1187.50	1146.70
Num	$\rho_l / \text{kg/m}^3$	1358.82	1327.48	1294.91	1260.87	1225.06	1187.06	1146.32
Ref	$\rho_v / \text{kg/m}^3$	6.78	10.04	14.43	20.23	27.78	37.54	50.09
Num	$\rho_v / \text{kg/m}^3$	6.77	10.02	14.40	20.19	27.73	37.46	49.96
Ref	$h_l / \text{kJ/kg}$	173.64	186.70	200.00	213.58	227.47	241.72	256.41
Num	$h_l / \text{kJ/kg}$	173.92	186.81	200.00	213.53	227.45	241.80	256.63
Ref	$h_v / \text{kJ/kg}$	386.55	392.66	398.60	404.32 7	409.75	414.82	419.43
Num	$h_v / \text{kJ/kg}$	390.58	398.16	405.93	413.88	422.00	430.30	438.77
Ref	$c_{p,l} / \text{kJ/kg.K}$	1.2930	1.3156	1.3410	1.3704	1.4049	1.4465	1.4984
Num	$c_{p,l} / \text{kJ/kg.K}$	1.2886	1.3113	1.3370	1.3668	1.4024	1.4466	1.5049
Ref	$c_{p,v} / \text{kJ/kg.K}$	0.8158	0.8544	0.8972	0.9455	1.0007	1.0655	1.1445
Num	$c_{p,v} / \text{kJ/kg.K}$	0.7528	0.7717	0.7904	0.8088	0.8271	0.8450	7 0.8628
Ref	$\mu_l / \mu\text{Pa} - \text{s}$	347.58	303.55	266.53	234.87	207.37	183.13	161.45
Num	$\mu_l / \mu\text{Pa} - \text{s}$	354.53	310.64	272.78	239.77	210.71	184.91	161.85
Ref	$\mu_v / \mu\text{Pa} - \text{s}$	10.00	10.36	10.73	11.10	11.49	11.91	12.37
Num	$\mu_v / \mu\text{Pa} - \text{s}$	10.05	10.47	10.89	11.31	11.72	12.12	12.52

Table A.25: continue...comparison of formulated R134a saturation properties with REFPROP data.

	$T / ^\circ \text{C}$	50	60	70	80	90
Ref	P / Bar	13.18	16.82	21.17	26.33	32.44
Num	P / Bar	13.16	16.80	21.14	26.30	32.41
Ref	$\rho_l / \text{kg/m}^3$	1102.30	1052.90	996.25	928.24	837.83
Num	$\rho_l / \text{kg/m}^3$	1102.00	1052.80	996.51	928.75	838.11
Ref	$\rho_v / \text{kg/m}^3$	66.27	87.38	115.57	155.08	216.76
Num	$\rho_v / \text{kg/m}^3$	66.09	87.10	115.16	154.44	215.39
Ref	$h_l / \text{kJ/kg}$	271.62	287.50	304.28	322.39	342.93
Num	$h_l / \text{kJ/kg}$	271.99	287.92	304.46	321.67	339.59
Ref	$h_v / \text{kJ/kg}$	423.44	426.63	428.65	428.81	425.42
Num	$h_v / \text{kJ/kg}$	447.41	456.21	465.16	474.27	483.50
Ref	$c_{p,l} / \text{kJ/kg.K}$	1.5661	1.6602	1.8039	2.0648	2.7559
Num	$c_{p,l} / \text{kJ/kg.K}$	1.5874	1.7155	1.9398	2.4054	3.7202
Ref	$c_{p,v} / \text{kJ/kg.K}$	1.2461	1.3868	1.6051	2.0122	3.1207
Num	$c_{p,v} / \text{kJ/kg.K}$	0.8804	0.8978	0.9150	70.9320	0.9488
Ref	$\mu_l / \mu\text{Pa} - \text{s}$	141.77	123.61	106.51	89.85	72.45
Num	$\mu_l / \mu\text{Pa} - \text{s}$	141.13	122.46	105.60	90.40	76.72
Ref	$\mu_v / \mu\text{Pa} - \text{s}$	12.92	13.59	14.48	15.77	18.02
Num	$\mu_v / \mu\text{Pa} - \text{s}$	12.92	13.31	13.70	14.08	14.46

Table A.26: Comparison of formulated R1234yf saturation properties with REFPROP data.

	$T / ^\circ \text{C}$	-20	- 10	0	10	20	30	40
Ref	P / Bar	1.509	2.217	3.158	4.375	5.917	7.835	10.184
Num	P / Bar	1.495	2.197	3.135	4.354	5.904	7.834	10.197
Ref	$\rho_l / \text{kg/m}^3$	1236.3	1207	1176.3	1144	1109.9	1073.3	1033.8
Num	$\rho_l / \text{kg/m}^3$	1235.87	1207.57	1177.65	1145.88	1111.92	1075.32	1035.43
Ref	$\rho_v / \text{kg/m}^3$	8.7093	12.559	17.647	24.267	32.796	43.729	57.753
Num	$\rho_v / \text{kg/m}^3$	8.62576	12.4347	17.50177	24.1329	32.7087	43.72213	57.84131
Ref	$h_l / \text{kJ/kg}$	174.87	187.26	200	213.1	226.6	240.51	254.9
Num	$h_l / \text{kJ/kg}$	174.764	187.355	200.22	213.329	226.7	240.399	254.54
Ref	$h_v / \text{kJ/kg}$	350.05	356.72	363.29	369.7	375.89	381.75	387.17
Num	$h_v / \text{kJ/kg}$	350.09	356.78	363.36	369.78	375.97	381.85	387.31
Ref	$c_{p,l} / \text{kJ/kg.K}$	1.2204	1.2539	1.2893	1.3274	1.3693	1.4166	1.4732
Num	$c_{p,l} / \text{kJ/kg.K}$	1.2113	1.23685	1.2801	1.33295	1.3825	1.41705	1.4321
Ref	$c_{p,v} / \text{kJ/kg.K}$	0.84663	0.8848	0.92618	0.97177	1.0237	1.0864	1.167
Num	$c_{p,v} / \text{kJ/kg.K}$	0.8433	0.8790	0.9165	0.9560	0.9978	1.0433	1.0945
Ref	$\mu_l / \mu\text{Pa} - \text{s}$	269.94	237.12	209.42	185.64	164.90	146.53	130.00
Num	$\mu_l / \mu\text{Pa} - \text{s}$	270.01	236.51	208.65	185.14	164.86	146.88	130.41
Ref	$\mu_v / \mu\text{Pa} - \text{s}$	10.340	10.741	11.152	11.581	12.043	12.55	13.152
Num	$\mu_v / \mu\text{Pa} - \text{s}$	10.484	10.370	10.300	9.956	9.750	11.315	12.054

Table A.27: continue...comparison of formulated R1234yf saturation properties with REFPROP data.

	$T / ^\circ \text{C}$	50	60	70	80	90
Ref	P / Bar	13.023	16.419	20.445	25.194	30.803
Num	P / Bar	13.049	16.4496	20.47219	25.21066	30.80812
Ref	$\rho_l / \text{kg/m}^3$	990.38	941.34	883.23	808.98	694.07
Num	$\rho_l / \text{kg/m}^3$	991.29	941.32	882.59	808.42	693.38
Ref	$\rho_v / \text{kg/m}^3$	75.884	99.754	132.33	180.33	269.1
Num	$\rho_v / \text{kg/m}^3$	76.01791	99.67243	130.9987	173.3993	232.0131
Ref	$h_l / \text{kJ/kg}$	269.85	285.53	302.22	320.54	342.79
Num	$h_l / \text{kJ/kg}$	269.285	284.844	301.475	319.484	339.225
Ref	$h_v / \text{kJ/kg}$	391.98	395.93	398.57	398.9	393.32
Num	$h_v / \text{kJ/kg}$	392.2285	396.4279	399.677	401.6901	402.1899
Ref	$c_{p,l} / \text{kJ/kg.K}$	1.5476	1.6564	1.8373	2.2269	4.1862
Num	$c_{p,l} / \text{kJ/kg.K}$	1.43635	1.4577	1.54925	1.7953	2.31735
Ref	$c_{p,v} / \text{kJ/kg.K}$	1.2775	1.4417	1.7235	2.3636	5.688
Num	$c_{p,v} / \text{kJ/kg.K}$	1.1522	1.2169	1.2885	1.3671	1.4540
Ref	$\mu_l / \mu\text{Pa} - \text{s}$	114.89	100.75	87.06	73.026	56.341
Num	$\mu_l / \mu\text{Pa} - \text{s}$	114.84	99.720	84.778	69.906	55.164
Ref	$\mu_v / \mu\text{Pa} - \text{s}$	13.878	14.817	16.126	18.185	22.518
Num	$\mu_v / \mu\text{Pa} - \text{s}$	12.324	12.407	13.981	15.021	15.920

Table A.28: Comparison of formulated R134a vapour properties with REFPROP data.

T	$^{\circ}\text{C}$	5	15	40	45	50	60	70	75	80
P	Bar	2	4	8	10	12	14	16	18	20
Ref	ρ_v	9.32	18.91	36.98	47.34	58.13	66.64	74.45	84.67	94.88
Num	ρ_v	9.34	18.92	37.00	47.35	58.12	66.64	74.47	84.69	94.91
Ref	h_v	405.45	409.38	424.59	425.44	426.41	433.62	441.4	443.48	445.77
Num	h_v	409.92	417.94	438.82	443.10	447.43	456.27	465.28	469.84	474.43
Ref	$c_{p,v}$	0.852	0.927	1.036	1.108	1.169	1.193	1.210	1.257	1.302
Num	$c_{p,v}$	0.799	0.818	0.862	0.871	0.880	0.897	0.915	0.923	0.932
Ref	μ_v	10.981	11.318	12.345	12.588	12.864	13.381	13.915	14.264	14.636
Num	μ_v	11.102	11.514	12.525	12.723	12.921	13.313	13.700	13.893	14.084

Table A.29: Comparison of formulated R1234yf vapour properties with REFPROP data.

T	$^{\circ}\text{C}$	5	15	40	45	50	60	70	75	80
P	Bar	2	4	8	10	12	14	16	18	20
Ref	ρ_v	10.46	21.309	42.116	54.298	67.228	77.43	86.772	99.366	112.11
Num	ρ_v	10.46	21.30	42.11	54.28	67.19	77.37	86.69724	99.21	111.83
Ref	h_v	370.59	375.41	392.17	393.36	394.58	402.19	410.4	412.6	414.98
Num	h_v	370.59	375.43	392.25	393.51	394.81	402.50	410.78	413.11	415.62
Ref	$c_{p,v}$	0.894	0.959	1.072	1.136	1.209	1.248	1.273	1.332	1.391
Num	$c_{p,v}$	0.892	0.949	1.042	1.083	1.123	1.148	1.166	1.192	1.216
Ref	μ_v	11.446	11.83	13.04	13.372	13.762	14.417	15.088	15.595	16.144
Num	μ_v	10.213	10.250	11.942	12.151	12.233	12.126	13.367	13.925	14.534

Estimation of uncertainties for various quantities of interest

Estimation of uncertainties for evaporator capacity, condenser heat rejection rate, refrigerant mass flow rate, compressor work and COP is given here. The dry bulb temperature, wet bulb temperature, cross sectional dimensions of evaporator and condenser ducts, compressor speed, electrical energy input to motor which drives the compressor and velocity of air flow in evaporator and condenser ducts are the measured quantities in the experimental runs. The uncertainty estimation in the above quantities is shown for a typical experimental data set with the following values: compressor speed $N = 600$ rpm, dry bulb temperature $T_D = 30^\circ$, wet bulb temperature $T_W = 20^\circ\text{C}$, air velocity for evaporator $V_{a, \text{evp}} = 2$ m/s, air velocity for condenser $V_{a, \text{cond}} = 1.5$ m/s, cross sectional dimensions of evaporator duct $l \times b = 0.18 \text{ m} \times 0.24 \text{ m}$, cross sectional dimensions of condenser duct $l \times b = 0.36 \text{ m} \times 0.4$, Electrical power input to motor $\dot{W}_m = 0.624$ kW.

1. Humidity ratio (W):

$$W = \frac{[h_{\text{fg},o} - (c_{p,\text{lw}} - c_{p,\text{wv}})T_W] W^* - c_{p,\text{da}}(T_D - T_W)}{h_{\text{fg},o} + c_{p,\text{wv}}T_D - c_{p,\text{lw}}T_W} \quad (\text{A.1})$$

where $h_{\text{fg},o}=2501.6$ kJ/kg, $c_{p,\text{lw}}=4.1868$ kJ/kg.K, $c_{p,\text{wv}}=1.868$ kJ/kg.K, $c_{p,\text{da}}=1.005$ kJ/kg.K and W^* is the saturation air humidity ratio given by the following equation:

$$W^* = 0.62198 \frac{P^*}{P_{\text{atm}} - P^*} \quad (\text{A.2})$$

Equation for P^* is given as:

$$P^* = (221.2 \times 10^2) 10^{q_s} \quad (\text{A.3})$$

$$q_s = -[3.13223 + 3.116 \times 10^{-6}(210 + T_W)^{2.066}] \left(\frac{647.3}{T_W + 273.15} - 1 \right) \quad (\text{A.4})$$

where P^* is the saturation pressure in kPa, $P_{\text{atm}}=89.3$ kPa is surrounding pressure, T_D is dry bulb temperature in $^\circ\text{C}$ and T_W is wet bulb temperature in $^\circ\text{C}$.

The humidity ratio is depends on dry bulb and wet bulb temperature. Therefore uncertainty w_W in humidity ratio W is given by:

$$w_W = \sqrt{\left(\frac{\partial W}{\partial T_D} w_{T_D}\right)^2 + \left(\frac{\partial W}{\partial T_W} w_{T_W}\right)^2} \quad (\text{A.5})$$

where w_{T_D} and w_{T_W} ($\pm 0.1^\circ\text{C}$ for both) are uncertainties in dry bulb temperature T_D and wet bulb temperature T_W respectively. The partial derivatives in Eq. A.5 are determined by finite differences.

2. Enthalpy of moist air (h_{ma}):

$$h_{\text{ma}} = c_{p,\text{da}}T_D + W(h_{\text{fg},o} + c_{p,\text{wv}}T_D) \quad (\text{A.6})$$

The enthalpy of moist air (h_{ma}) depends on dry bulb and humidity ratio. The uncertainty in moist air enthalpy $w_{h_{\text{ma}}}$ is given by:

$$w_{h_{\text{ma}}} = \sqrt{\left(\frac{\partial h_{\text{ma}}}{\partial T_D} w_{T_D}\right)^2 + \left(\frac{\partial h_{\text{ma}}}{\partial W} w_W\right)^2} \quad (\text{A.7})$$

where w_W is uncertainty in W calculate by Eq. A.5.

3. Evaporator capacity (\dot{Q}_{evp})

The evaporator capacity is calculated as follows:

$$\dot{Q}_{\text{evp}} = \frac{V_{\text{a,evp}}A_{\text{evp}}}{v_{\text{a,evp},o}}(\Delta h_{\text{ma}}) \quad (\text{A.8})$$

where $V_{\text{a,evp}}$ is the average air velocity in the evaporator duct, A_{evp} is the cross-sectional area of the evaporator duct, $v_{\text{a,evp},o}$ is air specific volume at the evaporator outlet, Δh_{ma} is change in

air specific enthalpy across evaporator inlet to outlet. Uncertainty in evaporator capacity $w_{\dot{Q}_{\text{evp}}}$ is given by:

$$w_{\dot{Q}_{\text{evp}}} = \sqrt{\left(\frac{\partial \dot{Q}_{\text{evp}}}{\partial V_{\text{a, evp}}} w_{V_{\text{a, evp}}}\right)^2 + \left(\frac{\partial \dot{Q}_{\text{evp}}}{\partial A_{\text{evp}}} w_{A_{\text{evp}}}\right)^2 + \left(\frac{\partial \dot{Q}_{\text{evp}}}{\partial h_{\text{ma}}} w_{h_{\text{ma}}}\right)^2} \quad (\text{A.9})$$

where $w_{V_{\text{a, evp}}} (\pm 0.03 \text{ m/s})$ is uncertainty in air velocity flowing in evaporator, $w_{A_{\text{evp}}} (\pm 0.0002285 \text{ m}^2)$ is uncertainty in cross sectional area of evaporator duct and $w_{h_{\text{ma}}}$ is uncertainty in moist air enthalpy.

4. Condenser heat rejection rate (\dot{Q}_{cond})

$$\dot{Q}_{\text{cond}} = \frac{V_{\text{a, cond}} A_{\text{cond}}}{v_{\text{a, cond, o}}} c_{\text{p, ma, cond}} (\Delta T_{\text{a}}) \quad (\text{A.10})$$

where $V_{\text{a, cond}}$ is the average air velocity in the condenser duct, A_{cond} is the cross-sectional area of the condenser duct, $v_{\text{a, cond, o}}$ is air specific volume at the condenser outlet, $c_{\text{p, ma, cond}}$ is specific heat of moist air and ΔT_{a} is change in air temperature across condenser inlet to outlet. Uncertainty in condenser heat rejection rate $w_{\dot{Q}_{\text{cond}}}$ is given by:

$$w_{\dot{Q}_{\text{cond}}} = \sqrt{\left(\frac{\partial \dot{Q}_{\text{cond}}}{\partial V_{\text{a, cond}}} w_{V_{\text{a, cond}}}\right)^2 + \left(\frac{\partial \dot{Q}_{\text{cond}}}{\partial A_{\text{cond}}} w_{A_{\text{cond}}}\right)^2 + \left(\frac{\partial \dot{Q}_{\text{cond}}}{\partial T_{\text{a}}} w_{T_{\text{a}}}\right)^2} \quad (\text{A.11})$$

where $w_{V_{\text{a, cond}}} (\pm 0.03 \text{ m/s})$ is uncertainty in air velocity flowing in condenser, $w_{A_{\text{cond}}} (\pm 0.0002285 \text{ m}^2)$ is uncertainty in cross sectional area of condenser duct and $w_{T_{\text{a}}} (\pm 0.1^\circ)$ is uncertainty in air temperature.

5. Compressor work (\dot{W}_{comp})

$$\dot{W}_{\text{comp}} = \frac{\Delta E}{t} \eta_{\text{motor}} \eta_{\text{tran}} + \dot{Q}_{\text{loss}} \quad (\text{A.12})$$

where ΔE is electrical energy in kWh, t time in hour, η_{motor} is motor efficiency, η_{tran} is transfer efficiency and \dot{Q}_{loss} is friction heat loss from compressor. Uncertainty in compressor work ($w_{\dot{Q}_{\text{comp}}}$) is given by:

$$w_{\dot{W}_{\text{comp}}} = \sqrt{\left(\frac{\partial \dot{W}_{\text{comp}}}{\partial \Delta E} w_{\Delta E}\right)^2 + \left(\frac{\partial \dot{W}_{\text{comp}}}{\partial \dot{Q}_{\text{loss}}} w_{\dot{Q}_{\text{loss}}}\right)^2} \quad (\text{A.13})$$

where $w_{\Delta E}$ (± 0.1 kWh) is uncertainty in electrical energy input, $w_{\dot{Q}_{\text{loss}}}$ is uncertainty in frictional heat loss determined as follows:

$$\dot{Q}_{\text{loss}} = 1.9728 \times 10^{-03} N + 38.2359 \quad (\text{A.14})$$

because frictional heat loss depends on compressor speed N . The uncertainty in frictional loss \dot{Q}_{loss} is given by:

$$w_{\dot{Q}_{\text{loss}}} = \left(\frac{\partial \dot{Q}_{\text{loss}}}{\partial N}\right) w_N \quad (\text{A.15})$$

where w_N (± 0.05 rpm) is uncertainty in N .

6. Refrigerant mass flow rate (\dot{m}_r)

$$\dot{m}_r = \frac{\dot{Q}_{\text{evp}}}{\Delta h_r} \quad (\text{A.16})$$

The uncertainty in refrigerant mass flow rate ($w_{\dot{m}_r}$) is given by:

$$w_{\dot{m}_r} = \left(\frac{\partial \dot{m}_r}{\partial \dot{Q}_{\text{evp}}}\right) w_{\dot{Q}_{\text{evp}}} \quad (\text{A.17})$$

where $w_{\dot{Q}_{\text{evp}}}$ is calculated from Eq. A.9. The calculated values of uncertainties for various quantities of interest are shown in Table. A.30.

Table A.30: Uncertainty estimation for various quantities of interest

Quantity	Symbol	Value with unit	Uncertainty with unit
Dry bulb temperature	T_D	30°C	± 0.1 °C
Wet bulb temperature	T_W	20°C	± 0.1 °C
Air velocity at evaporator	$V_{a,evp,o}$	2 m/s	± 0.03 m/s
Air velocity at condenser	$V_{a,cond,o}$	1.5 m/s	± 0.03 m/s
Compressor speed	N	600 rpm	± 0.05 rpm
Electrical energy	ΔE	0.052 kWh	± 0.1 kWh
Cross sectional area of evaporator duct	A_{evp}	0.0432 m ²	$\pm 2.285 \times 10^{-04}$ m ²
Cross sectional area of condenser duct	A_{cond}	0.144 m ²	$\pm 2.285 \times 10^{-04}$ m ²
Humidity ratio	W	1.17×10^{-02} kg/kg	$\pm 1.523 \times 10^{-04}$ kg/kg
Moist air enthalpy	h_{ma}	62.189 kJ/kg	± 0.403 kJ/kg
Evaporator capacity	\dot{Q}_{evp}	0.6249 kW	± 0.0368 kW
Condenser heat rejection rate	\dot{Q}_{cond}	1.75 kW	± 0.0324 kW
Compressor work	\dot{W}_{comp}	0.4606 kW	± 0.091 kW
Coefficient of performance	COP	1.356	± 0.0268
Refrigerant mass flow rate	\dot{m}_r	3.533×10^{-03} kg/s	$\pm 2.08 \times 10^{-04}$ kg/s

Bibliography

- [1] Webb, R. L. and Lee, H., Brazed aluminum heat exchangers for residential air-conditioning, *J. Enhanced Heat Transfer*, Vol. 8, pp. 1-14, 2000.
- [2] Wu, X. M. and Webb, R. L., Thermal and hydraulic analysis of a brazed aluminum evaporator, *Applied Thermal Engineering*, Vol. 22, pp. 1369-1390, 2002.
- [3] Chwalowski, M., Didion, D. A. and Domanski, P. A., Verification of evaporator computer models and analysis of performance of an evaporator coil, *ASHRAE Trans.*, Vol. 95 (Part 1), pp. 1229-1236, 1989.
- [4] Domanski, P.A., Simulation of an evaporator with nonuniform one-dimensional air distribution, *ASHRAE Trans.*, Vol. 97 (Part 1), pp. 793-802, 1991.
- [5] Carey, V.P., *Liquid-Vapor Phase-Change Phenomena*, CRC Press, Taylor and Francis Group, Boca Raton, 1992
- [6] Kuehn, T. H., Ramsey, J. W. and Threlkeld, J. L., *Thermal Environmental Engineering*, Third edition, Prentice-Hall, Inc., New Jersey, 1998.
- [7] Collier, J. G., *Convective Boiling and Condensation*, Third edition, McGraw-Hill Book Co. Inc., New York, 1994.
- [8] Shah, M. M., A general correlation for heat transfer during film condensation inside pipes, *Int. J. Heat Mass Transf.*, Vol. 22, pp. 547-556, 1978.
- [9] Darr, J. H. and Crawford, R. R., Modeling of an automotive air conditioning compressor based on experiment data, ACRC project 09, Mechanical and Industrial Engineering Dept, University of Illinois 1206 West Green Street Urbana IL 61801, 1992.
- [10] Steven, J. B., Samuel, F. and Domanski, P. A., Comparative analysis of an automotive air conditioning systems operating with CO₂ and R134a, *Int. J. Refrig.*, Vol. 25, pp. 19-32, 2002.
- [11] Ghodbane, M., An investigation of R152a and hydrocarbon refrigerants in mobile air conditioning, SAE Paper, No. 01-0874, 1999.
- [12] Yoo, S. Y. and Lee, D. W., Experimental study on performance of automotive air conditioning system using R152a refrigerant, *Int. J. Auto. Tech.*, Vol. 10(3), pp. 313-320, 2009.
- [13] Xiao, H. H., Li, P., Xu, Y. J., Zhang, Y. J., Wang, O. and Chen, G. M., Cycle performances of the mixture HFC-161/HFC-134a as the substitution of HFC-134a in automotive air conditioning systems, *Int. J. Refrig.*, Vol. 36, pp. 913-920, 2013.

- [14] Devotta, S., Waghmare, A. V., Sawant, N. N. and Domkundwar, B. M., Alternatives to HCFC-22 for air conditioners, *Applied Thermal Engineering*, Vol. 21, pp. 703-715, 2001.
- [15] Lee, Y. and Jung, D., A brief performance comparison of R1234yf and R134a in a bench tester for automobile applications, *Applied Thermal Engineering*, Vol. 35, pp. 240-242, 2012.
- [16] Pamela, R., Aute, V. and Reinhard, R., Refrigerant R1234yf performance comparison investigation, *Int. Refrig. and AC Conf.*, Purdue University, Purdue, 2010.
- [17] Navarro, E., Martnez, I. O, Nohales, J. and Gonzalvez-Macia, J., Comparative experimental study of an open piston compressor working with R1234yf, R134a and R290, *Int. J. Refrig.*, Vol. 36, pp. 768-775, 2013.
- [18] Navarro, J., Mendoza, J. M., Mota-Babiloni, A., Barragan, A. and Belman, J. M., Experimental analysis of R1234yf as a drop-in replacement for R134a in a vapour compression system, *Int. J. Refrig.*, Vol. 3, pp. 870-880, 2013.
- [19] Cho, H., Lee, H. and Park, C., Performance characteristics of an automobile air conditioning system with internal heat exchanger using refrigerant R1234yf, *Applied Thermal Engineering*, Vol. 61, pp. 563-569, 2013.
- [20] Navarro, J., Moles, F. and Barragan, A., Experimental analysis of the internal heat exchanger influence on a vapour compression system performance working with R1234yf as a drop-in replacement for R134a, *Applied Thermal Engineering*, Vol. 59, pp. 153-161, 2013.
- [21] Ozlem, D. and Hosoz, M., Energy and exergy analysis of an automobile air conditioning system using refrigerant R134a, *Erciyes University Fen Bilimleri Enstitusu Dergisi*, Vol. 23, pp. 188-203, 2007.
- [22] Alkan, A. and Hosoz, M., Comparative performance of an automotive air conditioning system using fixed and variable capacity compressors, *Int. J. Refrig.*, Vol. 33, pp. 487-495, 2010.
- [23] Jabardo, J. M. S., Mamani, W. G. and Ianella, M. R., Modeling and experimental evaluation of an automotive air conditioning system with a variable capacity compressor, *Int. J. Refrig.*, Vol. 25, pp. 1157-1172, 2002.
- [24] Tian, C., Liao, Y. and Li, X., A mathematical model of variable displacement swash plate compressor for automotive air conditioning system, *Int. J. Refrig.*, Vol. 29, pp. 270-280, 2006.
- [25] Lee, G. H. and Yoo, J. Y., Performance analysis and simulation of automobile air conditioning system, *Int. J. Refrig.*, Vol. 23, pp. 243-254, 2000.
- [26] Terry, J. H., Optimization of vehicle air conditioning systems using transient air conditioning performance analysis, *National Renewable Energy Laboratory*, Vol. 1, pp. 1734, 2001.
- [27] Kamar, H. M., Ahmadb, R., Kamsah, N. B. and Mustafa, A. F. M., Artificial neural networks for automotive air-conditioning systems for performance prediction, *Applied Thermal Engineering*, Vol. 50, pp. 63-70, 2013.
- [28] Hosoz, M., Alkan, A. and Metin, H. E., Modelling of an automotive air conditioning system using ANFIS, *J. Ther. Sci. and Tech.*, ISSN, pp. 1300-3615, 2013.

- [29] Bhatti, M. S., Enhancement of R134a automotive air conditioning system, SAE Paper, No. 01-0870, 1999.
- [30] Qi, Z., Zhao, Y. and Chen, J., Performance enhancement study of mobile air conditioning system using microchannel heat exchangers, *Int. J. Refrig.*, Vol. 33. pp. 301-312, 2010.
- [31] Miyagawa, K. and Kayukawa, H., Development of the swash plate type continuously variable displacement compressor, SAE Congress Paper, 980290, 1998.
- [32] Yuan, X. and Chen, Z., Displacement control and kinetic analysis of a novel variable displacement compressor for automotive air conditioner, *Chinese J. Mech. Engg.*, Vol. 14(4), pp. 325-329, 2001.
- [33] Tian, C. Q., Dou, C. P., Yang, X. J., Li, X. T., A mathematical model of variable displacement wobble plate compressor for automotive air conditioning system, *Appl. Therm. Eng.*, Vol. 24. pp. 2467-2486, 2004.
- [34] Tian, C. and Li, X., Transient behavior evaluation of an automotive air conditioning system with a variable displacement compressor, *Applied Thermal Engineering*, Vol. 25, pp. 1922-1948, 2005.
- [35] Tian, C., Xu, H., Zhang, L. and Li, Z., Experimental investigation on the characteristics of variable displacement swash plate compressor, *Applied Thermal Engineering* Vol. 29, pp. 2824-2831, 2009.
- [36] Beauvais, F. N., An aerodynamic look at automotive radiators, SAE Paper No. 650470, 1965.
- [37] Wong, L. T. and Smith, M. C., Air flow phenomena in the louvered fin heat exchanger, SAE Paper No. 730237, 1973.
- [38] Davenport, C. J., Heat transfer and fluid flow in louvered triangular ducts, Ph.D. Thesis, CNAALanchester Polytechnic, 1980.
- [39] Achaichia, A. and Cowell, T. A., Heat transfer and pressure drop characteristics of flat tube and louvered plated fin surfaces, *Expl. Thermal fluid Sci.* Vol. 1, pp. 147-157, 1988.
- [40] Achaichia, A. and Cowell, T. A., A finite difference analysis of fully developed periodic laminar flow in inclined louvere arrays, *Proc. 2nd UK National Heat Transfer Conference, Glasgow*, Vol. 2, pp. 883-888, 1988.
- [41] Howard, P., Preliminary report on flow visualization studies on a two dimensional model of a louvered fin heat exchanger, Penn State Project Report, 1987.
- [42] Kajino, M. and Hiramatsu, M., Research and development of automotive heat exchangers, *Heat transfer in high technology and power engineering*, Yang and Mori, Edition, pp. 420-432, Hemisphere, Washington, D.C., 1987.
- [43] Sahnoun, A. and Webb, R. L., Prediction of heat transfer and friction for the louver Fin geometry, *J. Heat Trans.*, Vol. 114/893, 1992.
- [44] Webb, R. L., Hang, Y. J. and Wang, C. C., Heat transfer and friction correlation for louver fin geometry, *Vehicle Thermal Management System Conference Proceeding*, pp. 533-541, 1995.

- [45] McLaughlin, W. and Webb, R. L., Wet air side performance of louver fin automotive evaporators, SAE Technical Paper 2000-01-0574, doi:10.4271/2000-01-0574, 2000.
- [46] Park, Y. G. and Jacobi, A. M., Air side heat transfer and friction correlations for flat tube louver fin heat exchangers, J. heat transf., Vol. 131, 021801-1,2009.
- [47] Park, Y. G. and Jacobi, A. M., The air side thermal-hydraulic performance of flat tube heat exchangers with louvered, wavy, and plain fins under dry and wet conditions, J. heat transf., Vol. 131, 061801-1, 2009.
- [48] Shah, M. M., A new correlation for heat transfer during boiling flow through pipes, ASHRAE Trans., Vol. 82(2), pp. 66-86, 1976.
- [49] Shah, M. M., Chart correlation for saturated boiling heat transfer: equations and further study, ASHRAE Trans. Vol. 86(1), pp. 185-196, 1982.
- [50] Gungor, K. E. and Winterton, R. H. S., A general correlation for flow boiling in tubes and annuli. Int. J. Heat Mass Transf., Vol. 29, pp. 351-358, 1986.
- [51] Gungor, K.E. and Winterton, R. H. S., Simplified general correlation for saturated flow boiling and comparisons of correlations with data. Chem. Eng. Res Des., Vol. 65, pp. 148-156, 1987.
- [52] Liu,Z. and Winterton, R. H. S., A general correlation for saturated and subcooled flow boiling in tubes and annuli based on a nucleate pool boiling equation. Int. J. Heat Mass Transf., Vol. 34(11). pp. 2759-2766, 1991.
- [53] Kim, S. and Mudawar, I., Universal approach to predicting saturated flow boiling heat transfer in mini/micro-channels Part II. Two-phase heat transfer coefficient, Int. J. Heat and Mass Transf., Vol. 64, pp. 1239-1256, 2013.
- [54] Ghiaasiaan, S. M., *Two-Phase Flow Boiling and Condensation*, Cambridge University Press, New York, 2008.
- [55] Kandlikar, S. G., History, advances, and challenges in liquid flow and flow boiling heat transfer in microchannels: a critical review, Int. J. Heat Transf., Vol. 134(3), 034001, 2012.
- [56] Kim, S. and Mudawar, I., Review of databases and predictive methods for heat transfer in condensing and boiling mini/micro-channel flows, Int. J. Heat and Mass Transf., Vol. 77, pp. 627-652, 2014.
- [57] Cheng, L. and Mewes, D., Review of two-phase flow and flow boiling of mixtures in small and mini channels, Int. J. Multiphase Flow, Vol. 32, pp. 183-207, 2006
- [58] Ong, C. L., Macro to microchannel transition in two-phase flow and evaporation, Doctorate thesis, Ecole Polytechnique, de Lausanne, Switzerland, 2010.
- [59] Kandlikar, S.G.,A general correlation for saturated two-phase flow boiling heat transfer inside horizontal and vertical tubes, J. Heat Transf., Vol. 112, pp. 219-228, 1990.
- [60] Cheng, P. and Wu, H. Y., Macro and microscale phase change heat transfer, Advances in Heat Transfer, Vol. 39, pp. 461-563, 2006.

- [61] Kew, P. A. and Cornwell, K., Correlations for prediction of flow boiling heat transfer in small-diameter channels, *Applied Thermal Engineering*, Vol. 17, pp. 705-715, 1997.
- [62] Brauner, N. and Ullmann, A., The prediction of flow boiling maps in minichannels. In 4th Japanese European Two-Phase Flow Group Meeting, Kyoto, 24-28, September, 2006.
- [63] Li, W. and Wu, Z., A general criterion for evaporative heat transfer in micro/mini-channels, *Int. J. Heat Mass Transf.*, Vol. 53, pp. 1967-1976, 2010.
- [64] Shah, M. M., Evaluation of general correlations for heat transfer during boiling of saturated liquids in tubes and annuli, *HVAC and Research*, Vol. 12(4), pp. 1047-1063, 2006.
- [65] Revellin, R. and Thome, J. R., Experimental investigation of R134a and R245fa two-phase flow in microchannels for different flow conditions. *Int. J. Heat and Fluid Flow*, Vol. 28, pp. 63-71, 2007.
- [66] Steiner, D. and Taborek, J., Flow boiling heat transfer in vertical tubes correlated by an asymptotic model. *Heat Transf. Engg.*, Vol. 13(2), pp. 43-68, 1992.
- [67] Shah, M. M., Unified correlation for heat transfer during boiling in plain mini/micro and conventional channels, *Int. J. Refrig.*, S0140-7007(16)30408-X, 2016.
- [68] Chen, J. C., A correlation for boiling heat transfer to saturated fluids in convective flow, *Ind. Engng Chem. Proc. Des. Dev.* Vol. 5(3), pp. 322-329, 1966.
- [69] Klimenko, V. V., A generalizes correlation for two-phase forced flow heat transfer, *Int. J. Heat Mass Transf.* Vol. 31(3), pp. 541-552, 1988.
- [70] Klimenko, V. V., A generalized correlation for two-phase forced flow heat transfer-second assessment, *Int. J. Heat Mass Transf.*, Vol. 33(10), pp. 2073-2088. 1990
- [71] Hinde, D. K., Dobson, M. K., Chato, J. C., Mainland, M. E. and Rhines, N., Condensation of R134a with and without oils, ACRC Technical Report 26, University of Illinois at Urbana-Champaign, 1992.
- [72] Chato, J. C., Laminar condensation inside horizontal and inclined tubes, *ASHRAE J.*, Vol. 4, pp. 52-60, 1996.
- [73] Hubbard, M. G. and Dukler, A. E., The characterization of flow regimes for horizontal two-Phase flow: statistical analysis of wall pressure fluctuations, proceedings of the 1966 heat transfer and fluid mechanics Institute, Stanford University Press, Stanford, CA, pp. 100-121, 1966.
- [74] Lin, P. Y. and Hanratty, T. J., Detection of slug flow from pressure measurements, *Int. J. Multiphase Flow*, Vol. 15(2), pp. 209-226, 1989.
- [75] Nicholson, M. K., Aziz, K. and Gregory, G. A, Intermittent two phase flow: predictive models, 27th Canadian Chemical Engineering Conference, Calgary, Alberta, 1978.
- [76] Barnea, D., Shoham, O., Taitel, Y. and Dukler, A. E., Flow pattern transition for gas-liquid flow in horizontal and inclined pipes:Comparisons of experimental data with theory, *Int. J. Multiphase Flow*, Vol. 6, pp. 217-225, 1980.
- [77] Baker, O., Simultaneous flow of oil and gas, *oil and Gas J.*, Vol. 53, pp. 185-195, 1954.

- [78] Mandhane, J. M., Gregory, G. A. and Aziz, K., A flow pattern map for gas-liquid flow in horizontal pipes, *Int. J. of Multiphase Flow*, Vol. 1, pp. 537-553, 1974.
- [79] Taitel, Y. and Dukler, A. E., A model for predicting flow regime transitions in horizontal and near horizontal gas-liquid flow, *AICE J.*, Vol. 22(1), pp. 47-55, 1976.
- [80] Butterworth, D., A visual study of mechanisms in horizontal, air- water flow, AERE Report M2556, Harwell, England, 1972.
- [81] Dukler, A. E. and Hubbard, M. G., A model for gas-liquid slug flow in horizontal and near horizontal tubes, *Ind. Eng. Chem. Fundamentals*, Vol.14, No. 4, pp. 337-347, 1975.
- [82] Soliman, H. M., On the annular-to-wavy flow pattern transition during condensation inside horizontal tubes, *The Canadian J. Chem. Engg.*, Vol. 60, pp. 475-481, 1982.
- [83] Soliman, H. M., Correlation of mist-to-annular transition during condensation, *The Canadian J. Chem. Engg.*, Vol. 61, pp. 178-182, 1983.
- [84] Dobson, M. K., Chato, J. C., Wattelet, J.P., Gaibel, J. A., Ponchner, M., Kenney, P. J., Shimon, R. L., Villaneuva, T. C., Rhines, N. L., Sweeney, K. A., Allen, D. G. and Hershberger, T. T., Heat transfer and flow regimes during condensation in horizontal tubes, ACRC Technical Report 57, University of Illinois at Urbana-Champaign, 1994.
- [85] Dobson, M. K., Chato, J. C., Hinde, D. K. and Wang, S. P., Experimental evaluation of internal condensation of refrigerants R12 and R134a, *ASHRAE Trans.*, Vol. 100(1), pp. 744-754, 1994.
- [86] Soliman, H. M., The mist-annular transition during condensation and its influence on the heat transfer mechanism, *Int. J. of Multiphase Flow*, Vol. 12(2), pp. 277-288, 1986.
- [87] Nusselt, W., Die oberflächenkondensation des Wasserdampfes, *Z.Verein Deutscher Ingenieure*, Vol. 60, pp. 541 -575, 1916.
- [88] Dhir, V. and Lienhard, J., Laminar film condensation on plane and axisymmetric bodies in non uniform gravity, *ASME J. Heat transf.*, Vol. 93, pp. 97-100, 1971.
- [89] Bromley, L. A., Effect of heat capacity on condensation, *Ind. Engg. Chem.*, Vol. 44, pp. 2966-2969, 1952.
- [90] Rohsenow, W. M., Heat transfer and temperature distribution in laminar film condensation, *Trans. ASME*, Vol. 78, pp. 1645-1648, 1956.
- [91] Jaster, H. and Kosky, P. G., Condensation in a mixed flow regime, *Int. J. Heat and Mass Transf.*, Vol. 19, pp. 95-99, 1976.
- [92] Rosson, H. F. and Meyers, J. A., Point values of condensing film coefficients inside a horizontal tube, *Chemical Engineering Progress Symposium Series*, Vol. 61, No. 59, pp. 190-199, 1965.
- [93] Tien, C. L., Chen, S. L. and Peterson, P. F., Condensation inside tubes, EPRI Project 1160-3 Final Report, EPRI, Palo Alto, CA, 1988.
- [94] Denglor, C. E. and Addoms, J. N., Heat transfer mechanism for vaporization of water in a vertical tube, *Chemical Engineering Progress Symposium Series*, Vol. 52(18), pp. 95-103, 1956.

- [95] Lockhart, R. W. and Martinelli, R. C., Proposed correlation of data for isothermal, two phase, two component flow in pipes, *Chemical Engineering Progress*, Vol. 45(1), pp. 39-48, 1947.
- [96] Dittus, F. W. and Boelter, L. M. K., Heat transfer in automotive radiators of the tubular type, *University of California Publications on Engineering*, Vol. 2(13), Berkeley, CA, p. 443, 1930.
- [97] Cavallini, A. and Zecchin, R., A dimensionless correlation for heat transfer in forced-convective condensation, proceedings of the fifth Int. Heat Transf. Conf., Japan Society of Mechanical Engineers, Vol.3, pp. 309-313, 1974.
- [98] Carpenter, E. F. and Colburn, A. P., The effect of vapour velocity on condensation inside tubes, proceedings of general discussion on heat transfer, *Inst. Mech. Eng. and ASME*, pp. 20-26, 1951.
- [99] Soliman, H. M., Schuster, J. R. and Berenson, P. J., A general heat transfer correlation for annular flow condensation, *ASME J. Heat transf.*, Vol. 90, pp. 267-276, 1968.
- [100] Chen, S. L., Gerner, F. M. and Tien, C. L., General film condensation correlations, *experimental heat transfer*, Vol. 1, pp. 93-107, 1987.
- [101] Solvay Fluor, *Solkane R134a Thermodynamics*, Technical Service, Refrigerants, Product bulletin No. T/09.04/01/E.
- [102] Cleland, A. C., Polynomial curve-fits for refrigerant thermodynamic properties: extension to include R134a, *Int. J. Refrig.*, Vol. 17(4), pp. 245-249, 1994.
- [103] Huber, M. L., Laesecke, A. and Perkins, R. A., Model for the viscosity and thermal conductivity of refrigerants, including a new correlation for the viscosity of R134a, *Ind. Eng. Chem. Res*, Vol. 42, pp. 3163-3178, 2003.
- [104] Tanaka, K. and Higashi, Y., Thermodynamic properties of HFO-1234yf (2,3,3,3-tetrafluoropropene), *Int. J. Refrig.*, Vol. 33, pp. 474-479, 2010.
- [105] Richter, M., McLinden, M. O. and Lemmon, E. W., Thermodynamic properties of 2,3,3,3-Tetrafluoropropene(R1234yf): Vapor pressure and $p - \rho - T$ measurements and an equation of state, *J. Chem. Eng. Data*, Vol. 56, pp. 3254-3264, 2011.
- [106] Moises, A. M. N. and Barbosa, J. R., Modeling of State and thermodynamic cycle properties of HFO-1234yf Using a cubic equation of state, *J. Braz. Soc. Mech. Sci. and Eng.*, Vol. XXXII(5), pp. 461, 2010.
- [107] Huber, M. L., Laesecke, A. and Perkins, R. A., Model for the viscosity and thermal conductivity of refrigerants, including a new correlation for the viscosity of R134a, *Ind. Eng. Chem. Res*, Vol. 42, pp. 3163-3178, 2003.
- [108] Huber, M. L. and Assael, M. J., Correlations for the viscosity of 2,3,3,3-tetrafluoropropene (R1234yf) and trans-1,3,3,3-tetrafluoropropene (R1234ze(E)), *Int. J. Refrig.*, Vol. 71, pp. 39-45, 2016.
- [109] Zhang, M. and Webb, R. L., A correlation of two-phase friction for refrigerants in small-diameter tubes, *Exp. Thermal Fluid Sci*, Elsevier, Vol. 25, pp. 131-139, 2001.

- [110] Leck, T. J., Evaluation of HFO-1234yf as a potential replacement for R134a in refrigeration applications, 3rd IIR Conference on Thermophysical Properties and Transfer Processes of Refrigerants, Paper No. IIR-155, Boulder, CO, pp. 23-26, 2009.
- [111] Lemmon, E. W. and McLinden, M. O., Thermodynamic properties of propane. III. A reference equation of state for temperatures from the melting line to 650 K and pressures up to 1000 MPa, J. Chem. Eng. Data, Vol. 54, pp. 3141-3180, 2009.
- [112] Perkins, R. A. and Huber, M. L., Measurement and correlation of the thermal conductivity of 2,3,3,3-Tetrafluoropropene (R1234yf) and trans-1,3,3,3-Tetrafluoropropene (R1234ze(E)), J. Chem. Eng. Data, Vol. 56, pp. 4868-4874, 2011.
- [113] Dymond, J. H., Bich, E., Vogel, E., Wakeham, W. A., Vesovic, V., Assael, M. J., Millat, J. and Castro, C. A., *Transport Properties of Fluids, Their Correlation, Prediction and Estimation*, Cambridge University Press, Cambridge, p. 66, 1996.
- [114] Ely, J. F. and Hanley, H. J. M., Prediction of transport properties: Thermal conductivity of pure fluids and mixtures, Ind. Eng. Chem. Fundam., Vol. 20, pp. 323332, 1981.
- [115] Zivi, S. M., Estimation of steady-state steam void-fraction by means of the principle of minimum entropy production, J. Heat Transf., Vol. 86, pp. 247-252, 1964.
- [116] Tsay, Y. L. and Lin, T. F., Combined heat and mass transfer in laminar gas stream flowing over an evaporating liquid film, *Warme und Stoffubertragung*, Springer, Vol. 25(4), pp. 221-231, 1990.
- [117] Churchill, S. W., A comprehensive correlating equation for laminar assisting force and free Convection, AICHE J., Wiley Online Library, Vol. 23(1), pp. 10-16, 1977.
- [118] Chen, T. S. and Armaly, B. F., *Mixed Convection in External Flow*, University of Missouri, Rolla Rolla, Missouri.
- [119] Cengel, Y. A. and Boles, M. A., *Thermodynamics*, Sixth edition, the McGraw-Hill Company, 2008.
- [120] Barnhart, J., An experimental investigation of flow patterns and liquid entrainment in a horizontal tube evaporator, Ph.D. thesis, Dept. of Mechanical and Industrial Engineering, University of Illinois at Urbana-Champaign, 1992.
- [121] Wattelet, J. P., Heat transfer flow regimes of refrigerants in a horizontal tube evaporator, Ph.D. thesis, Dept. of Mechanical and Industrial Engineering, University of Illinois at Urbana-Champaign, 1994.
- [122] Wattelet, J. P., Chato, J. C, Christoffersen, B. R. Gaibel, J. A., Ponchner, M., Kenney, P. J., Shimon, R. L., Villaneuva, T. C , Rhines, N. L., Sweeney, K. A., Allen, D. G., and Hershberger, T. T., Heat transfer flow regimes of refrigerants in a horizontal tube evaporator, ACRC Technical Report 55, University of Illinois at Urbana-Champaign, 1994.
- [123] Jeffreys, H., On the formation of water waves by wind, Proceedings of the royal society, Vol. A107, p. 189, 1925.

- [124] Jeffreys, H., On the formation of water waves by wind, Proceedings of the royal society, Vol. A110, p. 241, 1926.
- [125] McAdams, W. H., Heat Transmission, 3rd Edition, McGraw-Hill, New York, 1954.
- [126] Chisholm, D., A theoretical basis for the lockhart-martinelli correlation for two-phase flow, Int. J. heat and mass Trans., Vol. 10, p. 1767-1778, 1967.
- [127] Baroczy, C. J., A systematic correlation for two-phase pressure drop, Int. Chem. Engg. Prog. Symposium., Vol. 62(57), p. 232-249, 1965.
- [128] Chisholm, D. and , Sutherland, L. A., Prediction of pressure gradients in pipeline systems during two-phase flow, Proceedings of the institute mechanical engineers., Vol. 184(3c), p. 24-32, 1970.
- [129] Friedel, L., Improved friction pressure drop correlation for horizontal and vertical two-phase pipe flow, European two-phase flow group meeting, paper no. 2,Ispra, Italy, 1979.
- [130] Yang, C. Y. and Webb, R. L., Friction pressure drop of R12 in small hydraulic diameter extruded aluminum tubes with and without micro-fins, Int. J of heat and mass Tranf., Vol. 39(4), p. 801-805, 1996.
- [131] Wang, C. C. and Chang, Y. J., Two-phase flow heat transfer and friction characteristics of R22 and R407C, ASHRAE Trans., Vol. 102(1), p. 830-838, 1996.
- [132] Wang, C. C. and Lu, D. C., Two-phase flow pattern for R134a inside a 6.5 mm smooth tube, ASHRAE Trans., Vol. 103(1), p. 803-812, 1997.
- [133] Wang, C. C., Lu, D. C. and Chiang, C. S., Visual observation of two-phase flow pattern of R22, R134a and R407C in 6.5 mm smooth tube, Experimental thermal and fluid science, Vol. 15, p. 395-405, 1997.
- [134] Wambsganss, M. W., France, J. A., Jendrzejczyk, T. N. and Tran, T. N, Boiling heat transfer in a horizontal small tube, J. heat Tranf., Vol. 115(4), p. 963-972, 1993.
- [135] Wambsganss, M. W., France, J. A. and Tran, T. N, Small circular and rectangular channel boiling with two refrigerant, Int. J. multiphase flow., Vol. 22(3), p. 485-498, 1996.
- [136] Tran, T. N, Pressure drop and heat tranfer study of two phase flow in small channel, Ph.D. Dissertation,Texas Tech University,Lubbock, Texas, 1998.
- [137] Tran, T. N., Chyu, M. W.,Wambsganss, M. W. and France, D. M. , Two-phase pressure drop of refrigerants in small channel, Proceedings of the internatinal conference of compact heat exchangers and enhancement technology for process industries, Banff, Canada, p. 293-302, 1999.
- [138] Chang, S. D. and Ro, S. T., Pressure drop of pure refrigerant and their mixtures flowing in capillary tubes, Int. J. of multiphase flow, Vol. 22(3), p. 551-561, 1996.
- [139] Zhang, M. and webb, R. L., effect of oil on R134a condensation in parallel flow condensers, Vehicle thermal management systems conference proceedings, SAE, p. 369-376, 1997.

- [140] Cengel, Y. A. and Ghajar, A. J., *Heat and mass transfers*, forth edition, the McGraw-Hill Company, 2008.
- [141] Shah, M. M., Comprehensive correlations for heat transfer during condensation in conventional and mini/ micro channels in all orientations, *Int. J. Refrig.*, Vol. 67, p. 22-41. 2016.
- [142] Col, D. D., Torresin, D., Cavallini, A., Heat transfer and pressure drop during condensation of the low GWP refrigerant R1234yf, *Int. J. Refrig.*, Vol. 33, p. 1307-1318. 2010.